Functional characterization of PERM1-dependent control of metabolic activity and mitochondrial network remodeling in contractile tissues

Inaugural-Dissertation

zur

Erlangung des Doktorgrades

der Mathematisch-Naturwissenschaftlichen Fakultät

der Universität zu Köln

vorgelegt von

Theresa Bock

aus Boppard

Köln, 2023

Berichterstatter: (Gutachter)	Prof. Dr. Marcus Krüger
	Prof. Dr. Jan Riemer
Tag der mündlichen Prüfung:	27.10.2023

Content

Abstract I
Zusammenfassung II
Acknowledgements III
List of publications V
List of figures VI
List of tables VI
Abbreviations VII
1. Introduction 1
1.1. Cardiac and skeletal muscle physiology 1
1.2. Pre- and postnatal development of cardiac and skeletal muscle 6
1.3. Mitochondria in cardiac and skeletal muscle 8
1.3.1. Mitochondrial morphology and function 8
1.3.2. Mitochondrial dynamics 13
1.3.3. Mitochondrial skeletal muscle subpopulations 14
1.3.4. Skeletal muscle plasticity and mitochondrial biogenesis 16
1.4. PERM1 – PGC-1- and ERR-induced regulator in muscle 1 19
1.5. Aims of this thesis 23
2. Results 24
2.1. Publication (I): Phosphoproteomics of the developing heart identifies PERM1 – An outer mitochondrial membrane protein 24
2.1.1. Summary publication I 24
2.1.2. My contribution to publication I 25
2.2. Follow-up of publication I 25
2.2.1. PERM1 expression increases postnatally and *Perm1*$^{-/-}$ muscles develop mitochondrial phenotype 25
2.3. Publication II: PERM1 interacts with the MICOS-MIB complex to connect the mitochondria and sarcolemma via ankyrin B 30
2.3.1. Summary publication II 30
2.3.2. My contributions to publication II 30
2.4. Follow-up of publication II 31
2.4.1. ANKB interaction site is located between the amino acids 6-55 of PERM1 31
2.4.2. PERM1 interacts with the ankyrin-repeat domain of ANKB 33

3. Discussion 35
3.1. Pre- and postnatally increasing PERM1 levels might contribute to mitochondrial energy metabolism in a PGC-1- and ERR-dependent manner 35
3.2. PERM1 might be involved in the stabilization of the MICOS/MIB complex in cardiac and muscle tissue 37
3.3. PERM1 behaves like a MICOS/MIB complex protein of the OMM with so far unknown biogenesis and import pathway 40
3.4. Long PERM1 isoform interacts with the costamere organizer ANKB and anchors mitochondria to the sarcolemma 46
3.5. Conclusion and outlook 51
4. Experimental 54
4.1.1. Organisms 54
4.1.2. Constructs 54
4.1.3. Primers 55
4.2. Methods 56
4.2.1. Tissue lysis and digestion 56
4.2.2. Protein concentration determination 57
4.2.3. Plasmids 57
4.2.4. Cell culture and lysis 57
4.2.5. Immunoprecipitation of PERM1 and ANKB 58
4.2.6. In-solution/on-beads digestion 58
4.2.7. MS-based proteome analysis 59
4.2.8. MS data processing and analysis 59
4.2.9. Expression and purification of recombinant PERM1ΔTM and ANKB constructs 60
4.2.10. Surface plasmon resonance 61
5. References 62
6. Erklärung zur Dissertation 73
7. Curriculum Vitae 74
8. Appendix 76

Abstract

Cardiac and skeletal muscle have a great demand of energy for contraction and ion transport, which can be covered by high fluxes of ATP. Therefore, cardiac and skeletal muscle function, particularly during development, rely on a dense network of mitochondria and oxidative metabolism. Major regulators of mitochondrial biogenesis in striated muscle are members of the peroxisome proliferator-activated receptor γ coactivator 1 (PGC-1) and estrogen-related receptor (ERR) families. Here, we reported that PGC-1-and ERR-induced regulator in muscle 1 (PERM1) is increasingly expressed in cardiac and skeletal muscle tissue during early postnatal development. Furthermore, we determined the interactome of PERM1 and identified PERM1 as a tissue-specific interactor of the fully-assembled mitochondrial contact site and cristae organization system (MICOS)/mitochondrial intermembrane bridging (MIB) complex. Association of PERM1 with the outer mitochondrial membrane is dependent on a conserved C-terminal α-helical transmembrane domain. Moreover, we observed an interaction of the N-terminus of PERM1 with the N-terminal ankyrin-repeat domain of the costamere organizing protein ankyrin B (ANKB). Ablation of *Perm1* using a systemic knockout mouse revealed overall downregulation of mitochondrial proteins, reduction in mitochondrial DNA, diminished mitochondrial membrane potential, increased presence of reactive oxygen species and antioxidant proteins, and reduced oxygen flux in isolated skeletal muscle tissue. Moreover, *Perm1*$^{-/-}$ muscles revealed a reduction in peripheral, subsarcolemmal mitochondria, particularly around capillaries. We suggest that interaction with ANKB and the intermediate filament proteins vimentin and nestin contributes to the establishment of a functional mitochondrial reticulum and enables optimal transport and supply with metabolites and ATP, and that PERM1 acts as a scaffold protein. Therefore, PERM1 might represent a major regulator of cardiac and skeletal muscle modulating mitochondrial metabolism and capacity.

Zusammenfassung

Herz- und Skelettmuskeln haben einen hohen Energiebedarf für die Kontraktion und den Ionentransport, der durch hohe ATP-Ströme gedeckt werden kann. Daher ist die Funktion von Herz- und Skelettmuskeln und insbesondere ihre Entwicklung auf ein dichtes Netz von Mitochondrien und den oxidativen Stoffwechsel angewiesen. Zu den wichtigsten Regulatoren der mitochondrialen Biogenese in der quergestreiften Muskulatur gehören die Mitglieder der Familien des Peroxisom-Proliferator-aktivierten Rezeptor γ-Coaktivators 1 (PGC-1) und des Östrogen-verwandten Rezeptors (ERR). Hier beschrieben wir, dass PGC-1-und ERR-induzierter Regulator im Muskel 1 (PERM1) während der frühen postnatalen Entwicklung verstärkt in Herz- und Skelettmuskelgewebe exprimiert wird. Darüber hinaus bestimmten wir das Interaktom von PERM1 und identifizierten PERM1 als gewebespezifischen Interaktor des vollständig zusammengesetzten mitochondrialen Kontaktstellen- und Cristae-Organisationssystems (MICOS)/mitochondrialen Intermembran-Brücken-Komplexes (MIB). Die Assoziation von PERM1 mit der äußeren mitochondrialen Membran ist abhängig von einer konservierten C-terminalen α-helikalen Transmembrandomäne. Darüber hinaus beobachteten wir eine Interaktion des N-Terminus von PERM1 mit der N-terminalen Ankyrin-Repeat-Domäne des Costamer-organisierenden Proteins Ankyrin B (ANKB). Die Ablation von *Perm1* in systemischen Knockout-Mäusen ergab eine allgemeine Herunterregulierung mitochondrialer Proteine, eine Verringerung der mitochondrialen DNA, ein vermindertes mitochondriales Membranpotenzial, eine erhöhte Präsenz reaktiver Sauerstoffspezies und antioxidativer Proteine sowie einen verringerten Sauerstoffffluss in isoliertem Skelettmuskelgewebe. Darüber hinaus wiesen *Perm1*$^{-/-}$ Muskeln eine Verringerung der peripheren, subsarkolemmalen Mitochondrien auf, insbesondere um die Kapillaren herum. Wir vermuten, dass die Interaktion mit ANKB und den Intermediärfilamentproteinen Vimentin und Nestin zum Aufbau eines funktionellen mitochondrialen Retikulums beiträgt und einen optimalen Transport und eine optimale Versorgung mit Metaboliten und ATP ermöglicht, und dass PERM1 als Gerüstprotein fungiert. Daher könnte PERM1 einen wichtigen Regulator der Herz- und Skelettmuskulatur darstellen und den mitochondrialen Stoffwechsel und die mitochondriale Kapazität modulieren.

Acknowledgements

Accomplishing my PhD would have not been possible without the help of colleagues, collaborators, friends and family in the last four years.

First and foremost, I'd like to thank my supervisor Prof. Dr. Marcus Krüger. Thank you for your supervision, our fruitful discussions, and the close teamwork within the last years. Thank you for always being available to take questions, ideas, opinions etc.

Thank you to the rest of my thesis committee, Prof. Dr. Jan Riemer and Prof. Dr. Ulrich Baumann, who I've known now more than 8 years – what a time. Thank you not only for assessing my thesis but also for watching and helping me mature from a young bachelor student to this point right now. I'd like to thank my TAC committee Prof. Dr. Aleksandra Trifunovic and Prof. Dr. Ana García-Sáez for the ideas and support during the last years.

The biggest thank you goes to my Krügis, without you I couldn't have done anything. Thank you for brightening any work day, for being my best cheerleaders, for helping me out when I was about to give up, for the endless scientific and non-scientific discussions, the philosophic questions during lunchtime, the boardgame evenings (although I usually hate boardgames), the afterwork beer… I could go on forever probably. Luisa, Lena, Kerstin, Angela, Micha, Fred, Bianca, Patricia, Janica, Sebi, Dominik, Andreas, Hendrik, Uli, Sebastian, Zeinab, Sina, Saskia, Nitin, Minhaz – you are gems! Special thank you to my beloved Clara, who took me under her wing when I started as a Master student working on the PERM1 topic and was not only the best supervisor that I could have asked for, but also became a wonderful friend to me. Thank you, dear!

Thank you as well to the whole Proteomics Facility for helping wherever they could and being a secret part of the group. Thank you also to the CECAD Imaging Facility for their enthusiasm in providing their help at multiple stages of this project. Here, I'd also like to thank all my collaborators who were involved in this story, which include Hien Rozsivalova, Philipp Hammerschmidt, Susanne Brodesser, and Steffen Lütke, and all the others that were part of the project before I jumped in.

At this point, I'd like to thank my outstanding students, who contributed to this story and helped it to grow and move forward. Thank you, Sophie, Max, Caro, and Sějla!

Thank you to my lovely Montreal friend Heather, who read and edited this thesis. You're the best and you'll always hold a special place in my heart. Also, thank you to one of my best friends since first year Bachelor, Soto, for going through this roller coaster with me the last 10 years; for the endless Mensa dates where we were not only once questioning what were are doing here – but look at us now!

Thank you to all the wonderful members of the Reloc RTG. It wouldn't have been the same without you! I love how we grew together, loved the discussions, collaborations, and the relaxed get togethers. Thank you to the jGBM Cologne and the CECAD PhD & PostDoc Committee for the nice collaborations – I enjoyed our meetings and planning events during the last years.

And now I'd like to move on with the other people that helped me finishing this thesis – to my friends and family (that have no scientific background and no clue at all what I'm doing day after day at work). Thank you to "le Girls", the best friends I could have wished for! Thank you for everything – for celebrating the highs and crying with me through the lows (and there have been plenty), for every evening we sat together and ordered take out, for every vacation we went on together, for every night we danced until our feet were tired, and every time we laughed until our tummy hurt.

Thank you to my beloved family, my parents and my wonderful sister. And to my grandparents who are not here anymore, but who I'd loved to proudly present this thesis. You are my home and my biggest support system – love you to the moon!

List of publications

The two following publications form the basis of this thesis:

(I) Aravamudhan, S.*, Türk, C.*, **Bock, T.**, Keufgens, L., Nolte, H., Lang, F., Krishnan, R. K., König, T., Hammerschmidt, P., Schindler, N., Brodesser, S., Rozsivalova, D. H., Rugarli, E., Trifunovic, A., Brüning, J., Langer, T., Braun, T., Krüger, M. (2021). Phosphoproteomics of the developing heart identifies PERM1 – an outer mitochondrial membrane protein. *Journal of Molecular and Cellular Cardiology. 154 (2021) 41-59. doi: https://doi.org./10.1016/y.jmcc.2021.01.010.*

(II) **Bock, T.***, Türk, C.*, Aravamudhan, S., Keufgens, L., Bloch, W., Rozsivalova, D. H., Romanello, V., Nogara, L., Blaauw, B., Trifunovic, A., Braun, T., Krüger, M. (2021). PERM1 interacts with the MICOS-MIB complex to connect the mitochondria and sarcolemma via ankyrin B. *Nature Communications. (2021)12:4900. doi: https://doi-org/10.1038/s41467-021-25185-3.*

***** These authors contributed equally.

List of figures

Fig. 1: Heart wall and cardiomyocyte morphology. 2
Fig. 2: Hierarchical organization of skeletal muscle.. 4
Fig. 3: The electron transport system of mitochondria. 11
Fig. 4: Schematic and electron-microscopic representation of mitochondrial subpopulations in skeletal muscle fibers. 15
Fig. 5: Mitochondrial biogenesis is mediated by PGC-1α. 17
Fig. 6: Graphical abstract publication I. 24
Fig. 7: Proteomic profiling of postnatal *Perm1*$^{-/-}$ muscle tissue showed gradual downregulation of mitochondrial proteins. 26
Fig. 8: The conserved amino acids 6-55 of PERM1 are important for the interaction with ANKB. 32
Fig. 9: PERM1 interacts with the N-terminal 24ANK region of ANKB. 34
Fig. 10: PERM1 is downregulated in TAC-operated mouse hearts. 38
Fig. 11: MEMSAT predicted a transmembrane helix in ARMC1. 42
Fig. 12: PERM1 and OMP25 do not follow the predicted consensus sequence for OMM targeting. 43
Fig. 13: Model of dual function of PERM1 in the nucleus and mitochondria of skeletal muscle. 52

List of tables

Table 1: List of utilized mouse strains. 54
Table 2: List of used cell lines. 54
Table 3: List of utilized constructs. 54
Table 4: List of utilized primers. 55

Abbreviations

AE-MS	Affinity-enrichment mass-spectrometry
ACADM	Medium-chain specific acyl-CoA dehydrogenase (mitochondrial)
ACOX1	Peroxisomal acyl-coenzyme A oxidase 1
ADP	Adenosine diphosphate
AMPK	5' Adenosine monophosphate-activated protein kinase
ANKB/G/R	Ankyrin B/G/R
ANKRD	Ankyrin-repeat domain-containing protein
ARMC1	Armadillo repeat-containing protein 1
ATP	Adenosine triphosphate
BAG6	BCL2-associated athanogene 6
BCL2L13	BCL2-like protein 13
bHLH	Basic helix-loop-helix
BMP4	Bone morphogenic factor 4
BN-PAGE	Blue native polyacrylamide gel electrophoresis
BNIP3	BCL2/adenovirus E1B 19 kDa protein-interacting protein 3
Ca^{2+}	Calcium ions
CAA	Chloroacetamide
CaMKII	Ca^{2+}/calmodulin-dependent protein kinase II
CK2	Casein kinase 2
CKMT2	Creatine kinase S-type (mitochondrial)
CREB	Cyclic adenosine monophosphate-response element-binding protein
CPT1B/CPT2	Carnitine O-palmitoyltransferase 1 (muscle)/2
CTRP3	C1q/tumor necrosis factor-related protein-3
CV	Compensation voltage

DDA	Data-dependent acquisition
DRP1	Dynamin-1-like protein
DTT	Dithiothreitol
ER	Endoplasmic reticulum
ERR	Estrogen-related receptor
ERRE	Estrogen-related receptor response element
ETS	Electron transport system
FAD	Flavin adenine dinucleotide
FBN	Fibrillin
FIS1	Mitochondrial fission 1 protein
FKBP8	FK506-binding protein 8
FUNDC1	FUN14 Domain-containing 1
GCL	Glutamate-cysteine ligase
GCLM	Glutamate-cysteine ligase modifier
GLUT4	(facilitated) Glucose transporter member 4
GOBF	Gene Ontology biological function
GOCC	Gene Ontology cellular compartment
GOMF	Gene Ontology molecular function
GSH	Glutathione
GSSG	Glutathione disulfide
HEK	Human embryonic kidney (cells)
HIGD1A	Hypoxia-induced gene domain family-1a
IFM	Interfibrillar mitochondria
IMM	Inner mitochondrial membrane
IMS	Intermembrane space
IP_3R	Inositol 1,4,5-triphosphate receptor

IPTG	Isopropyl β- d-1-thiogalactopyranoside
IQR	Interquartile range
KANK1/2	KN motif and ankyrin-repeat domain-containing protein ½
K_D	Equilibrium dissociation constant
LFQ	Label-free quantification
LV	Left ventricle
MEF2	Myocyte enhancing factor 2
MFF	Mitochondrial fission factor
MFN1/2	Mitofusin 1/2
MHC	Myosin heavy chain
MIB	Mitochondrial intermembrane bridging complex
MICOS	Mitochondrial contact site and cristae organization system
MIM	Mitochondrial import (complex)
MTCH1/2	Mitochondrial carrier homolog1/2
mtDNA	Mitochondrial DNA
mtEF	(mitochondrial) Elongation factor
mtIF	(mitochondrial) Translation initiation factor
mtRRF	(mitochondrial) Ribosome-recycling factor
mtRF1L	(mitochondrial) Release factor-1-like
MTS	Mitochondrial targeting signal
MTX	Metaxin
MuSC	Muscle stem cell
MYF	Myogenic factor
MYL	Myosin light chain
MYOD	Myoblast determination protein
Na^+	Sodium ions

NCX	Sodium/calcium exchanger
NRF	Nuclear respiration factor
OD	Optical density
OMM	Outer mitochondrial membrane
OPA1	Optic atrophy 1
OXPHOS	Oxidative phosphorylation
P	Phosphate
PERM1	PGC-1- and ERR-induced regulator in muscle 1
PGC-1	Peroxisome proliferator-activated receptor γ coactivator 1
PINK1	PTEN-induced putative kinase 1
PM	Peripheral mitochondria
PPAR	Peroxisome proliferator-activated receptor
PPRE	PPAR response element
PROTACs	Proteolysis targeting chimeras
PODXL	Podocalyxin
PON	Paraoxonase
pSILAC	pulsed stable isotope labeling with amino acids in cell culture
PTM	Post-translational modification
PVALB	Parvalbumin
Q	Ubiquinone
QH_2	Ubiquinol
$Q^{\cdot -}$	Ubisemiquinone free radical
qRT-PCR	Quantitative real-time polymerase chain reaction
R	Resolution
ROS	Reactive oxygen species
RU	Response unit

rRNA	Ribosomal RNA
SAM	Sorting and assembly machinery
SAM50	Sorting and assembly machinery component 50 homolog
SDH	Succinate dehydrogenase
SDS	Sodium dodecyl sulfate
SHH	Sonic hedgehog protein
SIRT1/3	Silent information regulator 1/3
SPR	Surface plasmon resonance
SR	Sarcoplasmic reticulum
SSM	Subsarcolemmal mitochondria
SYNJ2B	Synaptojanin-2-binding protein
TAC	Transverse aortic constriction
TCA	Tricarboxylic acid cycle
TCEP	Tris(2-carboxyethyl)phosphine
TFAM	(mitochondrial) Transcription factor A
TIM	Translocase of inner mitochondrial membrane
TIF1β	Transcriptional intermediary factor 1β
TM	Transmembrane segment
TNNI1	Troponin I, slow skeletal muscle
TOB	Topogenesis of β-barrel proteins
TOM	Translocase of outer mitochondrial membrane
tRNA	Transfer RNA
UPS	Ubiquitin-proteasome system
VAMP1	Vesicle-associated membrane protein 1
VDAC	Voltage-dependent anion channel

1. Introduction

1.1. Cardiac and skeletal muscle physiology

The musculoskeletal system of mammals comprises three different types of muscle tissue – cardiac, skeletal, and smooth muscle. Cardiac muscle builds the walls of the heart responsible for the contraction of the heart and allowing the blood to be pumped through the cardiovascular system. Skeletal muscle is attached to bones to enable all body movements. Smooth muscle forms blood vessels and is found in the gastrointestinal tract, bronchioles, uterus, and bladder. While smooth muscle often contracts involuntarily and consists of different types of filaments that are not arranged in sarcomeres, cardiac and skeletal muscle are both classified as striated muscles because of their microscopic appearance.

Cardiac muscle, often known as myocardium, is located in the heart wall is the middle layer and is surrounded by the endocardium and the epicardium (**Fig. 1a**). The endocardium, forms the interface between the cardiac chamber and the cardiac wall and builds the cardiac valves. Further, it connects the blood vessels to the heart, as it continues with the epithelium of the blood vessels. The epicardium then, is surrounded by a double-membraned sac called the pericardium. It is composed of a fibrous membrane that is lined with a double-layered serous membrane producing pericardial fluid to protect and lubricate the heart.

The center part of the heart wall, the myocardium, consists of multiple sheets of cardiac muscle cells called cardiomyocytes, which form the contractile part of the wall. Their distinct orientation in a complex swirling pattern allows for effective blood circulation. Cardiomyocytes are the predominant cell type in atria and ventricles and form functional syncytia with neighboring cardiomyocytes via intercalated discs to form long fibers (**Fig. 1a**). Each cell is comprised of myofibrils, which are comprised of parallel thin and thick filaments forming the basic unit of contraction, the sarcomere (**Fig. 1b**). The regular orientation into sarcomeres is responsible for the striated appearance of cardiac muscle. Sarcomeres are described as the segment between two anchoring points of actin filaments called the Z-line or Z-disc. The Z-line is surrounded by a lighter I-band (mainly composed of thin actin filaments) followed by a darker A-band (composed of thin actin and thick myosin filaments). Besides myosin-binding protein C, titin, myomesin, and obscurin, all playing important structural and regulatory roles. A single thick filament contains >200 perfectly aligned myosin molecules assembled into highly ordered bundles with bipolar

nature [1]. While the myosin motor heads all face outwards, the long myosin rods all face inwards. The myosin heads have an actin binding site to form actomyosin cross-bridges in the overlap zone of the A-band. Thin filaments are mainly composed of actin, but also contain tropomyosin, which covers double-stranded actin filaments, and troponin located next to tropomyosin [2].

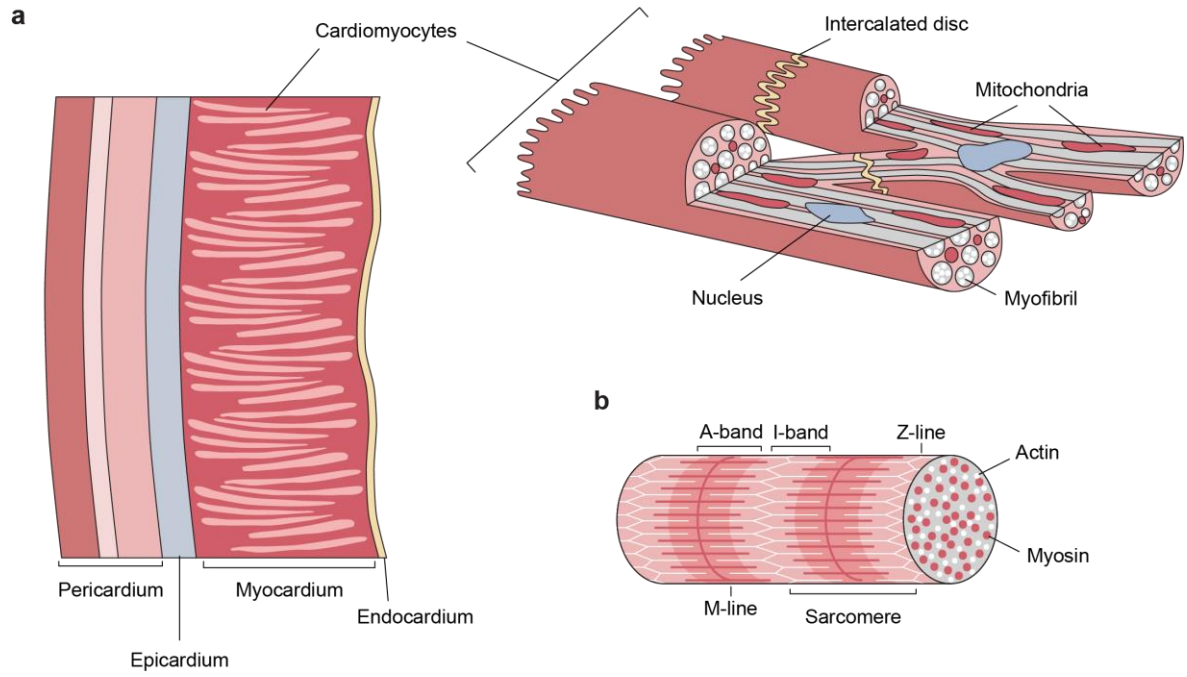


Fig. 1: Heart wall and cardiomyocyte morphology. (a, left) The heart wall is composed of pericardium, epicardium, myocardium, and endocardium (from outside to inside). (Right) The myocardium harbors multiple layers of cardiomyocytes that are mononucleated and connected to neighboring cells by intercalated discs. Each cardiomyocyte is composed of myofibrils. (b) Detailed view of myofibrils shows regular arrangement of actin and myosin fibers in sarcomeres. Thin actin fibers meet at the Z-line surrounded by the I-band free from myosin. Thick myosin fibers are overlapped with the actin fibers within the A-band, whereas the M-line is free from actin.

The complex interplay between thin and thick filaments, between actin and myosin, results in muscle contraction. The excitation-contraction coupling is initiated by an action potential which leads to a depolarization in the myocyte membrane. The action potential is produced spontaneously by the sinoatrial node in the wall of the right atrium [3]. The sinoatrial node is a group of specialized cardiomyocytes that are known as the primary pacemaker cells which set the rhythm for the heart contraction. They do not contain sarcomeres and are therefore only weakly contractile, but are connected to contractile cardiomyocytes through gap junctions. Action potentials travel as impulses along the sarcolemma (cell membrane of cardiac and skeletal muscle fibers) through these gap junctions and depolarization transmission is then mediated through transverse T-tubules penetrating the membrane

leading to the activation of dihydropyridine receptors on the T-tubule membrane that release calcium ions (Ca^{2+}) into the cell. The increase in cellular Ca^{2+} causes the opening of ryanodine receptors located on the sarcoplasmic reticulum (SR) inducing a calcium spark [4]. The SR forms a specialized form of endoplasmic reticulum (ER) in myocytes important for the storage of cellular calcium. By releasing calcium from the SR, troponin binds Ca^{2+} followed by a conformational change that subsequently induces tropomyosin to enable the interaction between actin and myosin, which it blocks when the muscle in inactive. As soon as actomyosin cross-bridges are formed, adenosine triphosphate (ATP) binds the ATP-binding domain of the myosin motor head resulting in the dissociation of myosin from actin. Hydrolyzation of ATP to adenosine diphosphate (ADP) and phosphate (P) causes a conformational change in the myosin head which then moves towards the positive end of actin, where it binds to a new location on the actin filament and thereby shortens the muscle. Subsequent ADP release resets myosin to its original position by moving the actin filament and causing a further shortening of the sarcomere. This cycle is repeated as long as intracellular Ca^{2+} levels are high [5]. The decrease in Ca^{2+} results in tropomyosin blocking the myosin-binding sites on actin preventing formation of actomyosin cross-bridges. The removal of Ca^{2+} from the cell is mediated by multiple ion transporters including the sarcoplasmic reticulum Ca^{2+}-ATPase, pumping Ca^{2+} back into the SR, the sarcolemmal sodium-calcium exchanger, pumping one Ca^{2+} out of the cell in exchange for sodium, the sarcolemmal Ca^{2+}-ATPase, pumping Ca^{2+} directly out of the cell using ATP, and the mitochondrial Ca^{2+} uniporters, pumping Ca^{2+} into the mitochondria [6].

Cardiac muscle tissue is under involuntary control by the autonomic nervous system of the body and leads to a resting heart rate between 60 and 100 bpm [7]. Heart contraction requires high energy amounts which is enabled by a constant blood flow to provide oxygen and nutrients and by a dense network of mitochondria to deliver ATP equivalents.

Although cardiac and skeletal muscle harbor similar features, they differ both on a structural and functional level. Skeletal muscle is attached to bones via tendons and consists of multiple fascicles of muscle fibers, where each structural unit (myofiber, fascicle, entire muscle) is surrounded by a different type of connective tissue (**Fig. 2**). Unlike cardiomyocytes, muscle fibers are polynucleated and form syncytia, with the nuclei, termed myonuclei, arranged along the inside of the sarcolemma. However, under pathological conditions or during development and regeneration, nuclei migrating to the center of a myofiber can be observed.

Fusion of myoblasts occurs during myogenesis and is mediated by the muscle-specific fusogens myomarker and myomerger; a single muscle fiber can contain hundreds to thousands of nuclei [8]. These myonuclei are post-mitotic, their shape is elongated and flattened, and they are evenly distributed along the longitudinal axis of the muscle fiber. Based on the paradigm of the myonuclear domain theory, it has been suggested that each nucleus has a limited transcriptional capacity, only synthesizing transcripts for use near the nucleus [9].

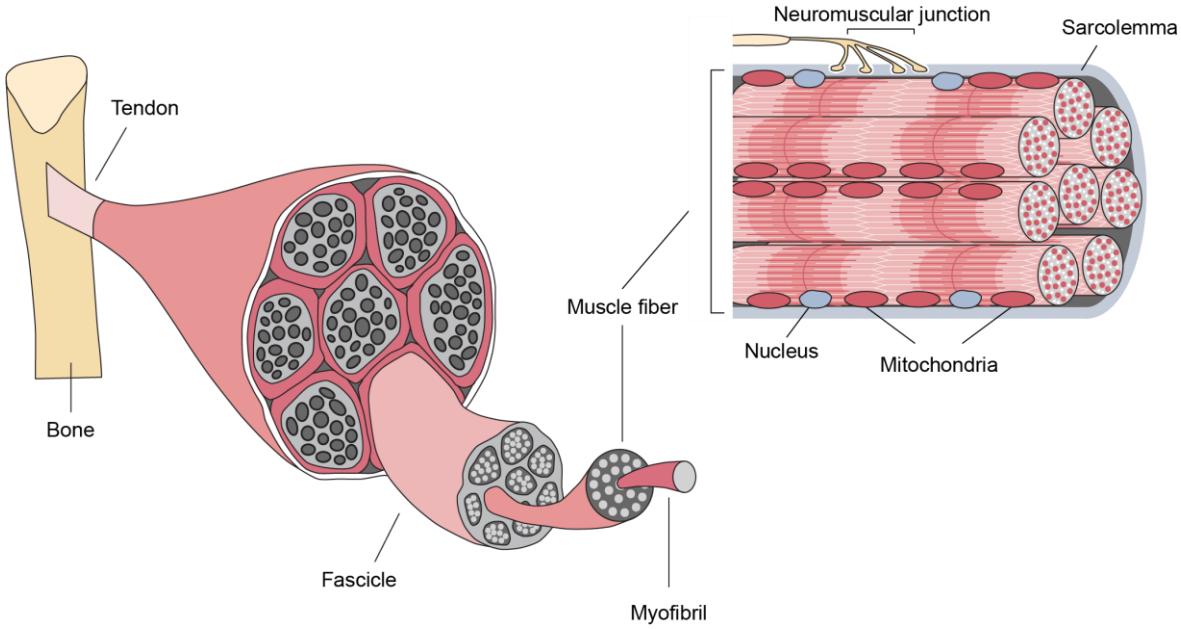


Fig. 2: Hierarchical organization of skeletal muscle. (Left) Muscles are attached via tendons to bones and contain multiple fascicles of muscle fiber which are comprised of myofibrils. (Right) Muscle fibers are polynucleated and form a syncytium with a dense network of mitochondria and are innervated by motoneurons at regions called neuromuscular junctions.

While cardiac muscle fibers are primarily innervated by the sinoatrial node, skeletal muscle fibers are innervated through neuromuscular junctions (**Fig. 2**). The neuromuscular junction is defined as the site where synaptic axon terminals of motor neurons come into close proximity with the sarcolemma of the muscle fiber, referred to as the motor end plate. Synaptic terminals in neuromuscular junctions are cholinergic, secreting acetylcholine. Ligand-gated ion channel-coupled nicotinic receptors bind the acetylcholine secreted by the axon which results in the opening of their channels and causes an influx of sodium ions (Na^+) into the fiber initiating membrane depolarization. Subsequent calcium influx cascades and contraction is similar to cardiomyocytes.

Almost all skeletal muscle contractions are initiated by the brain by electrochemical signals mediated through the nervous system to the motor neuron at neuromuscular junctions. In cases of involuntary reflexes, signals are not sent from the brain but originate in the spinal cord through a feedback loop with the grey matter.

The skeletal muscle mass consists of more than 600 individual muscles and therefore represents the largest tissue in the human body essential for motion and support [10]. Moreover, skeletal muscle helps to hold the body's posture, can store amino acids and maintains core body temperature. While the heart has limited fiber heterogeneity expressing only two myosin isoforms – with β-myosin heavy chain (MHC) predominantly found in ventricles of large animals and α-MHC expressed in the atria – skeletal muscle can be divided into two main fiber types with further subdivisions [11]. Type I fibers describe slow-twitch fibers, while type II fibers are defined as fast-twitch fibers. Every fiber type has distinct metabolic, contractile, and motor unit properties and can also be identified by the expression of specific MHC isoforms. Type I fibers are characterized by slow oxidative motor units, which generate slow twitches with small forces, but are highly resistant to fatigue. Their capillary density and myoglobin levels are high, which result in a dark red muscle color. These fibers are important for endurance and rely on aerobic, oxidative metabolism to generate ATP and, thus, they have abundant mitochondria. Type I fibers mainly express MHC-I encoded by *Myh7*. Fast-twitch type II fibers can be subdivided into two types, defined as oxidative type IIA and glycolytic type IIX fibers, whereas more subgroups have been identified in different organisms, with type IIB being particularly important for research as it is the main fiber type expressed in rodents (but absent in humans). Type IIA fibers resemble type I fibers in multiple aspects including high resistance to fatigue, high capillary supply, high myoglobin content, red color, and high amounts of mitochondria. They produce moderate levels of force and are identified by the expression of MHC-IIA encoded by *Myh2*. Lastly, type IIX fibers are the fastest fibers, able to exhibit large forces by using anaerobic glycolysis to meet the required energy need. Thus, their mitochondrial content is low, as well as their capillary density and myoglobin expression, resulting in a pale muscle color. Fast twitches with strong forces, however, come with the price of a low resistance to fatigue. Type IIX fibers be identified by MYH-IIX expression of *Myh1*. It has been observed that endurance athletes have higher levels of type I fibers, while sprint athletes are dependent on high levels of type IIX fibers [12, 13]. Shifting of fiber types between hybrid fibers (expressing two or

more MHC isoforms) and pure fibers, as well as between slow and fast fiber types, due to exercise has been proposed [14].

1.2. Pre- and postnatal development of cardiac and skeletal muscle

All three types of muscle tissue, cardiac, skeletal, and smooth, are derived from the mesoderm. In particular, cardiac muscle is derived from the lateral splanchnic mesoderm, while skeletal muscle is derived from the paraxial mesoderm and smooth muscle from the splanchnic mesoderm.

After gastrulation, the mesodermal layer differentiates into mesothelium, which will form the pericardium, endothelium, which will form the endocardium, and myocardium. A primitive heart tube is formed by the third week of human embryogenesis defined as the tubular heart which further develops chambers and blood vessels resulting in complete septa and valves by the end of the ninth week. During heart positioning, the myocardium also produces and deposits a thick layer of extracellular matrix. Within this time of the heart development, in humans at day 22, the heart starts beating.

At the stage of the primitive heart, the first cardiomyocytes develop from cardiomyocyte precursors in a first wave of heart growth and division of existing cardiomyocytes is subsequently the major mode of heart growth. While prenatally, the heart can grow through proliferation, the proliferative capability of adult cardiomyocytes to grow new muscle is very limited. The time point at which cardiomyocytes lose their regenerative capacity and ability to undergo the cell cycle is not fully resolved, but it coincides with the transition from hyperplastic to hypertrophic growth. In rodents, this transition happens approximately two weeks after birth, though it is assumed that this time point is species-specific and could be influenced by gestation time, number of offspring per birth, and maturity at birth [15, 16]. There have been several studies providing evidence that heart regeneration after injury is possible within the first few days after birth, and some studies even report regenerative capacity of adult mouse cardiomyocytes by inducing repair mechanisms after myocardial infarction [17, 18]. However, relatively little is known about both early postnatal heart development and cardiac regeneration and repair mechanisms in larger animals like pigs, chows, or sheep, and humans.

Although cardiac and skeletal muscle myogenesis both generate striated muscles, they follow different developmental mechanisms. All skeletal muscle is derived from the paraxial mesoderm. Somites differentiate first into sclerotome (which forms vertebrae) and dermomyotome through stimulation by myogenic regulatory factors including WNT, sonic hedgehog protein (SHH), and bone morphogenic protein 4 (BMP4) [10]. Subsequently, the dermomyotome splits to form the dermatome (which forms skin) and the myotome (which forms muscle).

To differentiate the myogenic progenitors into myofibers, orchestrated regulation of basic helix-loop-helix (bHLH) transcription factors, myoblast determination protein 1 (MYOD), myogenic factor 5 (MYF5), myogenin, and myogenic factor 6 (MYF6, also known as MRF4) is crucial. The transition from myogenic progenitors into myoblasts is mediated by MYOD and MYF5, while the differentiation from myoblasts into myotubes is regulated primarily by myogenin. These differentiation processes take place either in the somite, giving rise to muscles associated with the vertebral column, or the myoblasts, which migrate out into the body with the help of the connective tissue framework.

Similar to cardiac myogenesis, muscle growth in prenatal muscle tissue is achieved by hyperplasia and by fusion into polynucleated fibers specifically, while postnatal muscle growth primarily results from hypertrophy upon addition of novel myofibrils. Postnatal skeletal muscle development is mediated by a population of specialized cells, muscle stem cells (MuSC), also known as satellite cells, that derived from a subset of myogenic progenitors. Satellite cells are located underneath the basal lamina of skeletal muscle fibers and in adult muscle, it is well established that MuSCs are primarily in a quiescent state and become activated i.e. after injury.

The developing body requires distinct temporal and spatial control of transcription to correctly assign cell identities during embryogenesis. The heart is the first organ that is formed in the developing body that is essential for its survival. Post embryonic and fetal development, some tissues retain remarkable plasticity and regenerative capacity including skin, gut, liver, and skeletal muscle, the latter associated to some extent with the presence of MuSCs. Although neonatal heart still possesses considerable high differentiation and regeneration abilities, repair and regeneration processes are limited in adults. Therefore, cardiac dysfunction represents a key cause of morbidity and mortality.

1.3. Mitochondria in cardiac and skeletal muscle

Cardiac and skeletal muscle require large amounts of energy for contraction and ion transport. This is accomplished by high fluxes of ATP. Although skeletal muscle has developed an additional reservoir of energy through the expression of creatine kinase and the reversible conversion of creatine + ATP to phosphocreatine + ADP, the vast majority of the required ATP is generated by mitochondria. Besides energy production, mitochondria possess other important functions, including redox and calcium homeostasis, lipid biosynthesis, and regulation of apoptosis. While neonatal cardiomyocytes use glycolysis as major energy source and their mitochondria have been observed to have dynamic movement within the cytosol, adult cardiomyocytes rely on fatty acid oxidation with mitochondria exhibiting reduced cytosolic motility [19].

Mitochondria and mitochondria-related organelles originated due to bacterial endosymbiosis of the primitive forms of eukaryotic cells, due to more recent evidence most likely from *Rhodospirillales* or *Rickettsiales*, which was initially proposed in the late 1960s, and is now widely accepted [20, 21]. The 16.6 kb long mitochondrial genome is formed by double-stranded DNA, defined as mitochondrial DNA (mtDNA), and encodes 13 proteins, which are involved in oxidative phosphorylation (OXPHOS) and translation, as mitochondria encode their own transfer RNAs (tRNAs) and ribosomal RNAs (rRNAs). The remaining proteins found in mitochondria are expressed in the nucleus and subsequently transported into mitochondria. Therefore, mitochondria have a complex and essential relationship with the nucleus, as it expresses important mitochondrial enzymes, as well as mtDNA repair genes. Notably, one cardiomyocyte has around 7,000 copies of mtDNA, whereas one skeletal muscle fiber holds around 3,500 copies, underlining the importance and reliance on aerobic ATP production by the myocardium [22].

1.3.1. Mitochondrial morphology and function

Mitochondria are encased with a double membrane, resulting in four different compartments essential for their function: the outer mitochondrial membrane (OMM), the inner mitochondrial membrane (IMM), the enclosed intermembrane space (IMS), and the mitochondrial matrix. The matrix represents the core inner compartment of mitochondria which holds the mtDNA, ribosomes, enzymes and small molecules, as well as cofactors and

ions. Important metabolic pathways are situated in the matrix including the tricarboxylic acid (TCA) cycle, the urea cycle, and the beta oxidation of fatty acids.

The OMM is composed of a lipid bilayer similar to that of the plasma membrane and is equipped with numerous integrated membrane proteins – porins – formed by voltage-dependent anion channel (VDAC). VDAC is responsible for the transport of nucleotides, ions, and metabolites between the cytosol and the IMS. Furthermore, the OMM contains proteins that are essential for the folding and import of proteins to all mitochondrial compartments including proteins of the translocase of outer mitochondrial membrane (TOM) complex and the sorting and assembly machinery (SAM) complex. Matrix proteins containing a N-terminal presequence with a mitochondrial targeting signal (MTS) can cross the OMM via the TOM complex and are subsequently targeted to the translocase of inner mitochondrial membrane (TIM) complex that mediates the translocation to the matrix. Moreover, the OMM holds proteins that are involved in mitochondrial dynamics, as well as in mitophagy. PTEN-induced putative kinase 1 (PINK1) is constitutively imported from the cytosol into the mitochondrial intermembrane space and rapidly degraded by mitochondrial proteases and the proteasome under basal conditions. Under stress conditions, however, PINK1 import is inhibited and it is stabilized at the OMM where it phosphorylates mitochondrial ubiquitin and the E3 ligase Parkin following subsequent recruitment of Parkin to target and degrade OMM proteins including TOM20, VDAC, and mitofusion 1 and 2 (MFN1/2) [23]. PINK1/Parkin-independent mitophagy is mediated by the several OMM proteins, including BCL2/adenovirus E1B 19 kDa protein-interacting protein 3 (BNIP3), NIX (also known as BNIP3L), FUN14 domain-containing 1 (FUNDC1), FK506-binding protein 8 (FKBP8), and BCL2-like protein 13 (BCL2L13), particularly in cells under hypoxic or mitochondrial membrane potential dissipation conditions [24]. Furthermore, the OMM can associate with the ER to form structures known as mitochondrial-associated-membranes which are involved in calcium homeostasis and the regulation of lipid metabolism, autophagy, and mitophagy [25].

Although the enclosed space between the two mitochondrial membranes is only about 60 nm in diameter, the IMS is crucial for mitochondrial functions as it builds an important buffer system between the cytosol and the mitochondrial matrix by regulating the exchange and maintenance of metabolites, lipids, proteins, metals, and other enzyme cofactors necessary for mitochondrial function, as well as redox regulation [26]. Moreover, IMS proteins are

involved in the assembly and maintenance of some complexes of the respiratory chain, that are associated with the IMM and localize to cristae structures. Structurally, the IMS can be subdivided into two compartments, the peripheral IMS between the OMM and the IMM, and the intracristae space separated from the peripheral IMS through small connections formed by cristae junctions. These junctions also functionally divide the two IMS compartments as they restrict the diffusion of proteins and thereby increase the performance of the ATP synthesis. This might restrict the production of reactive oxygen species (ROS) to the intracristae space and, thus, reduces their subsequent migration to extramitochondrial compartments [27]. Apart from assembling OXPHOS complexes, proteins in the IMS are also part of the mitochondrial import machinery: CHCHD4/MIA40 is involved in import and oxidative protein folding of multiple IMS proteins containing disulfide bonds. The existence of proteins with disulfide bonds in the IMS might sound surprising at first, since the majority of the cell and cytosol have reducing properties. The IMS, however, is more oxidizing than the cytosol and the rest of the mitochondrion, and this redox state is maintained independently from the cytosol and the matrix by two primary redox regulatory systems that utilize thiol-disulfide redox chemistry – the glutathione (GSH)/glutathione disulfide (GSSG) redox couple and the reduced/oxidized thioredoxin redox couple [28].

As mentioned above, the IMS and the IMM, in particular the cristae, hold the heart the mitochondrion, the respiratory chain complexes, that produce ATP required for multiple cellular functions, that are particularly important for cardiomyocytes and oxidative skeletal muscle fibers which rely mainly on ATP derived from OXPHOS. The OXPHOS machinery linking the TCA cycle to ATP production is composed of five complexes with subunits that are encoded both by the nuclear and the mitochondrial genome. These complexes include NADH-ubiquinone oxidoreductase (complex I), succinate-ubiquinone oxidoreductase, also known as succinate dehydrogenase (SDH) (complex II), ubiquinol-cytochrome *c* oxidoreductase (complex III), cytochrome *c* oxidase (complex IV), and ATP synthase (complex V). Complexes I-IV, also defined as the electron transfer system (ETS), transfer electrons derived from the TCA cycle or fatty acid oxidation and import protons from the matrix to the IMS, generating an electrochemical proton gradient that drives the synthesis of ATP (**Fig. 3**).

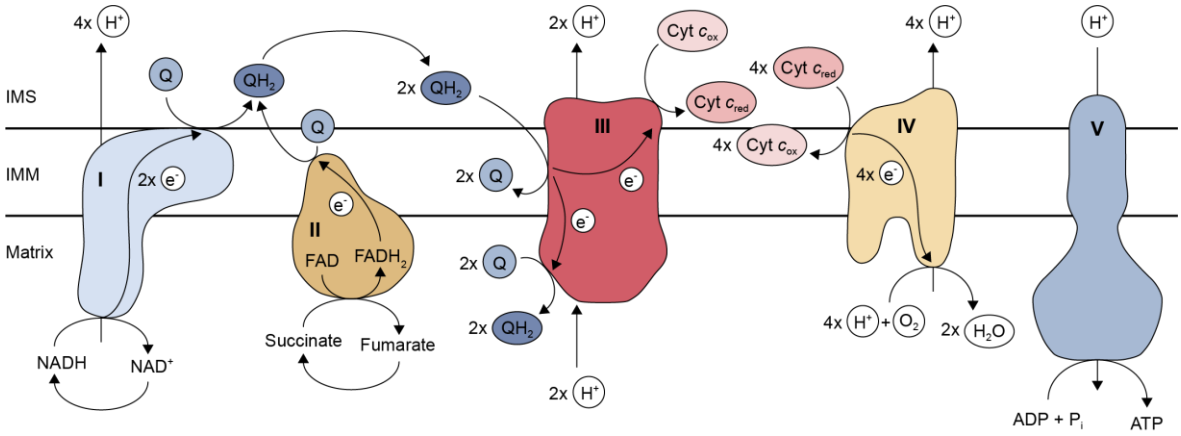


Fig. 3: **The electron transport system of mitochondria.** Complex I and complex II receive electrons from NADH and $FADH_2$ to reduce ubiquinone. The resulting ubiquinol can be oxidized by complex III in the two-step Q-cycle and the electrons are transferred on cytochrome *c*. Upon oxidation of cytochrome *c*, complex IV can use the electrons and transfer them to an oxygen molecule as the terminal electron acceptor. The protons pumped by complex I, III, and IV generate a proton gradient in the IMS that drive ATP synthesis executed by complex V. Adapted from [29].

With 45 subunits and a molecular weight of around 1 MDa, complex I is the biggest of the five OXPHOS complexes and it is characterized by its L-shape consisting of two different arms [30]. While the hydrophobic arm, only containing subunits encoded by the mtDNA, resides in the IMM, the hydrophilic arm faces the matrix. Upon oxidation of NADH to NAD^+ at the hydrophilic arm by flavin mononucleotide, two electrons are released and transferred on ubiquinone (Q), which is reduced to ubiquinol (QH_2), through eight iron-sulfur clusters, and four protons are directed across the IMM. Similar to complex I, complex II transfers two electrons to ubiquinone, however, no protons are added to the proton gradient at this step. These electrons are released upon oxidation of succinate from the TCA cycle to fumarate using the cofactor flavin adenine dinucleotide (FAD) and the three iron-sulfur clusters in the two matrix-facing subunits SDHA and SDHB. The other two of the four nuclear-encoded complex II subunits, SDHC and SDHD, are hydrophobic and embedded in the IMM. Both complex I and complex II represent entry points to the ETS. Moreover, there is a third entry point through the electron transfer flavoprotein-ubiquinone (ETF-Q) oxidoreductase accepting electrons from ETF in the mitochondrial matrix to reduce ubiquinone. The enzyme contains a flavin and a single iron-sulfur cluster and is an important electron acceptor in fatty acid beta oxidation [31]. Unlike the other complexes, ETF-Q is not integrated in the IMM.

Next, complex III, a symmetrical dimer with three core subunits, cytochrome *b*, cytochrome *c*, and an iron-sulfur cluster, transfers two electrons from ubiquinol to cytochrome *c* in a

process called the Q-cycle. This two-step cycle is necessary because only one of the electrons from ubiquinol to a cytochrome *c* can be transferred at a time. QH_2 binds, is oxidized and passes the electron to cytochrome *c* accompanied by a release of two protons to the IMS. The second electron is accepted by ubiquinone, which is reduced to the ubisemiquinone free radical $Q^{\cdot -}$ and remains bound to the complex, while ubiquinone and cytochrome *c* leave the complex. Then, another ubiquinol molecule binds and is again oxidized and passes one electron to cytochrome *c*. The ubisemiquinone radical accepts the second electron and two protons from the matrix and is reduced to ubiquinol, which is then released [32]. Upon each of the two oxidation steps, two protons are pumped to the IMS. Therefore, although reduction of $Q^{\cdot -}$ consumes two protons, complex III adds two protons to the protein gradient. The last enzyme of the ETS, complex IV, transfers four electrons from reduced cytochrome *c* to the terminal electron acceptor oxygen while pumping four protons across the membrane. Complex IV contains 14 different subunits in mammals, two heme molecules, and two binuclear copper centers [33].

Finally, all protons pumped into the IMS by complex I, III, and IV create a chemical and electrical gradient energizing the IMM, defined as the proton-motive force, that drives ATP production by the ATP synthase, complex V. This complex is composed of two different subunits, F_0, which is embedded in the IMM and harbors a ring of c subunits and the proton channel, and F_1, which is characterized by a peripheral stalk and a ball-shaped headpiece used to generate ATP through phosphorylation of ADP.

One major contributor to the ADP reservoir in the mitochondrial matrix required for ATP synthesis by the ATP synthase is the mitochondrial adenine nucleotide translocase, which comes in humans with four different isoforms AAC1 (SLC24A4), AAC2 (SLC25A5), AAC3 (SLC25A6), and AAC4 (SLC25A31), expressed in a tissue-dependent manner [34]. These proteins belong to the mitochondrial carrier family (solute carrier family 25, SLC25), which consists of more than 50 proteins and represents the largest solute transporter family in humans [34]. These proteins reside in the IMM and mediate the transport of amino acids, nucleotides, cofactors, inorganic ions, protons, fatty acids, and di- and tri-carboxylates operating as antiporters, uniporters, and symporters, and provide solutes important for various cellular processes, including oxidative phosphorylation of fats and sugars, amino acid catabolism and interconversion, and heme and iron-sulfur cluster synthesis [34].

1.3.2. Mitochondrial dynamics

Due to the establishment of cristae, the IMM is multiple times larger than the OMM. This maximizes the surface for OXPHOS and thereby ATP production. In cells with high energy demand, such as cardiomyocytes and muscle fibers, the number of cristae is higher compared to other cells [35]. While complex V is situated at the base of the crista, the crista junction is occupied by the mitochondrial contact site and cristae organization system (MICOS) protein complex. The mammalian MIC60, also known as mitofilin encoded by the *Immt* gene, is one of the three core members of the MICOS complex and has been reported to practically interact with all known MICOS members [36]. Depletion of MIC60 has been shown to affect mitochondrial morphology by a complete loss of the cristae structures and a strong reduction of various MICOS components, and MIC60 is therefore critical for the formation of cristae and cristae junctions [37, 38]. The other two core members of the MICOS complex are MIC19 encoded by *Chchd3* and MIC25 encoded by *Chchd6*. Followed by the association of the core complex, the remaining subunits assemble stepwise into the complete MICOS complex, and subsequently other proteins can associate [39]. The remaining subunits that are counted among the MICOS complex are MIC10/*Minos1*, MIC26/*Apoo*, MIC27/*Apool*, MIC13/*Qil1*, and possibly MIC14/*Chchd10*, and they form a second subcomplex [36]. It has been reported that the two subcomplexes have distinct functions: While the MIC60-subcomplex controls the formation of cristae junctions, the MIC10-subcomplex is crucial for the formation of lamellar cristae [40].

Since strong interactions have been described between the MICOS complex and proteins of the OMM including the sorting and assembly machinery component 50 homolog (SAM50), metaxin family members (MTX1, 2, and 3), and DNAJC11, the name mitochondrial intermembrane bridging complex, MIB complex, has been proposed [38]. The entire MIB complex has a size of 2.2-2.8 MDa [38]. Moreover, the stability of the MICOS/MIB complex can be directly linked to the biogenesis and the assembly of the respiratory chain complexes, as SAM50 has been reported to mediate the amounts and proper assembly of the complexes [38]. Genetic and physical interactions between the ATP synthase, optic atrophy 1 (OPA1), and MICOS have been demonstrated to control size and distribution of MICOS assemblies [40].

The IMM protein OPA1 is not only involved in shaping the cristae and cristae junctions but also in the dynamic network of mitochondria in a cell, which includes two major processes

– fusion and fission. While mitochondrial fusion describes the process of the formation of long filamentous mitochondria, mitochondrial fission results in smaller spherical mitochondria. Both processes are under tight control of a number of proteins, including besides OPA1 also MFN1 and MFN2, dynamin-1-like-protein (DRP1), mitochondrial fission 1 protein (FIS1), and mitochondria fission factor (MFF) [41]. Particularly in cardiac tissue, imbalances of fission and fusion events are associated with numerous cardiovascular diseases and heart failure, as these processes also control the homeostasis of ROS and apoptosis [42].

In adult cardiac and skeletal muscle, mitochondria are rigidly organized between bundles of myofilaments, under the sarcolemma, and around the nucleus, which impact their overall motility. Nevertheless, mitochondrial fusion is important for skeletal muscle and deletion of MFN1 and MFN2 has been reported to result in severe mitochondrial myopathy with decreased muscle mass, exercise intolerance, and lactic acidosis [43]. Interestingly, in myocytes, “kissing junctions” and “nanotunnels” have been described to allow continuous inter-mitochondrial communication between adjacent and long-range mitochondrial pairs permitting the exchange of proteins and metabolites [44]. Notably, increased proportion of fragmented mitochondria and nanotunnels has been identified as a discriminant signature of mitochondrial stress [45]. Moreover, it has been identified, that mitochondrial networks have distinct morphology and dynamics depending on the fiber type of the respective cell. While OXPHOS-dependent oxidative fibers harbor elongated mitochondrial networks with higher fusion rates mediated by MFN1 and MFN2, glycolytic fibers contain punctate mitochondria with minor fusion events [46]. Since switching from glycolytic to oxidative fibers has been observed to be accompanied by elongation of mitochondria, mitochondrial fusion might be linked to the metabolic state of the fiber [46]. In accordance with the myonuclear domain theory, histological data from aged and diseased fibers suggests that regionalization of organelles like mitochondria can also occur [47]. There is now evidence, that mitochondrial proteins are compartmentalized to distinct domains centered around their nuclei of origin, and that domain dimensions are dependent on the fiber type [46].

1.3.3. Mitochondrial skeletal muscle subpopulations

In order to respond to changes in energy demand upon increased workload, skeletal muscle fibers have developed a highly dynamic network of structurally and functionally different mitochondria [48]. These subpopulations include interfibrillar mitochondria (IFM) and

peripheral mitochondria (PM, historically classified as subsarcolemmal mitochondria, SSM), and possibly perinuclear mitochondria (**Fig. 4a**) [49]. IFM are located between the myofibrils arranged in pairs at the Z-line of each sarcomere and are characterized by elongated tubular shapes, while PM reside under the sarcolemma close to myonuclei and capillaries, filling the void myofibrillar space, with a generally more globular shape and less branches (**Fig. 4b**) [45].

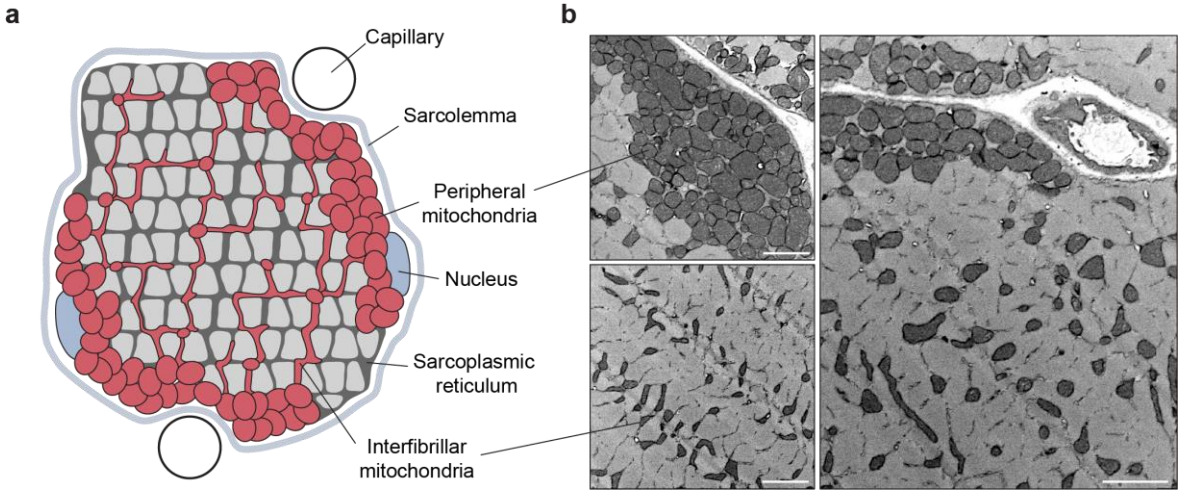


Fig. 4: Schematic and electron-microscopic representation of mitochondrial subpopulations in skeletal muscle fibers. (a) Overview of a muscle fiber and IFM between the myofibrils and the sarcoplasmic reticulum, as well as PM localized beneath the sarcolemma, close to capillaries and nuclei. Adapted from [50]. (b) Electron microscope images of IFM and PM population in soleus muscle display their different structural characteristics. Scale 2 µm.

Due to their alignment with myofibrils, IFM in human muscles are almost double the aspect ratio compared to PM, which provides a high surface area to volume ratio that might result in a high availability of ATP in this region of the fiber [45]. The fact that almost the entire IFM pool (>97%) has direct contact to the SR, the high surface area of IFM has been identified to be beneficial for Ca^{2+} signaling from the SR through the establishment of functional contact sites [51, 52]. Besides mitochondria-SR contacts, mitochondria in skeletal muscle fibers have also been reported to contact other mitochondria by the establishment of the aforementioned electron-dense junctions and nanotunnels [45, 49, 51, 53, 54]. Notably, this often results in a trans-mitochondrial alignment of cristae [53]. Therefore, the term mitochondrial reticulum has been proposed as there are structural capabilities for effective energy distribution throughout the entire fiber, which allow the transmission of mitochondrial membrane potentials across mitochondria with a distance greater than 10 µm in the IFM space [54]. Interestingly, PM form branches only where they project into the IFM space

which might be an indicator for a physical interaction and migration toward the IFM compartment and a strong interdependence between the subpopulations [45]. In this line, it has been suggested that PM are primarily involved in the generation of the proton-motive force near capillaries, whereas IFM use the proton-motive force transmitted through the mitochondrial reticulum to produce ATP required for muscle contractions in the sarcomere [49].

In a functional respect, there is evidence, that complex IV, a proton-motive-force-generating element, preferentially localizes to PM, whereas complex V, which is responsible for the phosphorylation of ADP to ATP using the generated proton-motive force is more concentrated in IFM [49]. Although PM and IFM subpopulations have been increasingly studied in the last decades and many structural features have been identified, other defining characteristics, such as molecular markers, remain elusive. Also, there is poor characterization of the mechanisms by which subcellular specialization of the skeletal muscle mitochondria is achieved and how it contributes to energy homeostasis in health and disease of working muscles. There is evidence that these subpopulations also exist in cardiac muscle, while other studies claim that mitochondria between the densely packed myofibrils of the heart are indistinguishable in terms of ATP production and energy supply [35, 55, 56].

1.3.4. Skeletal muscle plasticity and mitochondrial biogenesis

Members of the peroxisome proliferator-activated receptor γ coactivator 1 (PGC-1) family are important regulators of mitochondrial biogenesis in cardiac and skeletal muscle that contribute to their plasticity [57]. Loss of function of PGC-1α and PGC-1β are associated with defects in cardiac and skeletal muscle energetics and can cause cardiomyopathy [57, 58]. Therefore, knowledge of the mechanisms that regulate mitochondrial biogenesis and activity are central to our understanding of human diseases associated with skeletal muscle weakness and reduced cardiac function.

Mitochondrial biogenesis has been first described in the 1960s after researchers discovered that physical endurance training resulted in higher mitochondrial content levels, which caused increased glucose uptake by muscles [59]. Both intracellular stress signals and environmental stimuli, including exercise, can lead to the activation of mitochondrial biogenesis pathways. Notably, new mitochondria are not formed *de novo* but are generated from the ones already existing by fission events. Mitochondrial biogenesis is regulated

through coordination between the mitochondrial and the nuclear genome, in a complex and multistep process that involves (i) mtDNA transcription and translation and (ii) synthesis, import, and assembly of mitochondrial proteins encoded by nuclear DNA (**Fig. 5**).

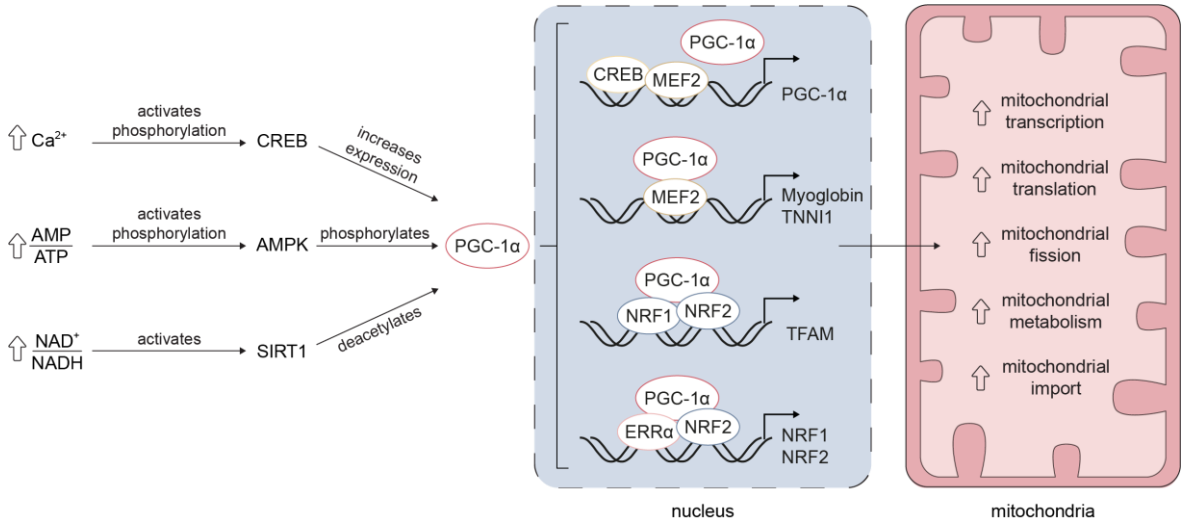


Fig. 5: **Mitochondrial biogenesis is mediated by PGC-1α.** PGC-1α-mediated activation of mitochondrial biogenesis is induced by different signaling pathways, including CREB, AMPK, and SIRT1. PGC-1α acts as a cofactor with MEF2, ERRα, NRF1, and NRF2 to promote the transcription of PGC-1α, NRF1, and NRF2 in a feed-forward loop, as well as slow-twitch muscle fiber genes and TFAM.

The master regulator of mitochondrial biogenesis is PGC-1α. Its expression is readily inducible by exercise training in rodents and humans and it can be activated by phosphorylation or deacetylation [60]. PGC-1α stimulates expression of genes of both nuclear and mitochondrial DNA through the coactivation of nuclear respiratory factors 1 and 2 (NRF1 and NRF2, respectively) and the estrogen-related receptor α (ERRα) [61], as well as by increasing the expression of the final effector of mtDNA transcription and replication TFAM. Finally, the induction of NRF1 and NRF2 leads to an increased expression of subunits of the electron transport chain complexes such as ATP synthase, and cytochrome *c* [61]. Translation of mtDNA-coded genes into proteins is mediated by translation factors encoded by nuclear DNA, including initiation factor mtIF2 and mtIF3, the elongation factors mtEFTu, mtEFTs, and mtEFG1, the translational release factor-1-like mtRF1L, as well as the recycling factors mtRRF1 and mtRRF2 [62].

C1q/tumor necrosis factor-related protein-3 (CTRP3) represents an endogenous modulator for mitochondrial biogenesis and promotes mitochondrial biogenesis in cardiomyocytes via the AMPK/PGC-1α pathway [63]. 5' Adenosine monophosphate-activated protein kinase

(AMPK) is an enzyme involved in energy homeostasis regulation by switching cells to an "energy saving" state through downregulation of anabolic processes and upregulation of catabolic processes to generate ATP [64]. AMPK has been shown to directly interact and phosphorylate PGC-1α and thereby influence glucose uptake, fatty acid oxidation and mitochondrial biogenesis [64].

Metabolic stress can lead to elevated levels of NAD^+ which provide substrates for sirtuins. Silent information regulator 1 (SIRT1) has not only been reported to influence skeletal muscle proliferation and differentiation upon inhibition of the expression of cell cycle inhibitors and direct or indirect interactions with the myogenic factors MyoD and myocyte enhancer factor-2 (MEF2), but also to affect mitochondrial biogenesis [65]. SIRT1 activity is modulated by the availability of its cofactor NAD^+ which is controlled by AMPK sensing the redox and energy state of the cell [66]. While AMPK activates PGC-1α through phosphorylation, SIRT1 is able to deacetylate PGC-1α and, thus, activate subsequent muscle adaptation responses [65].

Upon exercise and through the subsequent activation of calcium signaling pathways, stimulated PGC-1α transcription results in the activation of several transcription factors, including cyclic adenosine monophosphate-response element-binding protein (CREB) and MEF2, in a feed-forward loop. Upon coactivation of MEF2, PGC-1α simultaneously regulates the expression of slow-twitch muscle fiber genes, such as slow skeletal muscle troponin I, TNNI1. Thus, PGC-1α induces remodeling of skeletal muscle fiber composition by decreasing the ratio of glycolytic fibers to more oxidative fibers [60].

Despite their well-described roles in estrogen signaling, cancer, bone differentiation, and development, ERRα and the related receptors ERRβ and ERRɣ also contribute to oxidative metabolism by acting downstream and parallel to PGC-1 coactivators [67]. PGC-1α-dependent activation of ERRα results in transcriptional stimulation in oxidative tissues, including heart and slow-twitch skeletal muscle, for instance by targeting genes involved in mitochondrial fatty-acid oxidation [68]. It has been reported that mice lacking ERRα show similarities to mice lacking PGC-1α, as they have decreased mitochondrial gene expression, show defects in thermogenesis after cold exposure, and develop heart failure when stressed [69].

While boosting PGC-1α levels might be beneficial in some disease models, it can often meet contradictory results. For example, it has been shown that muscle-specific deletion of

Pgc-1α reduced endurance capacity with increased fiber damage, whereas PGC-1α overexpression could elevate exercise performance through increasing the slow-twitch muscle fiber content, however, causing insulin resistance in animals fed with a high-fat diet [70, 71]. Similarly, in heart, PGC-1$\alpha^{-/-}$ mice have a diminished ability to increase work output in response to chemical or electrical stimulation, but cardiac-specific overexpression of PGC-1α in mice caused uncontrolled mitochondrial proliferation in cardiomyocytes leading to loss of sarcomeric structure and a dilated cardiomyopathy [58, 72]. Therefore, fine-tuning of PGC-1α levels is essential for cardiac and skeletal muscle homeostasis and context-dependent.

In cardiac and skeletal muscle, the transcriptional regulation pathways induced by PGC-1α/β and other cofactors, including ERRα, respond to cellular stress and physical activity and drive the expression of sets of nuclear genes which are important for the adaptive responses. Thus, they are key regulators of muscle energy metabolism.

1.4. PERM1 – PGC-1- and ERR-induced regulator in muscle 1

A large number of exercise-induced regulators are highly expressed in skeletal muscle but are also present in various other tissues. Contrastingly, the PGC-1- and ERR-induced regulator in muscle 1 (PERM1) displays a protein that is exclusively expressed in heart, skeletal muscle, and brown adipose tissue. It was first described after a screening of genes that are induced by PGC-1α in differentiated C2C12 cells, an immortalized mouse myoblast cell line [73]. PERM1 expression was strongly elevated upon PGC-1α overexpression and this induction was lost when endogenous ERRα was suppressed. Further, PERM1 expression is also enhanced by the other members of the two families, PGC-1β, ERRβ, and ERRγ. Subcellular fractionation revealed the presence of PERM1 in multiple compartments, including nucleus, cytosol, and mitochondria in C2C12 cells, as well as SR in adult heart tissue [73, 74]. Loss- and gain-of-function studies in cell culture and muscle tissue showed that PERM1 regulates a subset of PGC-1/ERR-target genes associated with mitochondrial bioenergetics [73, 75]. These target genes include genes involved in mtDNA replication and transcription, such as *Tfam, Tfb1m,* the mitochondrial deacetylase *Sirt3*, as well as known exercise-induced genes important for nutrient utilization and energy transduction, such as the glucose transporter type 4 *Glut4* and the muscular isoform of the carnitine O-palmitoyltransferase 1 *Cpt1b* [75].

Transcriptional control of PGC-1- and ERR targets by PERM1 is mediated through direct interactions and binding to distinct promotor regions. PERM1 has been shown to induce the expression of ERRα and its target genes via activation of ERRα response elements (ERREs), DNA sequences in the promotor region of ERR target genes critical for transcriptional control [76]. This has been shown for the ERREs in the promotors of *Errα*, *Ndufv1* of OXPHOS complex I, *Sirt3*, and *Ckmt2*, the mitochondrial creatine kinase [74, 76]. Similarly, PERM1 interacts with proximal regions of peroxisome-proliferator-activated receptor (PPAR) response elements (PPREs) in promotors of genes involved in fatty acid oxidation, such as peroxisomal acyl-coenzyme A oxidase 1 (*Acox1*), *Cpt1b* and carnitine O-palmitoyltransferase 2 (*Cpt2*), as well as the mitochondrial medium-chain specific acyl-CoA dehydrogenase *Acadm*. Moreover, physical interaction of PERM1 with PGC-1α has been characterized multiple times in cultured cells and in tissue, as well as with ERRα and PPARα [74, 77, 78].

PERM1 expression is inducible by endurance exercise both in humans and rodents and downregulated in diseases that are characterized by decreased oxidative capacity, found in patients suffering from amyotrophic lateral sclerosis or heart failure [73, 76, 79-81]. Enhanced PERM1 expression results in elevated expression of OXPHOS proteins, mitochondrial biogenesis, oxidative capacity, fatigue resistance and fatty acid metabolism, both in skeletal muscle tissue and cultured cells [74-77, 81].

During myocardial ischemia/reoxygenation injury, a phenomenon of oxygen and nutrient deprivation in the blood occurring in hypoxic brain injury in stroke or brain failure following reversal of cardiac rest, irreversible mitochondrial dysfunction can be observed. This dysfunction is caused by alterations in mitochondrial metabolism and elevated production of ROS and might be reversed by restoring mitochondrial function and increasing mitochondrial biogenesis [82, 83]. Hypoxia/reoxygenation processes in cultured cells represent an *in vitro* model for ischemia/reoxygenation, leading to irreversible mitochondrial dysfunctions and, eventually, cardiomyocyte death. In cultured mouse neonatal cardiomyocytes, overexpression of PERM1 decreased the amount of hypoxia/reoxygenation-induced cellular damage (monitored by secreted levels of lactate dehydrogenase) and apoptosis which suggests that PERM1 might protect cardiomyocytes against hypoxia/reoxygenation-induced damage also *in vivo* [74].

Moreover, PERM1 has been reported to be upregulated in response to cold stress in inguinal white adipocytes [84]. Upon exposure to cold environment, the formation of brite ("brown-in-white") or beige adipocytes can be induced. Brite/beige adipocytes represent a subgroup of brown adipocytes that do not localize in distinct fat pads in the interscapular region but reside between white adipocytes throughout the body [85]. In mouse models exposed to cold stress, PERM1 has been identified as modulator of the conversion of white to brite/beige adipocytes, together with ERRγ, involved in mediating the transcriptional network associated with PGC-1α, hence, positively regulating mitochondrial capacity [84].

With the first paper included in this thesis, we were the first that published and characterized a knockout mouse model of *Perm1*. Recently, another group reported the generation of a systemic *Perm1*$^{-/-}$ mouse model and described the influence of *Perm1* depletion on fatty acid and energy metabolism in the heart [77, 78]. They showed that absence of *Perm1* had no effect of cardiac function at baseline, measured by echocardiographic analyses, including diastolic interventricular septum thickness, diastolic posterior wall thickness, end-diastolic left ventricle (LV) internal dimension, end-systolic LV internal dimension, systolic function ejection fraction, and heart rate, as well as organ weights and multiple weight/length ratios [77]. However, ejection fraction and fractional shortening were reduced in *Perm1*$^{-/-}$ hearts compared to wild-type controls in the study the group published a few months later [78]. Phosphocreatine-to-ATP ratios were reduced in *Perm1*$^{-/-}$ hearts and proteomic and metabolomic analyses displayed a downregulation of oxidative phosphorylation while an upregulation of glycolysis and polyol pathways was observed indicating that PERM1 regulates cardiac energetics [78]. RNA-sequencing, pathway enrichment analysis, and subsequent quantitative real-time polymerase chain reaction (qRT-PCR) of candidate genes revealed downregulation of genes involved in fatty acid and carbohydrate metabolism in heart [77].

As part of the publications described above, some interaction partners of PERM1 have been described. These include the already mentioned transcriptional regulators PGC-1α, PPARα, and ERRα. Before we published an interactome of PERM1 in cultured cells and in cardiac and skeletal muscle tissue within the second publication part of this thesis, an interaction with Ca^{2+}/calmodulin-dependent protein kinase II (CaMKII) was reported [81]. Recently, interactions with ankyrin-repeat domain-containing protein 1 (ANKRD1), KN motif and ankyrin-repeat domain-containing protein 1 (KANK1) and 2 (KANK2), BLC2-associated

anthanogene 6 (BAG6), and transcriptional intermediary factor 1β (TIF1β), have been observed by affinity-enrichment mass-spectrometry (AE-MS) and co-immunoprecipitations in cardiomyocytes pulling down overexpressed PERM1. However, the functions of these interactions have not yet been described.

In sum, the current knowledge positions PERM1 as an important transcriptional regulator of selective PGC-1α/β and ERRα targets to coordinate cardiac and skeletal muscle function and energy metabolism.

1.5. Aims of this thesis

To date, characterization of PERM1 almost exclusively focusses on transcriptional regulation and interactions with regulatory proteins and DNA regions in the nucleus. However, subcellular fractionation identified PERM1 to be enriched not only in the nucleus, but also in multiple extra-nuclear compartments including the cytosol and the mitochondria. Therefore, this thesis and the enclosed publications aimed to describe the function of PERM1 in these compartments by characterizing a knockout mouse model lacking *Perm1* and by identifying extra-nuclear interaction partners.

Publication (I): While embryonic and prenatal heart development is well described and had been studied extensively, knowledge about early postnatal processes is limited. Particularly in these early processes including myocyte proliferation, differentiation, and growth, post-translational modifications (PTMs) are involved to control multiple pathways. Here, we used wild-type mice of 2, 10, and 20 days and measured both the proteome and also the phosphoproteome to build a large repository but also to identify novel proteins involved in early postnatal heart development. As we identified PERM1, at this point it was known as C1ORF170, highly upregulated during this period of time, we aimed to characterize its localization, turnover, and function in *in vitro* and *in vivo* models by focusing mainly on cardiac tissue.

Publication (II): Since PERM1 is also highly expressed in skeletal muscle, we wanted to examine the function of PERM1 also in this tissue by characterizing *Perm1*$^{-/-}$ muscle tissue using proteomic and morphological approaches. Moreover, we aimed to describe the role of PERM1 in extra-nuclear compartments by resolving its interactome. Here, we used different cell culture models, as well as cardiac and skeletal muscle tissue to co-enrich PERM1 and its interaction partners.

Follow up: After identifying cytosolic and mitochondrial interaction partners, we aimed to integrate this information into sequence and structural analysis of PERM1 and discuss its importance in respect to skeletal muscle mitochondrial network remodeling. Here, we focused on the N-terminus of PERM1 and the interaction with ankyrin B and used different genetic and biochemical approaches to characterize this interaction.

2. Results

2.1. Publication (I): Phosphoproteomics of the developing heart identifies PERM1 – An outer mitochondrial membrane protein

2.1.1. Summary publication I

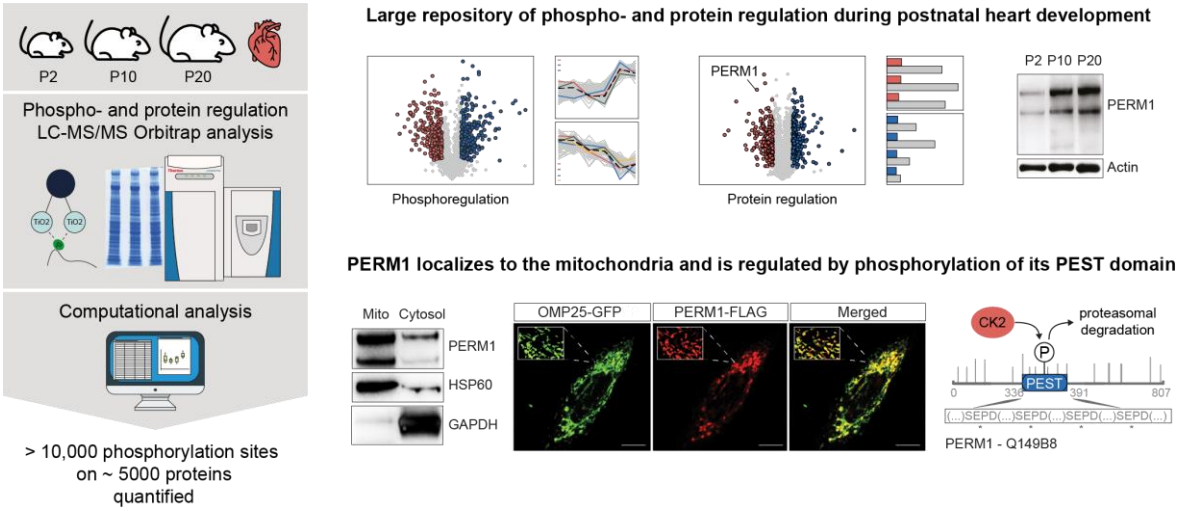


Fig. 6: Graphical abstract publication I. (Left) Schematic overview of the experimental strategy for determination of phosphorylation and protein regulation in postnatal hearts. (Right) PERM1 was identified as a candidate with significantly increasing abundance in the measured time course, is localized to the outer mitochondrial membrane, and is regulated by phosphorylation of its PEST domain by casein kinase 2 (CK2).

PTMs play an essential role in regulating various cardiac cell functions, particularly during heart development, including cardiomyocyte proliferation, differentiation, and morphogenesis. In this publication, we provided a large repository of phosphorylation and protein regulation focusing on early stages of cardiac postnatal development. We found PERM1 highly upregulated from postnatal day P2 to P20 and identified its localization at the OMM (**Fig. 6**). Furthermore, we demonstrated that PERM1 is rapidly degraded by the ubiquitin-proteasome system (UPS) through phosphorylation of four serines in its PEST motif (rich in proline, glutamic acid, serine, and threonine) by casein kinase 2 (CK2). Loss-of-function mutants of *Perm1* in adult heart tissue resulted in elevated phospholipid species, as well as in downregulation of mitochondrial transport proteins for amino acids and carnitines accompanied by altered levels of various lipid species, amino acids, and acylcarnitines in *Perm1*$^{-/-}$ mitochondria.

2.1.2. My contribution to publication I

Cell culture experiments for UPS response and cycloheximide treatments were performed by me, as well as proteomic profiling of *Perm1*$^{-/-}$ hearts, determination of mtDNA copy number, mTOR activity, and preparation and analysis of lipidomic and metabolomic screening (the latter assisted by Susanne Brodesser). The postnatal heart screening was performed by Sriram Aravamudhan and Franziska Lang and analyzed by Clara Hofmann (née Türk) and Hendrik Nolte. PERM1 localization experiments were performed by Sriram Aravamudhan and Clara Hofmann, as well as the turnover experiments and CK2 phosphorylation assays. Morphological studies and pulsed-SILAC experiments were performed by Clara Hofmann, imaging was performed by Clara Hofmann and Natalie Schindler, and Dieu Hien Rozsivalova helped with the OROBORUS measurements. Philipp Hammerschmidt assisted me in subcellular fractionation experiments. Franziska Lang performed Lys6 incorporation analysis and Lena Keufgens calculated half-lives. Aleksandra Trifunovic and Tim König did OXPHOS analysis and Ramesh Kumar Krishnan conducted radioactive kinase assays. Thomas Langer, Elena Rugarli, Thomas Braun, and Jens Brüning provided guidance during the study. I assembled all figures, handled the revision process, and assisted Marcus Krüger in writing the manuscript.

2.2. Follow-up of publication I

2.2.1. PERM1 expression increases postnatally and *Perm1*$^{-/-}$ muscles develop mitochondrial phenotype

As shown in the publication above, PERM1 was identified in the developing heart with increasing protein expression from P2 to 20. Notably, it has been demonstrated, that PERM1 expression was already detectable at embryonic day 9.5 and its expression continuously increases through postnatal stages [74]. To assess consequences of *Perm1* ablation during early development, *Perm1*$^{-/-}$ mice were mated in a homozygous manner, as well as wild-type controls, respectively, to obtain homozygous offspring cohorts. The offspring was euthanized 2, 10, and 20 days post birth and a pool of hind limb muscles including quadriceps, tibialis anterior, gastrocnemius, and soleus were isolated. *Perm1*$^{-/-}$ offspring sizes were six pups at P2, seven at P10, and four at P20, while wild-type control sizes were four at P2, seven at P10, and ten at P20.

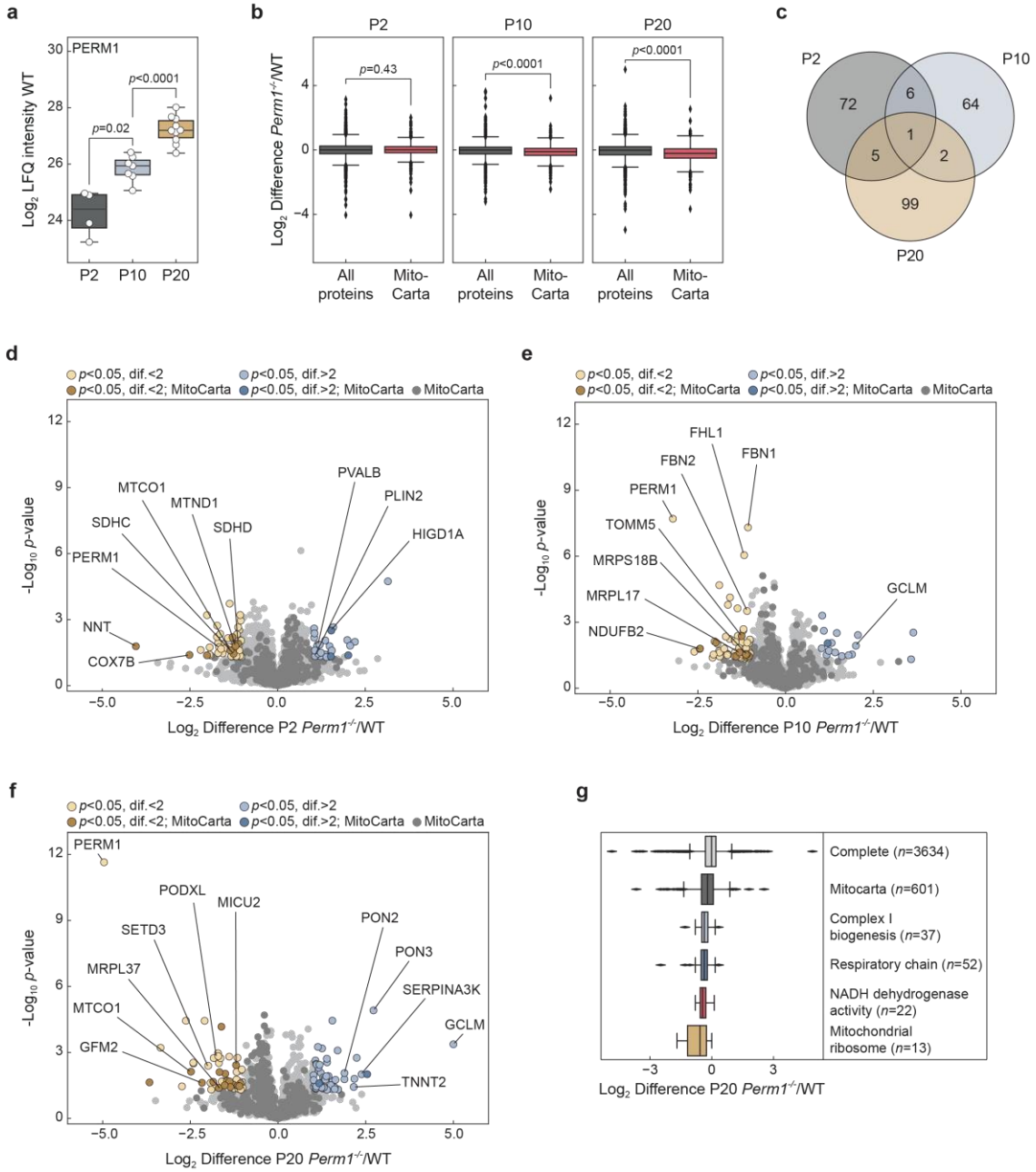


Fig. 7: Proteomic profiling of postnatal *Perm1*$^{-/-}$ muscle tissue showed gradual downregulation of mitochondrial proteins. (a) Increasing $\log_2$ intensities of PERM1 at P2, P10, and P20. (b) Comparison of the $\log_2$ differences in MitoCarta 3.0 proteins compared to the complete dataset revealed overall downregulation of mitochondrial proteins starting from P10. (c) Small overlap of significantly regulated proteins between *Perm1*$^{-/-}$ and wild-type control muscles at P2, P10, and P20. (d-f) Volcano plots depicting significantly regulated proteins in *Perm1*$^{-/-}$ muscles at (d) P2, (e) P10, and (f) P20 compared to wild-type controls. Cut-off was defined as p <0.05 with a fold change >2. Darker colors indicate the MitoCarta 3.0 annotations. (g) 1D enrichment using Gene Ontology and Reactome annotations revealed downregulation of mitochondrial function and compartments.

n= *Perm1*$^{-/-}$: six mice for P2, seven for P10, four for P20; wild type: four mice for P2, seven for P10, ten for P20. Box plots (a,b,g) represent the median, 25th, and 75th percentiles; maximum and minimum are connected through whiskers. Outliers are defined as Q1–1.8 interquartile range (IQR) and Q3+1.8 IQR. (a, d-f) Unpaired two-sided Welch's *t*-test. (b) Unpaired two-sided Mann-Whitney *U*-test.

Similar to what we observed in heart, PERM1 expression increases significantly from P2 to P20 (**Fig. 7a**) in skeletal muscle tissue of the wild-type animals. Since PERM1 is a mitochondrial protein and a reduction mtDNA copy number, as well as in global mitochondrial protein expression, was observed in adult skeletal muscle but not in heart, we were interested whether the reduction in skeletal muscle develops pre- or postnatally. While at P2, MitoCarta-associated proteins were equally expressed in *Perm1*$^{-/-}$ and wild-type animals, global mitochondrial protein expression decreases gradually from P2 to P10 and P20 (**Fig. 7b**). In accordance to what was observed in adult animals, different proteins were significantly changed (*p*-value <0.05, absolute difference >2) in the muscle of *Perm1*$^{-/-}$ mice compared to the wild-type control at the three early postnatal time points (**Fig. 7c**). PERM1 was the only protein being significantly regulated at all time points. Notably, it has to be considered that PERM1 was solely detected in the wild-type samples but appears in the list of downregulated proteins because missing values were imputed to be able to calculate $\log_2$ differences and *p*-values.

At the earliest time point that was investigated, P2, an upregulation (*p*-value <0.05, absolute difference >2) of parvalbumin (PVALB) was observed, which is a calcium-binding protein that is highly expressed in skeletal muscle (**Fig. 7d**). Interestingly, it has been shown that upregulation of PVALB decreased mitochondrial volume, as well as the transcription of mitochondrial genes associated with mitochondrial Ca^{2+} transport and mitochondrial membrane potential [86]. Similarly, upregulation of hypoxia-induced gene domain family-1a (HIGD1A), that has been identified as a marker for metabolic stress which is increased during elevated levels of reactive oxygen species, was also discovered to impair mitochondrial membrane potential [87]. Furthermore, perilipin 2, a protein inversely correlated with skeletal muscle strength and associated with sarcopenia, was upregulated in *Perm1*$^{-/-}$ muscles at P2 [88]. Although there was no global downregulation of mitochondrial proteins observed for the early time point, proteins of the respiratory chain were downregulated (*p*-value <0.05, absolute difference <2) in *Perm1*$^{-/-}$ muscles at P2, including COX7B that is part of the cytochrome *c* oxidase and MTCO1 and MTND1, which are both OXPHOS proteins encoded by mitochondrial DNA, as well as two of the four subunits of the succinate dehydrogenase, SDHC and SDHD. While SDHA and SDHB form the catalytic core of complex II, SDHC and SDHD are membrane-anchored and it has been reported that mutations and downregulation of both SDHC and SDHD resulted in elevated ROS production due to dysfunctions in mitochondrial respiration [89]. Notably, a 16-fold

downregulation was observed for the mitochondrial NAD(P) transhydrogenase NNT, which is involved in the maintenance of a high GSH/GSSG ratio to control oxidative stress and lower levels of NNT have been observed in human failing myocardium concomitant with higher levels of oxidized glutathione, impacting NADPH-dependent enzymes and impairing the maintenance of the mitochondrial membrane potential [90]. These findings might indicate that elevated oxidative stress and impairment of mitochondrial respiration, as well as membrane potential, that we observed in adult skeletal muscle could already be identified at early time points of development.

Global downregulation of mitochondrial proteins at P10, which was not observed at P2, is also visible in the volcano plot (**Fig. 7e**). Moreover, nine of the 57 significantly downregulated proteins are associated to the MitoCarta, while only one mitochondrial protein was upregulated in *Perm1*$^{-/-}$ muscles compared to the wild-type controls. Downregulated mitochondrial proteins include proteins of the mitochondrial ribosome MRPL17 and MRPS18B, one of the three small subunits of the TOM complex associated with TOMM40, TOMM5, whose function is not fully understood yet, but might play a role in stabilizing the TOM complex, and NDUFB2 which represents an accessory subunit of complex I of the respiratory chain [91].

Furthermore, both of the rodent fibrillins, fibrillin-1 (FBN1) and fibrillin-2 (FBN2) showed a significant downregulation in *Perm1*$^{-/-}$ muscles. While FBN1 expression is persistent during life and FBN1 can form homopolymeric microfibrils with other FBN1 molecules, FBN2 is thought to be predominantly expressed during early development and it can only form heteropolymeric mircofibrils with FBN1 [92]. Fibrillin microfibrils have been identified to serve as a scaffold in the extracellular matrix of different organs and mutations in both genes are associated with various connective tissue disorders [92]. The sarcoplasmic and subsarcolemmal four-and-a-half LIM domain protein 1 (FHL1) was less abundant in *Perm1*$^{-/-}$ muscles at P10. FHL1 knockout mice demonstrated age-dependent myopathies along with sarcoplasmic and sarcolemmal disorganization, as FHL1 has been identified to be highly expressed in postnatal skeletal muscle and might be involved in sarcomere synthesis and formation [93]. Interestingly, the glutamate-cysteine ligase modifier subunit GCLM which encodes the regulatory subunit of glutamate-cysteine ligase (GCL) catalyzing the rate-limiting step of glutathione synthesis was 4-fold upregulated in *Perm1*$^{-/-}$ muscles compared to wild-type controls [94]. To sum, profiling at P10 showed the start of global mitochondrial

downregulation, as well as continuous alterations in proteins involved in regulation of oxidative stress levels.

While GCLM was upregulated 4-fold at P10, it reached a 32-fold upregulation in *Perm1*$^{-/-}$ muscles at P20 compared to wild-type controls (**Fig. 7f**). Furthermore, more proteins associated with antioxidant properties, such as the paraoxonase (PON) family members 2 and 3 and the extracellular serine proteinase inhibitor SERPINA3K [95]. In retinal cells, SERPINA3K has been reported to protect cells from oxidative stress-induced cell death by preventing H_2O_2-induced intracellular calcium overload [96]. Upregulation of antioxidant proteins in *Perm1*$^{-/-}$ muscles may hint to continuously elevated oxidative stress levels. Interestingly, the cardiac troponin cTnT encoded by the *Tnnt2* gene was also upregulated in *Perm1*$^{-/-}$ muscles. CTnT has been identified to solely be present in cardiac muscle but may also represent a development marker in embryonic skeletal muscle that is re-expressed in skeletal muscle disorders and during skeletal muscle regeneration [97].

Notably, Gene Ontology and Reactome pathway enrichment analysis revealed global downregulation of proteins associated with complex I biogenesis (Reactome), respiratory chain (GOCC), NADH dehydrogenase activity (GOMF), and mitochondrial ribosome (GOCC) (**Fig. 7g**). Besides proteins of the respiratory chain and the mitochondrial ribosome, the histone methyltransferase SETD3 was downregulated, as well as podocalyxin (PODXL). Both of these proteins are linked to myogenic differentiation, as it has been reported that knockdown of SETD3, which regulates myogenin, retards muscle cell differentiation, while PODXL has been identified as an early myogenic-committed progenitor [98, 99]. This suggests that cell differentiation is delayed in *Perm1*$^{-/-}$ muscles and might explain the upregulation of TNNT2.

Proteomic profiling of postnatal muscle tissue of *Perm1*$^{-/-}$ animals revealed that global mitochondrial protein downregulation observed in adult muscle tissue develops postnatally and is accompanied by downregulation of proteins associated with myogenic differentiation and upregulation of proteins with antioxidant potential indicating elevated levels of oxidative stress.

2.3. Publication II: PERM1 interacts with the MICOS-MIB complex to connect the mitochondria and sarcolemma via ankyrin B

2.3.1. Summary publication II

In this publication, we focused on the consequences of *Perm1* ablation in skeletal muscle and on the interactome of PERM1. We observed a reduction of skeletal muscle subsarcolemmal mitochondria, decrease in muscle force, diminished mitochondrial membrane potential and oxygen flux in *Perm1*$^{-/-}$ muscles compared to wild-type controls. Furthermore, complexome profiling and immunoprecipitation approaches identified an interaction of PERM1 with the mitochondrial MICOS-MIB complex and the intracellular adapter protein ankyrin B (ANKB). We described a C-terminal transmembrane helix that integrates PERM1 into the OMM and suggested a scaffolding function of PERM1 in connecting the mitochondria to the sarcolemma of skeletal muscle fibers.

2.3.2. My contributions to publication II

For this manuscript, I performed morphological analysis including histochemical and immunofluorescence staining and subsequent analysis. I conducted quantification of mtDNA copy number, circadian rhythm studies and proteomic profiling of *Perm1*$^{-/-}$ TA, as well as all immunoprecipitations in mouse tissue and cells of PERM1 and ANKB. I generated the ΔTM mutant and performed further analysis. Sriram Aravamudhan and Clara Hofmann designed and performed proteomic profiling of young and aged muscles. SSM and IFM separation and proteomes were performed by Clara Hofmann, as well as EM imaging, pulsed stable isotope labeling with amino acids in cell culture (pSILAC) experiments, and complexome profiling. Lena Keufgens calculated half-lives, Dieu Hien Rozsivalova helped with OROBORUS measurements, and Wilhelm Bloch performed running experiments and weight tests. Vanina Romanello, Leonardo Nogara, and Bert Blaauw were involved in skeletal muscle force and mitochondrial membrane potential measurements. Aleksandra Trifunovic and Thomas Braun provided guidance during the study. I prepared all figures, handled the revision process, and assisted Marcus Krüger in writing the manuscript.

2.4. Follow-up of publication II

2.4.1. ANKB interaction site is located between the amino acids 6-55 of PERM1

In the publication above, we focused particularly on the C-terminus with the integration to the outer mitochondrial membrane and the interaction of PERM1 with the MICOS-MIB complex. According to the AlphaFold prediction model of the PERM1 structure, besides one α-helix at the N-terminus and two α-helices at the C-terminus, of which the second last was identified as the transmembrane region, the rest of the protein is predicted to be intrinsically disordered and has low and very low confidence scores [100]. Notably, the overall sequence similarity between mouse and human PERM1 is only 56%, while there is higher similarity both at the N-terminus (aa 1-96; 79%) and the C-terminus (aa 728-807/716-790; 77%), particularly in the regions with predicted secondary structure (**Fig. 8a**). In the AlphaFold model, the N- and the C-terminus are in close proximity. Since we proposed a scaffolding function of PERM1 by connecting the mitochondria and the sarcolemma in muscle fibers, a closed conformation with N- and C-terminus being spatially close to each other seemed disadvantageous, while an open conformation would allow flexibility.

We, therefore, hypothesized that the interaction site with the cytosolic interactors is mediated by regions at the N-terminus of PERM1. This was initially supported by the fact that, when using a *Perm1* plasmid with the FLAG-tag attached to the N-terminal site of the open reading frame, the enrichment of ANKB after AE-MS was significantly reduced compared to the previously used plasmid with a C-terminal FLAG peptide (**Fig. 8b**). Notably, the enrichment of PERM1 and of the identified MICOS-MIB proteins was comparable. This suggests, that the interaction with ANKB is impaired by the FLAG peptide when attached to the N-terminus.

When aligning the PERM1 sequence to additional species, including pig, chicken, alligator, and killifish, several distinct regions of high similarity were observed in the very N-terminal segment. These regions implied the amino acids 6-96, with the amino acids 6-55 being particularly conserved, as well as the part between the amino acids 82-96. As we identified the interaction also in human heart tissue (data not shown), it is assumed that ANKB is an interactor not only in mouse and human, but also in the other species and that the interaction site is likely to be conserved between the organisms. Therefore, three deletion constructs were generated, Δ6-96, Δ6-55, and Δ82-96, and transfected into human embryonic kidney (HEK293T) cells followed by AE-MS (**Fig. 8c**). While the measured ANKB intensity was

high in the enrichment with the wild-type PERM1, as well as with the Δ82-96 mutant, ANKB was not detected in the IPs with the Δ6-96 and Δ6-55 mutants (**Fig. 8d**). Again, the enrichment of the MICOS-MIB interactors was not influenced by the deletions at the N-terminus. For visualization and statistical purposes, missing values were imputed.

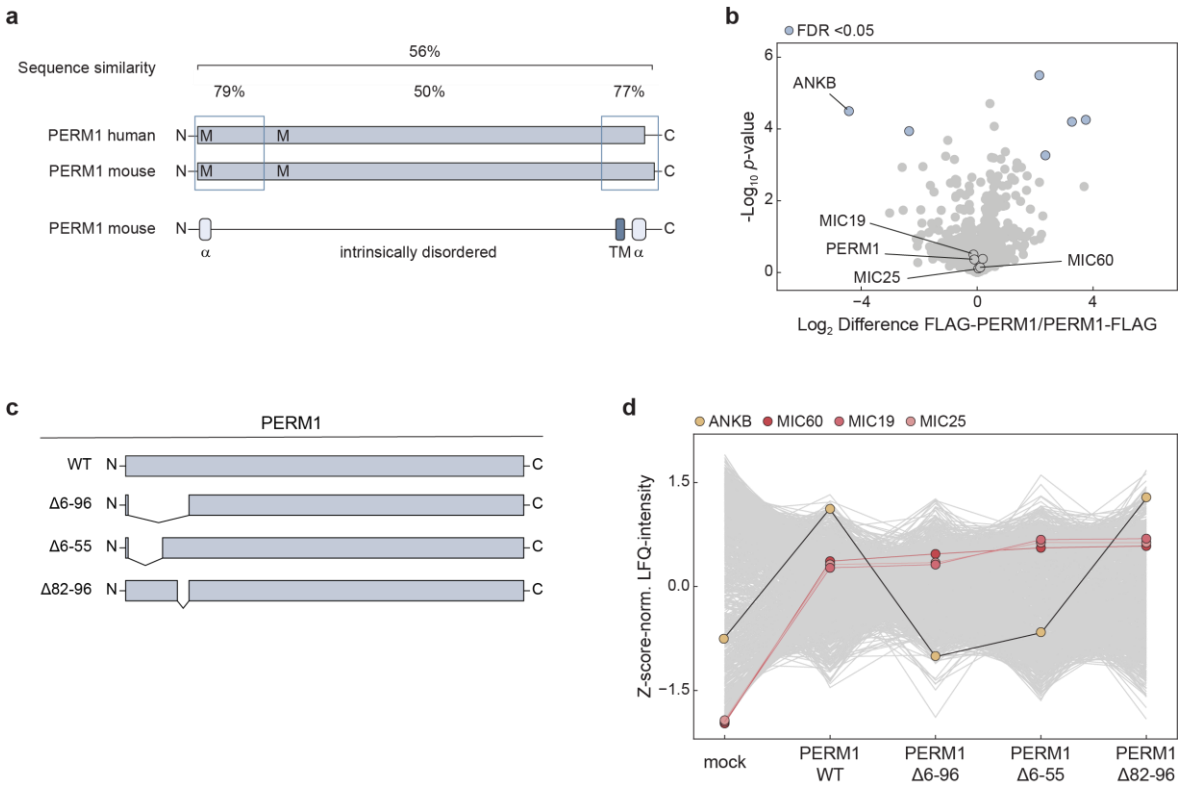


Fig. 8: The conserved amino acids 6-55 of PERM1 are important for the interaction with ANKB. (a) Alignment of the amino acid sequences of human and mouse PERM1 revealed overall low similarity, but higher similarity was observed at the N- and C-terminus. (b) Volcano plot depicting the reduction of ANKB after IP of N-terminally FLAG-tagged PERM1 compared to C-terminally FLAG-tagged PERM1 (*n*=3 samples per group). The cut-off was set to an FDR <0.05. PERM1, MIC60, MIC19, and MIC25 were similarly enriched in C-and N-terminally FLAG-tagged PERM1 IPs. (c) Schematic representation of PERM1 deletion mutants. (d) Line plots visualizing the Z-score normalized LFQ intensities of ANKB, MIC60, MIC19, and MIC25 after IP of wild-type PERM1 and the different N-terminal deletion mutants (*n*=3 samples per group). ANKB was undetectable in the Δ6-96 and Δ6-55 mutants, intensities were imputed.

(b) Unpaired two-sided Student's *t*-test, S_0=0.1, permutation-based FDR <0.05, 500 randomizations. TM=transmembrane segment

These data support the hypothesized open conformation of PERM1 with the C-terminus anchored to the mitochondria interacting with the MICOS-MIB complex and the very N-terminus interacting with ANKB to build the bridge between the mitochondria and the sarcolemma.

2.4.2. PERM1 interacts with the ankyrin-repeat domain of ANKB

Next, we aimed to identify the interaction region on the ANKB sequence. To allow for multiple biochemical analyses, higher volumes of protein input were necessary. Therefore, different constructs for recombinant protein expression were generated and purified to focus on the interaction between PERM1 and ANKB. Since we already narrowed down the interaction region on the PERM1 sequence to the very N-terminus and we wanted to generate constructs that could also be used in mammalian systems, we used the ΔTM (TM = transmembrane segment) construct for PERM1 expression in *E. coli*, which lacks the C-terminal transmembrane helix and results in a soluble protein residing in the cytosol, and tagged it C-terminally with a His-tag. Furthermore, for the 220 kDa large ANKB protein, an N-terminally His-tagged full-length version was generated, as well as a construct only comprising the 24 ankyrin-repeat domains (24ANKB), as these domains are known to mediate protein-protein interactions [101]. As a control, the counterpart to the 24ANKB, a construct lacking the ankyrin-repeat domains (Δ24ANK), was designed.

To characterize the predicted interactions, PERM1ΔTM was immobilized on the dextran surface of a surface plasmon resonance (SPR) crystal and a series of different ANKB dilutions was injected through the microflow system (**Fig. 9a-c**). Association and dissociation rates, as well as equilibrium dissociation constants (K_D) were calculated by the increase and reduction in SPR signal (expressed in response units, RU). The determined K_D value of immobilized PERM1ΔTM and full-length ANKB was 11.1 ± 6.88 nM, with 24ANKB 34.1 ± 9.3 nM, demonstrating a strong interaction between PERM1 and ANKB (**Fig. 9a+b**). Notably, no interaction was observed with the ANKB construct lacking the N-terminal fragment (**Fig. 9c**).

Next, the constructs PERM1ΔTM and 24ANK, which showed a strong interaction during the SPR measurement, were submitted to size-exclusion chromatography, elution profiles were analyzed, and peaks were collected separately in fractions. PERM1ΔTM elutes over three peaks whereas Coomassie stain showed an enrichment of the 100-120 kDa high running PERM1 in the fractions 2 and 3 and a separation of the at around 70 kDa running extra band which most likely represents the chaperone HSP70 which was co-purified with PERM1 (**Fig. 9d+e**). 24ANKB alone eluted almost exclusively at a volume of 15.7 ml within fraction 5 running at a size of ~100 kDa. Migration of the 24ANKB elution profile into the PERM1 elution profile was observed when the two proteins were mixed before submission to size-

exclusion chromatography and Coomassie staining substantiated the migration of 24ANKB to the fractions 2 and 3. These data collectively showed that PERM1 interacts with the N-terminal ankyrin-repeat domains of ANKB.

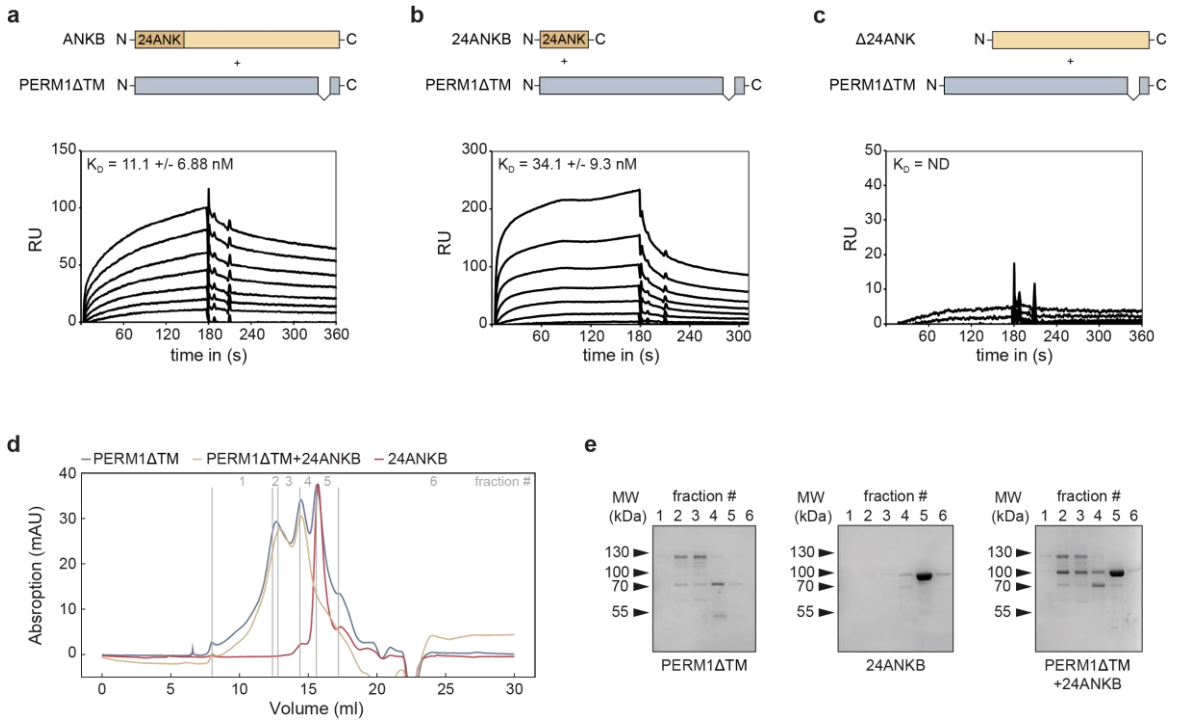


Fig. 9: PERM1 interacts with the N-terminal 24ANK region of ANKB. (a-c) SPR profiles and determined K_D values of immobilized PERM1ΔTM analyzed with (a) full-length ANKB, (b) 24ANKB, and (c) Δ24ANK showed low K_D values for the full-length and the 24ANKB with PERM1. (*n*=3 runs per construct) (d) Size-exclusion profiles of PERM1ΔTM, 24ANKB, and a mix of PERM1ΔTM and 24ANKB. The mix showed co-elution of 24ANKB with PERM1ΔTM at fractions 2 and 3. (e) Coomassie staining of the collected fractions 1-6 from size-exclusion chromatography. RU = response units.

3. Discussion

Mitochondrial biogenesis is crucial for the development and the maturation of cardiac and skeletal muscle, and mitochondria are reorganized profoundly in the early postnatal phase. Here, we provided detailed insight into the proteomic and phosphoproteomic regulation within the first 20 days of murine postnatal heart development. We observed PERM1 protein levels strongly upregulated between P2 and P20 and identified PERM1 as an OMM protein in tissue and cultured cells. Notably, PERM1 has also been observed to localize to the cytosol, the nucleus, and the SR [74]. Since characterization of PERM1 in the literature, however, predominantly focuses on its role in transcriptional regulation with nuclear interaction partners, this thesis and the enclosed publications investigated the function of PERM1 in extra-nuclear compartments, particularly in the cytosol and the mitochondria. We used a genetic mouse model lacking *Perm1* and multiple *in-vitro* methods to characterize PERM1 and its interactome.

3.1. Pre- and postnatally increasing PERM1 levels might contribute to mitochondrial energy metabolism in a PGC-1- and ERR-dependent manner

The expression of PERM1 is induced by factors of two families that are major regulators of mitochondrial biogenesis – PGC-1 and ERR – and PERM1 has been shown to regulate proteins associated with energy metabolism [73-78, 81, 84]. We found PERM1 highly upregulated during the early postnatal phase and recently, it has been reported, that PERM1 expression already starts as early as embryonic day E9.5 with gradually increasing expression levels throughout pre-and postnatal cardiac development [74]. Increasing PERM1 expression coincides with increasing expression of PGC-1α, PGC-1β, and ERRα during prenatal stages, however, expression patterns differ postnatally [74, 102]. While PERM1 expression still gradually increases with its maximum obtained in adult mice, the expression levels of PGC-1α, PGC-1β, and ERRα reach their maxima at P0 or P1 and show decreased expression at later time points [74]. Particularly during postnatal cardiac development, when mitochondrial oxidative metabolism increases and hearts switch from glycolysis to oxidative phosphorylation, PERM1 expression increases. During this metabolic maturation, cardiomyocytes require elevated mitochondrial capacity. Notably, PERM1 is not essential

for proper heart development, as hearts of *Perm1*$^{-/-}$ mice develop normal and show no or only slightly impaired baseline parameters [77, 78].

Surprisingly, also *Pgc-1α*$^{-/-}$ mice exhibit a minimal phenotype under basal physiological conditions, suggesting that PGC-1α is dispensable for mitochondrial biogenesis during pre- and postnatal development. It has been reported that *Pgc-1α*$^{-/-}$ mice with age develop abnormally elevated body fat, as well as decreased mitochondrial number and respiratory capacity, leading to reduced performance and exercise capacity in skeletal muscle. *Pgc-1α*$^{-/-}$ hearts show normal mitochondrial volume but have reduced mitochondrial enzymatic activity, which is mildly pronounced at normal baseline conditions but becomes more evident during increased workload [58]. These mice are more susceptible to cardiac hypertrophy and heart failure, which has been observed in a transverse aortic constriction (TAC) model [103]. Taken together, while PGC-1α is not essential for development, it is necessary to adequately adapt to metabolic and physiological stress during postnatal life.

The phenotype of *Pgc-1β*$^{-/-}$ mice is similar to *Pgc-1α*$^{-/-}$ mice, though generally milder, and is accelerated upon stress induction, showing reduced mitochondrial volume, impairment in adaptive thermogenesis, and liver insulin resistance [104]. Comparing the observed phenotypes underlines the assumption that PGC-1α and PGC-1β control overlapping subsets of target genes, such as PERM1, which might indicate the ability for compensation upon loss of one of the genes. Notably, doubly deficient *Pgc-1αβ*$^{-/-}$ mice have been observed to shortly die after birth in consequence of heart failure associated with a perinatal developmental arrest in cardiac maturation accompanied by impaired mitochondrial biogenesis [105].

Genetic ablation of *Errα* results in mice that are viable and show no apparent defects, except for reduced body weight and peripheral fat deposits, which has been identified to be a consequence of lower lipid absorption capacity by the intestine [106]. Conversely, genetic ablation of one of the other two ERR family members, *Errβ* and *Errγ*, results in embryonic lethality or death shortly after birth, respectively [106]. Similar to what has been observed for the members of the PGC-1 family, loss of one of the ERR members does not completely abolish mitochondrial biogenesis and capacity, and compensatory mechanisms are in part observed. While multiple functions of ERRs in skeletal muscle are in coordination with PGC-1α, including transcriptional activation of mitochondrial genes, both ERRα and ERRγ possess PGC-1α-independent functions that are linked to the AMPK pathway regulating aerobic metabolism, vascularization, and mitochondrial biogenesis [107, 108].

In this study, we used a systemic *Perm1* knockout mouse model. Compensatory and adaptational mechanisms as described in PGC-1- and ERR knockouts cannot be excluded here. While overexpression of PERM1 in cultured cells or virus-mediated injection of a vector containing PERM1 into mouse skeletal muscle has been observed to result in elevated mRNA levels of PGC-1α and ERRα, we did not observe alterations in gene expression of these factors (data not shown) [74, 75]. Notably, virus-mediated knockdown of endogenous *Perm1* in leg muscles of adult mice caused reduction in PGC-1α and increase in ERRα protein levels ten weeks after virus injection, which was more pronounced after endurance exercise training [81]. This might indicate that muscles try to compensate for PERM1 reduction through induction of ERRα as an initial response and during enhanced work load, but that alterations in both PGC-1α and ERRα might not be observable anymore in adult mice of a constitutive knockout line at baseline conditions.

Although the phenotype of *Perm1*$^{-/-}$ hearts is very mild compared to loss of function of some of the PGC-1 and ERR factors, their cardiac expression patterns show large similarities and their increasing proteins levels are in line with pre- and postnatal increases in ETS complexes and mtDNA [74]. Thereby, PERM1 may contribute to mitochondrial biogenesis in a PGC-1- and ERR-dependent manner throughout cardiac development and maturation.

3.2. PERM1 might be involved in the stabilization of the MICOS/MIB complex in cardiac and muscle tissue

In contrast to its contribution to activate mitochondrial metabolism in cardiac biogenesis, PERM1 has been reported to be downregulated in failing hearts from patients with dilated cardiomyopathy [74]. Moreover, we found PERM1 downregulated in a different study in a mouse heart failure model with TAC-induced hypertrophy (**Fig. 10**) (unpublished data). PERM1 was unchanged between sham- and TAC operated hearts two days post surgery, but significantly downregulated at day 7 and day 21 (**Fig. 10a+b**). Notably, downregulation of PERM1 was stronger than those of the MICOS/MIB complex (**Fig. 10b**). Our data is in accordance with several publications observing PERM1 downregulation upon TAC surgery [74, 76, 109].

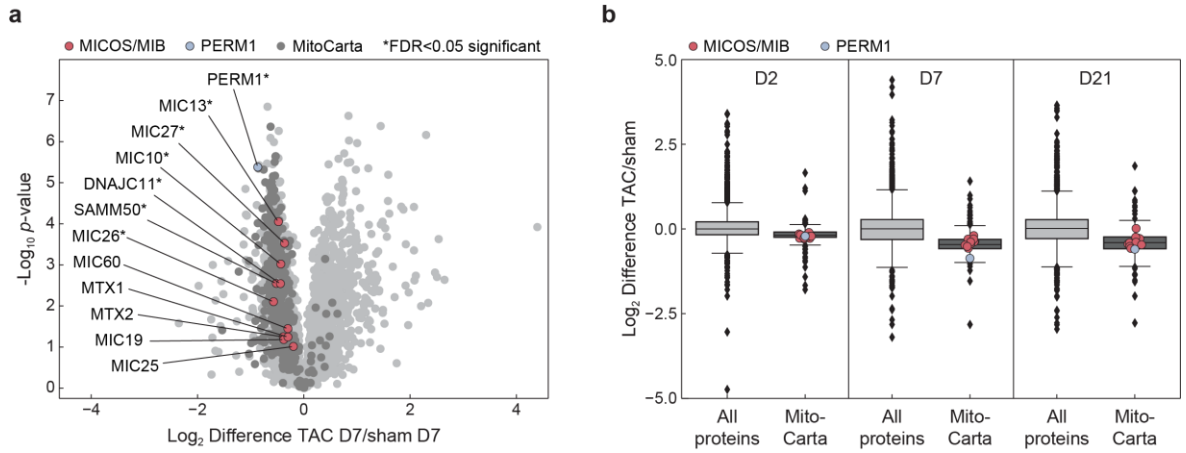


Fig. 10: PERM1 is downregulated in TAC-operated mouse hearts. (a) Volcano plot depicting downregulation of PERM1 and MICOS/MIB proteins at day 7 post TAC surgery compared to sham controls. (b) Comparison of the $\log_2$ differences of MICOS/MIB proteins and PERM1 compared to the complete dataset and the MitoCarta annotated proteins revealed stronger downregulation of PERM1 at day 7 and day 21 compared to the MICOS/MIB proteins.

(a) Unpaired two-sided Student's *t*-test, S_0=0.1, permutation-based FDR <0.05, 500 randomizations. (b) Box plots represent the median, 25th, and 75th percentiles; maximum and minimum are connected through whiskers. Outliers are defined as Q1–1.8 IQR and Q3+1.8 IQR.

PGC-1α has also been reported to be downregulated in heart failure [103]. Therefore, it is possible that downregulation of PERM1 in heart failure is a result of loss of PGC-1α-dependent mitochondrial and metabolic dysfunction, a key aspect of patients suffering from cardiomyopathy.

Besides the assumption that depletion of PERM1 is a result of downregulation of PGC-1α, the fast downregulation of PERM1 in comparison to the majority of mitochondrial proteins and the MICOS/MIB complex might also be explained by the short half-life of PERM1 and the presence of the PEST motif. PEST motifs have been associated with proteins with short half-lives and are considered to serve as a phosphodegron for the degradation by the UPS [110]. We demonstrated that phosphorylation of four serines in the PEST motif of PERM1 by CK2 mediates degradation of PERM1 *in vitro* and, therefore, suggest that fast depletion of PERM1 during heart failure or amyotrophic lateral sclerosis might be mediated both by phosphorylation of serines 347, 358, 369, and 380 by CK2, and by downregulation of PGC-1α.

A recent study investigated the effect of PERM1 in stressed heart by generating a transgenic mouse model with a cardiac-specific overexpression of PERM1 (PERM1cTG) and subjected these mice to TAC: While wild-type mice developed severely reduced heart function,

changes in PERM1cTG mice were significantly reduced with preserved mitochondrial function [109]. Interestingly, pathway enrichment analysis from proteomic profiling of TAC-operated PERM1cTG left ventricular tissue revealed the term “mitochondrial organization” as the most upregulated term, followed by “ATP metabolic process”, and “mitochondrial transport” [109]. Important contributors to mitochondrial organization are the members of the MICOS complex involved in the formation of the cristae and the cristae junctions and, in orchestration with the SAM complex, in maintaining the correct distance of IMM and OMM. While we did not observe a global downregulation of MICOS/MIB proteins in *Perm1*$^{-/-}$ tissues, MICOS proteins MIC60, MIC19, and MIC10 were upregulated in PERM1cTG sham and TAC hearts [109]. Even upon downregulation of MIC60 via shRNA in cultured cardiomyocytes, overexpression of PERM1 could rescue protein levels of MIC60 and multiple MICOS/MIB proteins and consequently also partially preserve OXPHOS protein levels, however, maximal respiration could not be restored [109].

In our mouse model, *Perm1*$^{-/-}$ skeletal muscle possessed a higher turnover of mitochondrial proteins, particularly of MICOS/MIB members, indicating that the stability and integrity of mitochondria might be affected upon loss of PERM1. This is supported by electron microscopic analysis of *Perm1*$^{-/-}$ hearts displaying remarkably reduced cristae density and increased mitochondrial disorganization, which has also been observed in failing hearts [78, 103]. Furthermore, altered MIC60 levels and mitochondrial ultrastructure have been associated with impaired mitochondrial membrane potential, which contributes to elevated ROS production [111]. ROS are chemically reactive species containing oxygen and include peroxides, superoxide, and hydroxyl radical. In general, they are formed as a natural byproduct during normal metabolic pathways and are important for redox homeostasis and cell signaling. A certain relatively low amount of ROS is essential for cell viability, since ROS regulate growth, proliferation, differentiation, and adaptation, while increased ROS formation, however, is associated with DNA/RNA damage, apoptosis, aging, and aging-related diseases [111]. Skeletal muscle, in general, consumes large amounts of oxygen and the oxygen flux increases significantly under conditions of exercise and muscle contraction. Thus, it is not surprising that muscle is particularly vulnerable to oxidative stress, since the increase in oxygen flow is associated with an increase in free oxygen radicals. Here, we reported increased ROS in *Perm1*$^{-/-}$ muscles and determined an overall downregulation of mitochondrial proteins and an upregulation of proteins involved in the antioxidant defense. Moreover, we observed altered mitochondrial membrane potential and lower levels of

oxygen flux in all assessed stages at baseline conditions, particularly for complex I. Complex I is the major contributor to ROS production and dysfunction or inhibition of complex I result in increased ROS levels [112].

Therefore, we hypothesize that PERM1 contributes to the stability of the MICOS complex and thereby maximizes oxidative capacity through interaction with MIC60. This might support mitochondrial integrity and prevent excessive ROS production.

3.3. PERM1 behaves like a MICOS/MIB complex protein of the OMM with so far unknown biogenesis and import pathway

The composition of the MICOS/MIB complex is not static but rather dynamic under different cellular conditions and in different tissues [113]. Potential novel constituents of the human MICOS/MIB complex include proteins of the OMM, such as the E3 ubiquitin ligase MUL1, the GTPase RHOT2, which is involved in mitochondrial trafficking, and the IMM protein TMEM11 [36]. Another interesting candidate that has been associated with the MICOS/MIB complex is the armadillo repeat-containing protein 1 (ARMC1). While the armadillo repeat-containing protein family has been identified to be involved in tumor development and some members, such as β-catenin are well described, the function of ARMC1 remains so far elusive. Similar to PERM1, ARMC1 localizes both to the cytosol and the mitochondria, and although no integration into the OMM via a transmembrane region has been identified, it is postulated that association with the OMM is mediated by the C-terminus, leaving the rest of the protein exposed to the cytosol [114]. ARMC1 has been identified as an interactor of several proteins of the MICOS/MIB complex, including MIC60, MIC19, MIC10, SAM50, MTX1, and DNAJC11 [36, 114]. Downregulation of MIC60 in cultured cells has been reported to strongly reduce levels of ARMC1, similarly to what has been observed for the levels of PERM1 upon downregulation of MIC60 in primary cultured neonatal mouse cardiomyocytes [109, 114]. Blue-native polyacrylamide gel electrophoresis (BN-PAGE) analysis of HEK cells transfected with ARMC1 identified the presence of the protein in a high molecular weight protein complex that was similar to the one formed by MIC60 and SAM50 [114]. According to the Human Protein Atlas, ARMC1 is expressed in multiple tissues, with a maximum detected in brain and only moderate expression in skeletal muscle and heart tissue, which represents a complementary expression pattern to PERM1, which is highly expressed in cardiac and skeletal muscle but absent from brain. Equivalently to

BN-PAGE analysis of ARMC1, we could identify endogenous PERM1 co-migrating with the fully-assembled MICOS/MIB complex by BN-PAGE and following complexome profiling analysis. Here, protein complexes were isolated under native conditions from heart mitochondria, separated on a native protein gel, and gel lines were sliced into 70 pieces that were subjected to mass spectrometry analysis that allowed profiling of proteins in a range from 40-4,000 kDa. The resulting profiles of PERM1 were congruent with the profiles we obtained for SAM50 and MTX2, displaying a peak at around 2.2-2.3 MDa, which correlates with the fully-assembled MICOS/MIB complex. Taken together, PERM1 behaves as a component of the MICOS/MIB complex in cardiac and skeletal muscle, as it interacts with other MICOS/MIB complex subunits and is affected by complex destruction as shown by downregulation of MIC60.

Interestingly, a secondary structure and topology prediction of all-helix integral membrane proteins using MEMSAT3 [115] could predict a helical transmembrane region between the amino acids 162 and 177 of mouse ARMC1 (**Fig. 11**). Against an earlier hypothesis, this TM is not at the C-terminus but rather in the middle of the protein, like it is seen e.g. for the protein MIM1 in yeast. However, it should be noted that the C-terminal tail that is considered to face the IMS is >100 amino acids, which might possibly be too large for the 60 nm wide IMS. If the TM prediction of ARMC1 is correct and whether the protein might be a substrate to C-terminal protein processing at some point of its maturation and biogenesis has to be investigated in future experiments. The assumption that the TM is at the C-terminus of ARMC1 was made based on the observation that a fraction of FLAG-ARMC1 localizes to the mitochondria, while ARMC1-FLAG is completely soluble [114]. Alignment of multiple mammalian species, including mouse, human, bovine, and rat, as well as reptiles and fish, reveals an overall highly conserved sequence (70.0-99.7%), not only at the C-terminus, as the paper claimed. The C-terminal region is conserved between some of the here considered species, but is different e.g. in *Alligator mississippiensis*. The MEMSAT-predicted TM is 16 amino acids long and is almost 100% identical in all the mentioned species.

Similar to ARMC1, the MEMSAT-predicted hydrophobic transmembrane helix of mouse PERM1 from amino acids 740-755 is 16 amino acids long, and it is followed by a 52 amino acids long tail. We could demonstrate that this C-terminal helical structure is responsible for mitochondrial localization of PERM1, as deletion of the region resulted in a loss of PERM1 in the mitochondrial fraction after subcellular fractionation. Moreover, deletion of the helix

prevented interactions between PERM1 and the MICOS proteins MIC60, MIC19, and MIC25 in AE-MS experiments. It is suggested that the 52 amino acid long C-terminal tail is exposed to the IMS, enabling the interaction with the MICOS/MIB complex.

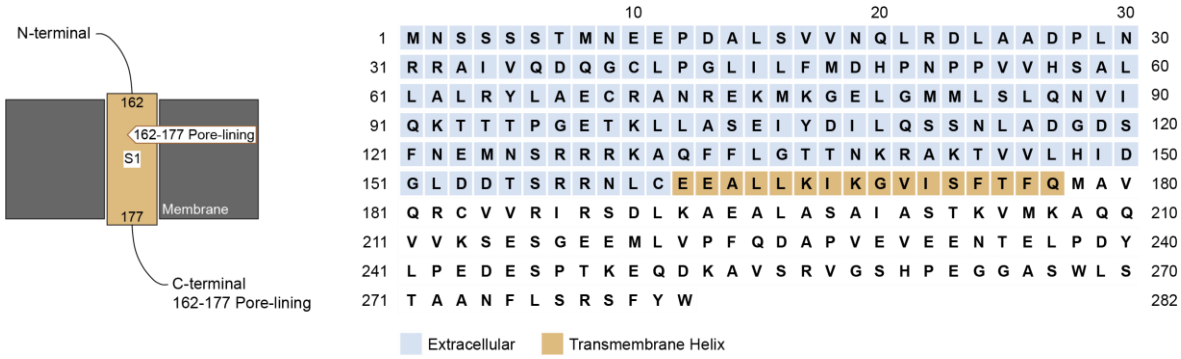


Fig. 11: MEMSAT predicted a transmembrane helix in ARMC1. The predicted TM is 16 amino acids long and located in the middle of the ARMC1 protein sequence.

There are two types of integral membrane proteins in the OMM: proteins with a transmembrane β-barrel and those that comprise single or multiple TMs of α-helical structures. While β-barrel protein biogenesis and import by the TOM, the TIM, and the SAM complex has been largely studied, import of α-helically anchored proteins involve a number of different import pathways, many of which are poorly characterized yet [116, 117]. Depending on the topology of the helical TM, single-span integral OMM proteins can be assigned to different categories, including signal-anchored proteins, harboring the TM at the N-terminus, and tail-anchored proteins, the class of α-helically anchored proteins PERM1 is part of, where the TM is located at the C-terminus. In both cases, only a small fragment is located within the IMS, while the bulk of the protein is facing the cytosol. Since the TM is at the C-terminal site of the protein, targeting to the membrane must be a post-translational process rather than a co-translational one, which is observed for proteins harboring an N-terminal MTS. Described members of tail-anchored proteins in yeast imply the small TOM subunits TOM5, TOM6, and TOM7, and FIS1. In mammalian cells, C-terminal TMs have been identified in proteins of the BLC-2 family, NIX, mitochondrial cytochrome *b*5, MTX1, vesicle-associated membrane protein 1 (VAMP1), and synaptojanin-2-binding protein (SYNJ2BP, also known as OMP25) [118].

All known tail-anchored proteins do not share sequence conservation in their tail region, and it has been postulated that mitochondrial-targeting information is dependent on the structural properties of the TM [119]. Overall, the TM is moderately hydrophobic and relatively short.

Notably, the length of the TM can be critical, since hydrophobic TMs of more than 20 amino acids might function as an ER-targeting signal [120]. Moreover, TM flanking regions have been observed to be rich in basic amino acids with positive charges, which has been emphasized for the BCL-2 proteins: BCL-XL integrates in the OMM, whereas its family member BCL-2 localizes to the nuclear envelope and the ER [121]. While both proteins have TMs with similar hydrophobicity and length, the two positively charged amino acids at either side of the TM in BCL-XL are essential for the specific targeting of BCL-XL to mitochondria [121]. A consensus sequence for OMM targeting of tail-anchored proteins was suggested in the form of $Bx_{0–9}$ $Bx_{0–2}$-TM-$x_{0–1}$ $Bx_{0–6}$ B (where B is for basic residues and x for any amino acid), which is followed by NIX, BAK, mitochondrial cytochrome *b*5, VAMP1, TOM5, and MTX1[121]. In spite of the fact that we have shown that PERM1 associates with mitochondria dependent on a C-terminal sequence, the region around the MEMSAT-predicted 16 amino-acid long TM of PERM1 contains basic amino acids at the -12 and -7 position and the +2 and the +13 position in human and mouse, which does not match the putative consensus sequence (**Fig. 12**). Similarly, the TM of OMP25, which is asserted in UniProt, is 21 amino acids long and contains basic residues at the positions -18, -7, +1, and +3 in human and mouse, which also breaches the predicted consensus sequence and shows that, although it matches to a lot of C-tail anchored proteins and might help in identifying novel candidates, there are exceptions to the rule. Notably, depending on the prediction tool that is used for identification, the borders of the TMs are not well-defined, which makes assessment of consensus sequence, in general, difficult.

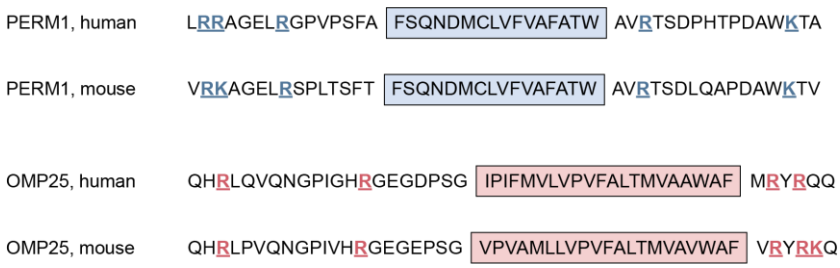


Fig. 12: PERM1 and OMP25 do not follow the predicted consensus sequence for OMM targeting. Amino acid sequences from human and mouse PERM1 and OMP25 TMs and flanking regions differ from the putative consensus sequence for OMM targeting of tail-anchored proteins. TM is marked with a box; basic amino acids are highlighted.

In yeast, tail-anchored proteins can follow various routes: one involves mediation by the TOM complex receptors and subsequent insertion by the mitochondrial import (MIM)

complex; the second one requires the MIM complex and further the topogenesis of β-barrel protein (TOB)/SAM complex [122, 123]. For decades, the TOB/SAM complex, comprising TOB55 (SAM50), TOB38 (SAM35), and MAS37 (SAM37), was thought to be dedicated only to the biogenesis of β-barrel proteins, but recent research suggests an essential function also for some tail-anchored proteins [123-125]. While the small TOM components can be inserted independently of TOB55 and require only MAS37, the biogenesis of the bigger complex member TOM22 is dependent on proper functioning of the entire SAM complex [125]. Multiple homologues of TOB55 have been identified in all known eukaryotes and also outside eukaryotes, including SAM50 in mammals, and MAS37 has been reported to show significant homology to MTX1 in mammals. Although no clear sequence-based similarities to non-fungal proteins have been observed, TOB37 might be related to MTX2 in the mammalian system [118].

Most of the knowledge of mitochondrial protein import derived from research in yeast. While homologues proteins for the TOB/SAM complex have been identified in mammals, the MIM complex was not yet found in mammalian cells. However, few proteins have been suggested as key players in the targeting and import of C-tail-anchored OMM proteins. One study proposed that membrane integration of the tail-anchored proteins of the BLC-2 family members BAK and BCL-XL, as well as OMP25, might share a common import pathway that is TOM complex-independent, and that VDAC2 is important for import of BAK [126]. Moreover, the study observed that targeting of C-tail anchored proteins proceeded autonomously in the absence of cytoplasmic recognition factors, but required cytoplasmic chaperones in case that the cytoplasmic domains of the imported proteins possess import-incompetent conformations [126].

Besides VDAC2, recently, mitochondrial carrier homolog 2 (MTCH2) and its paralog MTCH1, have been identified to be required for the insertion of biophysically diverse tail-anchored, signal-anchored, and multipass proteins, but not outer membrane β-barrel proteins [127]. Loss of MTCH2 affected the insertion of several mitochondrial tail-anchored proteins including OMP25, BCL2L1, and cytochrome *b*5, and based on structure prediction, the hydrophilic surface of MTCH2 generates a groove that regulates the biogenesis of MTCH2-dependent substrates [127]. Therefore, VDAC2, MTCH2, and possibly MTCH1, represent important members of OMM protein insertases mediating the insertion of C-tail anchored proteins into human, most likely overall in mammalian, mitochondria.

If and how these proteins are involved in the biogenesis and import of PERM1 has to be determined in future studies. In the PERM1 interactome study, we found MTCH2 enriched upon pulldown of PERM1 in mouse heart, and VDAC2 was co-eluted after PERM1 enrichment in C2C12 myoblasts. SAM50 was pulled down in almost all PERM1 enrichments, and it is hard to evaluate if SAM50 co-enrichment is the result of its possible involvement in PERM1 biogenesis or its presence in the MICOS/MIB complex.

Since PERM1 is only expressed at a very low level in C2C12 myotubes under basal conditions, investigation of PERM1 maturation is challenging. Overexpression of PERM1 in cells after shRNA-mediated knockdown of potential insertases gives the cell a lot of time to transport the protein and impairment in transport might be compensated for, since sufficient knockdown of e.g. SAM50 is only achieved after five days [128]. To overcome the problem of a slow turnover, the use of proteolysis targeting chimeras (PROTACs) might be beneficial. PROTACs are heterobifunctional molecules consisting of a E3-ubiquitin ligase binding domain and a second binding domain to bind the target protein, and they are capable of removing target proteins by targeting them to the UPS for degradation [129]. Moreover, it is crucial to distinguish between fully imported PERM1 and PERM1 interacting with the surface, with the latter one possibly being particularly boosted upon overexpression of PERM1. Therefore, mitochondrial import assays using radiolabeled PERM1 might offer valuable information on the dynamics of PERM1 import, especially when using isolated mitochondria of cells after downregulation of SAM50, VDAC2 or MTCH1/2.

Furthermore, a mitochondrial split-GFP approach might be used to identify the import pathway of PERM1 by attaching the small portion of the split-GFP system (GFP11) to the C-terminus of PERM1 and the large portion (GFP1-10) to the potential insertase, such as VDAC or MTCH1/2, and expressing these proteins in cell culture systems. Upon interaction of PERM1 with either of the potential import proteins, self-assembly of the split-GFP should be observable. In the case of SAM50, interaction of PERM1 with the fully-assembled MICOS/MIB complex might already lead to an assembly of the split-GFP which makes it difficult to assess its role for PERM1 import using this approach.

3.4. Long PERM1 isoform interacts with the costamere organizer ANKB and anchors mitochondria to the sarcolemma

On western blot, PERM1 appears as a double band, with the lower band running at approximately 85 kDa and the upper band shortly above 100 kDa. These two bands have been described to arise from two conserved in-frame translational start sites, with the second one at amino acid position 138 [74]. Since we determined the TM at the C-terminus of PERM1, it is not surprising to find both isoforms in mitochondria and mitochondria-associated compartments. Moreover, both the long and the short isoform are equally present in heart and skeletal muscle tissue and in all identified subcellular compartments, including the nucleus and the cytosol. Therefore, compartment- or tissue-specific roles of the different isoforms are rather unlikely, which challenges the characterization of the function of the individual isoform.

We here identified the interaction region with ANKB within the amino acids 6-55 of PERM1. This indicates that only the long isoform interacts with ANKB, while the short isoform is not able to associate. Preliminary elution profiles from size-exclusion chromatography using recombinantly expressed short PERM1 and ANKB confirmed that assumption (data not shown). ANKB, encoded by the *Ank2* gene, is one of three members of the ankyrin family of plasma membrane adaptor proteins that have been described to be involved in the organization and anchoring of integral membrane complexes to the spectrin- and actin-based cytoskeleton [130]. All vertebrate ankyrins, including ANKR, encoded by *Ank1*, ANKG, encoded by *Ank3*, and ANKB evolved from a single ankyrin gene in the invertebrate urochordate *Ciona intestinalis* [131]. They share a highly conserved primary sequence, as well as a similar domain organization, including the N-terminal ankyrin-repeat domain. This domain is followed by a $ZU5_2$-UPA domain module, which holds the β-spectrin binding site, a death domain of unknown function, and lastly, a C-terminal regulatory domain [131]. Unlike the rest of the protein, the regulatory domain displays the highest diversity among the three ankyrins.

While ANKR is predominantly expressed in erythrocytes, ANKG is ubiquitously expressed among most tissues in human and mouse. ANKB has originally been discovered in brain, where it is highly expressed, but it possesses high expression levels in other tissues as well, including skeletal muscle and heart. Alternative splicing results in a series of ankyrin gene products that exhibit specific subcellular distributions and functional properties [131]. The

220 kDa isoform is the predominant isoform in most of the tissues where ANKB is expressed, whereas a 440 kDa isoform has only been identified in the neuronal axon [132]. Despite their homology and shared expression in tissues such as heart and skeletal muscle, ANKB and ANKG own different subcellular localizations and non-overlapping functions. Two examples include rod photoreceptors, where ANKG exclusively localizes at the outer segment responsible for segregation processes, whereas ANKB is present in the inner segment mediating the localization of the sodium/calcium exchanger (NCX) and Na/K ATPase [131]; and skeletal muscle, where ANKB plays a role in the transport process of β-dystroglycan and a fraction of microtubules to the costameres, while ANKG is involved in the maintenance of β-dystroglycan and dystrophin at those structures [133].

Using different ANKB deletion mutants, we identified the ankyrin-repeat domain to interact with PERM1. This highly organized domain has been reported to be involved in many protein-protein interactions and is a 33-residue motif consisting of two alpha helices separated by loops. Although ankyrin repeats are also present in bacteria and archaea, they are far more abundant in eukaryotes [134]. Proteins containing ankyrin-repeat domains possess various functions, including signal transduction, cell cycle and transcriptional regulation, cytoskeletal organization, and molecule transport. The motif is rather defined by its folding architecture than its function, and sequence similarity between the repeats is low. Interaction partners of the ankyrin-repeat domain of ANKB include NCX, Na/K ATPase, inositol 1,4,5-trisphosphate receptor (IP_3R), and dystrophin [135]. Direct interaction of ANKB with NCX requires multiple consecutive ankyrin-repeat β-hairpin loop tips in the repeats 16-18, while interaction with IP_3R is mediated by the β-hairpin loop tips of the consecutive repeats 22-24 [136, 137]. Consequently, these interactions require only small regions of the ankyrin-repeat domain, while the majority of the domain is accessible to mediate interactions with additional proteins. Moreover, ankyrins are able to bind multiple proteins at the same time [138]. To localize the region where ANKB interacts with PERM1, similar approaches as those that were used to identify the responsible repeats for NCX and IP_3R could be used: GFP-tagged ANKB mutants with consecutive β-hairpin loop tip mutations (i.e. repeats 5-6, 4-6, 3-6, 2-6, and 1-6 in four sets of six ANK repeats 1-6, 7-12, 13-18, and 19-24) were expressed in HEK-293T cells and interaction with the potential target was assessed by immunoprecipitation [137].

PERM1 has been identified to interact with other proteins containing ankyrin repeats, including ANKB's closest family member ANKG, but also ANKRD1, KANK1, and KANK2 [78]. KANK1 and KANK2 are also known as ANKRD15 and ANKRD25. While ANKB contains 24 ankyrin repeats, ANKG has 23, and ANKRD1, KANK1, and KANK2 harbor five repeats. At this point, it is hard to evaluate if the presence of ankyrin-repeat domains is responsible for the co-enrichment with PERM1 in pulldown experiments, since ankyrin repeats are so diverse and have low similarities in sequence or amino acid properties. Moreover, in contrast to other protein-binding domains, such as SH2 or SH3 domains, proteins containing ankyrin repeats do not recognize specific sequences of their targets or binding partners and binding might involve discontinuous patches of residues distributed over the entire molecules of both the ankyrin-repeat-containing protein and its binding partner [139]. Still, binding of ankyrin-repeat proteins is considered specific, but binding of multiple ankyrin-repeat proteins to the same target has been described, for example in the case of the kinase CDK4, which physically interacts with INK4 proteins, gankyrin, and IκBα, containing four, seven, and six ankyrin repeats, respectively [139].

In ANKB-depleted muscle, dystrophin remains intracellular and destabilization of costamere-associated microtubules and general muscle fragility have been observed [133]. On a molecular level, cells of *AnkB*$^{+/-}$ mice possess reduced expression and atypical localization of ANKB binding partners, such as Na/K ATPase and NCX, and in computational models, loss of these proteins have been associated with increased SR calcium stores leading to cardiac dysfunction characterized by bradycardia, sinus arrhythmia, idiopathic ventricular fibrillation, catecholaminergic polymorphic ventricular tachycardia, and risk of sudden death [140]. *AnkB*$^{-/-}$ mice die shortly after birth in consequence of nervous system defects, dilated ventricles, and extensive degeneration of the optic nerve [141]. It has been reported that *AnkB*$^{+/-}$ mice can live to adulthood but suffer from heart rate variability and sudden death in response to exercise [142].

In humans, ANKB loss of function has been associated with cardiovascular diseases. Since the first ANKB myopathy has been identified in the late 90s, which was caused by a point mutation at position 4,274 in exon 36, leading to the p.E1425G mutant, and resulting in type 4 long QT syndrome (now described as ankyrin-B syndrome) in a large French kindred with sinus node dysfunction and episodes of atrial fibrillation, more ANKB dysfunction variants have been reported, particularly in patients with ventricular arrhythmias [143].

Mislocalization of Na/K ATPase, NCX, and IP_3R to T-tubules/SR as a consequence of loss of interaction with ANKB, as seen in *AnkB*$^{+/-}$ mice, is the reason for human arrhythmia in patients with the p.E1425G variant [135].

As of today, more than 2,600 *Ank2* variants have been submitted to the ClinVar archive. Loss-of-function variants mostly concentrate on mutations in the regulatory domain, although the ankyrin-repeat domain is the largest part of the protein and is directly responsible for the interaction with the membrane-bound ion channels and transporters, as well as with PERM1. Interestingly, the C-terminal domain can bind the ankyrin-repeat domain and thereby control the localization of its binding partners [144]. How and if mutations in ANKB may result in loss of interaction with PERM1 and how this might be connected with the observed phenotypes in ankyrin-B syndrome is, therefore, hard to anticipate. Notably, there has been only one missense mutation reported for PERM1 to the ClinVar archive leading to an exchange of valine to alanine at the C-terminal tail, which might not affect the interaction of PERM1 with ANKB.

In this study, we hypothesize that the PERM1-ANKB-interaction is important for the organization of the mitochondrial network in skeletal muscle fibers. Similar to localizing the sarcolemma-bound channels and transporters, ANKB might be involved in the correct positioning and transport of the mitochondria through interaction with PERM1. Beyond its location at the sarcolemma, ANKB associates with IP_3R at the SR, where it might also interact with PERM1. Moreover, as a spectrin-organizer, ANKB is also connected with the cytoskeleton. Two other cytoskeleton-associated proteins were enriched in PERM1 interactome studies, vimentin and nestin, which belong to the class of intermediate filaments. It has been reported that vimentin colocalizes with mitochondria, mediates their mobility and distribution, and influences the rate of ATP synthesis and the mitochondrial membrane potential [145]. Heteropolymeric intermediate filaments consisting of nestin and vimentin have been described, and they might be responsible for the connection of myofibrillar Z-lines via interactions with α-actinin to costameres [146].

Interestingly, in embryonic heart tissue, from E9.5 to E15.5, the predominant isoform of PERM1 is the short isoform, which we think is uncapable to interact with ANKB [74]. From E17.5 onwards and persistent throughout postnatal to adult development, both PERM1 isoforms display an equal expression. As discussed above, postnatal hearts switch their energy supply and mitochondrial oxidative phosphorylation becomes the main source of

ATP. Similarly, upon addition of new myonuclei and hypertrophic growth of skeletal muscle fibers, oxidative metabolism is critical for muscle function, particularly in oxidative fibers. It might, thus, become majorly important for fiber integrity to stabilize and maintain the mitochondrial reticulum. Considering the reported assumption that trans-mitochondrial alignment of cristae is possible, and energy can be distributed throughout the fiber, correct positioning of the mitochondria is important and nutrient and oxygen supply by adjacent capillaries needs to be sustained. Increased ROS levels, upregulation of proteins involved in the antioxidant defense, and downregulation of mitochondrial proteins, which we observed in the absence of *Perm1*, might also be connected to the diminished anchoring of mitochondria to the sarcolemma and the impaired nutrient supply.

Therefore, we suggest that PERM1 does not only contribute to cardiac and skeletal muscle development by increasing mitochondrial biogenesis dependent on PGC-1 and ERR and mitochondrial internal integrity through interaction with MIC60, but also through the early establishment of a functional mitochondrial reticulum by interacting with ANKB and the cytoskeletal proteins vimentin and nestin.

3.5. Conclusion and outlook

Cardiac and skeletal muscle development and function is dependent on a dense mitochondrial network and oxidative metabolism to generate the required amounts of ATP for contraction. Here, we described that the cardiac- and skeletal muscle-specific protein PERM1 is increasingly expressed in these tissues during postnatal development. Moreover, we identified PERM1 to interact and behave like a tissue-specific MICOS/MIB complex member through its insertion in the OMM by a C-terminal α-helical TM. The N-terminus of PERM1 interacted with the N-terminal ankyrin-repeat domain of ANKB, which we observed using multiple approaches.

Combining what has been studied about PERM1 in literature and the new insights we gained within the here presented thesis, we hypothesize a model of dual regulation of mitochondrial biogenesis and oxidative capacity (**Fig. 13**). PERM1 in the nucleus might bind to ERRE and PPRE in the promotor regions of known ERRα and PPARα target genes in a PGC-1α-dependent and possibly also -independent manner. Identified target genes are known to promote OXPHOS, fatty acid metabolism, mtDNA replication, and mediate exercise-induced responses. This ultimately leads to enhanced mitochondrial biogenesis and oxidative capacity, which is thought to be particularly important during cardiac and skeletal muscle development and upon exercise, where PERM1 levels are elevated, similar to the levels of PGC-1- and ERR factors.

Besides its role as a transcriptional co-factor, we here suggest that PERM1 is also contributing to mitochondrial oxidative capacity through interaction with the MICOS/MIB complex and ANKB outside the nucleus. Since ablation of *Perm1* has been reported to disrupt cristae integrity, and we observed PERM1 behaving like a MICOS/MIB complex protein, PERM1 may contribute to mitochondrial integrity and proper formation of mitochondrial cristae junctions by stabilizing the MICOS/MIB complex. Moreover, through interaction with the costamere organizer ANKB and the intermediate filament proteins vimentin and nestin, PERM1 could contribute to early establishment of a functional mitochondrial reticulum in skeletal and cardiac muscle to maintain optimal transport and supply with metabolites and ATP. In sum, we propose PERM1 is a major, although not essential, regulator of cardiac and skeletal muscle maximal mitochondrial oxidative metabolism and capacity, particularly during events of high energy needs such as during development and after exercise.

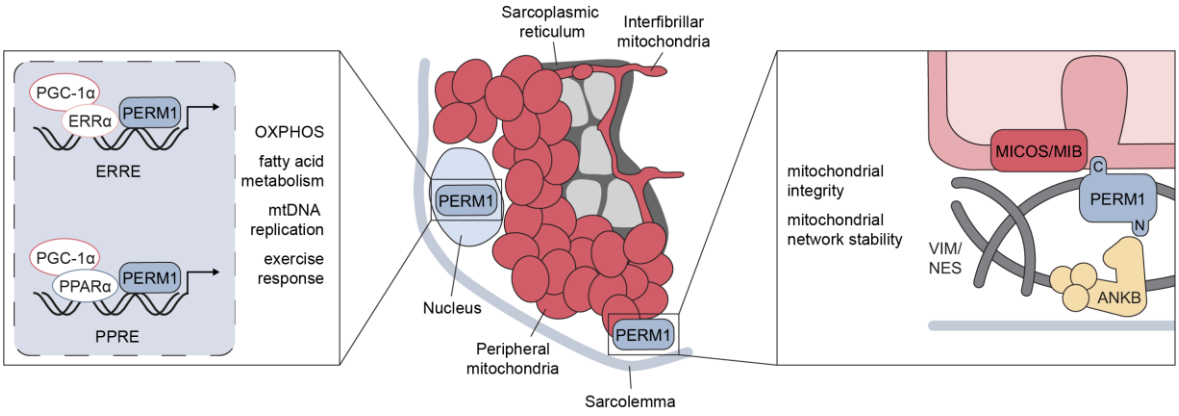


Fig. 13: Model of dual function of PERM1 in the nucleus and mitochondria of skeletal muscle. PERM1 activates the transcription of genes that are important for mitochondrial biogenesis and metabolism by binding to ERRE and PPRE dependent on PGC-1α, ERRα, and PPARα. By interacting with the MICOS/MIB complex, ANKB, and cytoskeletal proteins, PERM1 contributes to both internal mitochondrial integrity and to the establishment of a robust mitochondrial network.

Future studies might shed more light on the regulation of PERM1. We identified more than 30 phosphorylation sites on PERM1, however, could not assign specific functions to most of them. We observed highly dynamic PERM1 levels with a short half-life in cardiac and skeletal muscle and identified CK2 to be responsible for the phosphorylation of four serines in the PEST motif in the center of the PERM1 protein. While we presented a way of how degradation of PERM1 is mediated via the UPS, detailed knowledge of how PERM1 is activated, either by transcriptional feedback loops or possibly by PTMs, remains elusive. Moreover, it is still unknown, if cytosolic, mitochondrial, or SR-associated PERM1 might be transported back into the nucleus upon receival of a specific signal or if the different PERM1 pools are regulated and function independently of each other. Further approaches should also focus on the roles of vimentin and nestin interaction and evaluate if these interactions are important for transport and localization of mitochondria to the fiber periphery and if PERM1 is responsible for the effectiveness of the cytoskeletal attachment of mitochondria. To evaluate protective capacities of PERM1 in pressure overload and ischemic heart disease, it can be helpful to subject *Perm1*$^{-/-}$ animals to hypertrophy models, such as TAC, and hypoxia-reoxygenation treatments.

Virus-induced overexpression of *Perm1* in intact skeletal muscle increased mitochondrial biogenesis, oxidative capacity, as well as capillary density and resistance to fatigue [75]. To further decipher the functional mechanisms behind these effects, we plan to establish a genetic mouse model overexpressing *Perm1* based on a ROSA26 knock-in vector and mating

with skeletal muscle- or heart-specific Cre mouse lines. Alternatively, a CRISPR/Cas9-loxP-based approach could be used. This model will be a useful complementation to the existing *Perm1*$^{-/-}$ model.

Overall, PERM1 is suggested to be responsible for rewiring mitochondrial activity. Further studies under different metabolic conditions will help to elucidate the function of PERM1 in more detail.

4. Experimental

4.1.1. Organisms

Different model organisms were used for this study. Mouse strains are listed in table 1, cell lines in table 2.

Table 1: List of utilized mouse strains.

Name	Background	Purpose	Source
Perm1$^{+/+}$ = WT	C57BL6J x 129 agouti	characterization	AG Krüger
Perm1$^{-/-}$ = KO	C57BL6J x 129 agouti	characterization	AG Krüger

Table 2: List of used cell lines.

Strain	Description	Purpose	Source
HEK-293T	human embryonic kidney cell line	immunoprecipitation	ATCC
DH5α	competent *E. coli* strain	cloning + expression	AG Schwarz

4.1.2. Constructs

The constructs in table 3 were used during this project.

Table 3: List of utilized constructs.

Name	Vector	Purpose	Source
TO5-STOP-FLAG	pcDNA5/TO	transfection	AG Krüger
***Perm1*-FLAG**	pcDNA5/TO	transfection	AG Krüger
FLAG-*Perm1*	pcDNA5/TO	transfection	this study
***Perm1Δ6-96*-FLAG**	pcDNA5/TO	transfection	this study
***Perm1Δ6-55*-FLAG**	pcDNA5/TO	transfection	this study
***Perm1Δ82-96*-FLAG**	pcDNA5/TO	transfection	this study
Perm1ΔTM	pcDNA5/TO	cloning	AG Krüger
GFP-AnkB	pEGFP-C2	cloning	Vincenzo Sorrentino

***Perm1ΔTM*-HIS**	pET26b+	expression	this study
HIS-*AnkB*	pQE80	expression	this study
HIS-24*AnkB*	pQE80	expression	this study
HIS-*Δ24Ank*	pQE80	expression	this study

4.1.3. Primers

The following primers in table 4 were used for cloning.

Table 4: List of utilized primers.

Name	Target vector	Sequence
FLAG-*Perm1*-insert-for	*Perm1*-FLAG	TATAAGGATGATGATGATAAGGACA ACTTCCAGTACAGCGT
FLAG-*Perm1*-insert-rev	*Perm1*-FLAG	GGGCCCTCTAGATCAGCAGCTGGGGT TTGAGCTGGA
FLAG-*Perm1*-backbone-for	pcDNA5/TO	TGATCTAGAGGGCCCGTTTAAACCCG CTGATCAGCC
FLAG-*Perm1*-backbone-rev	pcDNA5/TO	ATCATCATCCTTATAATCCATCTCGA GCGGCCGCCACTGTG
***Perm1Δ6-96*-FLAG-for**	*Perm1*-FLAG	ACTTCCAGGAGGCCAGTCATCAG GTAGCC
***Perm1Δ6-96*-FLAG-rev**	*Perm1*-FLAG	TGGCCTCCTGGAAGTTGTCCATGG TACCAAGC
***Perm1Δ6-55*-FLAG-for**	*Perm1*-FLAG	ACTTCCAGCCCCCACCCCTCTTCACT G
***Perm1Δ6-55*-FLAG-rev**	*Perm1*-FLAG	GTGGGGGCTGGAAGTTGTCCATGGTA CCAAGC
***Perm1Δ82-96*-FLAG-for**	*Perm1*-FLAG	TGGCTGCTGAGGCCAGTCATCAGGTA GCC
***Perm1Δ6-55*-FLAG-rev**	*Perm1*-FLAG	TGGCCTCAGCAGCCACGTCCTCCAAC
***Perm1ΔTM*-HIS-insert-for**	*Perm1*-FLAG	GAAGGAGATATACATATGGACAACT TCCAGTACAGC

***Perm1ΔTM*-HIS-insert-rev**	*Perm1*-FLAG	GTGGTGGTGCTCGAGGCAGCTGGGG TTTGAG
***Perm1ΔTM*-HIS-backbone-for**	pET26b+	CTCGAGCACCACCAC
***Perm1ΔTM*-HIS-backbone-rev**	pET26b+	CATATGTATATCTCCTTCTTAAAGTT AAACAAAATTATTTCTAG
HIS-*AnkB*-insert-for	GFP-AnkB	TGCGAGCTCGGTACCATGATGAACG AAGATGCAGCTC
HIS-*AnkB*-insert-rev	GFP-AnkB	GGTCGACCCGGGTCACTCATTGTTGT CCTCTGACTG
HIS-*24AnkB*-insert-rev	GFP-AnkB	GGTCGACCCGGGTCAGTCATCACCCA GTTCTTTTAGGTC
HIS-*Δ24Ank*-insert-for	GFP-AnkB	TGCGAGCTCGGTACCTCACTACCCAG CAGTCAGTT
HIS-*AnkB*-backbone-for	pQE80	TGACCCGGGTCGAC
HIS-*AnkB*-backbone-rev	pQE80	GGTACCGAGCTCGCA

4.2. Methods

4.2.1. Tissue lysis and digestion

Skeletal muscle pools of TA, quadriceps, soleus and gastrocnemius of *Perm1*$^{-/-}$ and wild-type pups were lysed in prewarmed (~60 °C) 4% sodium dodecyl sulfate (SDS). Lysates were sonicated and cell debris was pelleted by centrifugation at maximum speed for 10 min. 25 µg of protein sample was used for further processing, reduction and alkylation was performed using 5 mM tris(2-carboxyethyl)phosphine (TCEP) and 15 mM chloroacetamide (CAA) and incubation for 10 min at 70 °C. Samples were precipitated in ice-cold acetone overnight and precipitates were reconstituted in urea buffer (6 M urea, 2 M thiourea in 50 mM HEPES, pH 8.0). Next, samples were digested with LysC (Wako) at an enzyme:protein ratio of 1:200 for 2 h at RT, diluted with 50 mM ABC to a urea concentration of 2 M and digested with trypsin (Serva) at an enzyme:protein ratio of 1:100 overnight at RT. Peptides were acidified to 1% FA and purified using StageTips.

4.2.2. Protein concentration determination

Protein concentration was determined using a Pierce Protein Assay (Thermo Fisher). BSA solutions with concentrations ranging from 0.05 mg/ml to 1.0 mg/ml were used as a standard. Protein samples were diluted 1:10-1:20 in the respective buffer. Absorptions were measured at 660 nm. To enable measurement of protein samples diluted in SDS-containing buffer, Pierce 660 nm Protein Assay Reagent was supplemented with the accessory Ionic Detergent Compatibility Reagent (Thermo Fisher).

4.2.3. Plasmids

To generate different the different deletion constructs of PERM1, amino acids 6-96, 6-55, or 82-96, were deleted in the pcDNA5/TO-*Perm1*-FLAG plasmid using the In-Fusion cloning technique (TaKaRa Bio Inc.) following the manufacturer's instructions. The FLAG-*Perm1* construct was generated using the same cloning strategy. In brief, 10 ng *Perm1*-FLAG construct was amplified using PrimeSTAR GXL DNA polymerase (TaKaRa Bio Inc.), the PCR product was isolated by gel extraction, In-fusion cloning reaction was performed using the In-Fusion Snap Assembly Master Mix for 15 min at 50 °C, reaction mixture was transformed into competent DH5α cells, and DNA was isolated using the E.Z.N.A Plasmid DNA Kit (Omega).

For cloning of the HIS-tagged constructs used for recombinant protein expression, the sequence of *Perm1ΔTM* was amplified from the pcDNA5/TO-*Perm1ΔTM*-FLAG plasmid, the different ANKB constructs were generated using a pEGFP-C2-*AnkB* plasmid as template. Gibson cloning strategy was followed. In brief, insert and backbone were amplified by PCR using Q5 DNA Polymerase (NEB), the PCR products were isolated by gel extraction, Gibson Assembly reaction was performed using HiFi DNA Assembly Master Mix (NEB) for 15 min at 50 °C, reaction mixture was transformed into competent DH5α, and DNA was isolated using the E.Z.N.A Plasmid DNA Kit (Omega).

All primers are listed in table 4. All constructs were verified by sequencing.

4.2.4. Cell culture and lysis

HEK-293T cells were cultivated as an adherent fibroblastoid monolayer in 10 cm dishes at 37 °C and 5% CO_2 in DMEM (Gibco), supplemented with 10 % FBS (Gibco) and

1X Penicillin-Streptavidin-Glutamine (Gibco) mix. Cells were harvested in 500 µl modified RIPA buffer (50 mM Tris/HCl pH 7.5, 150 mM NaCl, 1 % Nonidet P40, 1 mM EDTA, 0.1 % sodium deoxycholate) supplemented with protease and phosphatase inhibitors (Bimake) after washing once with ice-cold PBS. Lysates were incubated for 30 min at 4 °C, rotating, and DNA was sheared by sonification. To pellet cell debris, lysates were centrifuged at maximum speed and 4 °C for 10 min.

4.2.5. Immunoprecipitation of PERM1 and ANKB

For immunoprecipitation of PERM1 in HEK-293T, cells were grown to 70-80% confluency before transfection for 24 h using the calcium phosphate. In brief, for 10 cm dishes, 8-10 µg DNA was mixed with 37 µl 2 M $CaCl_2$ before 300 µl 2X HBS buffer (50 mM HEPES, 280 mM NaCl, 1.5 mM NaH_2PO_4, pH 7.0) was added. After incubation of 20 min, transfection mix was added to the cells. Cells were lysed as described above. After removing the cell debris, supernatants were transferred into a fresh precooled tube and 30 µl anti-FLAG (Miltenyi) beads were added. The mixture was incubated for 1 h at 4 °C, rotating. The separation was achieved using the magnetic µMACS system (Miltenyi) running at 4 °C. µColumns were equilibrated with lysis buffer and loaded with the lysate-bead-suspension. The columns were washed thrice with 200 µl lysis buffer followed by washing thrice with 50 mM ABC. Elution was performed at RT by applying 20 µl urea buffer (4) for 10 min and collecting the eluate with 50 µl urea buffer. Finally, samples were prepared for MS analysis with an in-solution/on-beads digest.

4.2.6. In-solution/on-beads digestion

Eluates from immunoprecipitation experiments were prepared for MS analysis by in-solution/on-beads digestion. Urea-containing samples were reduced and alkylated by applying TCEP to a final concentration of 5 mM and CAA to a final concentration of 15 mM for 1 h at RT. Next, the samples were digested with 1 µl LysC (Wako) for 2 h at RT, diluted with 50 mM ABC to a urea concentration of 2 M and incubated with 1 µl trypsin (Serva) overnight at RT. The next day, samples were acidified to 1% FA and sample purification on StageTips was performed.

4.2.7. MS-based proteome analysis

Proteome samples were analyzed using a liquid chromatography tandem mass spectrometry set up in an Orbitrap Eclipse Tribit Mass Spectrometer (Thermo Fisher) equipped with a FAIMS.Pro interface (Thermo Fisher). Chromatographic peptide separation was achieved on an in-house packed C18 analytical column (30 cm, 150 µm inside diameter, 1.9 µm ReproSil-Pur C18 beads; Dr. Maisch) coupled to an EASY-nLC 1200 HPLC system (Thermo Fisher) with an integrated column oven (50 °C, PRSO-V1, Bruker) and a binary buffer system consisting of buffer A (0.1% FA) and B (80% ACN, 0.1% FA). In-solution digested muscle samples were measured over a 90 min gradient. Buffer B was increased from 3% to 23% over 65 min, from 23% to 55% over 13 min, and from 55% to 95% over 12 min. Peptides were analyzed in a data-dependent acquisition (DDA) mode with two compensation voltages (CVs) of -50 V and -70 V at the FAIMS device. Full MS spectra (350–1,800 m/z) were recorded at a resolution (R) of 15,000 and AGC target at 300%. MS2 spectra were recorded at R = 30,000.

Samples derived from immunoprecipitation approaches were measured on a Quadrupole Orbitrap Plus Mass Spectrometer (Thermo Fisher) coupled to an EASY nLC 1000 HPLC system (Thermo Fisher) using the same columns and buffer solutions as described above. In-solution/on-beads digestied samples were measured over a 100 min gradient. Content of buffer B was increased from 13 to 48% within 75 min, followed by an increase to 75% over 5 min, washing with 95% buffer B for 10 min, reduction to 5% within 5 min and re-equilibration with 5% buffer B for 5 min. Full MS spectra (300–1,750 m/z) were recorded at a R of 70,000, a maximum injection time (IT) of 20 ms, and AGC target at 300%. MS2 spectra were recorded at R = 35,000, max. IT of 120 ms, and AGC target of 500%.

4.2.8. MS data processing and analysis

Spectra derived from the Eclipse were split according to their CV using FAIMS-MzXML-Generator-master (version). All generated MS raw data files were analyzed using the MaxQuant analysis software and the implemented Andromeda software (1.6.14.0). Peptides and proteins were identified using a canonical mouse UniProt database with common contaminants (FASTA files downloaded 08/2019, 17014 proteins) or a canonical human UniProt database with common contaminants (FASTA files downloaded 08/2019,

20392 proteins). All parameters in MaxQuant were set to the default values. Trypsin was selected as the digestion enzyme, and a maximum of two missed cleavages was allowed. Methionine oxidation and N-terminal acetylation were set as variable modifications, and carbamidomethylation of cysteines was chosen as a fixed modification. The label-free quantification (LFQ) algorithm was used to quantify the measured peptides and "match between runs" option was only enabled to quantify peptides with a missing MS2 spectrum for the proteome analysis, not for the immunoprecipitation analyis. Subsequent statistical analysis was performed by using the Perseus (1.6.5.15) software. Potential contaminants and reverse peptides were excluded, and values were log_2 transformed for following t-tests. ProteinGroups were filtered for three valid values in at least one group and missing values were imputed from a normal distribution (width: 0.3; down shift: 1.3). Unpaired two-sided Student's or Welch's *t*-tests with S_0=0.1 and a permutation-based FDR of 0.05 with 500 randomizations were used to identify differentially expressed proteins between groups defined by the genotype (*Perm1*$^{-/-}$ or wild type) or condition (for immunoprecipitation). Identified peptides were annotated with the following Gene Ontology terms: Biological Process, Molecular Function, and Cellular Compartment as well as using the Reactome database. Finally, graphical visualization was done using the Instant Clue software [147].

4.2.9. Expression and purification of recombinant PERM1ΔTM and ANKB constructs

For recombinant protein expression 4-6 l LB-medium equipped with 100 µg/ml kanamycin or 100 µg/ml ampicillin, respectively, were inoculated with 50 ml starter cultures for the different constructs and incubated at 37 °C until it reached an optical density $(OD)_{600}$ of ~0.2. Temperature was decreased to 28 °C and 0.1 mM isopropyl ß-D-1-thiogalactopyranoside (IPTG) was added at an OD_{600} of 0.6-0.8. Cells were harvested after 4 h, lysed in ice-cold lysis buffer (50 mM Tris/HCl, pH 7.5, 300 mM NaCl, 3.7 mg/l culture lysozyme, 5 mM β-mercaptoethanol, 25 µg/ml DNAse) equipped with protease inhibitors (Sigma), sonicated with 30 sec on, 30 sec off for 6 min pulse on, and centrifuged for 30 min at 30,000 *g* at 4 °C. The cleared lysate was applied to 20 ml Ni-NTA resin equilibrated with >10 column volumes H_2O and >1 column volume equilibration buffer (50 mM HEPES, pH 8.0, 500 mM NaCl, 2 mM dithiothreitol (DTT)), incubated for 20 min at 4 °C and flow-through was reapplied to the column. This was followed by washing with 10 column volumes of wash buffer 1

(50 mM HEPES, pH 8.0, 500 mM NaCl, 2 mM DTT, 10 mM imidazole) and wash buffer 2 (50 mM HEPES, pH 8.0, 500 mM NaCl, 2 mM DTT, 20 mM imidazole). Elution was performed with 1.5 column volumes elution buffer (50 mM HEPES, pH 7.5, 300 mM NaCl, 2 mM DTT, 400 mM imidazole) for 20 min before collection and was repeated with 1 column volume. Both elution fractions were combined and concentrated with two subsequent Vivaspin 20 concentrators (Sigma) with a 100 kDa cutoff.

For further purification, concentrated protein samples were submitted to preparative size-exclusion chromatography using a HiLoad Superdex 16/600 200 pg column (Sigma) in ÄKTA purification system (Cytiva) equilibrated with 1 column volume storage buffer (50 mM HEPES, pH 7.5, 300 mM NaCl, 2 mM DTT) at a flow rate at 4 °C of 0.5 ml/min. Protein samples were injected with a flow rate at 4 °C of 0.4 ml/min and fractioned in fractions of 1.5 ml. Based on the chromatogram, fraction containing high protein concentrations were selected and assessed by SDS-PAGE and subsequent Coomassie staining.

4.2.10. Surface plasmon resonance

Binding of the different ANKB constructs to PERM1ΔTM was measured using a BIAcore 2000 system (Biacore). PERM1ΔTM in 10 mM sodium acetate at pH 4.0 were coupled to the carboxymethylated dextran layer of CM-5 chips which were activated with 50 mM N-ethyl-N'-(3-diethylaminopropyl)-carbodiimide and 50 mM N-hydroxysuccinimide according to the manufacturer's recommendations. Interaction between PERM1 and ANKB variants was analyzed in HBS-EP buffer (0.01 M HEPES pH 7.4, 0.15 M NaCl, 3 mM EDTA, 0.005% v/v Surfactant P20) and chip regeneration was performed with 10 mM Glycine pH 1.5.

5. References

[1] H.A. Al-Khayat, Three-dimensional structure of the human myosin thick filament: clinical implications, Glob Cardiol Sci Pract 2013(3) (2013) 280-302.

[2] J. Squire, Special Issue: The Actin-Myosin Interaction in Muscle: Background and Overview, Int J Mol Sci 20(22) (2019).

[3] O. Monfredi, H. Dobrzynski, T. Mondal, M.R. Boyett, G.M. Morris, The anatomy and physiology of the sinoatrial node--a contemporary review, Pacing Clin Electrophysiol 33(11) (2010) 1392-406.

[4] R. Hinch, J.L. Greenstein, A.J. Tanskanen, L. Xu, R.L. Winslow, A simplified local control model of calcium-induced calcium release in cardiac ventricular myocytes, Biophys J 87(6) (2004) 3723-36.

[5] A.M. Gordon, E. Homsher, M. Regnier, Regulation of contraction in striated muscle, Physiol Rev 80(2) (2000) 853-924.

[6] C.W. Balke, T.M. Egan, W.G. Wier, Processes that remove calcium from the cytoplasm during excitation-contraction coupling in intact rat heart cells, The Journal of physiology 474(3) (1994) 447-62.

[7] R. Gordan, J.K. Gwathmey, L.H. Xie, Autonomic and endocrine control of cardiovascular function, World J Cardiol 7(4) (2015) 204-14.

[8] V. Prasad, D.P. Millay, Skeletal muscle fibers count on nuclear numbers for growth, Semin Cell Dev Biol 119 (2021) 3-10.

[9] Z.W. Hall, E. Ralston, Nuclear domains in muscle cells, Cell 59(5) (1989) 771-2.

[10] J. Chal, O. Pourquié, Making muscle: skeletal myogenesis in vivo and in vitro, Development 144(12) (2017) 2104-2122.

[11] L. Gorza, S. Sartore, S. Schiaffino, Myosin types and fiber types in cardiac muscle. II. Atrial myocardium, J Cell Biol 95(3) (1982) 838-45.

[12] N. Serrano, L.M. Colenso-Semple, K.K. Lazauskus, J.W. Siu, J.R. Bagley, R.G. Lockie, P.B. Costa, A.J. Galpin, Extraordinary fast-twitch fiber abundance in elite weightlifters, PloS one 14(3) (2019) e0207975.

[13] P.A. Tesch, J. Karlsson, Muscle fiber types and size in trained and untrained muscles of elite athletes, J Appl Physiol (1985) 59(6) (1985) 1716-20.

[14] D.L. Plotkin, M.D. Roberts, C.T. Haun, B.J. Schoenfeld, Muscle Fiber Type Transitions with Exercise Training: Shifting Perspectives, Sports (Basel) 9(9) (2021).

[15] F. Li, X. Wang, J.M. Capasso, A.M. Gerdes, Rapid transition of cardiac myocytes from hyperplasia to hypertrophy during postnatal development, J Mol Cell Cardiol 28(8) (1996) 1737-46.

[16] N. Velayutham, E.J. Agnew, K.E. Yutzey, Postnatal Cardiac Development and Regenerative Potential in Large Mammals, Pediatr Cardiol 40(7) (2019) 1345-1358.

[17] E.R. Porrello, A.I. Mahmoud, E. Simpson, J.A. Hill, J.A. Richardson, E.N. Olson, H.A. Sadek, Transient regenerative potential of the neonatal mouse heart, Science 331(6020) (2011) 1078-80.

[18] E. Tzahor, K.D. Poss, Cardiac regeneration strategies: Staying young at heart, Science 356(6342) (2017) 1035-1039.

[19] G.D. Lopaschuk, M.A. Spafford, D.R. Marsh, Glycolysis is predominant source of myocardial ATP production immediately after birth, American Journal of Physiology-Heart and Circulatory Physiology 261(6) (1991) H1698-H1705.

[20] L. Sagan, On the origin of mitosing cells, J Theor Biol 14(3) (1967) 255-74.

[21] C. Esser, N. Ahmadinejad, C. Wiegand, C. Rotte, F. Sebastiani, G. Gelius-Dietrich, K. Henze, E. Kretschmann, E. Richly, D. Leister, D. Bryant, M.A. Steel, P.J. Lockhart, D. Penny, W. Martin, A genome phylogeny for mitochondria among alpha-proteobacteria and a predominantly eubacterial ancestry of yeast nuclear genes, Mol Biol Evol 21(9) (2004) 1643-60.

[22] F.J. Miller, F.L. Rosenfeldt, C. Zhang, A.W. Linnane, P. Nagley, Precise determination of mitochondrial DNA copy number in human skeletal and cardiac muscle by a PCR-based assay: lack of change of copy number with age, Nucleic acids research 31(11) (2003) e61.

[23] A.W. Greene, K. Grenier, M.A. Aguileta, S. Muise, R. Farazifard, M.E. Haque, H.M. McBride, D.S. Park, E.A. Fon, Mitochondrial processing peptidase regulates PINK1 processing, import and Parkin recruitment, EMBO Rep 13(4) (2012) 378-85.

[24] H. Xian, Y.C. Liou, Functions of outer mitochondrial membrane proteins: mediating the crosstalk between mitochondrial dynamics and mitophagy, Cell Death Differ 28(3) (2021) 827-842.

[25] P. Hammerschmidt, D. Ostkotte, H. Nolte, M.J. Gerl, A. Jais, H.L. Brunner, H.G. Sprenger, M. Awazawa, H.T. Nicholls, S.M. Turpin-Nolan, T. Langer, M. Kruger, B. Brugger, J.C. Bruning, CerS6-Derived Sphingolipids Interact with Mff and Promote Mitochondrial Fragmentation in Obesity, Cell 177(6) (2019) 1536-1552 e23.

[26] R. Edwards, S. Gerlich, K. Tokatlidis, The biogenesis of mitochondrial intermembrane space proteins, 401(6-7) (2020) 737-747.

[27] J.M. Herrmann, J. Riemer, The Intermembrane Space of Mitochondria, Antioxidants & Redox Signaling 13(9) (2010) 1341-1358.

[28] A. Holmgren, C. Johansson, C. Berndt, M.E. Lönn, C. Hudemann, C.H. Lillig, Thiol redox control via thioredoxin and glutaredoxin systems, Biochem Soc Trans 33(Pt 6) (2005) 1375-7.

[29] J.-L. Li, T.-Y. Lin, P.-L. Chen, T.-N. Guo, S.-Y. Huang, C.-H. Chen, C.-H. Lin, C.-C. Chan, Mitochondrial Function and Parkinson's Disease: From the Perspective of the Electron Transport Chain, Frontiers in Molecular Neuroscience 14 (2021).

[30] L.K. Sharma, J. Lu, Y. Bai, Mitochondrial respiratory complex I: structure, function and implication in human diseases, Curr Med Chem 16(10) (2009) 1266-77.

[31] F.J. Ruzicka, H. Beinert, A new iron-sulfur flavoprotein of the respiratory chain. A component of the fatty acid beta oxidation pathway, Journal of Biological Chemistry 252(23) (1977) 8440-8445.

[32] C. Hunte, H. Palsdottir, B.L. Trumpower, Protonmotive pathways and mechanisms in the cytochrome bc1 complex, FEBS Lett 545(1) (2003) 39-46.

[33] T. Tsukihara, H. Aoyama, E. Yamashita, T. Tomizaki, H. Yamaguchi, K. Shinzawa-Itoh, R. Nakashima, R. Yaono, S. Yoshikawa, The Whole Structure of the 13-Subunit Oxidized Cytochrome c Oxidase at 2.8 Å, Science 272(5265) (1996) 1136-1144.

[34] J.J. Ruprecht, E.R.S. Kunji, The SLC25 Mitochondrial Carrier Family: Structure and Mechanism, Trends Biochem Sci 45(3) (2020) 244-258.

[35] J.M. Hollander, D. Thapa, D.L. Shepherd, Physiological and structural differences in spatially distinct subpopulations of cardiac mitochondria: influence of cardiac pathologies, Am J Physiol Heart Circ Physiol 307(1) (2014) H1-14.

[36] V. Guarani, E.M. McNeill, J.A. Paulo, E.L. Huttlin, F. Frohlich, S.P. Gygi, D. Van Vactor, J.W. Harper, QIL1 is a novel mitochondrial protein required for MICOS complex stability and cristae morphology, Elife 4 (2015).

[37] G.B. John, Y. Shang, L. Li, C. Renken, C.A. Mannella, J.M. Selker, L. Rangell, M.J. Bennett, J. Zha, The mitochondrial inner membrane protein mitofilin controls cristae morphology, Mol Biol Cell 16(3) (2005) 1543-54.

[38] C. Ott, K. Ross, S. Straub, B. Thiede, M. Gotz, C. Goosmann, M. Krischke, M.J. Mueller, G. Krohne, T. Rudel, V. Kozjak-Pavlovic, Sam50 functions in mitochondrial intermembrane space bridging and biogenesis of respiratory complexes, Mol Cell Biol 32(6) (2012) 1173-88.

[39] M.A. Huynen, M. Muhlmeister, K. Gotthardt, S. Guerrero-Castillo, U. Brandt, Evolution and structural organization of the mitochondrial contact site (MICOS) complex and the mitochondrial intermembrane space bridging (MIB) complex, Biochim Biophys Acta 1863(1) (2016) 91-101.

[40] T. Stephan, C. Brüser, M. Deckers, A.M. Steyer, F. Balzarotti, M. Barbot, T.S. Behr, G. Heim, W. Hübner, P. Ilgen, F. Lange, D. Pacheu-Grau, J.K. Pape, S. Stoldt, T. Huser, S.W. Hell, W. Möbius, P. Rehling, D. Riedel, S. Jakobs, MICOS assembly controls mitochondrial inner membrane remodeling and crista junction redistribution to mediate cristae formation, The EMBO Journal 39(14) (2020) e104105.

[41] Y.J. Liu, R.L. McIntyre, G.E. Janssens, R.H. Houtkooper, Mitochondrial fission and fusion: A dynamic role in aging and potential target for age-related disease, Mechanisms of Ageing and Development 186 (2020) 111212.

[42] L. Chen, Q. Gong, J.P. Stice, A.A. Knowlton, Mitochondrial OPA1, apoptosis, and heart failure, Cardiovascular research 84(1) (2009) 91-9.

[43] H. Chen, M. Vermulst, Y.E. Wang, A. Chomyn, T.A. Prolla, J.M. McCaffery, D.C. Chan, Mitochondrial Fusion Is Required for mtDNA Stability in Skeletal Muscle and Tolerance of mtDNA Mutations, Cell 141(2) (2010) 280-289.

[44] X. Huang, L. Sun, S. Ji, T. Zhao, W. Zhang, J. Xu, J. Zhang, Y. Wang, X. Wang, C. Franzini-Armstrong, M. Zheng, H. Cheng, Kissing and nanotunneling mediate intermitochondrial communication in the heart, Proc Natl Acad Sci U S A 110(8) (2013) 2846-51.

[45] A.E. Vincent, K. White, T. Davey, J. Philips, R.T. Ogden, C. Lawless, C. Warren, M.G. Hall, Y.S. Ng, G. Falkous, T. Holden, D. Deehan, R.W. Taylor, D.M. Turnbull, M. Picard, Quantitative 3D Mapping of the Human Skeletal Muscle Mitochondrial Network, Cell reports 26(4) (2019) 996-1009 e4.

[46] P. Mishra, G. Varuzhanyan, Anh H. Pham, David C. Chan, Mitochondrial Dynamics Is a Distinguishing Feature of Skeletal Muscle Fiber Types and Regulates Organellar Compartmentalization, Cell Metabolism 22(6) (2015) 1033-1044.

[47] J.L. Elson, D.C. Samuels, M.A. Johnson, D.M. Turnbull, P.F. Chinnery, The length of cytochrome c oxidase-negative segments in muscle fibres in patients with mtDNA myopathy, Neuromuscular Disorders 12(9) (2002) 858-864.

[48] R. Ferreira, R. Vitorino, R.M.P. Alves, H.J. Appell, S.K. Powers, J.A. Duarte, F. Amado, Subsarcolemmal and intermyofibrillar mitochondria proteome differences disclose functional specializations in skeletal muscle, PROTEOMICS 10(17) (2010) 3142-3154.

[49] B. Glancy, L.M. Hartnell, D. Malide, Z.X. Yu, C.A. Combs, P.S. Connelly, S. Subramaniam, R.S. Balaban, Mitochondrial reticulum for cellular energy distribution in muscle, Nature 523(7562) (2015) 617-20.

[50] T.B. Willingham, P.T. Ajayi, B. Glancy, Subcellular Specialization of Mitochondrial Form and Function in Skeletal Muscle Cells, Frontiers in Cell and Developmental Biology 9 (2021).

[51] V. Eisner, G. Csordás, G. Hajnóczky, Interactions between sarco-endoplasmic reticulum and mitochondria in cardiac and skeletal muscle - pivotal roles in Ca^{2+} and reactive oxygen species signaling, J Cell Sci 126(Pt 14) (2013) 2965-78.

[52] E. Tubbs, S. Chanon, M. Robert, N. Bendridi, G. Bidaux, M.A. Chauvin, J. Ji-Cao, C. Durand, D. Gauvrit-Ramette, H. Vidal, E. Lefai, J. Rieusset, Disruption of Mitochondria-Associated Endoplasmic Reticulum Membrane (MAM) Integrity Contributes to Muscle Insulin Resistance in Mice and Humans, Diabetes 67(4) (2018) 636-650.

[53] M. Picard, M.J. McManus, G. Csordás, P. Várnai, G.W. Dorn, 2nd, D. Williams, G. Hajnóczky, D.C. Wallace, Trans-mitochondrial coordination of cristae at regulated membrane junctions, Nat Commun 6 (2015) 6259.

[54] C.K.E. Bleck, Y. Kim, T.B. Willingham, B. Glancy, Subcellular connectomic analyses of energy networks in striated muscle, Nature communications 9(1) (2018) 5111.

[55] A. Riva, B. Tandler, F. Loffredo, E. Vazquez, C. Hoppel, Structural differences in two biochemically defined populations of cardiac mitochondria, Am J Physiol Heart Circ Physiol 289(2) (2005) H868-72.

[56] U.B. Hendgen-Cotta, S. Esfeld, H. Jastrow, M. Totzeck, J. Altschmied, C. Goy, J. Haendeler, E. Winterhager, T. Rassaf, Mouse cardiac mitochondria do not separate in subsarcolemmal and interfibrillar subpopulations, Mitochondrion 38 (2018) 1-5.

[57] G.C. Rowe, A. Jiang, Z. Arany, PGC-1 coactivators in cardiac development and disease, Circ Res 107(7) (2010) 825-38.

[58] Z. Arany, H. He, J. Lin, K. Hoyer, C. Handschin, O. Toka, F. Ahmad, T. Matsui, S. Chin, P.-H. Wu, I.I. Rybkin, J.M. Shelton, M. Manieri, S. Cinti, F.J. Schoen, R. Bassel-Duby, A. Rosenzweig, J.S. Ingwall, B.M. Spiegelman, Transcriptional coactivator PGC-1α controls the energy state and contractile function of cardiac muscle, Cell Metabolism 1(4) (2005) 259-271.

[59] J.O. Holloszy, Biochemical Adaptations in Muscle: EFFECTS OF EXERCISE ON MITOCHONDRIAL OXYGEN UPTAKE AND RESPIRATORY ENZYME

ACTIVITY IN SKELETAL MUSCLE, Journal of Biological Chemistry 242(9) (1967) 2278-2282.

[60] C. Handschin, J. Rhee, J. Lin, P.T. Tarr, B.M. Spiegelman, An autoregulatory loop controls peroxisome proliferator-activated receptor gamma coactivator 1alpha expression in muscle, Proc Natl Acad Sci U S A 100(12) (2003) 7111-6.

[61] C. Liu, J.D. Lin, PGC-1 coactivators in the control of energy metabolism, Acta Biochim Biophys Sin (Shanghai) 43(4) (2011) 248-57.

[62] T. Yokokawa, K. Kido, T. Suga, T. Isaka, T. Hayashi, S. Fujita, Exercise-induced mitochondrial biogenesis coincides with the expression of mitochondrial translation factors in murine skeletal muscle, Physiol Rep 6(20) (2018) e13893.

[63] C.L. Zhang, H. Feng, L. Li, J.Y. Wang, D. Wu, Y.T. Hao, Z. Wang, Y. Zhang, L.L. Wu, Globular CTRP3 promotes mitochondrial biogenesis in cardiomyocytes through AMPK/PGC-1α pathway, Biochim Biophys Acta Gen Subj 1861(1 Pt A) (2017) 3085-3094.

[64] S. Jäger, C. Handschin, J. St.-Pierre, B.M. Spiegelman, AMP-activated protein kinase (AMPK) action in skeletal muscle via direct phosphorylation of PGC-1α, Proceedings of the National Academy of Sciences 104(29) (2007) 12017-12022.

[65] P.S. Pardo, A.M. Boriek, The physiological roles of Sirt1 in skeletal muscle, Aging (Albany NY) 3(4) (2011) 430-7.

[66] M. Fulco, V. Sartorelli, Comparing and contrasting the roles of AMPK and SIRT1 in metabolic tissues, Cell Cycle 7(23) (2008) 3669-79.

[67] J. Huss, R. Kopp, D. Kelly, PGC-1α coactivates the cardiac-enriched nuclear receptors estrogen-related receptor-α and-γ, J. Biol. Chem 277 (2002) 40265-40274.

[68] J.M. Huss, I.P. Torra, B. Staels, V. Giguere, D.P. Kelly, Estrogen-related receptor α directs peroxisome proliferator-activated receptor α signaling in the transcriptional control of energy metabolism in cardiac and skeletal muscle, Molecular and cellular biology 24(20) (2004) 9079-9091.

[69] J.M. Huss, K.-i. Imahashi, C.R. Dufour, C.J. Weinheimer, M. Courtois, A. Kovacs, V. Giguère, E. Murphy, D.P. Kelly, The Nuclear Receptor ERRα Is Required for the Bioenergetic and Functional Adaptation to Cardiac Pressure Overload, Cell Metabolism 6(1) (2007) 25-37.

[70] C. Handschin, S. Chin, P. Li, F. Liu, E. Maratos-Flier, N.K. Lebrasseur, Z. Yan, B.M. Spiegelman, Skeletal muscle fiber-type switching, exercise intolerance, and myopathy in PGC-1alpha muscle-specific knock-out animals, J Biol Chem 282(41) (2007) 30014-21.

[71] S. Miura, Y. Kai, M. Ono, O. Ezaki, Overexpression of peroxisome proliferator-activated receptor gamma coactivator-1alpha down-regulates GLUT4 mRNA in skeletal muscles, J Biol Chem 278(33) (2003) 31385-90.

[72] L.K. Russell, C.M. Mansfield, J.J. Lehman, A. Kovacs, M. Courtois, J.E. Saffitz, D.M. Medeiros, M.L. Valencik, J.A. McDonald, D.P. Kelly, Cardiac-specific induction of the transcriptional coactivator peroxisome proliferator-activated receptor gamma coactivator-1alpha promotes mitochondrial biogenesis and reversible cardiomyopathy in a developmental stage-dependent manner, Circ Res 94(4) (2004) 525-33.

[73] Y. Cho, B.C. Hazen, A.P. Russell, A. Kralli, Peroxisome proliferator-activated receptor gamma coactivator 1 (PGC-1)- and estrogen-related receptor (ERR)-induced regulator in muscle 1 (Perm1) is a tissue-specific regulator of oxidative capacity in skeletal muscle cells, J Biol Chem 288(35) (2013) 25207-25218.

[74] Y. Cho, S. Tachibana, K. Lam, Y. Arita, S. Khosrowjerdi, O. Zhang, A. Liang, R. Li, A. Andreyev, A.N. Murphy, R.S. Ross, Perm1 promotes cardiomyocyte mitochondrial biogenesis and protects against hypoxia/reoxygenation-induced damage in mice, J Biol Chem (2021) 100825.

[75] Y. Cho, B.C. Hazen, P.G. Gandra, S.R. Ward, S. Schenk, A.P. Russell, A. Kralli, Perm1 enhances mitochondrial biogenesis, oxidative capacity, and fatigue resistance in adult skeletal muscle, FASEB J 30(2) (2016) 674-87.

[76] S.I. Oka, A.D. Sabry, A.K. Horiuchi, K.M. Cawley, S.A. O'Very, M.A. Zaitsev, T.S. Shankar, J. Byun, R. Mukai, X. Xu, N.S. Torres, A. Kumar, M. Yazawa, J. Ling, I. Taleb, Y. Saijoh, S.G. Drakos, J. Sadoshima, J.S. Warren, Perm1 regulates cardiac energetics as a downstream target of the histone methyltransferase Smyd1, PloS one 15(6) (2020) e0234913.

[77] C.-y. Huang, S.-i. Oka, X. Xu, C.-F. Chen, C.-Y. Tung, Y.-Y. Chang, Y. Mourad, O. Vehra, A. Ivessa, G. Yehia, P. Romanienko, C.-P. Hsu, J. Sadoshima, PERM1 regulates genes involved in fatty acid metabolism in the heart by interacting with PPARα and PGC-1α, Scientific Reports 12(1) (2022) 14576.

[78] S.-i. Oka, K. Sreedevi, T.S. Shankar, S. Yedla, S. Arowa, A. James, K.G. Stone, K. Olmos, A.D. Sabry, A. Horiuchi, K.M. Cawley, S.A. O'very, M. Tong, J. Byun, X. Xu, S. Kashyap, Y. Mourad, O. Vehra, D. Calder, T. Lunde, T. Liu, H. Li, J.A. Mashchek, J. Cox, Y. Saijoh, S.G. Drakos, J.S. Warren, PERM1 regulates energy metabolism in the heart via ERRα/PGC−1α axis, Frontiers in Cardiovascular Medicine 9 (2022).

[79] M. Schild, A. Ruhs, T. Beiter, M. Zugel, J. Hudemann, A. Reimer, I. Krumholz-Wagner, C. Wagner, J. Keller, K. Eder, K. Kruger, M. Kruger, T. Braun, A. Niess, J. Steinacker, F.C. Mooren, Basal and exercise induced label-free quantitative protein profiling of m. vastus lateralis in trained and untrained individuals, J Proteomics 122 (2015) 119-32.

[80] C. Brinkmann, A. Kuckertz, T. Schiffer, W. Bloch, H.G. Predel, K. Brixius, Endurance training alters YKL40, PERM1, and HSP70 skeletal muscle protein contents in men with type 2 diabetes mellitus, Endocr Res 44(1-2) (2019) 1-8.

[81] Y. Cho, S. Tachibana, B.C. Hazen, J.J. Moresco, J.R. Yates, 3rd, B. Kok, E. Saez, R.S. Ross, A.P. Russell, A. Kralli, Perm1 regulates CaMKII activation and shapes skeletal muscle responses to endurance exercise training, Mol Metab 23 (2019) 88-97.

[82] A. Stepanova, A. Kahl, C. Konrad, V. Ten, A.S. Starkov, A. Galkin, Reverse electron transfer results in a loss of flavin from mitochondrial complex I: Potential mechanism for brain ischemia reperfusion injury, Journal of Cerebral Blood Flow & Metabolism 37(12) (2017) 3649-3658.

[83] M. Ikeuchi, H. Matsusaka, D. Kang, S. Matsushima, T. Ide, T. Kubota, T. Fujiwara, N. Hamasaki, A. Takeshita, K. Sunagawa, H. Tsutsui, Overexpression of mitochondrial transcription factor a ameliorates mitochondrial deficiencies and cardiac failure after myocardial infarction, Circulation 112(5) (2005) 683-90.

[84] S. Müller, A. Perdikari, D.H. Dapito, W. Sun, B. Wollscheid, M. Balaz, C. Wolfrum, ESRRG and PERM1 Govern Mitochondrial Conversion in Brite/Beige Adipocyte Formation, Frontiers in Endocrinology 11 (2020).

[85] B. Cousin, S. Cinti, M. Morroni, S. Raimbault, D. Ricquier, L. Penicaud, L. Casteilla, Occurrence of brown adipocytes in rat white adipose tissue: molecular and morphological characterization, Journal of cell science 103(4) (1992) 931-942.

[86] T. Henzi, B. Schwaller, Antagonistic Regulation of Parvalbumin Expression and Mitochondrial Calcium Handling Capacity in Renal Epithelial Cells, PloS one 10(11) (2015) e0142005.

[87] T. Li, W.J. Xian, Y. Gao, S. Jiang, Q.H. Yu, Q.C. Zheng, Y. Zhang, Higd1a Protects Cells from Lipotoxicity under High-Fat Exposure, Oxid Med Cell Longev 2019 (2019) 6051262.

[88] M. Conte, F. Vasuri, G. Trisolino, E. Bellavista, A. Santoro, A. Degiovanni, E. Martucci, A. D'Errico-Grigioni, D. Caporossi, M. Capri, A.B. Maier, O. Seynnes, L. Barberi, A. Musarò, M.V. Narici, C. Franceschi, S. Salvioli, Increased Plin2 Expression in Human Skeletal Muscle Is Associated with Sarcopenia and Muscle Weakness, PloS one 8(8) (2013) e73709.

[89] K. Hadrava Vanova, M. Kraus, J. Neuzil, J. Rohlena, Mitochondrial complex II and reactive oxygen species in disease and therapy, Redox Report 25(1) (2020) 26-32.

[90] F.L. Sheeran, J. Rydström, M.I. Shakhparonov, N.B. Pestov, S. Pepe, Diminished NADPH transhydrogenase activity and mitochondrial redox regulation in human failing myocardium, Biochimica et Biophysica Acta (BBA) - Bioenergetics 1797(6) (2010) 1138-1148.

[91] D. Mokranjac, W. Neupert, Thirty years of protein translocation into mitochondria: Unexpectedly complex and still puzzling, Biochimica et Biophysica Acta (BBA) - Molecular Cell Research 1793(1) (2009) 33-41.

[92] S. Peeters, P. De Kinderen, J.A.N. Meester, A. Verstraeten, B.L. Loeys, The fibrillinopathies: New insights with focus on the paradigm of opposing phenotypes for both FBN1 and FBN2, Human Mutation 43(7) (2022) 815-831.

[93] M.J. Morgan, A.J.A. Madgwick, The LIM Proteins FHL1 and FHL3 Are Expressed Differently in Skeletal Muscle, Biochemical and Biophysical Research Communications 255(2) (1999) 245-250.

[94] Y. Yang, M.Z. Dieter, Y. Chen, H.G. Shertzer, D.W. Nebert, T.P. Dalton, Initial Characterization of the Glutamate-Cysteine Ligase Modifier Subunit Gclm(−/−) Knockout Mouse: NOVEL MODEL SYSTEM FOR A SEVERELY COMPROMISED OXIDATIVE STRESS RESPONSE*, Journal of Biological Chemistry 277(51) (2002) 49446-49452.

[95] C.J. Ng, D.J. Wadleigh, A. Gangopadhyay, S. Hama, V.R. Grijalva, M. Navab, A.M. Fogelman, S.T. Reddy, Paraoxonase-2 Is a Ubiquitously Expressed Protein with Antioxidant Properties and Is Capable of Preventing Cell-mediated Oxidative Modification of Low Density Lipoprotein*, Journal of Biological Chemistry 276(48) (2001) 44444-44449.

[96] B. Zhang, J.-x. Ma, SERPINA3K Prevents Oxidative Stress Induced Necrotic Cell Death by Inhibiting Calcium Overload, PloS one 3(12) (2009) e4077.

[97] S. Ciciliot, S. Schiaffino, Regeneration of mammalian skeletal muscle. Basic mechanisms and clinical implications, Curr Pharm Des 16(8) (2010) 906-14.

[98] G.H. Eom, K.B. Kim, J.H. Kim, J.Y. Kim, J.R. Kim, H.J. Kee, D.W. Kim, N. Choe, H.J. Park, H.J. Son, S.Y. Choi, H. Kook, S.B. Seo, Histone methyltransferase SETD3 regulates muscle differentiation, J Biol Chem 286(40) (2011) 34733-42.

[99] Sunny S.-K. Chan, Hannah R. Hagen, Scott A. Swanson, R. Stewart, Karly A. Boll, J. Aho, James A. Thomson, M. Kyba, Development of Bipotent Cardiac/Skeletal Myogenic Progenitors from MESP1+ Mesoderm, Stem Cell Reports 6(1) (2016) 26-34.

[100] M. Varadi, S. Anyango, M. Deshpande, S. Nair, C. Natassia, G. Yordanova, D. Yuan, O. Stroe, G. Wood, A. Laydon, A. Žídek, T. Green, K. Tunyasuvunakool, S. Petersen, J. Jumper, E. Clancy, R. Green, A. Vora, M. Lutfi, M. Figurnov, A. Cowie, N. Hobbs, P. Kohli, G. Kleywegt, E. Birney, D. Hassabis, S. Velankar, AlphaFold Protein Structure Database: massively expanding the structural coverage of protein-sequence space with high-accuracy models, Nucleic acids research 50(D1) (2022) D439-D444.

[101] L.K. Mosavi, T.J. Cammett, D.C. Desrosiers, Z.-y. Peng, The ankyrin repeat as molecular architecture for protein recognition, Protein Science 13(6) (2004) 1435-1448.

[102] E. Bonnelye, J.M. Vanacker, N. Spruyt, S. Alric, B. Fournier, X. Desbiens, V. Laudet, Expression of the estrogen-related receptor 1 (ERR-1) orphan receptor during mouse development, Mech Dev 65(1-2) (1997) 71-85.

[103] Z. Arany, M. Novikov, S. Chin, Y. Ma, A. Rosenzweig, B.M. Spiegelman, Transverse aortic constriction leads to accelerated heart failure in mice lacking PPAR-gamma coactivator 1alpha, Proc Natl Acad Sci U S A 103(26) (2006) 10086-91.

[104] C.J. Lelliott, G. Medina-Gomez, N. Petrovic, A. Kis, H.M. Feldmann, M. Bjursell, N. Parker, K. Curtis, M. Campbell, P. Hu, D. Zhang, S.E. Litwin, V.G. Zaha, K.T. Fountain, S. Boudina, M. Jimenez-Linan, M. Blount, M. Lopez, A. Meirhaeghe, Y.M. Bohlooly, L. Storlien, M. Strömstedt, M. Snaith, M. Oresic, E.D. Abel, B. Cannon, A. Vidal-Puig, Ablation of PGC-1beta results in defective mitochondrial activity, thermogenesis, hepatic function, and cardiac performance, PLoS Biol 4(11) (2006) e369.

[105] L. Lai, T.C. Leone, C. Zechner, P.J. Schaeffer, S.M. Kelly, D.P. Flanagan, D.M. Medeiros, A. Kovacs, D.P. Kelly, Transcriptional coactivators PGC-1alpha and PGC-lbeta control overlapping programs required for perinatal maturation of the heart, Genes & development 22(14) (2008) 1948-61.

[106] É. Audet-walsh, V. Giguére, The multiple universes of estrogen-related receptor α and γ in metabolic control and related diseases, Acta Pharmacologica Sinica 36(1) (2015) 51-61.

[107] V.A. Narkar, W. Fan, M. Downes, R.T. Yu, J.W. Jonker, W.A. Alaynick, E. Banayo, M.S. Karunasiri, S. Lorca, R.M. Evans, Exercise and PGC-1α-independent synchronization of type I muscle metabolism and vasculature by ERRγ, Cell Metab 13(3) (2011) 283-93.

[108] C.R. Dufour, B.J. Wilson, J.M. Huss, D.P. Kelly, W.A. Alaynick, M. Downes, R.M. Evans, M. Blanchette, V. Giguère, Genome-wide orchestration of cardiac functions by the orphan nuclear receptors ERRalpha and gamma, Cell Metab 5(5) (2007) 345-56.

[109] S. Tachibana, N.-K. Yu, R. Li, C. Fernandez-Costa, A. Liang, J. Choi, D. Jung, C. Xiao, A. Kralli, J.R. Yates, R.S. Ross, Y. Cho, Perm1 Protects the Heart From Pressure

Overload–Induced Dysfunction by Promoting Oxidative Metabolism, Circulation 147(11) (2023) 916-919.

[110] S. Rogers, R. Wells, M. Rechsteiner, Amino acid sequences common to rapidly degraded proteins: the PEST hypothesis, Science 234(4774) (1986) 364-8.

[111] M.T. Lin, M.F. Beal, Mitochondrial dysfunction and oxidative stress in neurodegenerative diseases, Nature 443(7113) (2006) 787-795.

[112] G. Lenaz, The Mitochondrial Production of Reactive Oxygen Species: Mechanisms and Implications in Human Pathology, IUBMB Life 52(3-5) (2001) 159-164.

[113] V. Kozjak-Pavlovic, The MICOS complex of human mitochondria, Cell Tissue Res 367(1) (2017) 83-93.

[114] F. Wagner, T.C. Kunz, S.R. Chowdhury, B. Thiede, M. Fraunholz, D. Eger, V. Kozjak-Pavlovic, Armadillo repeat-containing protein 1 is a dual localization protein associated with mitochondrial intermembrane space bridging complex, PloS one 14(10) (2019) e0218303.

[115] D.T. Jones, Improving the accuracy of transmembrane protein topology prediction using evolutionary information, Bioinformatics 23(5) (2007) 538-544.

[116] A. Chacinska, C.M. Koehler, D. Milenkovic, T. Lithgow, N. Pfanner, Importing mitochondrial proteins: machineries and mechanisms, Cell 138(4) (2009) 628-44.

[117] T. Ulrich, D. Rapaport, Biogenesis of beta-barrel proteins in evolutionary context, Int J Med Microbiol 305(2) (2015) 259-64.

[118] D.M. Walther, D. Rapaport, Biogenesis of mitochondrial outer membrane proteins, Biochimica et Biophysica Acta (BBA) - Molecular Cell Research 1793(1) (2009) 42-51.

[119] D. Rapaport, Finding the right organelle. Targeting signals in mitochondrial outer-membrane proteins, EMBO Rep 4(10) (2003) 948-52.

[120] C. Horie, H. Suzuki, M. Sakaguchi, K. Mihara, Characterization of signal that directs C-tail-anchored proteins to mammalian mitochondrial outer membrane, Mol Biol Cell 13(5) (2002) 1615-25.

[121] T. Kaufmann, S. Schlipf, J. Sanz, K. Neubert, R. Stein, C. Borner, Characterization of the signal that directs Bcl-x(L), but not Bcl-2, to the mitochondrial outer membrane, J Cell Biol 160(1) (2003) 53-64.

[122] T. Becker, S. Pfannschmidt, B. Guiard, D. Stojanovski, D. Milenkovic, S. Kutik, N. Pfanner, C. Meisinger, N. Wiedemann, Biogenesis of the mitochondrial TOM complex: Mim1 promotes insertion and assembly of signal-anchored receptors, J Biol Chem 283(1) (2008) 120-127.

[123] L. Drwesh, D. Rapaport, Biogenesis pathways of α-helical mitochondrial outer membrane proteins, Biol Chem 401(6-7) (2020) 677-686.

[124] A. Gupta, T. Becker, Mechanisms and pathways of mitochondrial outer membrane protein biogenesis, Biochim Biophys Acta Bioenerg 1862(1) (2021) 148323.

[125] D. Stojanovski, B. Guiard, V. Kozjak-Pavlovic, N. Pfanner, C. Meisinger, Alternative function for the mitochondrial SAM complex in biogenesis of α-helical TOM proteins, Journal of Cell Biology 179(5) (2007) 881-893.

[126] K. Setoguchi, H. Otera, K. Mihara, Cytosolic factor- and TOM-independent import of C-tail-anchored mitochondrial outer membrane proteins, Embo j 25(24) (2006) 5635-47.

[127] A. Guna, T.A. Stevens, A.J. Inglis, J.M. Replogle, T.K. Esantsi, G. Muthukumar, K.C.L. Shaffer, M.L. Wang, A.N. Pogson, J.J. Jones, B. Lomenick, T.-F. Chou, J.S. Weissman, R.M. Voorhees, MTCH2 is a mitochondrial outer membrane protein insertase, Science 378(6617) (2022) 317-322.

[128] V. Kozjak-Pavlovic, K. Ross, N. Benlasfer, S. Kimmig, A. Karlas, T. Rudel, Conserved roles of Sam50 and metaxins in VDAC biogenesis, EMBO Rep 8(6) (2007) 576-82.

[129] K.M. Sakamoto, K.B. Kim, A. Kumagai, F. Mercurio, C.M. Crews, R.J. Deshaies, Protacs: Chimeric molecules that target proteins to the Skp1–Cullin–F box complex for ubiquitination and degradation, Proceedings of the National Academy of Sciences 98(15) (2001) 8554-8559.

[130] V. Bennett, A.J. Baines, Spectrin and ankyrin-based pathways: metazoan inventions for integrating cells into tissues, Physiol Rev 81(3) (2001) 1353-92.

[131] M. He, W.C. Tseng, V. Bennett, A single divergent exon inhibits ankyrin-B association with the plasma membrane, J Biol Chem 288(21) (2013) 14769-79.

[132] M. Kunimoto, A neuron-specific isoform of brain ankyrin, 440-kD ankyrinB, is targeted to the axons of rat cerebellar neurons, Journal of Cell Biology 131(6) (1995) 1821-1829.

[133] G. Ayalon, J.Q. Davis, P.B. Scotland, V. Bennett, An ankyrin-based mechanism for functional organization of dystrophin and dystroglycan, Cell 135(7) (2008) 1189-200.

[134] P. Bork, Hundreds of ankyrin-like repeats in functionally diverse proteins: mobile modules that cross phyla horizontally?, Proteins 17(4) (1993) 363-74.

[135] P.J. Mohler, J.Q. Davis, V. Bennett, Ankyrin-B coordinates the Na/K ATPase, Na/Ca exchanger, and InsP3 receptor in a cardiac T-tubule/SR microdomain, PLoS Biol 3(12) (2005) e423.

[136] S.R. Cunha, N. Bhasin, P.J. Mohler, Targeting and Stability of Na/Ca Exchanger 1 in Cardiomyocytes Requires Direct Interaction with the Membrane Adaptor Ankyrin-B*, Journal of Biological Chemistry 282(7) (2007) 4875-4883.

[137] P.J. Mohler, J.Q. Davis, L.H. Davis, J.A. Hoffman, P. Michaely, V. Bennett, Inositol 1,4,5-Trisphosphate Receptor Localization and Stability in Neonatal Cardiomyocytes Requires Interaction with Ankyrin-B*, Journal of Biological Chemistry 279(13) (2004) 12980-12987.

[138] P. Michaely, V. Bennett, The ANK Repeats of Erythrocyte Ankyrin Form Two Distinct but Cooperative Binding Sites for the Erythrocyte Anion Exchanger (∗), Journal of Biological Chemistry 270(37) (1995) 22050-22057.

[139] J. Li, A. Mahajan, M.-D. Tsai, Ankyrin Repeat: A Unique Motif Mediating Protein−Protein Interactions, Biochemistry 45(51) (2006) 15168-15178.

[140] P.J. Mohler, I. Splawski, C. Napolitano, G. Bottelli, L. Sharpe, K. Timothy, S.G. Priori, M.T. Keating, V. Bennett, A cardiac arrhythmia syndrome caused by loss of ankyrin-B function, Proceedings of the National Academy of Sciences 101(24) (2004) 9137-9142.

[141] P. Scotland, D. Zhou, H. Benveniste, V. Bennett, Nervous system defects of AnkyrinB (-/-) mice suggest functional overlap between the cell adhesion molecule L1 and 440-kD AnkyrinB in premyelinated axons, J Cell Biol 143(5) (1998) 1305-15.

[142] P.J. Mohler, J.-J. Schott, A.O. Gramolini, K.W. Dilly, S. Guatimosim, W.H. duBell, L.-S. Song, K. Haurogné, F. Kyndt, M.E. Ali, T.B. Rogers, W.J. Lederer, D. Escande, H.L. Marec, V. Bennett, Ankyrin-B mutation causes type 4 long-QT cardiac arrhythmia and sudden cardiac death, Nature 421(6923) (2003) 634-639.

[143] J.J. Schott, F. Charpentier, S. Peltier, P. Foley, E. Drouin, J.B. Bouhour, P. Donnelly, G. Vergnaud, L. Bachner, J.P. Moisan, et al., Mapping of a gene for long QT syndrome to chromosome 4q25-27, Am J Hum Genet 57(5) (1995) 1114-22.

[144] K.M. Abdi, P.J. Mohler, J.Q. Davis, V. Bennett, Isoform specificity of ankyrin-B: a site in the divergent C-terminal domain is required for intramolecular association, J Biol Chem 281(9) (2006) 5741-9.

[145] O.E. Nekrasova, M.G. Mendez, I.S. Chernoivanenko, P.A. Tyurin-Kuzmin, E.R. Kuczmarski, V.I. Gelfand, R.D. Goldman, A.A. Minin, Vimentin intermediate filaments modulate the motility of mitochondria, Mol Biol Cell 22(13) (2011) 2282-9.

[146] R.M. Bellin, T.W. Huiatt, D.R. Critchley, R.M. Robson, Synemin may function to directly link muscle cell intermediate filaments to both myofibrillar Z-lines and costameres, J Biol Chem 276(34) (2001) 32330-7.

[147] H. Nolte, T.D. MacVicar, F. Tellkamp, M. Kruger, Instant Clue: A Software Suite for Interactive Data Visualization and Analysis, Sci Rep 8(1) (2018) 12648.

6. Erklärung zur Dissertation

„Hiermit versichere ich an Eides statt, dass ich die vorliegende Dissertation selbstständig und ohne die Benutzung anderer als der angegebenen Hilfsmittel und Literatur angefertigt habe. Alle Stellen, die wörtlich oder sinngemäß aus veröffentlichten und nicht veröffentlichten Werken dem Wortlaut oder dem Sinn nach entnommen wurden, sind als solche kenntlich gemacht. Ich versichere an Eides statt, dass diese Dissertation noch keiner anderen Fakultät oder Universität zur Prüfung vorgelegen hat; dass sie - abgesehen von unten angegebenen Teilpublikationen und eingebundenen Artikeln und Manuskripten - noch nicht veröffentlicht worden ist sowie, dass ich eine Veröffentlichung der Dissertation vor Abschluss der Promotion nicht ohne Genehmigung des Promotionsausschusses vornehmen werde. Die Bestimmungen dieser Ordnung sind mir bekannt. Darüber hinaus erkläre ich hiermit, dass ich die Ordnung zur Sicherung guter wissenschaftlicher Praxis und zum Umgang mit wissenschaftlichem Fehlverhalten der Universität zu Köln gelesen und sie bei der Durchführung der Dissertation zugrundeliegenden Arbeiten und der schriftlich verfassten Dissertation beachtet habe und verpflichte mich hiermit, die dort genannten Vorgaben bei allen wissenschaftlichen Tätigkeiten zu beachten und umzusetzen. Ich versichere, dass die eingereichte elektronische Fassung der eingereichten Druckfassung vollständig entspricht."

Teilpublikationen:

(I) Aravamudhan, S.*, Türk, C.*, **Bock, T.**, Keufgens, L., Nolte, H., Lang, F., Krishnan, R. K., König, T., Hammerschmidt, P., Schindler, N., Brodesser, S., Rozsivalova, D. H., Rugarli, E., Trifunovic, A., Brüning, J., Langer, T., Braun, T., Krüger, M. (2021). Phosphoproteomics of the developing heart identifies PERM1 – an outer mitochondrial membrane protein. *Journal of Molecular and Cellular Cardiology. 154 (2021) 41-59. doi: https://doi.org./10.1016/y.jmcc.2021.01.010.*

(II) **Bock, T.***, Türk, C.*, Aravamudhan, S., Keufgens, L., Bloch, W., Rozsivalova, D. H., Romanello, V., Nogara, L., Blaauw, B., Trifunovic, A., Braun, T., Krüger, M. (2021). PERM1 interacts with the MICOS-MIB complex to connect the mitochondria and sarcolemma via ankyrin B. *Nature Communications. (2021)12:4900. doi: https://doi-org/10.1038/s41467-021-25185-3.*

***** Diese Autor:innen waren gleichermaßen beteiligt.

Köln, 10.08.2023, Theresa Bock Theresa Bock Digitally signed by Theresa Bock Date: 2023.08.10 14:19:13 +02'00'

7. Curriculum Vitae

Theresa Bock

Mayener Str. 12
50935 Köln
theresa.bock@t-online.de

Date of birth 12.06.1994

Nationality German

Education

since 10/2019 **PhD Student University of Cologne/CECAD Research Center**
Supervisor: Prof. Dr. Marcus Krüger

04/2017-08/2019 **Master of Science in Biochemistry, University of Cologne**
Overall grade: 1.1
Master thesis: Functional identification of a novel mitochondria-associated protein PERM1
Supervisor: Prof. Dr. Marcus Krüger

10/2013-01/2017 **Bachelor of Science in Biology, University of Cologne**
Overall grade: 1.6
Bachelor thesis: Identification and characterization of internally acetylated human and murine sulfite oxidase
Supervisor: Prof. Dr. Günter Schwarz

Experiences

04/2018-07/2018 **Internship at McGill University, Montreal, Canada**
Project title: Characterization of testicular toxicity of bisphenol A and its alternatives in mouse Leydig cells using a high content screening approach
Supervisor: Dr. Bernard Robaire

02/2016-04/2018 **Student Assistant in Biochemistry, University of Cologne**
Supervision of Bachelor students in the laboratory, evaluation of reports and oral presentations

10/2015-11/2015 **Internship at National Center for Tumor Diseases, Heidelberg**
Project title: SNP analysis as potential indicator for the survival of CRC patients
Supervisor: Dr. Petra Schrotz-King

Publications

Späth, M. R., Hoyer-Allo, K. J. R., Seufert, L., Höhne, M., Lucas, C., **Bock, T.**, et al. (2023). Organ Protection by Caloric Restriction Depends on Activation of the De Novo NAD+ Synthesis Pathway. *Journal of the American Society of Nephrology: JASN*, 34(5), 772–792.

Croon, M., Szczepanowska, K., Popovic, M., Lienkamp, C., Senft, K., Brandscheid, C. P., **Bock, T.**, et al. (2022). FGF21 modulates mitochondrial stress response in cardiomyocytes only under mild mitochondrial dysfunction. *Science advances*, 8(14), eabn7105.

Klapproth, S., Richter, K., Türk, C., **Bock, T.**, et al. (2021). Low kindlin-3 levels in osteoclasts of kindlin-3 hypomorphic mice result in osteopetrosis due to leaky sealing zones. *Journal of cell science*, 134(22), jcs259040.

Bock, T., Türk, C., et al. (2021). PERM1 interacts with the MICOS-MIB complex to connect the mitochondria and sarcolemma via ankyrin B. *Nature Communications*. (2021)12:4900.

Aravamudhan, S., Türk, C., **Bock, T.**, et al. (2021). Phosphoproteomics of the developing heart identifies PERM1 – an outer mitochondrial membrane protein. *Journal of Molecular and Cellular Cardiology*. 154 (2021) 41-59

Solagna, F., Nogara, L., Dyar, K. A., Greulich, F., Mir, A. A., Türk, C., **Bock, T.**, et al. (2020). Exercise-dependent increases in protein synthesis are accompanied by chromatin modifications and increased MRTF-SRF signalling. *Acta physiologica*, 230(1), e13496.

Kallabis, S., Abraham, L., Müller, S., Dzialas, V., Türk, C., Wiederstein, J. L., **Bock, T.**, et al. (2020). High-throughput proteomics fiber typing (ProFiT) for comprehensive characterization of single skeletal muscle fibers. *Skeletal muscle*, 10(1), 7.

8. Appendix

Publication I: Phosphoproteomics of the developing heart identified PERM1 – an outer mitochondrial membrane protein.

Journal of Molecular and Cellular Cardiology 154 (2021) 41–59

Contents lists available at ScienceDirect

Journal of Molecular and Cellular Cardiology

journal homepage: www.elsevier.com/locate/yjmcc

Phosphoproteomics of the developing heart identifies PERM1 - An outer mitochondrial membrane protein

Sriram Aravamudhan [a,1], Clara Türk [b,1], Theresa Bock [b], Lena Keufgens [b], Hendrik Nolte [c], Franziska Lang [d], Ramesh Kumar Krishnan [e], Tim König [f], Philipp Hammerschmidt [g], Natalie Schindler [h], Susanne Brodesser [b], Dieu Hien Rozsivalova [b], Elena Rugarli [b], Aleksandra Trifunovic [b], Jens Brüning [g], Thomas Langer [c], Thomas Braun [i], Marcus Krüger [b,j,*]

[a] *Cell Signaling Technology, Dellaertweg 9b, 2316 WZ Leiden, Netherlands*
[b] *CECAD Research Center, Institute for Genetics, University of Cologne, Joseph-Stelzmann-Str. 26, 50931 Cologne, Germany*
[c] *Max Planck Institute for Biology of Ageing, 50931 Cologne, Germany*
[d] *TRON - Translational Oncology at the University Medical Center of the Johannes Gutenberg University Mainz, 55131 Mainz, Germany*
[e] *Excellence Cluster Cardio-Pulmonary Institute (CPI), Aulweg 130, 35392 Giessen, Germany*
[f] *Montreal Neurological Institute, McGill University, 3801 University Street, H3A 2B4 Montreal, QC, Canada*
[g] *Department of Neuronal Control of Metabolism, Max Planck Institute for Metabolism Research, Gleueler Strasse 50, 50931 Cologne, Germany*
[h] *Institut für Entwicklungsbiologie und Neurobiologie (IDN), Fachbereich Biologie (FB 10), Johannes Gutenberg University (JGU) Mainz, Germany c/o Institute of Molecular Biology gGmbH (IMB), Ackermannweg 4, 55128 Mainz, Germany*
[i] *Max Planck Institute for Heart and Lung Research, Ludwigstr. 43, 61231 Bad Nauheim, Germany*
[j] *Center for Molecular Medicine (CMMC), University of Cologne, 50931 Cologne, Germany*

ARTICLE INFO

Keywords:
Heart development
Phosphoproteomics
SILAC
Mitochondria
PERM1
Lipid metabolism

ABSTRACT

Heart development relies on PTMs that control cardiomyocyte proliferation, differentiation and cardiac morphogenesis. We generated a map of phosphorylation sites during the early stages of cardiac postnatal development in mice; we quantified over 10,000 phosphorylation sites and 5000 proteins that were assigned to different pathways. Analysis of mitochondrial proteins led to the identification of PGC-1- and ERR-induced regulator in muscle 1 (PERM1), which is specifically expressed in skeletal muscle and heart tissue and associates with the outer mitochondrial membrane. We demonstrate PERM1 is subject to rapid changes mediated by the UPS through phosphorylation of its PEST motif by casein kinase 2. Ablation of *Perm1* in mice results in reduced protein expression of lipin-1 accompanied by accumulation of specific phospholipid species. Isolation of *Perm1*-deficient mitochondria revealed significant downregulation of mitochondrial transport proteins for amino acids and carnitines, including SLC25A12/13/29/34 and CPT2. Consistently, we observed altered levels of various lipid species, amino acids, and acylcarnitines in *Perm1*$^{-/-}$ mitochondria. We conclude that the outer mitochondrial membrane protein PERM1 regulates homeostasis of lipid and amino acid metabolites in mitochondria.

Abbreviations: 4EBP1, Eukaryotic initiation factor 4E binding protein 1; ABC, Ammonium bicarbonate; ACN, Acetonitrile; AMD1, S-adenosylmethionine decarboxylase proenzyme 1; BAC, Bacterial artificial chromosomes; BN-PAGE, Blue native polyacrylamide gel electrophorese; CaMKII, Ca^{2+}/calmodulin-dependent protein kinase; CK2, Casein kinase 2; CLPTM1, Cleft lip and palate transmembrane protein 1 homolog; DAG, Diacylglycerol; DGC, Dystrophin glycoprotein complex; DTT, Dithiothreitol; ECM, Extracellular matrix; ER, Endoplasmic reticulum; ETS, Electron transfer system; FASP, Filter-aided sample preparation; FCCP, Trifluoromethoxyphenylhydrazone; fld, fatty liver dystrophic; FSTL1, Follistatin-related protein 1; H&E, Haematoxylin and eosin; IAA, Iodacetamide; IKK, I kappa B kinase; IT, Injection time; LPIN1, Lipin-1; MAM, Mitochondria-associated membrane; MCM, Minichromosome maintenance; MFN2, Mitofusin 2; MKL2, Myocardin-related transcription factor B; NCE, Nominal collisional energy; NMM, Non-mitochondrial membrane; NO, Nitric oxide; PA, Phosphatidic acid; PAP, Phosphatidic acid phosphatase; PE, Phosphatidylethanolamine; PECAM-1, Platelet-endothelial cell adhesion molecule-1; PERM1, Peroxisome proliferator–activated receptor γ coactivator 1- and Estrogen-related receptor–induced regulator in muscle 1; PF4, Platelet factor 4; PI, Phosphatidylinositol; PTM, Post-translational modification; ROX, Residual oxygen consumption; S6K1, Protein S6 kinase; SCX, Strong cation exchange chromatography; SDH, Succinate dehydrogenase; SILAC, Stable isotope labeling with heavy amino acids in cell culture; SLC, Solute carrier family; TBB, 4,5,6,7-tetrabromobenzotriazole; TFA, Trifluoroacetic acid; TiO_2, Titanium dioxide.

* Corresponding authors.
E-mail address: marcus.krueger@uni-koeln.de (M. Krüger).
[1] These authors contributed equally to this work.

https://doi.org/10.1016/j.yjmcc.2021.01.010
Received 1 July 2020; Received in revised form 5 January 2021; Accepted 11 January 2021
Available online 5 February 2021
0022-2828/© 2021 The Author(s). Published by Elsevier Ltd. This is an open access article under the CC BY-NC-ND license (http://creativecommons.org/licenses/by-nc-nd/4.0/).

1. Introduction

The development of the neonatal heart is characterized by rapid and extensive functional changes. To date, the molecular mechanisms, regulatory expression profiles of proteins, and post-translational modifications (PTMs) that control neonatal cardiomyocyte proliferation and the switch to maturation and differentiation are poorly described. It has been claimed recently that metabolic changes associated with the exposure to a postnatal normoxic environment favour acquisition of the postmitotic state of cardiomyocytes [1]. Protein phosphorylation plays a crucial role in temporary modulation of protein function, enzyme activity, and protein interactions [2]. Indeed, phosphorylation during heart development is a key function that is essential for the regulation of myocardial contraction and metabolism [3].

Recent advancements in high-resolution mass spectrometry-based proteomics have enabled site-specific identification of hundreds of thousands of PTMs *in vivo*. Moreover, phosphopeptide enrichment methods—together with improvements in mass spectrometry instrumentation—have provided a powerful tool to profile phosphorylation sites in unpreceded detail [4–6].

The function of the heart highly depends on energy provided by mitochondria, which undergo dynamic changes in protein content at different developmental stages. Fetal cardiomyocytes mainly generate ATP by oxidation of glucose. After birth, cardiomyocytes switch to β-oxidation of lipids, which generates larger amounts of ATP [7,8] [9]. Oxidative phosphorylation and ATP production occurs in the cristae of the inner mitochondrial membrane and depends on the electron transport between the OXPHOS complexes I-IV. Additionally, the change in fuel utilization is accompanied by a broad rewiring of the mitochondrial proteome. Although this switch in metabolism is known for quite some time, a detailed mechanistic understanding of this modulation on the protein level and posttranslational regulation is not well resolved.

In this study, we provide a comprehensive dataset of dynamic changes in the proteome and phosphoproteome of mouse hearts during postnatal development. Using stable isotope labelling with heavy amino acids in cell culture (SILAC), we investigated three postnatal time points and quantified 4412 proteins and 13,972 phosphorylation sites. Moreover, by integrating protein abundances with phosphorylation levels, we distinguished the regulation of protein phosphorylation from differential protein expression. We focussed our studies on the highly phosphorylated protein PERM1 (peroxisome proliferator-activated receptor γ coactivator 1- and estrogen-related receptor-induced regulator in muscle 1) [10], which we found to be strongly upregulated during postnatal heart development. Our data further reveal that PERM1 is an outer mitochondrial membrane protein. Genetic ablation of *Perm1* in mice led to accumulation of phospholipids and basic amino acids in cardiomyocyte mitochondria but did not impair mitochondrial mass and morphology.

2. Results

2.1. Proteome-wide mapping of phosphorylation sites and quantitative analysis of post-natal heart development

To gain a thorough insight into regulation of the phosphoproteome and changes in protein levels during early post-natal heart development during the first 20 days after birth, we employed a combination of spike-in SILAC quantification and high-resolution LC-MS/MS analysis using a quadrupole Orbitrap mass spectrometer. Neonatal hearts of mice were isolated 2 (P2), 10 (P10), and 20 (P20) days after birth and mixed with age-matched hearts of Lys6 ($^{13}C_6$-Lysine)-labelled mice. These experiments were done in biological duplicates and analyzed in 72 LC-MS/MS runs for the proteome and 81 LC-MS/MS runs for phosphoproteome on 2.5 h-long chromatographic gradients (Fig. 1A, SI Fig. S1A).

In total, we identified 24,366 phosphorylation sites mapped to 4953 proteins. Of these, 17,438 sites (72%) had a localization probability of >0.75 and we observed the majority of them (74%) as singly phosphorylated peptides (SI Fig. 1B). 84.3% (20,541) of all phosphopeptides were serine phosphorylated, 15.3% (3728) were threonine phosphorylated and 0.4% (97) were tyrosine phosphorylated (SI Fig. 1B). Principal component analysis (PCA) showed high similarity among the duplicates of P2, P10 and P20 and the components of the different groups were clearly separated, showing high differential regulation of proteins between each time-point (Fig. 1B). Here, PCA components two and three are depicted, as for proteomics data, component one only divides proteins according to their abundance but differences between the samples are visible when comparing component two and three.

We filtered the data using a fold-change >1.5 and FDR < 0.05 to identify significantly regulated phosphorylation sites (Fig. 1C, D) at P2 and P20 with respect to P10. To exclude changes in the abundance of phosphorylation events due to differential protein expression, we normalized the ratios of the phosphorylated peptides against the corresponding parental protein SILAC ratios. For example, we found mTOR S1261 phosphorylation was significantly upregulated at P20 compared to P10 and P2 in developing heart tissues (Fig. 1D).

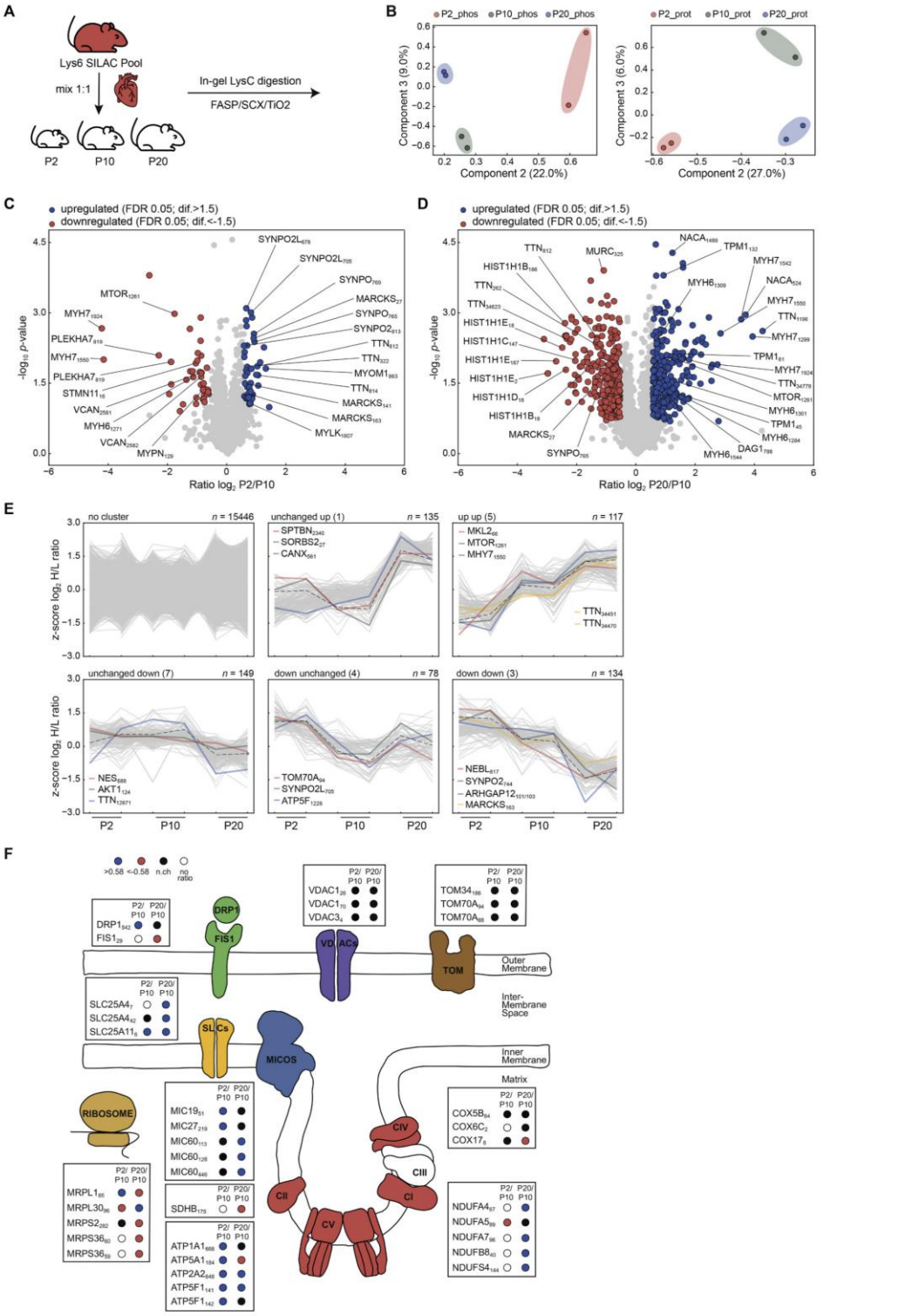
Normalization of the phosphorylation site intensities to the protein intensities lead to the identification of 89 and 573 significantly regulated phosphopeptides (fold-change >1.5; FDR < 0.05) at P2 and P20 with respect to P10, respectively (SI Table S1). For example, differential phosphorylation was observed for the giant protein titin, 80 of the 210 phosphorylation sites were quantified at a single time-point and 24 at all three time-points (SI Table S1, SI Fig. S2A). We observed significant upregulation (fold-change >1.5; FDR <0.05) of 21 titin phosphorylation sites during early heart development. Significant downregulation of six titin phosphorylation sites in the N-terminus within the *Z*-disk domain (aa 262–814) was also observed during the early heart development stages. Conversely, phosphorylation of two sites next to the Z-disk, pS1196 and pS2080, increased during development. Phosphorylation within the N2A-PEVK segment increases titin stiffness; our analysis revealed downregulation of seven sites between P2 and P20, four of which were significant (pS9144, pT10276 pS12871, pS12884; SI Fig. S2A). Moreover, five titin phosphorylation sites at the C-terminus within the M-band (aa 34,009–35,128) were significantly upregulated during development. In summary, significant changes in the phosphorylation status of the N- and C-terminal regions of titin were observed. These changes might influence the elasticity of the heart during development, re-appearance of early perinatal phosphorylation sites under disease conditions may contribute to pathobiological processes [11].

Next, we wanted to identify groups of phosphopeptides that are similarly regulated during heart development. All SILAC ratios were z-score-normalized and *k*-means clustering was used to associate proteins with similar phosphorylation profiles into seven clusters (Fig. 1E, SI Table S1). Although classes of phosphorylation sites were assigned to different clusters. Clusters 1 and 5 contained 252 phosphorylation sites that were upregulated during development, including pS1261 of mTOR and pS66 of myocardin-related transcription factor B (MKL2). Members of the myocardin family are serum response coactivators and key regulators for myogenic differentiation [12].

Interestingly, we also mapped 495 phosphorylation sites with a mitochondrial annotation. Several subunits of the OXPHOS complex displayed changes in phosphorylation levels during development at specific sites (Fig. 1F, SI Table S1). Likewise, we observed enhanced phosphorylation of S115, S128 and S446 in the core MICOS complex member MIC60 from P10 onwards.

2.2. PERM1 is upregulated during early heart development from P2-P20

In addition to the phosphoproteome, our proteomic analysis revealed 4412 differently regulated proteins across all three postnatal time points. Moreover, 2759 proteins were identified at all three time points, indicating that ~60% of the proteome is expressed between P2 and P20 (SI Table 1). The Andromeda score distributions that assess the quality



(caption on next page)

Fig. 1. Proteome-wide mapping of phosphorylation sites and quantitative phosphoproteomic analysis of post-natal heart development. (A) Schematic overview of the experimental workflow and samples analyzed. Detailed experimental approaches are specified in SI Fig. S1A. (B) Principal component analysis indicated clustering of the respective overall H/L ratios for the samples from each time point in both the phosphopeptide enrichment analysis and proteomic analysis. (C + D) Volcano plots depicting significantly regulated phosphorylation at P2 (C) and P20 (D) with respect to P10 ($n = 2$). The cut-off was a FDR < 0.05 and a fold change >1.5. (E) Five selected clusters (of seven clusters; *k*-means clustering) indicating the regulation of phosphorylation between P2, P10, and P20. Ratios were *z*-score normalized. (F) Overview of phosphosite regulation during post-natal development with respect to mitochondrial import, mitochondrial ribosomes, and the OXPHOS complex.

of phosphorylated and unmodified peptides are shown in SI Fig. 1C. Biological duplicates of the proteome analysis resulted in an average Pearson correlation coefficient of 0.8 (SI Fig. 1D, E). In total, we quantified 3823 proteins at P2, 3521 proteins at P10, and 3523 proteins at P20, leading to the identification of 370 and 1598 significantly regulated proteins at P2 and P20 with respect to P10, respectively (Fig. 2A- B, SI Table S1). 1D enrichment substantiated a remodelling of metabolic pathways and proteins associated with muscle contraction (Fig. 2C). Interestingly, proteins associated with the extracellular matrix, including agrin and periostin significantly increased during early heart development. These findings are in line with earlier studies describing these molecules as promotors of early postnatal cardiomyocyte proliferation [13]. A map of proteins associated with the extracellular matrix and dystrophin-associated complex members illustrates the dynamic

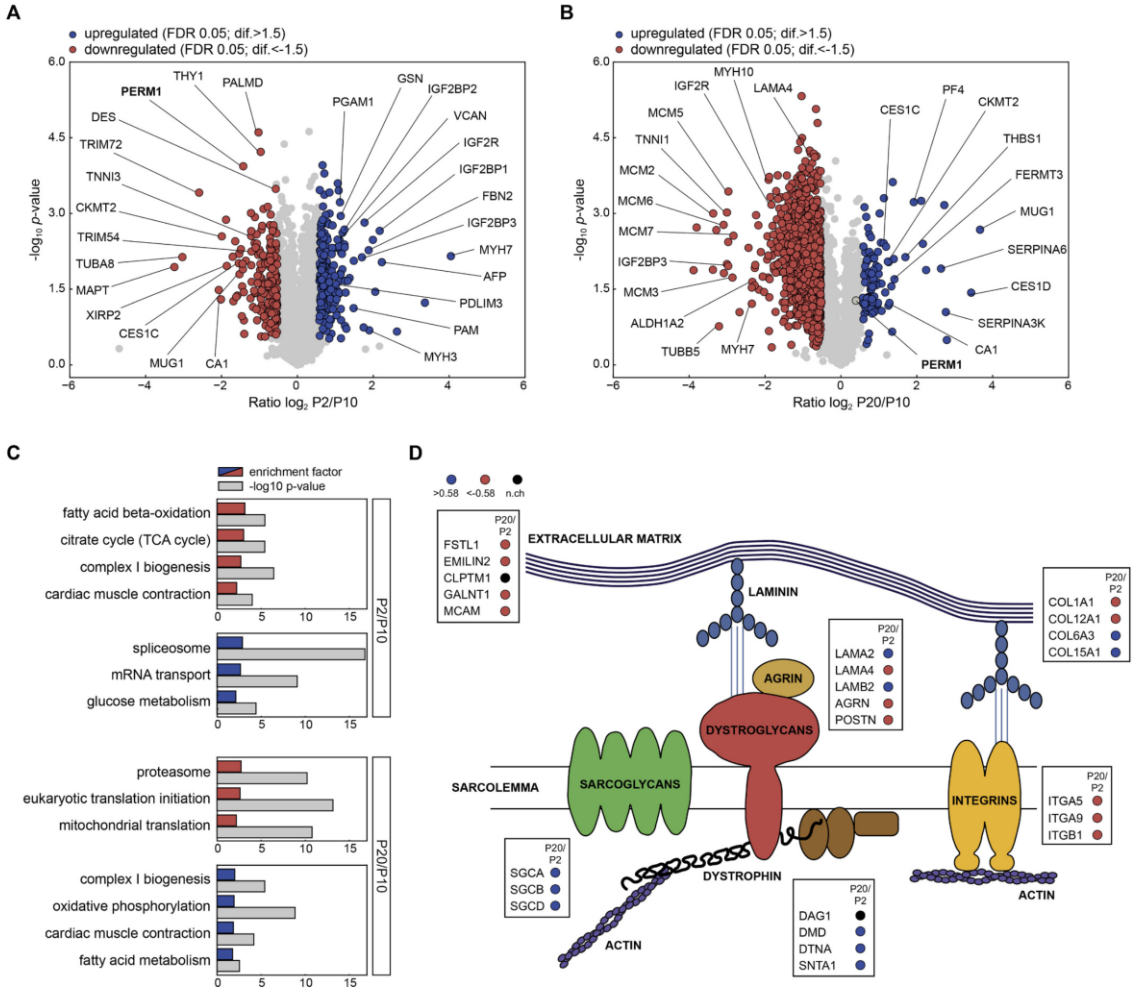


Fig. 2. Proteomic analysis of post-natal heart development. (A + B) Volcano plots depicting significantly regulated proteins at P2 (A) and P20 (B) with respect to P10 ($n = 2$). The cut-off was a FDR < 0.05 and a fold change >1.5. (C) Enrichment of gene ontology terms that are upregulated during heart development. Fischer's exact test showing the enrichment factor and *p*-value of gene ontology terms upregulated at P2 and P20 with respect to P10. Red dyed bars indicate downregulation of respective terms at P2 or P20 with respect to P10; blue dyed bars indicate upregulation of respective terms. (D) Overview of protein regulation during post-natal development with respect to the extracellular matrix and dystrophin-associated complex. (For interpretation of the references to colour in this figure legend, the reader is referred to the web version of this article.)

protein expression during heart development (Fig. 2D). It has been shown that the extracellular matrix (ECM) strongly influences cardiac proliferation and regeneration [14]. For example, agrin inhibits maturation and assembly of the dystrophin glycoprotein complex (DGC) and the development of myofibrillar structures during early neonatal cardiac development [13] [15]. The increased protein abundance of membrane-associated protein complexes, including dystrophin (DMD), dystroglycan (DAG1) and sarcoglycans, reflects progressive stabilization of the cardiac sarcolemma during heart development. Taken together, our data reveal dynamic regulation of protein expression and phosphorylation during early postnatal heart development and provide a valuable dataset for future studies on heart development.

Recent global expression profiling of developing heart tissues revealed general upregulation of sarcomeric and mitochondrial proteins after birth [16]. Likewise, our quantitative proteomics study showed clear upregulation of those compartments. We became particularly interested in PERM1, since (i) PERM1 is assumed to play a pivotal role in energy metabolism [10]; (ii) PERM1 was strongly upregulated during early heart development. SILAC quantification (Fig. 3A) and immunoblotting (Fig. 3B) revealed a clear increase in PERM1 concentrations after birth. Sequence analysis of the PERM1 protein indicated a PEST motif (rich in P, E, S, T amino acids) and several cysteine residues, including two C-terminal $CX_{13}C$ motifs (Fig. 3C) [17]. In addition, we mapped 34 PERM1 phosphorylation sites. Immunoblotting with an anti-PERM1 antibody and qPCR analysis validated expression of the *Perm1* gene in terminally differentiated heart and skeletal muscle cells (Fig. 3D, SI Fig. S2B).

2.3. PERM1 is a mitochondrial outer membrane protein

To investigate whether PERM1 is a soluble or membrane-associated protein, we separated the cytosolic and mitochondrial fractions from mouse heart tissues. Although PERM1 has no canonical N-terminal mitochondrial targeting sequence, PERM1 was identified in the mitochondrial fraction, similarly to HSP60 (Fig. 3E). Next, we performed biochemical fractionation based on alkaline sodium carbonate extraction of isolated mitochondria from mouse hearts. PERM1, monitored by the anti-PERM1 antibody, was predominantly found in the membrane fraction, together with the outer membrane protein (OMM) TOM20, whereas the matrix protein HSP60 was efficiently released into the soluble fraction (Fig. 3F). To determine the sub-mitochondrial localization of PERM1 more precisely, we performed swelling experiments combined with protease digestion (Fig. 3G). When intact mitochondria were treated with Proteinase K, the outer membrane protein mitofusin 2 (MFN2) and PERM1 disappeared, indicating that PERM1 localizes outside the mitochondrial membrane. This is further supported by the fact that the epitope, which is addressed by the anti-PERM1 antibody, spans a large part of the C-terminal region of the PERM1 protein that correspondingly has to be outside of OMM facing the cytosol. When mitochondria were subjected to osmotic shock—which leads to opening of the outer membrane—and then treated with Proteinase K, the inner membrane protein TIM23 was also digested. HSP60 was used as a digestion-resistant control mitochondrial matrix protein. The appearance of an additional lower band reflects the fragmentation of HSP60 after a longer incubation period with PK (Fig. 3G, right lane). Next, we examined the subcellular localization of PERM1 using C2C12 myoblasts transiently transfected with FLAG-tagged *Perm1* and GFP-tagged *Omp25* (outer membrane protein 25). Confocal laser scanning microscopy revealed clear co-localization of PERM1 with the mitochondrial marker OMP25-GFP (Fig. 3H). In addition, the mitochondrial localization of PERM1 in human heart sections was assessed by parallel immunohistochemical staining with human PERM1 and TOM20 antibodies; co-localization of both proteins was observed (Fig. 3I). In agreement with these data, we only detected PERM1 in F-actin positive cells in human heart sections, indicating cardiomyocyte-specific expression of PERM1 (Fig. 3J).

Hence, we conclude that PERM1 is a mitochondrial protein localized at the outer mitochondrial membrane of muscle cells.

2.4. The stability of PERM1 is regulated by phosphorylation of its PEST motif by CK2

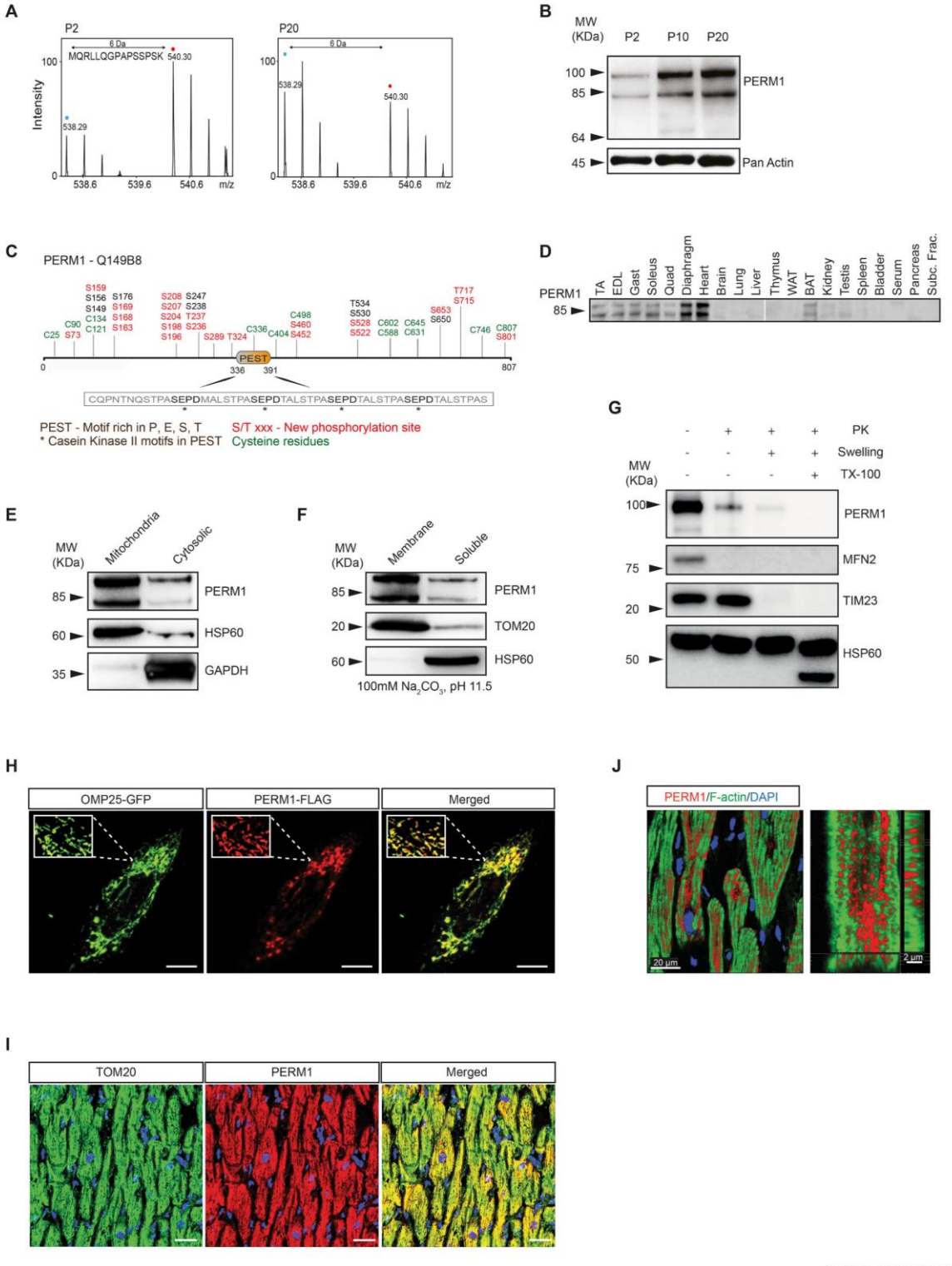
In addition to the phosphorylation events detected on PERM1, motif analysis indicated the presence of a 56-amino acid PEST motif that contains four repeated casein kinase 2 (CK2) substrate motifs (S/T-X-X-E/D/pS, Fig. 3C) [18]. PEST regions usually serve as signals for rapid proteasomal degradation [19] and phosphorylation of the PEST motifs further regulates protein turnover by leading to the exposure of degrons through induction of a conformational change [20].

To monitor the dynamics of PERM1 in heart tissue, we fed adult C57BL/6 mice with a $^{13}C_6$- lysine-containing mouse diet for 1–4 weeks and the labelled proteins were subjected to LysC digestion and LC-MS/MS analysis. The ratio between non-labelled and labelled peptides indicates the rate of $^{13}C_6$-lysine incorporation into newly synthesized proteins. PERM1 had a faster Lys6-incorporation compared to other mitochondrial marker proteins, including HSP60, COX5B and VDAC2 (Fig. 4A; SI Fig. S2C; SI Table S2). To estimate the $T_{1/2}$ of the measured Lys6-incorporation rates, we used a recently developed tool to calculate the absolute half-lives [21]. Using three labelling time-points between 7 and 28 days, we calculated a $T_{1/2}$ of 6.4 days for PERM1, which is much shorter than the average for all mitochondrial proteins ($T_{1/2}$~13 days; SI Fig. S2C; SI Table S2).

Next, we examined the changes in PERM1 using a previously generated data set on muscle atrophy after unilateral incision of the sciatic nerve [22]. Although all selected mitochondrial proteins exhibited slightly reduced protein levels two weeks after denervation, we observed a much stronger turnover of PERM1 (Fig. 4B). The long-lived protein dystrophin served as a control and exhibited no protein changes during this period, whereas S-adenosylmethionine decarboxylase proenzyme 1 (AMD1) was selected as an example of a rapidly degraded protein.

Since the PEST sequence in PERM1 contains consensus sequences for CK2 phosphorylation (Fig. 3C), we tested the hypothesis that PEST-mediated protein stability is phosphorylation-dependent. First, a radioactive kinase assay on immunoprecipitated FLAG-tagged *Perm1* with recombinant protein kinase CK2 revealed that PERM1 is phosphorylated by CK2 kinase, while the CK2 inhibitor TBB (4,5,6,7-tetrabromobenzotriazole) reduced phosphorylation of PERM1 (Fig. 4C). IKK (I kappa B kinase) served as a negative control. To identify the predicted phosphorylation sites within the PERM1 PEST motif, we performed *in vitro* kinase assays with immunoprecipitated FLAG-tagged *Perm1* in the absence of CK2 (control), in the presence of CK2, and in the presence of CK2 and TBB. PERM1 was eluted from the beads and digested in-solution. Although mass-spectrometric identification of the phosphorylation sites was challenging due to the absence of lysine or arginine in the 56-amino acid PEST motif, we identified all four predicted phosphosites, S347, S358, S369, and S380, as shown by the MS/MS spectra using the unspecific protease elastase (SI Fig. S3; SI Table S3). Moreover, based on the MS peak intensities, we only observed high signal intensities for these phosphorylation sites in the presence of CK2 (Fig. 4D). These results suggest that CK2 phosphorylates the serine residues within the PEST motif of PERM1.

Next, we investigated whether the phospho-PEST domain influences proteasomal degradation of PERM1. To detect the degree of ubiquitin proteasomal degradation induced by phosphorylation of the PEST motif, we mutated all four serine residues within the PEST domain to alanine; we termed the mutated form PERM1 SSSS/AAAA. We performed ubiquitination assays in HEK293T cells overexpressing FLAG-tagged *Perm1* and HA-tagged ubiquitin. In the presence of the proteasomal inhibitor MG-132, wild-type PERM1 exhibited a slightly reduced ubiquitination after inhibition of CK2 by TBB (Fig. 4E, SI Fig. S4A—B). In contrast, ubiquitination of the PERM1 SSSS/AAAA mutant was significantly



(caption on next page)

Fig. 3. PERM1 is upregulated during heart development and localizes to the outer mitochondrial membrane. (A) MS spectra and (B) Western blot depicting upregulation of PERM1 from P2 to P20. (C) Sequence landscape of PERM1, indicating the presence of casein kinase 2 motifs (SEPD) on the PEST domain, cysteine residues, and identified phosphorylation sites. (D) Western blot of various organs isolated from a wild-type mouse demonstrating PERM1 is specifically expressed in skeletal muscle and heart tissue. (E) Biochemical fractionation of cytosolic and mitochondrial fractions from mouse hearts, showing enrichment of PERM1 in the mitochondrial fraction—similarly to HSP60. (F) Sodium carbonate extraction of the membrane and soluble fractions of mouse heart mitochondria, showing enrichment of PERM1 in the membrane-associated fraction—similarly to TOM20. (G) Proteinase K assay to determine the submitochondrial localization of PERM1 in isolated mitochondria from TREx-293 cells stably overexpressing FLAG-tagged *Perm1*. Signals of anti-PERM1 antibody indicate that PERM1 associates with the outer mitochondrial membrane—similarly to MFN2. (H) Immunofluorescent microscopy of C2C12 myoblasts, indicating mitochondrial co-localization of overexpressed FLAG-tagged *Perm1* (red) with overexpressed OMP25-GFP (green). Scale 10 μm. (I) Immunohistochemistry of human heart sections showing mitochondrial co-localization of endogenous PERM1 (red) with TOM20 (green). Scale, 30 μm. (J) Immunohistochemistry of human heart sections showing localization of PERM1 (red) in F-actin (green)-positive cardiomyocytes. (For interpretation of the references to colour in this figure legend, the reader is referred to the web version of this article.)

reduced, even in the absence of inhibition of CK2. Further addition of TBB did not affect the degree of ubiquitination of PERM1 SSSS/AAAA. The reduction in phosphorylation after TBB treatment or mutation of the serines is shown by the pCK2 substrate blot. These results corroborate that CK2 phosphorylation of serines 347, 358, 369, and 380 in the PEST motif regulates the stability of PERM1.

To further compare the stability of wild-type and mutant *Perm1*, HEK293T cells were independently transfected with FLAG-tagged wild-type and SSSS/AAAA mutant *Perm1*. Twenty-four hours after transfection, the cells were treated with 20 μg/mL cycloheximide for 6, 12, and 24 h to inhibit translation. Immunoblotting using the FLAG antibody revealed a significantly more rapid degradation of wild-type PERM1 than the mutant form (Fig. 4F, SI Fig. S4C—D).

2.5. *Perm1*-deficient mitochondria exhibit enhanced protein synthesis in heart tissue

To gain additional insight into the function of PERM1, we generated a knock-out mouse strain by homologous recombination. *Perm1* gene ablation was achieved by replacing the coding region from exon 2 with a GFP cassette (SI Fig. S4E). The deletion was confirmed by mass spectrometry using the *in vivo* SILAC approach (Fig. 5A) and immunoblotting (Fig. 5B). *Perm1* mutants were viable, fertile and did not exhibit any obvious changes in body, heart, and muscle weight (Fig. 5C). Haematoxylin and eosin (H&E) staining of heart tissue cross sections revealed no apparent changes in the cardiomyocyte morphology of adult *Perm1*$^{-/-}$ mutants compared to wild-type mice (Fig. 5D). Similarly, enzymatic succinate dehydrogenase (SDH) staining and immunohistochemistry with an anti-dystrophin antibody and co-staining with phalloidin revealed no obvious changes in cell morphology between *Perm1*$^{-/-}$ and wild-type control hearts (Fig. 5D). An earlier study demonstrated that enhanced levels of PERM1 in skeletal muscles increase vascularization [23]. However, genetic ablation of *Perm1* did not alter the distribution of platelet-endothelial cell adhesion molecule-1 (PECAM-1; CD31) positive cells, indicating a similar density of capillaries in *Perm1*$^{-/-}$ and wild-type heart tissues (SI Fig. S4F).

Additionally, the amounts of mtDNA and mitochondrial proteins in the heart tissues of

Perm1$^{-/-}$ mutants were not affected (Fig. 5E, F). Administration of a diet containing Lys6 to label newly synthesized proteins revealed slightly enhanced labelling of mitochondrial proteins compared to all proteins detected in *Perm1*$^{-/-}$ hearts relative to control wild-type hearts (Fig. 5G-H, SI Table S4). Notably, this trend was not observed in mitochondria from brain tissue (Fig. 5I; SI Fig. S4G), suggesting slightly enhanced turnover of *Perm1*-deficient mitochondria. Next, we explored whether the oxidative phosphorylation system is affected in *Perm1*$^{-/-}$ mice. We isolated mitochondria from heart tissue and measured mitochondrial respiration by high resolution respirometry (Oroboros); no differences in oxygen flux per volume were observed between wildtype and *Perm1*$^{-/-}$ mitochondria (Fig. 5J). Similarly, BN-PAGE assessment indicated equivalent in-gel activity for complex I, IV, and V between the two genotypes (SI. Fig. S4H).

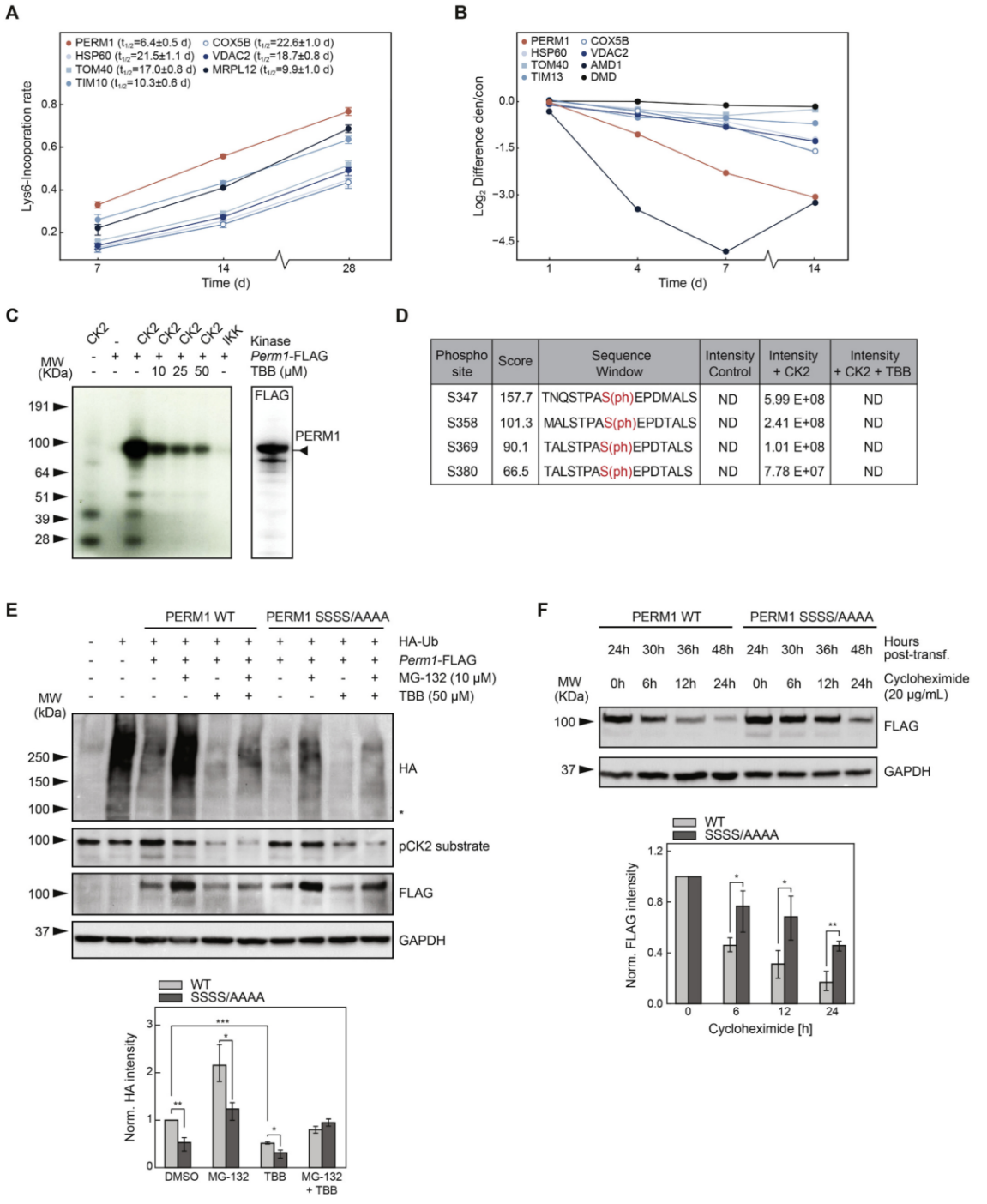
2.6. Expression of lipin-1 and several mitochondrial solute carrier membrane proteins (SLCs) is reduced in *Perm1*$^{-/-}$ heart tissue

Next, we used a MS label-free protein quantification approach to investigate protein changes in the intact heart tissues of *Perm1*$^{-/-}$ and wild-type control animals ranging at age from 3 to 24 months (SI Table S5). We quantified an average of 4636 proteins and two-sided *t*-tests revealed 40 (in young) and 25 (in aged) differently regulated proteins between *Perm1*$^{-/-}$ and wild-type hearts, respectively. Similarly, analysis of isolated mitochondria from young and aged *Perm1*$^{-/-}$ mutants revealed no major protein changes and we did not observe any correlations in the regulated proteins between young and aged animals (SI. Fig. S5A—D).

Since PERM1 exhibited fast Lys6-incorporation and its expression is induced in response to physical activity [24–27], we hypothesized that *Perm1*$^{-/-}$ mutants might exhibit greater changes in mitochondrial activity and protein expression during nocturnal activities than under daytime resting conditions. To test this hypothesis, we isolated hearts and mitochondria during the night and analyzed the protein changes by mass spectrometry between *Perm1*$^{-/-}$ mutants and controls. The statistical analysis revealed 67 significantly regulated proteins (Fig. 5K; SI Table S5). Enhanced abundance of several platelet proteins, including Kindlin-3 (FERMT3), several integrins (ITGA2, ITGA2B, ITGB3), and platelet factor 4 (PF4) suggest that circulating platelets accumulate in *Perm1*$^{-/-}$ mutant hearts. Serum proteins such as serum albumin and serotransferrin were not altered, indicating equal contamination with blood proteins.

Next, we asked whether mitochondria isolated during the night exhibited more protein changes than mitochondria isolated during the day. We quantified 3188 proteins ($n = 2$), including 849 mitochondrial proteins. Although the majority of mitochondrial proteins were distributed equally between *Perm1*$^{-/-}$ and control hearts (Fig. 5L; dark grey dots), we detected 17 mitochondrial proteins with significantly decreased abundances in *Perm1*$^{-/-}$ mutants. For example, the cardiac lipin-1 (LPIN1) protein was exhibited a 1.5-fold decrease (p-value <0.05) in isolated *Perm1*$^{-/-}$ mitochondria. LPIN1 catalyzes the formation of diacylglycerol from phosphatidic acids (PA) and lack of LPIN1 in the fatty liver dystrophic (fld) mouse model leads to neonatal hepatic steatosis, insulin resistance, and increased risk of atherosclerotic lesions [28,29]. It is important to note that, similarly to PERM1, LPIN1 is controlled by the transcription factors PGC-1α and ERRα/γ [30]. Since LPIN1 is a direct mTOR substrate and inhibited by phosphorylation, we quantified mTOR protein expression and phosphorylation. Interestingly, immunoblotting analysis revealed clear downregulation of mTOR phosphorylation, but no changes in mTOR protein expression in *Perm1*$^{-/-}$ hearts compared to wild type hearts (Fig. 6A).

To address whether the lipostasis is affected by the decreased levels of LPIN1 in *Perm1*$^{-/-}$ mutant hearts compared to wild-type control animals, we evaluated the levels of several phospholipid classes in heart tissues by mass spectrometry. Similar to the muscle-specific ablation of LPIN1, the lipid analysis revealed significant increase of the levels of phosphatidic acid (PA), phosphatidylinositol (PI), and phosphatidylethanolamine (PE) ($n = 8$ mice per group) (Fig. 6B; SI Table S6). It



(caption on next page)

Fig. 4. Rapid turnover of PERM1 is regulated by CK2 phosphorylation of the PERM1 PEST motif. (A) Line graph depicting faster Lys6-incorporation of PERM1 compared to other mitochondrial marker proteins in the heart tissue of wild-type mice fed a SILAC diet for 7, 14, and 28 days. (B) Line graph demonstrating faster protein degradation of PERM1 compared to other mitochondrial proteins in muscle after unilateral section of the sciatic nerve. (C) FLAG-tagged *Perm1* was overexpressed and immunoprecipitated from HEK293T cells. Radioactive kinase assay with the kinases CK2 or IKK in the presence of absence of the CK2 inhibitor TBB indicated that PERM1 is phosphorylated by CK2. (D) CK2 kinase assay followed by elastase digestion and LC-MS/MS analysis, indicating CK2 phosphorylates serines 347, 358, 369, and 380 of FLAG-tagged *Perm1*. (E) HEK293T cells were transfected with wild-type or mutant *Perm1*, after 24 h the cells were treated with 10 μM MG-132 and/or 50 μM TBB for 4 h. TBB significantly reduced ubiquitination of wild-type PERM1; ubiquitination of the mutant was unaffected by TBB. * indicates the molecular weight of PERM1, HA quantification was performed from 100 kDa to the top. HA intensities were normalized to GAPDH and are shown relative to the wild-type control (DMSO) sample. (F) Western blot analysis revealing slower degradation of overexpressed mutant PERM1 in comparison to overexpressed wild-type PERM1. HEK293T cells were transfected with FLAG-tagged *Perm1* wild-type or SSSS/AAAA mutant form and 24 h after transfection, cells were treated with 20 μg/mL cycloheximide for 6, 12, and 24 h. FLAG intensities were normalized to GAPDH and are shown relative to time point 0 h of the cycloheximide treatment. Data are the mean ± 0.95 CI. *, **, and *** indicate $p < 0.05$, 0.01, and 0.001, respectively; Student's *t*-test.

should be noted that other lipids tested, including PC (*p*-value 0.08), PS (*p*-value 0.16), and PG (*p*-value 0.06), were also upregulated but without statistical significance. (Fig. 6B). Important to note, the overall phospholipid composition was not altered (Fig. 6C). A profile of different PA species is shown in SI Fig. S5A and consistent with earlier studies in the fld mouse model, we also observed enhanced levels of the PA species 34:1 and 34:2 in *Perm1*$^{-/-}$ mutants (Fig. S5E).

Metabolites are transported within the cell between different compartments for further processing. Mitochondrial solute carrier proteins (SLCs) transport and exchange metabolites, including amino acids, nucleotides, coenzymes and carboxylates [31]. Overall, our mass spectrometric analyses revealed differential regulation of 53 SLCs in *Perm1*$^{-/-}$ mice, including 28 members of the SLC25 family (SI Table S5). For example, the glutamate/aspartate transporters SLC25A12 (Aralar1) and SLC25A13 (Aralar2), which exhibited very high signal intensities among all detected transporters, were significantly downregulated in mitochondria isolated from *Perm1*$^{-/-}$ mutants compared to controls. Likewise, SLC25A29, a mitochondrial transporter for lysine and arginine [32] was downregulated by ~four-fold (p-value 0.02) in *Perm1*$^{-/-}$ mitochondria (SI Table S5). Another SLC25 family member, SLC25A34, which shares sequence similarity with the oxalacetate carrier YKL120w in yeast [33], was also significantly downregulated (p-value 0.03).

Next, we asked whether the reduced protein expression levels of several mitochondrial SLCs in *Perm1*$^{-/-}$ mutants influences the homoeostasis of various metabolites in mitochondria. Mass spectrometric analysis of 21 amino acids revealed elevated levels of 11 amino acids, including three basic (Lys, Arg, His) and three branched chain amino acids (Leu, Ile, Val) in *Perm1*$^{-/-}$ mitochondria compared to controls ($n = 6$; Fig. 6D; SI Table S6).

Carnitine palmitoyltransferases belong to another transport system associated with mitochondrial metabolism that transfers long chain fatty acids from the cytoplasm to the mitochondrial matrix. The carnitine palmitoyl transferase CPT2 was downregulated and we identified significantly reduced levels of the acylcarnitines C2:0, C14:0, and C18:0 in mitochondria isolated from *Perm1*$^{-/-}$ hearts ($n = 6$; Fig. 6E; SI Table S6). In contrast, no significant changes were observed for metabolites such as ADP, ATP, pyruvate, lactate and TCA cycle intermediates in *Perm1*$^{-/-}$ mitochondria compared to wild-type controls ($n = 6$; SI Fig. S5F).

Together, these findings highlight a role of PERM1 in mitochondrial fatty acid transport and metabolism in the heart.

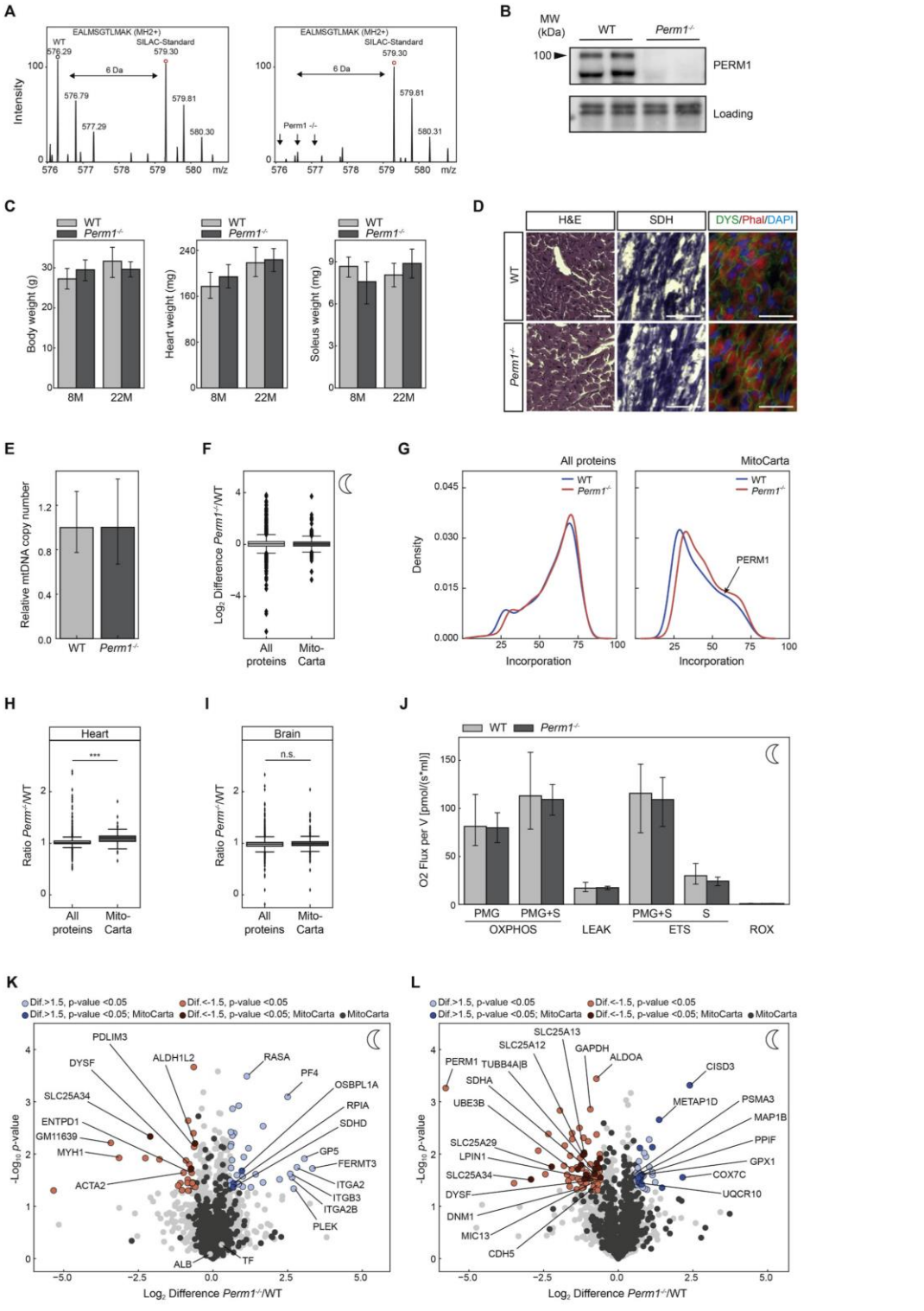
3. Discussion

Mitochondrial biogenesis represents an important feature of cardiomyocyte maturation [34] and although intracellular energy pathways during post-natal heart development have been studied [35], a comprehensive analysis of protein expression and phosphorylation based on quantitative mass spectrometry events was critically missing. The use of a SILAC mouse approach enabled us to robustly quantify protein expression levels *in vivo*, and validated previous reports. [11,13–15,36]Mitochondria in neonatal hearts undergo profound reorganisation during development similar to the ECM. We found that PERM1 protein levels are strongly upregulated between P2 and P20 (Fig. 2B). So far, detailed insight into the physiological function of PERM1 in heart tissues was missing. We observed PERM1 mainly at the outer mitochondrial membrane in TREx-293 and C2C12 cells, mouse and human heart tissue (Fig. 3*E*-I). However, our results are in contrast to an earlier report which showed that PERM1 is predominantly located in the nucleus, the cytosol and possibly in mitochondria of C2C12 cells [10]. In addition, *Perm1* is induced by PGC-1α and ERR and may regulate proteins associated with energy metabolism and the contractile apparatus. Overexpression of PERM1 in myotubes induced mitochondrial biogenesis and enhanced oxidative capacity [23]. A recent report observed decreased PERM1 concentrations in the heart tissue of mice after phenylephrine-induced hypertrophic stress, in hearts after transaortic constriction (TAC) and in patients with heart failure [37]. These results support the role of PERM1 in modulating heart metabolism. Moreover, MS revealed a specific protein-protein interaction between PERM1 and the Ca^{2+}/calmodulin-dependent protein kinase (CaMKII) [25]. Based on the lack of a canonical N-terminal targeting sequence, strong membrane association and high PK sensitivity (Fig. 3), we conclude that PERM1 is associated with the OMM facing the cytosol and makes PERM1 accessible for the interaction with other proteins such as the cytosolic CaMKII.

The ubiquitin proteasome system is implicated in the degradation of proteins in the mitochondrial outer membrane [38] [39]. The increased stability of the PERM1 phospho-mutant compared to the wild-type protein clearly indicates that CK2 phosphorylation of the PEST motif of PERM1 crucially regulates the turnover of PERM1. However, the exact mechanism and conditions under which CK2 phosphorylates PERM1 *in vivo* remain to be elucidated.

To gain more insight into the physiological function of PERM1, we ablated the *Perm1* gene in mice by targeted mutagenesis. Previous studies showed that adenoviral-mediated overexpression of PERM1 in skeletal muscle elevated mitochondrial biogenesis and increased the density of capillaries [23]. Our proteomics analysis revealed a significant increase in several platelet marker proteins in *Perm1*$^{-/-}$ hearts (Fig. 5K), but we did not observe obvious alterations in the density of capillaries in *Perm1*$^{-/-}$ mutants (SI Fig. S4F). It is tempting to speculate that our finding indicates altered capillary permeability and/or is caused by increased platelet adhesion to the walls of capillaries, as observed in inflammatory processes. Importantly, blood contamination can be excluded as the levels of abundant serum proteins such as albumin, haemoglobin and myoglobin were similar in *Perm1*$^{-/-}$ and wild-type control hearts (Fig. 5L; SI Table S5). Interestingly, a study showed that adeno-associated viral overexpression of *Perm1* improves skeletal muscle vascularisation and increases expression of vascular endothelial growth factor A (Vegfa) [23]. Therefore, a more comprehensive morphometric and structural analysis of capillaries and endothelia is necessary to clarify whether *Perm1* ablation affects angiogenesis in cardiac tissue.

In addition, a previous report showed that knockdown of *Perm1* using shRNA in C2C12 myotubes downregulated several sarcomeric proteins [40], suggesting an involvement of PERM1 in the regulation of components of the contractile apparatus. Since different isoforms of



(caption on next page)

Fig. 5. Characterization of *Perm1*-deficient heart tissue and mitochondria. (A) MS spectra and (B) Western blot confirming successful depletion of PERM1 in *Perm1*$^{-/-}$ heart tissue. (C) Body, heart, and muscle weights of 8- and 22-month-old *Perm1*$^{-/-}$ mutant mice; no significant differences compared to wild-type controls were observed ($n = 8$ mice per group). (D) Haematoxylin and eosin (H&E), succinate dehydrogenase (SDH), and immunohistochemical staining for dystrophin (green), phalloidin (red) and DAPI (blue) of mouse heart cross sections; no differences were observed between *Perm1*$^{-/-}$ and wild-type mice. Scale, 50 μm. (E) qPCR analysis showed no differences in the mtDNA copy number of *Perm1*$^{-/-}$ heart tissue compared to wild-type mice ($n = 3$ mice per group). For quantification, cytochrome B gene expression (mitochondrial) was normalized to the nuclear beta-actin gene. (F) Comparison of $\log_2$ differences of MitoCarta 2.0 proteins compared to the complete dataset revealed no changes in overall regulation of mitochondrial proteins in *Perm1*$^{-/-}$ hearts compared to controls ($n = 2$ mice per group). (G) Density plot and (H + I) ratios of *Perm1*$^{-/-}$ to wild-type Lys6-incorporation rates for MitoCarta 2.0 proteins in comparison to the complete dataset from (H) heart tissue after feeding with a SILAC diet for 14 days. Enhanced labelling of mitochondrial proteins was observed in *Perm1*$^{-/-}$ hearts but not in (I) *Perm1*$^{-/-}$ brains ($n = 3$ mice per group). (J) High-resolution respirometry of isolated heart mitochondria, indicating no changes in oxygen flux per volume in *Perm1*$^{-/-}$ mitochondria compared to wild-type ($n = 3$ mice per group). (K + L) Volcano plot depicting significantly regulated proteins in *Perm1*$^{-/-}$ heart tissue (K) and isolated heart mitochondria (L) compared to wild-type ($n = 2$ mice per group). Cut-off was defined as $p < 0.05$ and a fold change >1.5. Darker colours indicate the MitoCarta 2.0 annotations. (For interpretation of the references to colour in this figure legend, the reader is referred to the web version of this article.)
Samples obtained at night time are indicated with a moon symbol. Data are the mean ± 0.95 CI. *, **, and *** indicate $p < 0.05$, 0.01, and 0.001, respectively; Whitney-Mann-*U* test. PMG (pyruvate, malate, glutamate), S (succinate), ETS (electron transfer system), ROX (residual oxygen consumption).

sarcomeric proteins have high sequence similarity, we used only unique peptides for protein quantification to avoid incorrect interpretation of our proteomics data set. Of the 45 quantified proteins associated with the contractile actin-myosin complex (SI Table S5), we only observed significant downregulation of the atrial isoform of myosin regulatory light chain 2 (gene: Myl7) and myozenin-2 (also known calcarcin 1; SI Fig. S5G). MYL7 is component of the cardiac thick filament and controls myosin motility. However, no other core components of the filaments were altered in *Perm1*$^{-/-}$ mutants compared to control hearts, arguing against a direct involvement of *Perm1* in the regulation of developmental and contractile properties of cardiomyocytes.

Similar to PERM1, the soluble and ER-associated enzyme LPIN1 is another target of PGC-1α and ERRα. LPIN1 converts PA to diacylglycerol (DAG). Due to its phosphatidic acid phosphatase (PAP) activity, LPIN1 is an essential modulator of lipid homeostasis. LPIN1 also acts as a transcriptional coactivator to enhance expression of genes involved in lipogenesis and the loss of *Lpin1* gene, as in the fld mouse model [41]) and humans [42], is associated with rhabdomyolysis, lipodystrophy and neurodegeneration.

On the molecular level, loss of LPIN1-mediated PAP activity results in accumulation of lipid species in muscle and heart tissues [43]. In addition, muscle-specific inactivation of *Lpin1* led to autophagy disturbances, lysosomal dysfunction, and sarcoplasmic reticulum stress in mice, suggesting that LPIN1 plays a crucial role in mitochondrial activity [44]. MS analysis of lipid species in heart tissues revealed significant accumulation of PA species, although we only observed a moderate decrease in LPIN1 in mitochondria isolated from *Perm1*$^{-/-}$ mutants. This finding is similar to the phenotype of the TG9 mouse, a transgenic model which express high levels of the Cre recombinase in the heart *via* the α-MHC promotor. Besides the upregulation of heart failure markers [45], the TG9 mouse model shows a reduced LPIN1, PGC-1α, ERRα, and ERRγ protein expression [29]. Furthermore, muscle-specific ablation of LPIN1 also increased the levels of glycerolipids [46]. Since we only observed reduced LPIN1 protein levels in isolated *Perm1*$^{-/-}$ mitochondria and not in total heart lysates, PERM1 might link LPIN1 to mitochondria and MAMs. Given the complex pathways of lipid synthesis and conversion, we cannot exclude the possibility that other enzymes are also involved in lipid accumulation.

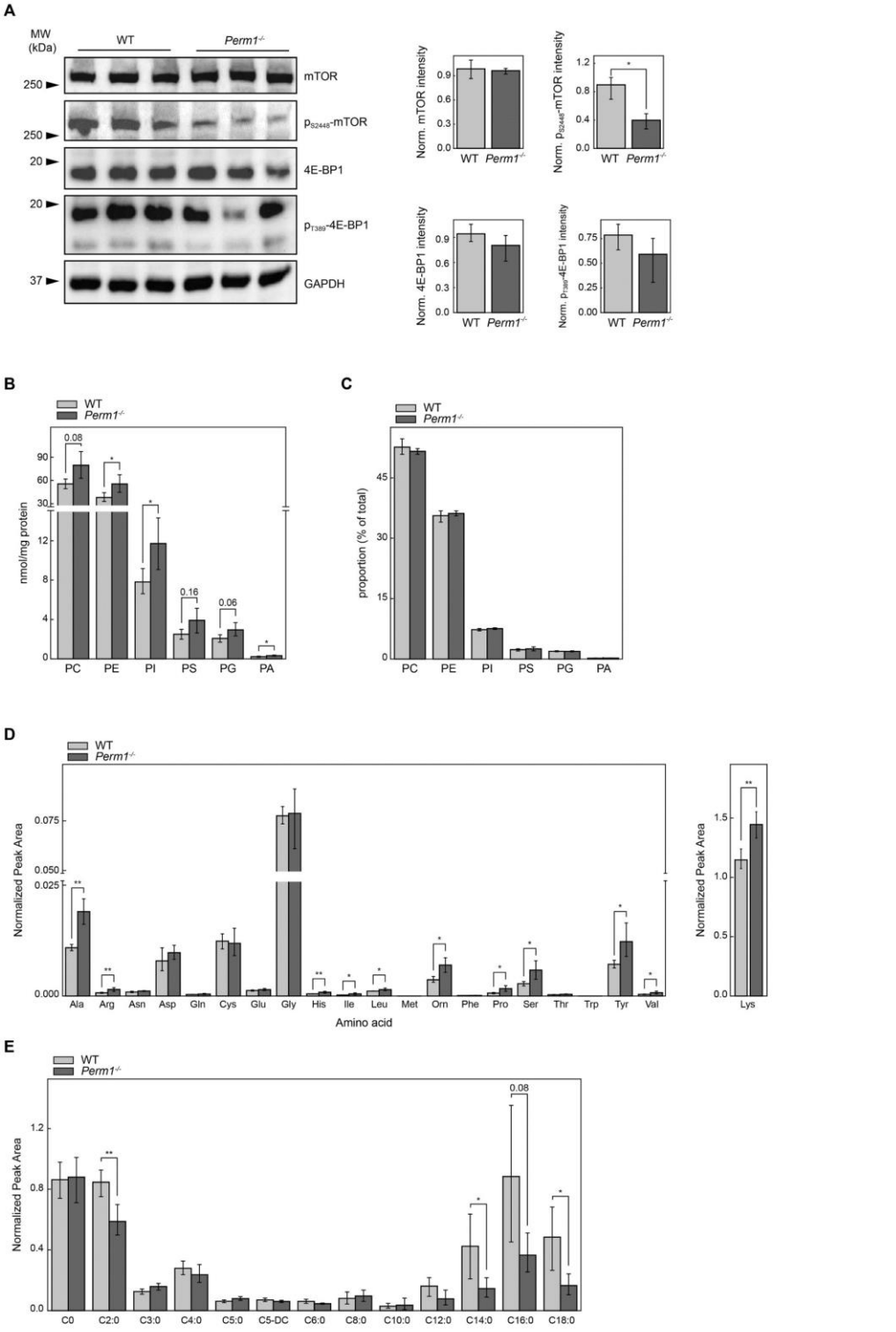
Consistently, the localization of LPIN1 depends on its phosphorylation mediated by the kinase mTOR. The mTOR kinase was downregulated in *Perm1*$^{-/-}$ hearts, without a corresponding change of the mTOR target 4E-BP1 phosphorylation. Since the phosphorylation on S2448 inhibits the function of mTOR, it is possible that suppressed mTOR activity contributes to a change of the LPIN1 localization in *Perm1*$^{-/-}$ hearts [47].

The solute carrier protein family is a large group of over 300 transporters that facilitate the transport of diverse molecules, either as uniporter or exchangers [31]. The SLC25 family is responsible for the transport of nucleotides, fatty acids, cofactors, amino acids, and carboxylic acids through the inner membrane of the mitochondria, and their function is essential to many cellular processes [48]. We observed significant downregulation in the intact heart and/or isolated mitochondria for four SLC25 transporters in *Perm1*$^{-/-}$ mice (Fig. 5K-L). For example, the aspartate/glutamate carriers AGC1 (SLC25A12) and AGC2 (SLC25A13) import glutamate along with a proton and export aspartate. Both transporters are calcium-dependent and are associated with the malate-aspartate shuttle, gluconeogenesis and the urea cycle [49]. Despite the reduced levels of SLC25A12 and SLC25A13, our MS amino acid analysis revealed no changes in the levels of aspartate and glutamate in *Perm1*$^{-/-}$ mutants compared to wild-type control mitochondria. Since many SLC transporters are orphans with unknown functions and substrates, other SLC transporters may compensate for the reduced levels of SLC25A12 and SLC25A13.

Slightly enhanced levels of the folate transporter SLC25A32 and pyrimidine nucleotide transporter SLC25A36 were observed in *Perm1*$^{-/-}$ mitochondria. Exchange of these nucleotides between the cytoplasm and mitochondria is important for the synthesis and degradation of mitochondrial DNA and RNA. Since we observed a slightly increased Lys6-incorporation in *Perm1*$^{-/-}$ mitochondria, an elevated translation rate may affect the need for (deoxy) nucleosides. Alternatively, the yeast homolog of SLC25A36, RIM2p protein, is not only a pyrimidine exchanger but is also involved in promoting mitochondrial iron utilization promoting iron-sulfur (Fe—S) protein maturation [50]. Interestingly, the iron-sulfur mitochondrial outer-membrane protein CISD3 (also known as Miner2) exhibited the most distinct upregulation of all mitochondrial proteins in *Perm1*$^{-/-}$ mutants compared to wild type mitochondria (Fig. 5L). CISD3 is a member of the CDGSH iron-sulfur protein family and may serve as a dynamic redox-sensitive outer mitochondrial membrane protein involved in electron shuttling through the electron transport chain and regulation of enzymatic activity [51] [52].

Another SLC25 family member, the basic amino acid transporter SLC25A29, was also downregulated in *Perm1*$^{-/-}$ mitochondria. A recent report provides clear evidence that SLC25A29 transports the basic amino acids arginine, lysine, and ornithine into mitochondria. However, instead of reduced concentrations of arginine or lysine, we observed increased concentrations of basic (R, K, H) and branched chain amino acids (I, L, V) in *Perm1*$^{-/-}$ mitochondria. These results indicate that SLC25A29 is unlikely to contribute significantly to the mitochondrial arginine and lysine pool. Moreover, since the vast majority of mitochondrial proteins are imported, degradation of these proteins into individual amino acids by peptidases could provide sufficient concentrations of amino acids for translation of mitochondrial proteins. We assume that accumulation of amino acids in *Perm1*$^{-/-}$ hearts are caused by increased degradation of mitochondrial proteins or reduced conversion of specific amino acids into other metabolites utilized for the TCA cycle. The observation that the aminopeptidase N (ANPEP) was upregulated two-fold in *Perm1*$^{-/-}$ mitochondria compared to wild-type controls indicates increased degradation of peptides.

In addition to the transport of metabolites *via* SLC transporters, mitochondria have established another efficient mitochondrial transport



(caption on next page)

Fig. 6. Abundance of phospholipids and free amino acids in *Perm1*-deficient hearts. (A) Evaluation of mTOR activity in heart tissue of *Perm1*$^{-/-}$ and wild-type mice by western blot incubated with antibodies against mTOR, p_{S2448} mTOR and the substrates 4E-BP1 and p_{T386} 4E-BP1. The level of p_{S2448} mTOR was reduced in the heart tissue of *Perm1*$^{-/-}$ mice. Intensities were normalized to GAPDH. (B) Phospholipidomic analysis of *Perm1*$^{-/-}$ and wild-type hearts, showing enhanced amounts of all indicated phospholipid classes. Values are normalized to the protein content of *Perm1*$^{-/-}$ and control hearts ($n = 8$ mice per group). (C) The amounts of the indicated phospholipid classes as a proportion of total phospholipids were not different between *Perm1*$^{-/-}$ and wild-type hearts. (D) Peak areas of free amino acids for heart mitochondria isolated from *Perm1*$^{-/-}$ and wild-type mice revealed higher levels of basic and branched chain amino acids in *Perm1*$^{-/-}$ mitochondria. Peak areas were normalized to internal standards ($n = 6$ mice per group). (E) Peak areas of aclycarnitine species measured in heart mitochondria isolated from *Perm1*$^{-/-}$ and wild-type mice; peak areas were reduced for C2:0 and species with long C-chains ≥14. Peak areas were normalized to internal standards ($n = 6$ mice per group). Data are the mean ± 0.95 CI. * and ** $p < 0.05$ and 0.01, respectively, Welch's *t*-test. PC (Phosphatidylcholine), PE (phosphatidylethanolamine), PI (phosphatidylinositol), PS (phosphatidylserine), PG (phosphatidylglycerol), PA (phosphatidic acid).

system for fatty acids, which contains two carnitine palmitoyltransferases localized in the outer (CPT1) and inner (CPT2) mitochondrial membrane. Although we only observed a decreased abundance of CPT2 in *Perm1*$^{-/-}$ mitochondria, this could explain the reduced levels of long chain acylcarnitines (Fig. 6E). Our data indicate that the reduced fatty acid content alters metabolism in *Perm1*$^{-/-}$ mitochondria. However, the mechanisms by which PERM1 regulates the abundance of transporters in the SLC family and CPT2—or whether PERM1 rather plays a direct role in transport—are currently unclear.

It is important to note that the cellular architecture and mitochondria of *Perm1*$^{-/-}$ cardiomyocytes did not exhibit changes under baseline conditions. In addition, quantitative mass spectrometric analysis of the lysates from intact heart tissue and isolated mitochondria did not reveal a loss of mitochondria or a substantial change in the composition of the mitochondrial proteome between *Perm1*$^{-/-}$ and wild-type mice, neither did we detect changes in the amount of mtDNA. Finally, oxygraph measurements of mitochondria from *Perm1*$^{-/-}$ hearts did not indicate any changes in respiratory activity compared to wild-type hearts under normal conditions.

Additionally, the short half-life of PERM1 compared to other mitochondrial proteins might be essential to achieve rapid changes in protein concentrations. We hypothesize that PERM1 also functions as a sensor at the outer mitochondrial membrane, to monitor the workload and energy demand of mitochondria. The high fluctuations in the energy requirement of heart and skeletal muscle might also explain why PERM1 is only detected in these tissues and not in the liver or brain, which tend to have more constant energy requirements.

In summary, our quantitative proteomic and phosphoproteomic analysis revealed substantial changes of metabolic activities within mitochondria during early heart development and demonstrate that PERM1 plays an important role in this process. The stability of PERM1, which localizes to the outer mitochondrial membrane, is regulated by CK2-dependent phosphorylation of the PEST domain of PERM1, although other kinases might be involved as well. We propose that PERM1 plays an important role in the regulation of mitochondrial energy metabolism by contributing to lipid and amino acid homeostasis.

4. Methods

4.1. Antibodies

The following antibodies were used for immunoblotting, immunocytochemistry, and immunohistochemistry: PERM1 (Sigma, #HPA031711), pan-actin (Cell Signaling, #4968), FLAG (Sigma, #F1804), HSP60 (Abcam, #ab46798), GAPDH (Cell Signaling, #14C10), rabbit TOM20 (Santa Cruz Biotech, #FL-145), mouse TOM20 (Abcam, #ab56783), GFP (Evrogen, #AB121), MFN2 (Abnova, #H00055669), TIM23 (BD Biosciences, #611222), sarcomeric α-actinin (Sigma, #A7811), Dystrophin (Abcam, #ab15277), Phalloidin iFluor 594 (Abcam, #ab176757), mTOR (Cell Signaling, #2983), p_{S2448} mTOR (Cell Signaling, #5536), 4E-BP1 (Cell Signaling, #9482), p_{T389} 4E-BP1 (Cell Signaling, #2855), phosphor Ser/Thr CK2 substrate (Cell Signaling, #8738), and GAPDH (Cell Signaling, #2118), diluted 1:1000, HA-HRP (Sigma, #H6533) and FLAG M2-Peroxidase HRP (Sigma, #A8592), diluted 1:5000, anti-mouse Alexa Fluor 594 (Life Technologies, #A-11005), anti-rabbit Alexa Flour 594 (Life Technologies, #A-11012), anti-mouse Alexa Flour 488 (Life Technologies, #A-11001), anti-rabbit Alexa Flour 488 (Life Technologies, #A-11008), and anti-mouse IgG1 Alexa Fluor 488 (Life Technologies, #A-21121), diluted 1:4000, and anti-mouse HRP (Sigma, #9044) and anti-rabbit HRP (Sigma, #0545), diluted 1:4000.

4.2. SILAC mice

To generation the SILAC mouse colony, C57BL/6 mice were fully labelled with $^{13}C_6$ lysine (heavy)-containing mouse diet (Silantes GmbH, Germany), as previously described [53]. This labelling leads to complete exchange of naturally occurring $^{12}C_6$ lysine (light) with $^{13}C_6$ (heavy). Several hearts from non-labelled P2, P10, and P20 mice were pooled to obtain sufficient material for phosphopeptide enrichment, using a mixture of age-matched hearts from Lys6 ($^{13}C_6$-Lysine)-labelled SILAC mice as a 'spike-in' heavy standard to quantify non-labelled experimental conditions. For the generation of the heavy protein standard we pooled 4 x P2, 2 x P10 and 1 P20 SILAC labelled hearts.

4.3. Tissue lysis

Mouse heart tissues were snap frozen in liquid nitrogen and ground to a fine powder using a mortar and pestle. The powder was resuspended in either SDS lysis buffer (4% SDS in

100 mM Tris/HCl, pH 7.6) or modified RIPA buffer (100 mM Tris/HCl pH 7.5, 300 mM NaCl, 2% Nonidet P40, 2 mM EDTA, 0.2% sodium deoxycholate) supplemented with protease and phosphatase inhibitors at a buffer to tissue ratio of 15:1. SILAC-labelled heart tissues from mice ranging in age from P2 to P20 were lysed in SDS lysis buffer and pooled to obtain the heavy standards. The lysates were boiled at 95 °C for homogenization and the crude extracts were clarified by centrifugation at 13,000 rpm for 10 min. Tissues lysed in modified RIPA buffer were incubated with rotation for 30 min at 4 °C and sonicated for 10 min with 30 s intervals at 4 °C using a Bioruptor® Pico (Diagenode). Cell debris was pelleted by centrifugation at 18,000 *g* for 10 min at 4 °C.

4.4. Protein concentration determination

Protein concentrations were determined using a Pierce Protein Assay (Thermo Fisher). BSA solutions with concentrations ranging from 0.05 mg/mL to 1.0 mg/mL were generated by diluting a 2 mg/mL BSA solution (Thermo Fisher) and used as standards. Protein samples were diluted 1:10 in the respective buffer. Absorption was measured at 660 nm using an EnSpire® Multimode Plate Reader (Perkin Elmer). To enable measurement of protein samples diluted in SDS-containing buffer, Pierce 660 nm Protein Assay Reagent was supplemented with the accessory Ionic Detergent Compatibility Reagent (Thermo Fisher) according to manufacturer's instructions.

4.5. In-gel digestion and sample purification

Heart tissue and isolated heart mitochondria proteomic samples were processed using a modified version of the in-gel digestion protocol

by [54]. Briefly, lysates were precipitated overnight in four volumes (*v:v*) of ice-cold acetone. Protein pellets were extracted by centrifugation at 13,000 *g* for 10 min and dissolved in Bolt LDS sample buffer (Invitrogen). Dithiothreitol (DTT) was added to a final concentration of 10 mM, the mixtures were heated to 70 °C for 10 min, iodacetamide (IAA) was added to a final concentration of 55 mM and the samples were incubated in the dark for 20 min. Proteins were separated using Bolt 4–12% Bis-Tris Plus gels (Invitrogen), Coomassie-stained, and each lane was cut into six to twelve slices. Each slice was chopped into 1 mm cubes, destained with 50% acetonitrile (ACN) and dehydrated with 100% ACN. For protein digestion, 3 ng/μL trypsin/LysC solution (90% trypsin/10% LysC) was added, incubated for 30 min at 4 °C, 50 mM ammonium bicarbonate (ABC) was added to the swollen gel pieces, incubated overnight at 37 °C and the digestions were stopped by acidifying the samples with trifluoroacetic acid (TFA). Tryptic peptides were extracted with increasing concentrations of ACN and organic compounds were evaporated using a SpeedVac concentrator Plus (Eppendorf). Acidified samples were desalted using Stop and Go extraction tips (StageTipping [55],). Lys6-labelled and non-labelled proteins were mixed in equal proportions and in-gel digested using this protocol but digestion was only performed with LysC.

4.6. Filter-aided sample preparation (FASP)

For phosphoproteomics analysis, the FASP method of protein digestion was performed as described previously [56]. In brief, 15 mg of the SILAC-mixed protein samples lysed in SDS lysis buffer were reduced with 10 mM DTT and heated at 70 °C for 10 min. Next, the sampleswere loaded onto Amicon Ultra-15 Centrifugal Filter Units (Millipore) equilibrated with urea buffer (6 M urea, 2 M thiourea). SDS in the samples was exchanged with urea buffer, followed by alkylation with 55 mM IAA in the dark. Urea was washed out four times with 50 mM Tris/HCl (pH 8.5). Proteins in the filter were digested overnight with LysC at 30 °C at an enzyme:protein ratio of 1:100. The next day, digested peptides were collected by centrifugation at 4000 *g* for 10 min. The filter was washed once with water to collect remaining peptides.

4.7. Strong cation exchange chromatography (SCX)

Peptides were adjusted to a pH of 2.6 with TFA and then 30% ACN, and then loaded onto a 1 mL Resource S column (GE Healthcare) pre-equilibrated with at least five times the column volume of 30% ACN containing 7 mM KH_2PO_4 (pH 2.65). Peptides bound to the column were eluted using a 30-min increasing salt gradient in buffer containing 30% ACN, 7 mM KH_2PO_4 and 350 mM KCl (pH 2.65). The column was washed between runs with a buffer containing 50 mM $K_2HPO_4.3H_2O$ and 500 mM NaCl (pH 7.5). The eluted fractions were pooled based on the chromatogram to obtain a total of nine fractions.

4.8. Phosphopeptide enrichment using TiO_2 beads

To enrich for phosphorylated peptides, ~15 mg of labelled and non-labelled heart tissue lysates were digested with LysC and fractionated using strong cation exchange chromatography (SCX). Each fraction was subjected to sequential enrichment using titanium dioxide beads (TiO_2) beads to enrich phosphorylated peptides.

The flow-through and fractions obtained from SCX were vacuum concentrated on a SpeedVac (Eppendorf) and adjusted to 80% ACN/6% TFA (binding buffer condition). The TiO_2 beads were washed with 60% NH_3/40% ACN (elution buffer), followed by 70% ACN to wash out the ammonia, and then with 80% ACN/3% TFA (wash buffer). Washed beads were resuspended in 80% ACN/6% TFA (binding buffer). The flow-through was extracted three times with 5 mg TiO_2 beads and the fractions were extracted twice with 3 mg TiO_2 beads. The multiple extractions of each sample were pooled and loaded onto one layer stacked-C8 StageTips for washing. Beads were washed thrice with binding buffer and thrice with wash buffer. Phosphopeptides were eluted three times from the beads using 25 μL elution buffer. Eluates were vacuum concentrated in a SpeedVac. Concentrated phosphopeptides were acidified using 0.1% formic acid and subjected to LC-MS/MS analysis.

4.9. Isolation of crude mitochondria from tissue

To isolate crude mitochondria, freshly collected heart or muscle samples were washed once in cold PBS and incubated in 4 mL Mito buffer A (220 mM mannitol, 70 mM sucrose, 20 mM HEPES/KOH, 0.5 mM PMSF, 2 mg/mL BSA, 1 mM EDTA/Tris pH 7.4) supplemented with protease and phosphatase inhibitors on ice. The tissues were homogenized in a motor-driven potter (20 strokes, 1000 rpm) and cell debris was pelleted at 800 *g* for 5 min at 4 °C. The supernatant was collected, the pellet was subjected to a second homogenization (20 strokes, 1000 rpm), centrifuged at 800 *g* for 5 min at 4 °C, the supernatant was combined with the supernatant from the first homogenization, and centrifuged at 8000 *g* for 5 min at 4 °C. The supernatant was discarded and the pellet was resuspended in 1 mL Mito buffer B (220 mM mannitol, 70 mM sucrose, 20 mM HEPES/KOH, 0.5 mM PMSF, 1 mM EDTA/Tris pH 7.4), centrifuged twice at 8000 *g* for 5 min at 4 °C and the mitochondrial pellet was resuspended in 1 mL buffer B. Finally, the samples were centrifuged at 10,000 *g* for 5 min at 4 °C and the mitochondria were resuspended in 300–500 μL Mito buffer B. For the metabolomics study of heart mitochondria, isolation was performed as described above, except KPBS buffer (136 mM KCl, 10 mM H_2KPO_4, pH 7.25) was used instead of Mito buffer A and B.

4.10. In-solution digestion

Samples from subcellular fractionation were prepared for MS analysis by in-solution digestion. Urea-containing samples were reduced by adding DTT at a final concentration of 5 mM for 1 h at RT. Alkylation with IAA at a final concentration of 40 mM was performed for 30 min in the dark at RT. Next, the samples were digested with 1 μL LysC for 2–3 h at RT. Finally, the samples were diluted with 50 mM ABC to a urea concentration of 2 M and incubated with 1 μL 0.5 mg/mL trypsin overnight at RT, acidified to 1% FA and purified on StageTips.

4.11. MS-based proteome analysis

Proteome samples were analyzed using a liquid chromatography tandem mass spectrometry on a Q-Exactive™ Plus Hybrid Quadrupole-Orbitrap™ (Thermo Fisher). Chromatographic peptide separation was achieved on PoroShell 120 packed 50 cm analytical columns coupled to an EASY-nLC 1000 HPLC system and a binary buffer system consisting of buffer A (0.1% FA) and buffer B (80% ACN/0.1% FA). In-gel digested samples were analyzed over a 150 min gradient, raising the content of buffer B from 9 to 29% over 119 min, from 29 to 68% over 5 min, and from 68% to 95% over 16 min. The column was washed with 95% buffer B, then buffer B was reduced to 5% over 5 min and the column was re-equilibrated with 5% buffer B for 5 min. Full MS spectra (300–1750 *m/z*) were recorded at a resolution (R) of 70,500, maximum injection time (max. IT) of 20 ms and AGC target of 3e6. The ten most abundant ion peptides in each full MS scan were selected for HCD fragmentation at nominal collisional energy (NCE) of 25. MS2 spectra were recorded at $R = 17{,}500$, a maximum IT of 60 ms and an AGC target of 5e5.

In-solution digested whole homogenate samples from the subcellular fractionation were analyzed over a 240 min gradient. Buffer B was increased from 5% to 34% over 215 min, from 34% to 55% over 5 min, and from 55% to 90% over 5 min. This was followed by washing with 90% buffer B for 5 min, reducing buffer B to 5% over 5 min and re-equilibration with 5% buffer B for 5 min. Samples from the other fractions were analyzed using the same 150 min gradient used for in-gel digested samples.

4.12. MS data processing and analysis

The generated MS raw data were analyzed using MaxQuant analysis software and the implemented Andromeda software (1.5.3.8) [57,58]. Peptides and proteins were identified using the mouse UniProt database with common contaminants (FASTA file downloaded on 16/6/2017, size: 16890 entries). All parameters in MaxQuant were set to the default values. Trypsin was selected as the digestion enzyme, and a maximum of two missed cleavages was allowed. For SILAC, peptide pairs were quantified by setting Lys6 as the heavy label. Enzyme specificity was set to LysC/Trypsin with an additional allowance of cleavage N-terminal to proline, or unspecific search for elastase digestion.

Methionine oxidation and N-terminal acetylation were set as variable modifications, and carbamidomethylation of cysteines was chosen as a fixed modification. For phosphoproteomic analysis, phosphorylation of STY (Serine, Threonine, and Tyrosine) was also set as a variable modification. The label-free quantification (LFQ) algorithm was used to quantify the measured peptides and the "match between runs" option was enabled to quantify peptides with a missing MS2 spectrum. A minimum ratio count of 2 was used for SILAC quantification.

Subsequent statistical analysis was performed using Perseus (1.5.5.3–1.6.5.0) software. Potential contaminants and reverse peptides were excluded, and values were $\log_2$ transformed for *t*-tests. Two-sided t-tests were used to identify differentially expressed proteins between groups defined by the genotype (WT or KO). Permutation-based estimation of the False Discovery Rate (FDR) using 500 permutations and a fudge factor S_0 of 0.1 was used. The cut-off was set to 0.05 [59]. Identified peptides were annotated with the following Gene Ontology terms: Biological Process, Molecular Function, and Cellular Compartment, and Kyoto Encyclopedia of Genes and Genomes terms. Finally, graphical visualization was achieved using Instant Clue software [60].

4.13. Generation of *Perm1*$^{-/-}$ mice

Constitutive knockout *Perm1*$^{-/-}$ mice were generated using a recombineering based method to subclone DNA from bacterial artificial chromosomes (BACs) into high-copy plasmids, together with Flp recombinase to introduce FRT sites into the subcloned DNA. In the first step, two sets of primers were used to amplify two ~500 bp regions of the BAC (obtained from mouse bMQ BAC library, Source BioScience). The region of the BAC containing Venus-GFP, Neo cassette and the FRT sites was excised and transformed into ES cells. The Neo positive clones and recombination positive clones of ES cells were confirmed using southern blotting and one was chosen and inject into the mouse. Chimeric mice were crossed with Flp recombinase mice to cut out the Neo cassette between the FRT sites. Further breeding and back crossings are being performed to generate heterozygous and homozygous mice and remove the Flp deletor gene.

4.14. Quantitative PCR of PERM1 expression

RNA was extracted using Trizol reagent (Ambion, Life Technologies), incubated with DNase I, reverse transcribed to cDNA using the Superscript II Reverse Transcriptase Kit (Invitrogen), and subjected to quantitative PCR analysis using the StepOne and StepOnePlus Real Time PCR system (Life Technologies). The primers used for *Perm1* were Fw5`-GAAAACAGTCTTGCTCGCCAA-3` and Rev5`-CTTGTCACCTGGGTTCGTCT-3`. Real-time qPCR analysis was performed using the KAPA SYBR Green Fast reagent (KAPA Biosystems) *via* the standard curve method. The expression levels of *Perm1* were normalized to the levels of 18S rRNA as the endogenous control.

4.15. Plasmids

The mouse PERM1 coding sequence was cloned into pcDNA5/TO vectors containing either a C-terminal FLAG tag or C-terminal EGFP. The FANTOM Riken cDNA clone for the mouse gene 2310042D19Rik (purchased from Source Bioscience) was used as template for Phusion Polymerase (Finnzymes)-based PCR amplification. For subsequent cloning, we introduced *Kpn*I (5`) and *Xho*I (3`) restriction sites flanking the coding sequence of *Perm1* using the oligonucleotides *Perm1* fw: 5`-AAAGGGAAAGGTACCATGGACAA CTTCCAGTACAG-3` and *Perm1* rev: 5`-TTTCCCTTTCTCGAGGCAGCTGGGGTTTGA-3`. The Omp25-GFP plasmid was used [61] to label mitochondria. HA-Ubiquitin used in the ubiquitination assays was a gift of Prof. Ivan Dikic (Goethe-Universitaet, Frankfurt, Germany). The phospho mutant *Perm1* (SSSS/AAAA) was purchased from Life Technologies (GeneArt Gene Synthesis).

4.16. Cell culture

All used cell lines were cultivated as an adherent fibroblastoid monolayer in 10 cm dishes at 37 °C and 5% CO_2 in DMEM (Gibco) supplemented with 10% FBS and 1× Penicillin-Streptavidin-Glutamine mix.

4.17. Pulsed-SILAC labeling

To monitor newly synthesized proteins *in vivo*, time-dependent Lys6-incorporation was investigated. In the first study, wild-type mice were labelled for 7–28 days (n = 3 mice per time point) with the Lys6-containing SILAC diet. In the second study, three mice of each genotype (*Perm1*$^{-/-}$ and wild-type control) were Lys6-labelled for two weeks. Mice were voluntarily fed in each case with 3.0 g of $^{13}C_6$-lysine containing diet (Silantes GmbH, Lys(6)-SILAC-Mouse Diet, purity >97%). Several tissues of interest were pulverized, lysed in modified RIPA buffer and in-gel- or in-solution digestion was performed.

4.18. Radioactive in vitro kinase assay and MS identification of CK2 sites

FLAG-tagged *Perm1* was transfected into HEK293T cells. After 30 h, the cells were serum-starved overnight and PERM1 was immunoprecipitated using anti-Flag M2 affinity gel (Sigma). Constitutively active Casein Kinase II (CK2) (New England BioLabs) was incubated with the immunoprecipitate in the presence of CK2 buffer, 10 µM cold ATP (Cell Signaling) and 5 µCi γ^{32}-ATP (Hartmann Analytic GmbH) for 1 h at 30 °C. The reaction was stopped by adding 4× Laemmli buffer and boiling for 5 min at 95 °C. Samples were separated using SDS-PAGE and the gels was dried and exposed to X-ray film (GE Healthcare). For MS analysis to identify CK2 phosphorylation sites, the *in vitro* kinase assay was performed with only cold ATP. The proteins were eluted from the beads by boiling with 4% SDS in 0.1 M Tris/HCl pH 7.6 at 95 °C for 5 min. Eluted proteins were precipitated with 4 volumes of ice-cold acetone for 1 h at −20 °C. The protein pellet was reconstituted in 6 M urea/2 M thiourea/0.1 M HEPES pH 7.4, reduced with 10 mM DTT, alkylated with 55 mM IAA, diluted to 2 M urea with 100 mM ABC and digested with 2 µg elastase overnight. Digested peptides were desalted using StageTips and subjected to LC-MS/MS analysis.

4.19. Subcellular and submitochondrial localization

Mitochondria were isolated from tissues as previously described [62]. The carbonate procedure was used to separate the membrane and soluble mitochondrial fractions [63]. Mouse heart mitochondria were solubilized in 100 mM Na_2CO_3, pH 11.5, for 30 min on ice and ultracentrifuged at 50,000 rpm for 1 h at 4 °C. The pellet consisting of the membrane fraction and soluble proteins in the supernatant were precipitated using 10% trichloroacetic acid. Swelling experiments combined with proteinase K treatment were performed to assess submitochondrial localization [64].

4.20. Immunocytochemistry

C2C12 cells on cover slips were transfected with FLAG-tagged *Perm1* and GFP-tagged Omp25 using Turbofect transfection reagent (Thermo Scientific) in reduced serum OPTI-MEM media (Life Technologies). After 24 h, cells were fixed in 4% paraformaldehyde for 10 min, permeabilized with 0.1% Triton X-100 in PBS for 10 min, and stained with anti-FLAG antibody for 1–2 h at RT. The coverslips were mounted in Mowiol 4–88 Reagent. Confocal imaging was performed with a Zeiss LSM700 confocal microscope and ZEN2011 software.

Neonatal cardiomyocytes were cultured on cover slips in Nunc Lab-Tek II 8-chamber slides (Thermo Scientific), transfected with Tom20, fixed with 4% paraformaldehyde for 20 min, permeabilized with 0.05% Triton X-100 for 15 min and stained using anti-TOM20 and anti-F-actin antibodies. The cover slips were mounted in Mowiol 4–88 reagent and confocal imaging was performed on a TCS SP8 confocal microscope (Leica microsystems) using LASX software.

4.21. Human heart tissue

For performed immunohistochemical analysis of human myocardial tissues from five individuals who underwent subvalvular myectomy during surgical aortic valve replacement; these tissues served as control samples in a previous study [65]. These samples exhibited preserved cardiac function (ejection fraction ≥60%), and the resected myocardial tissues did not show any signs of myocardial hypertrophy or ischemic damage. The ethics committee of the Medical Council of the State of Hessen approved this study. Informed consent was obtained from patients and the study complied with the requirements of the Medical Council of the State of Hessen and institutional ethics guidelines of the Kerckhoff Hospital, Bad Nauheim, Germany.

4.22. Immunohistochemistry

Cross sections of heart tissue (10 μm) were prepared by snap-freezing whole muscles in liquid nitrogen-cooled isopentane. Sections were fixed in −20 °C cold acetone for 8 min and blocked in 0.1% Triton, 5% goat serum and 2% BSA in TBS for 1 h at RT, incubated with the primary antibody in 1:10 blocking solution at 4 °C overnight in a humidified chamber, mounted with Aqua Poly mount (Polysciences) and imaged using a DMi8A inverse microscope.

Human heart sections were fixed in 4% paraformaldehyde for 15 min, permeabilized in 0.05% Triton X-100 for 20 min, and incubated with anti-PERM1 and TOM20. Images were captured on a Leica TCS laser confocal microscope with appropriate filters.

4.23. Western blot analysis

For protein separation, 10–20 μg protein lysates were incubated with 4× Laemmli buffer and 50 mM DTT for 10 min at 70 °C. SDS-PAGE was performed according to standard procedures using stain-free casting solutions from Bio-Rad. Proteins were electroblotted onto polyvinylidene fluoride (PVDF) membranes using a Trans-Blot Turbo Transfer System (Bio-Rad). The unblotted gel was developed using the ChemiDoc™ Touch Imaging System (Bio-Rad) with the stain-free option implemented. Western blotting was performed using a Trans-Blot Turbo Transfer System (Bio-Rad). Membranes were developed using Clarity Western ECL Substrate (Bio-Rad). The intensity of the bands was quantified using ImageJ software [66]. The values were normalized to the stain-free images.

4.24. Oxygen consumption measurements

Oxygraphic measurements generally performed as previously described [67]. Briefly, 50 μg of isolated heart mitochondria were used each oxygraphic measurement. The Oxygraph-2 k (Oroboros Instruments) was used to measure oxygen consumption rate. The mitochondria were added after air equilibration of the mitochondrial respiration buffer. First, the OXPHOS state for complex I was determined by adding 5 mM pyruvate, 2 mM malate, 20 mM glutamate, and 2 mM ADP. Convergent electron flow through complexes I and II was measured by adding 10 mM succinate. Next, LEAK respiration was assessed by inhibition of the ATP synthase with oligomycin (1.5 μg/mL). Carbonyl cyanide-*p*- trifluoromethoxy-phenylhydrazone (FCCP, 0.5 μM) was titrated to determine maximal electron transfer system (ETS) capacity. Subsequently, complex I was inhibited by addition of 0.5 μL rotenone to determine the maximal ETS capacity with electron flow through complex II only. Finally, residual oxygen consumption (ROX) was measured by inhibiting complex III using 2.5 μM antimycin A.

4.25. BN-PAGE and in-gel activity staining

3–13% blue native polyacrylamide gel electrophorese (BN-PAGE) was performed as previously described [68] with minor modifications. In brief, mitochondria were solubilized in digitonin-containing (1% [g/v]; 4 g digitonin/g protein) buffer (50 mM NaCl, 5 mM 6-aminohexanoic acid, 50 mm imidazole/HCl [pH 7.0], 50 mM KPi-buffer [pH 7.4], 10% glycerol). In-gel activity staining was performed at RT using the following substrate solutions: complex I (2 mM Tris/HCl [pH 7.4], 0.1 mg/mL NADH, 2.5 mg/mL Nitro Blue Tetrazolium), complex IV (50 mM KPi-buffer [pH 7.4], 220 mM Sucrose, 0.5 mg/mL 3,3'-Diaminobenzidine, 1 nM Catalase, 1 mg/mL Cytochrome *c*) and complex V (270 mM Glycine and 35 mM Tris/HCl [pH 8.3], 14 mM $MgSO_4$, 0.2% $Pb(NO_3)_2$, 8 mM ATP).

4.26. Determination of relative mtDNA copy number

DNA was extracted from tissue lysates to determine relative mtDNA content of heart tissues. Briefly, heart lysates from *Perm1*$^{-/-}$ and control mice were incubated at 55 °C overnight in 350 μL DNA extraction buffer (0.5% SDS, 0.1 M NaCl, 50 mM Tris/HCl pH 8.0, 20 mM EDTA) supplemented with proteinase K, 350 μL phenol-chloroform-isoamylalcohol was added to the samples, mixed gently, and centrifuged for 5 min at 2500 rpm and 4 °C. The upper phase was transferred to a new tube and 350 μL phenol-chloroform-isoamylalcohol was added, mixed gently, and centrifuged as before. The upper phase was transferred to a new tube, mixed with 650 μL of 100% ethanol and 65 μL of 7.5 mM ammonium acetate, incubated at −20 °C for 1 h. centrifuged at 13,000 rpm for 30 min at 4 °C, and the pellet was washed with 70% ethanol and resuspended in 10 mM Tris/HCl pH 8.5.

The extracted DNA (25 ng) was subsequently used for qPCR with two technical replicates. The expression of the cytochrome B gene (primers: GCTTTCCACTTCATCTTACCATTT and TGTTGGGTTGTTTGATCCTG) was normalized to the nuclear beta-actin gene (primers: GGAAAAGAGCCTCAGGGCAT and GAAGAGCTATGAGCTGCCTGA). The qPCR reactions were performed using KiCqStart® SYBR® Green qPCR ReadyMix™ (Sigma) on a CFX connect real-time PCR detection system (Bio-Rad) at 95 °C for 7 min, followed by 35 cycles of 95 °C for 10 s and 60 °C for 30 s.

4.27. Lipidomics/metabolomics

4.27.1. Glycerophospholipids

Glycerophospholipids (PC, PE, PI, PS, PG, PA) in mouse heart were analyzed by Nano-ESI-MS/MS with direct infusion of the lipid extract (Shotgun Lipidomics): Samples of mouse heart tissue were homogenized in Milli-Q water (1 mg / 10 μL) using the Precellys 24 Homogenisator (Peqlab, Erlangen, Germany) at 6.500 rpm for 30 s. The protein content of the homogenate was routinely determined using bicinchoninic acid. To 25 μL of the homogenate, 475 μL of Milli-Q water, 1.875 mL of methanol/chloroform 2:1 (*v*/v), and internal standards (125 pmol PC 17:0–20:4, 132 pmol PE 17:0–20:4, 118 pmol PI 17:0–20:4, 131 pmol PS

17:0–20:4, 62 pmol PG 17:0–20:4, 75 pmol PA 17:0–20:4; Avanti Polar Lipids) were added. Lipid extraction and Nano-ESI-MS/MS analysis were performed as previously described [69]. Endogenous glycerophospolipids were quantified by referring their peak areas to those of the internal standards. The calculated glycerophospolipid amounts were normalized to the protein content of the tissue homogenate.

4.27.2. Nucleotides and intermediates of glycolysis and tricarboxylic acid (TCA) cycle

Levels of nucleotides and intermediates of glycolysis and TCA cycle in isolated mouse heart mitochondria were determined by Ion Chromatography coupled to Electrospray Ionization High-Resolution Mass Spectrometry (IC-ESI-HRMS) using a procedure previously described [70] with several modifications:

Mitochondria pellets containing 200 μg of protein were suspended in 200 μL of ice-cold methanol/water 4:1 (v/v) with 0.2% formic acid. 15 μL of each sample were mixed for the quality control. To all samples, 10 μL of a mixture of isotope-labelled internal standards

(50 μM 13C10-adenosine 5′-triphosphate (13C10-ATP), Sigma-Aldrich; 5 μM 13C6-D-glucose-6-phosphate (13C6-G6P) and 5 μM D4-succinic acid (D4-SUC), both Eurisotop) were added. After thorough mixing and centrifugation (16,100 *g*, 5 min, 4 °C), 160 μL of supernatant were dried under a stream of nitrogen. The residue was resolved in 100 μL of Milli-Q water, transferred to autoinjector vials and immediately measured.

IC-HRMS analysis was performed using a Dionex Integrion RFIC system (Thermo Scientific) equipped with a Dionex IonPac AS11-HC column (2 mm × 250 mm, 4 μm particle size, Thermo Scientific) and a Dionex IonPac AG11-HC guard column (2 mm × 50 mm, 4 μm, Thermo Scientific) and coupled to a Q Exactive HF quadrupole-orbitrap mass spectrometer (Thermo Scientific). 5 μL of sample were injected using a Dionex AS-AP at 10 °C. The IC was operated at a flow rate of 0.38 mL/min with a potassium hydroxide gradient which was produced by an eluent generator with a potassium hydroxide cartridge and Milli-Q water. The gradient started with 10 mM KOH over 3 min, 10–50 mM from 3 to 12 min, 50–100 mM from 12 to 19 min, held at 100 mM from 19 to 25 min, and re-equilibrated at 10 mM for 3 min. The total run time was 28 min. An Dionex ADRS 600, 2 mm suppressor was operated with 95 mA, and methanol was used to produce a make-up flow at a flow rate of 0.15 mL/min.

The mass spectrometer was operated in the negative ion mode. Full MS scans in the range of *m/z* 60–900 were acquired with a resolution of 60,000, an Automatic Gain Control (AGC) target value of 1 × 106 and a maximum injection time (IT) of 100 ms. Spectrum data were collected in the centroid mode. The ESI source was operated with flow rates for sheath gas, auxiliary gas, and sweep gas of 50, 14 and 3, respectively. The spray voltage setting was 2.75 kV, the capillary temperature 230 °C, the S-lens RF level 45, and the auxiliary gas heater temperature 380 °C [70].

The exact m/z traces of the internal standards and endogenous nucleotides, organic acids, and sugar phosphates were extracted and integrated using Skyline 20.1 (open-source). The peak areas of the endogenous metabolites were normalized to those of the internal standards: 13C10-ATP was used as internal standard for endogenous nucleotides, 13C6-G6P for sugar phosphates, and D4-SUC for organic acids.

4.27.3. Amino acids

Amino acids of isolated mouse heart mitochondria were derivatized with benzoyl chloride and quantified by Liquid Chromatography coupled to Electrospray Ionization Tandem Mass Spectrometry (LC-ESI-MS/MS) using a procedure previously described (Wong et al., 2016) [71] with several modifications: Mitochondria pellets containing 200 μg of protein were suspended in 100 μL of ice-cold acetonitrile/water 4:1 (*v/v*). After thorough mixing and centrifugation (16,100 *g*, 5 min, 4 °C), 50 μL of supernatant were transferred to a new tube and used for the analysis of acylcarnitines (see below). For the amino acid analysis, 20 μL of supernatant were mixed with 10 μL of an internal standard mixture, containing isotope-labelled amino acids (Sigma-Aldrich) at concentrations of 200 μM. Amino acids were derivatized by adding 10 μL of freshly prepared 2% benzoyl chloride in acetonitrile and 10 μL of 100 mM sodium carbonate in water and thorough mixing. After addition of 50 μL of Milli-Q water and centrifugation (16,100 *g*, 5 min, 4 °C), 80 μL of supernatant were transferred to autoinjector vials.

LC-MS/MS analysis was performed by injection of 5 μL of sample onto a Core-Shell Kinetex C18 column (100 mm × 2.1 mm ID, 2.6 μm particle size, 100 Å pore size, Phenomenex) and detection using a QTRAP 6500 triple quadrupole/linear ion trap mass spectrometer (SCIEX). The LC (Nexera X2 UHPLC System, Shimadzu) was operated at 30 °C and at a flow rate of 0.4 mL/min with a mobile phase of 10 mM ammonium formate and 0.15% formic acid in water (solvent A) and acetonitrile (solvent B). Benzoylated amino acids were eluted with the following gradient: initial, 0% B; 0.01 min, 15% B; 0.5 min, 17% B; 14 min, 55% B; 14.5 min, 100% B; 16.5 min, 100% B; 16.6 min, 0% B; and 20 min, 0% B.

Benzoylated amino acids were monitored in the positive ion mode with their specific Multiple Reaction Monitoring (MRM) transitions [71]. The instrument settings for nebulizer gas (Gas 1), turbogas (Gas 2), curtain gas, and collision gas were 50 psi, 70 psi, 40 psi, and medium, respectively. The interface heater was on, the Turbo V ESI source temperature was 500 °C, and the ionspray voltage was 5.5 kV. For all MRM transitions the values for declustering potential, entrance potential, and cell exit potential were 80 V, 10 V, and 10 V, respectively. The collision energies ranged from 10 to 30 V.

The LC chromatogram peaks of benzoylated endogenous amino acids and internal standards were integrated using the MultiQuant 3.0.2 software (SCIEX). The peak areas of the benzoylated endogenous amino acids were normalized to those of the internal standards.

4.27.4. Acylcarnitines

Acylcarnitines of isolated mouse heart mitochondria were derivatized to butyl esters and quantified by LC-ESI-MS/MS using a procedure previously described [72] with several modifications: To 50 μL of the extract prepared for the amino acid analysis (see above), 25 μL of an internal standard mixture, containing deuterated acylcarnitines (lyophilized Internal Standard MassChrom Amino Acids and Acylcarnitines from Dried Blood, Chromsystems, reconstituted in 2.5 mL, then 1:40 diluted), were added. The samples were dried under a stream of nitrogen and treated with 200 μL of freshly prepared derivatization solution (*n*-butanol/acetyl chloride 95:5 (*v/v*)). After incubation for 20 min at 60 °C in a ThermoMixer (Eppendorf) at 800 rpm, the samples were again dried under nitrogen. After addition of 100 μL of methanol/water 3:1 (v/v) and centrifugation (16,100 *g*, 5 min, 4 °C), 80 μL of supernatant were transferred to autoinjector vials.

LC-MS/MS analysis was performed using the Nexera X2 UHPLC and the QTRAP 6500 and by injection of 5 μL of sample onto the Kinetex C18 column described above. The LC column oven was operated at 40 °C, and the mobile phase of consisted of 2.5 mM ammonium acetate, 0.1% formic acid and 0.005% heptafluorobutyric acid (HBFA) in water (solvent A) and 2.5 mM ammonium acetate, 0.1% formic acid and 0.005% HBFA in acetonitrile/water 99:1 (v/v) (solvent B). Acylcarnitine butyl esters were eluted with the following gradient: initial, 15% B (0.6 ml/min); 0.7 min, 15% B; 13.6 min, 98% B; 16 min, 98% B (0.65 ml/min); 22.9 min, 98% B (0.6 ml/min); 23 min, 15% B; 28 min, 15% B.

Acylcarnitine butyl esters were monitored in the positive ion mode with their specific Multiple Reaction Monitoring (MRM) transitions [72]. The instrument settings for nebulizer gas (Gas 1), turbogas (Gas 2), curtain gas, and collision gas were 50 psi, 70 psi, 40 psi, and medium, respectively. The interface heater was on, the Turbo V ESI source temperature was 600 °C, and the ionspray voltage was 5.5 kV. For all MRM transitions the values for entrance potential and cell exit potential were 10 V and 15 V, respectively. The declustering potentials ranged from 40 to 110 V, and collision energies ranged from 18 to 70 V (Giesbertz et al.,

2015).

The LC chromatogram peaks of butyl esters of endogenous acylcarnitines and internal standards were integrated using the MultiQuant 3.0.2 software (SCIEX). The peak areas of the derivatized endogenous acylcarnitines were normalized to those of the internal standards.

4.27.5. Accession numbers

The mass spectrometry proteomics and metabolomics data have been deposited to the ProteomeXchange Consortium *via* the PRIDE partner repository with the dataset identifiers PXD020395 and PXD020469.

Supplementary data to this article can be found online at https://doi.org/10.1016/j.yjmcc.2021.01.010.

Author contributions

S.A., C.T., T.B., M.K. designed the experiments and analyzed results. S.A., F.L. performed biochemical sample preparation of phosphopeptides. H.N. performed statistical analysis of proteomics data. S.A., C.T., T.B. performed characterization of PERM1 and mass spectrometric analysis. N.S. performed immunofluorescence microscopy of C2C12 cells, helped with the molecular cloning of PERM1 and provided expert advice on mitochondrial proteins. P. H. assisted subcellular fractionation experiments, L.K., F.L. performed Lys6 incorporation analysis and calculated absolute half-lives. D.H.H. performed oxygraph analysis, E.R. performed electron microscopy analysis of mitochondria. S.B. performed lipidomics analysis, A.T., T.K. performed OXPHOS analysis and helped with data interpretation, T.L., T.B., J.B. provided guidance throughout the study. R.K.K. performed radioactive kinase assays. S.A. and M.K. wrote the manuscript and all authors read and approved the final version of the manuscript.

Acknowledgements

We acknowledge Sylvia Jeratsch, Lena Abraham and Christina Lucas for technical assistance and Kerstin Selbach for helpful comments on this manuscript. This work was supported by the Cologne Cluster of Excellence on Cellular Stress Responses in Ageing-associated Diseases (CECAD) EXC 299/2 and the Deutsche Forschungsgemeinschaft (DFG, German Research Fundation) SFB 1218 under project number 269925409.

References

[1] B.N. Puente, W. Kimura, S.A. Muralidhar, J. Moon, J.F. Amatruda, K.L. Phelps, D. Grinsfelder, B.A. Rothermel, R. Chen, J.A. Garcia, C.X. Santos, S. Thet, E. Mori, M.T. Kinter, P.M. Rindler, S. Zacchigna, S. Mukherjee, D.J. Chen, A.I. Mahmoud, M. Giacca, P.S. Rabinovitch, A. Aroumougame, A.M. Shah, L.I. Szweda, H.A. Sadek, The oxygen-rich postnatal environment induces cardiomyocyte cell-cycle arrest through DNA damage response, Cell 157 (3) (2014) 565–579.

[2] E.L. Huttlin, M.P. Jedrychowski, J.E. Elias, T. Goswami, R. Rad, S.A. Beausoleil, J. Villen, W. Haas, M.E. Sowa, S.P. Gygi, A tissue-specific atlas of mouse protein phosphorylation and expression, Cell 143 (7) (2010) 1174–1189.

[3] R.V. Raju, R. Kakkar, J.M. Radhi, R.K. Sharma, Biological significance of phosphorylation and myristoylation in the regulation of cardiac muscle proteins, Mol. Cell. Biochem. 176 (1–2) (1997) 135–143.

[4] M. Zarei, A. Sprenger, F. Metzger, C. Gretzmeier, J. Dengjel, Comparison of ERLIC-TiO2, HILIC-TiO2, and SCX-TiO2 for global phosphoproteomics approaches, J. Proteome Res. 10 (8) (2011) 3474–3483.

[5] A. Lundby, K. Lage, B.T. Weinert, D.B. Bekker-Jensen, A. Secher, T. Skovgaard, C. D. Kelstrup, A. Dmytriyev, C. Choudhary, C. Lundby, J.V. Olsen, Proteomic analysis of lysine acetylation sites in rat tissues reveals organ specificity and subcellular patterns, Cell Rep. 2 (2) (2012) 419–431.

[6] A. Lundby, M.N. Andersen, A.B. Steffensen, H. Horn, C.D. Kelstrup, C. Francavilla, L.J. Jensen, N. Schmitt, M.B. Thomsen, J.V. Olsen, In vivo phosphoproteomics analysis reveals the cardiac targets of beta-adrenergic receptor signaling, Sci. Signal. 6 (278) (2013) rs11.

[7] G.D. Lopaschuk, J.S. Jaswal, Energy metabolic phenotype of the cardiomyocyte during development, differentiation, and postnatal maturation, J. Cardiovasc. Pharmacol. 56 (2) (2010) 130–140.

[8] G.D. Lopaschuk, M.A. Spafford, D.R. Marsh, Glycolysis is predominant source of myocardial ATP production immediately after birth, Am. J. Phys. Heart Circ. Phys. 261 (6) (1991) H1698–H1705.

[9] L. Lai, T.C. Leone, C. Zechner, P.J. Schaeffer, S.M. Kelly, D.P. Flanagan, D. M. Medeiros, A. Kovacs, D.P. Kelly, Transcriptional coactivators PGC-1alpha and PGC-lbeta control overlapping programs required for perinatal maturation of the heart, Genes Dev. 22 (14) (2008) 1948–1961.

[10] Y. Cho, B.C. Hazen, A.P. Russell, A. Kralli, PGC-1 and ERR-induced Regulator in Muscle 1 (PERM1) is a tissue-specific regulator of oxidative capacity in skeletal muscle cells, J. Biol. Chem. 288 (35) (2013) 25207–25218, jbc. M113. 489674.

[11] F. Koser, C. Loescher, W.A. Linke, Posttranslational modifications of titin from cardiac muscle: how, where, and what for? FEBS J. 286 (12) (2019) 2240–2260.

[12] D.Z. Wang, S. Li, D. Hockemeyer, L. Sutherland, Z. Wang, G. Schratt, J. A. Richardson, A. Nordheim, E.N. Olson, Potentiation of serum response factor activity by a family of myocardin-related transcription factors, Proc. Natl. Acad. Sci. U. S. A. 99 (23) (2002) 14855–14860.

[13] E. Bassat, Y.E. Mutlak, A. Genzelinakh, I.Y. Shadrin, K. Baruch Umansky, O. Yifa, D. Kain, D. Rajchman, J. Leach, D. Riabov Bassat, Y. Udi, R. Sarig, I. Sagi, J. F. Martin, N. Bursac, S. Cohen, E. Tzahor, The extracellular matrix protein agrin promotes heart regeneration in mice, Nature 547 (7662) (2017) 179–184.

[14] Y. Yahalom-Ronen, D. Rajchman, R. Sarig, B. Geiger, E. Tzahor, Reduced matrix rigidity promotes neonatal cardiomyocyte dedifferentiation, proliferation and clonal expansion, Elife 4 (2015).

[15] D.J. Glass, D.C. Bowen, T.N. Stitt, C. Radziejewski, J. Bruno, T.E. Ryan, D.R. Gies, S. Shah, K. Mattsson, S.J. Burden, P.S. DiStefano, D.M. Valenzuela, T.M. DeChiara, G.D. Yancopoulos, Agrin acts via a MuSK receptor complex, Cell 85 (4) (1996) 513–523.

[16] G. Dobreva, T. Braun, The transcriptional landscape of regenerating newborn mouse hearts, Circ. Res. 116 (5) (2015) 767–769.

[17] M. Rechsteiner, S.W. Rogers, PEST sequences and regulation by proteolysis, Trends Biochem. Sci. 21 (7) (1996) 267–271.

[18] F. Meggio, L.A. Pinna, One-thousand-and-one substrates of protein kinase CK2? FASEB J. 17 (3) (2003) 349–368.

[19] S. Rogers, R. Wells, M. Rechsteiner, Amino acid sequences common to rapidly degraded proteins: the PEST hypothesis, Science 234 (4774) (1986) 364–368.

[20] M.M. Garcia-Alai, M. Gallo, M. Salame, D.E. Wetzler, A.A. McBride, M. Paci, D. O. Cicero, G. de Prat-Gay, Molecular basis for phosphorylation-dependent, PEST-mediated protein turnover, Structure 14 (2) (2006) 309–319.

[21] E.F. Fornasiero, S. Mandad, H. Wildhagen, M. Alevra, B. Rammner, S. Keihani, F. Opazo, I. Urban, T. Ischebeck, M.S. Sakib, M.K. Fard, K. Kirli, T.P. Centeno, R. O. Vidal, R.U. Rahman, E. Benito, A. Fischer, S. Dennerlein, P. Rehling, I. Feussner, S. Bonn, M. Simons, H. Urlaub, S.O. Rizzoli, Precisely measured protein lifetimes in the mouse brain reveal differences across tissues and subcellular fractions, Nat. Commun. 9 (1) (2018) 4230.

[22] F. Lang, S. Aravamudhan, H. Nolte, C. Turk, S. Holper, S. Muller, S. Gunther, B. Blaauw, T. Braun, M. Kruger, Dynamic changes in the mouse skeletal muscle proteome during denervation-induced atrophy, Dis. Model. Mech. 10 (7) (2017) 881–896.

[23] Y. Cho, B.C. Hazen, P.G. Gandra, S.R. Ward, S. Schenk, A.P. Russell, A. Kralli, Perm1 enhances mitochondrial biogenesis, oxidative capacity, and fatigue resistance in adult skeletal muscle, FASEB J. 30 (2) (2016) 674–687.

[24] M. Schild, A. Ruhs, T. Beiter, M. Zugel, J. Hudemann, A. Reimer, I. Krumholz-Wagner, C. Wagner, J. Keller, K. Eder, K. Kruger, M. Kruger, T. Braun, A. Niess, J. Steinacker, F.C. Mooren, Basal and exercise induced label-free quantitative protein profiling of m. vastus lateralis in trained and untrained individuals, J. Proteome 122 (2015) 119–132.

[25] Y. Cho, S. Tachibana, B.C. Hazen, J.J. Moresco, J.R. Yates 3rd, B. Kok, E. Saez, R. S. Ross, A.P. Russell, A. Kralli, Perm1 regulates CaMKII activation and shapes skeletal muscle responses to endurance exercise training, Mol Metab 23 (2019) 88–97.

[26] H.C. Rundqvist, A. Montelius, T. Osterlund, B. Norman, M. Esbjornsson, E. Jansson, Acute sprint exercise transcriptome in human skeletal muscle, PLoS One 14 (10) (2019), e0223024.

[27] C. Brinkmann, A. Kuckertz, T. Schiffer, W. Bloch, H.G. Predel, K. Brixius, Endurance training alters YKL40, PERM1, and HSP70 skeletal muscle protein contents in men with type 2 diabetes mellitus, Endocr. Res. 44 (1–2) (2019) 1–8.

[28] K. Reue, P. Xu, X.P. Wang, B.G. Slavin, Adipose tissue deficiency, glucose intolerance, and increased atherosclerosis result from mutation in the mouse fatty liver dystrophy (fld) gene, J. Lipid Res. 41 (7) (2000) 1067–1076.

[29] M.S. Mitra, J.D. Schilling, X. Wang, P.Y. Jay, J.M. Huss, X. Su, B.N. Finck, Cardiac lipin 1 expression is regulated by the peroxisome proliferator activated receptor gamma coactivator 1alpha/estrogen related receptor axis, J. Mol. Cell. Cardiol. 51 (1) (2011) 120–128.

[30] B.N. Finck, M.C. Gropler, Z. Chen, T.C. Leone, M.A. Croce, T.E. Harris, J. C. Lawrence Jr., D.P. Kelly, Lipin 1 is an inducible amplifier of the hepatic PGC-1alpha/PPARalpha regulatory pathway, Cell Metab. 4 (3) (2006) 199–210.

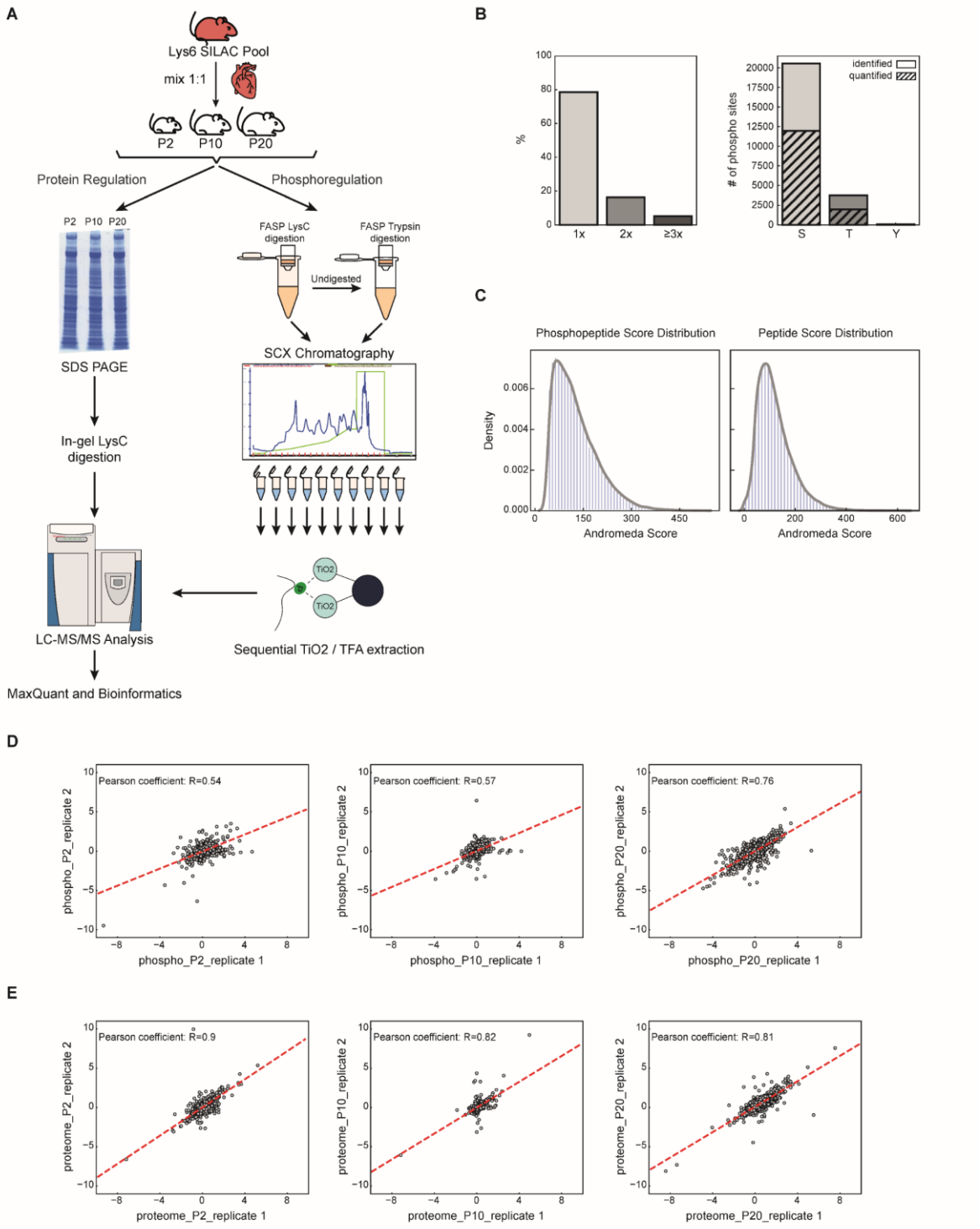
[31] L. Lin, S.W. Yee, R.B. Kim, K.M. Giacomini, SLC transporters as therapeutic targets: emerging opportunities, Nat. Rev. Drug Discov. 14 (8) (2015) 543–560.

[32] V. Porcelli, G. Fiermonte, A. Longo, F. Palmieri, The human gene SLC25A29, of solute carrier family 25, encodes a mitochondrial transporter of basic amino acids, J. Biol. Chem. 289 (19) (2014) 13374–13384.

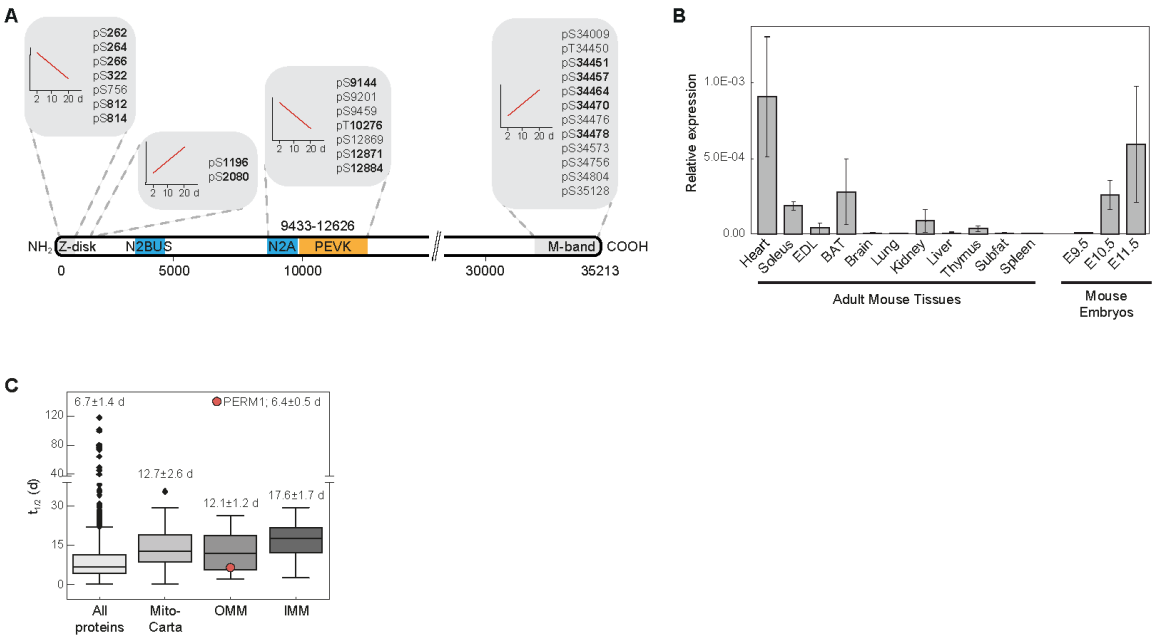
[33] L. Palmieri, A. Vozza, G. Agrimi, V. De Marco, M.J. Runswick, F. Palmieri, J. E. Walker, Identification of the yeast mitochondrial transporter for oxaloacetate and sulfate, J. Biol. Chem. 274 (32) (1999) 22184–22190.

[34] J.L. Pohjoismaki, M. Kruger, N. Al-Furoukh, A. Lagerstedt, P.J. Karhunen, T. Braun, Postnatal cardiomyocyte growth and mitochondrial reorganization cause multiple

changes in the proteome of human cardiomyocytes, Mol. BioSyst. 9 (6) (2013) 1210–1219.
[35] J. Piquereau, M. Novotova, D. Fortin, A. Garnier, R. Ventura-Clapier, V. Veksler, F. Joubert, Postnatal development of mouse heart: formation of energetic microdomains, J. Physiol. 588 (Pt 13) (2010) 2443–2454.
[36] K. Wei, V. Serpooshan, C. Hurtado, M. Diez-Cunado, M. Zhao, S. Maruyama, W. Zhu, G. Fajardo, M. Noseda, K. Nakamura, X. Tian, Q. Liu, A. Wang, Y. Matsuura, P. Bushway, W. Cai, A. Savchenko, M. Mahmoudi, M.D. Schneider, M. J. van den Hoff, M.J. Butte, P.C. Yang, K. Walsh, B. Zhou, D. Bernstein, M. Mercola, P. Ruiz-Lozano, Epicardial FSTL1 reconstitution regenerates the adult mammalian heart, Nature 525 (7570) (2015) 479–485.
[37] S.I. Oka, A.D. Sabry, A.K. Horiuchi, K.M. Cawley, S.A. O'Very, M.A. Zaitsev, T. S. Shankar, J. Byun, R. Mukai, X. Xu, N.S. Torres, A. Kumar, M. Yazawa, J. Ling, I. Taleb, Y. Saijoh, S.G. Drakos, J. Sadoshima, J.S. Warren, Perm1 regulates cardiac energetics as a downstream target of the histone methyltransferase Smyd1, PLoS One 15 (6) (2020), e0234913.
[38] J. Lavie, H. De Belvalet, S. Sonon, A.M. Ion, E. Dumon, S. Melser, D. Lacombe, J. W. Dupuy, C. Lalou, G. Benard, Ubiquitin-dependent degradation of mitochondrial proteins regulates energy metabolism, Cell Rep. 23 (10) (2018) 2852–2863.
[39] P. Bragoszewski, M. Turek, A. Chacinska, Control of mitochondrial biogenesis and function by the ubiquitin-proteasome system, Open Biol. 7 (4) (2017).
[40] Y. Cho, B.C. Hazen, A.P. Russell, A. Kralli, Peroxisome proliferator-activated receptor gamma coactivator 1 (PGC-1)- and estrogen-related receptor (ERR)-induced regulator in muscle 1 (Perm1) is a tissue-specific regulator of oxidative capacity in skeletal muscle cells, J. Biol. Chem. 288 (35) (2013) 25207–25218.
[41] M. Peterfy, J. Phan, G.M. Oswell, P. Xu, K. Reue, Genetic, physical, and transcript map of the fld region on mouse chromosome 12, Genomics 62 (3) (1999) 436–444.
[42] G.G. Schweitzer, S.L. Collier, Z. Chen, J.M. Eaton, A.M. Connolly, R.C. Bucelli, A. Pestronk, T.E. Harris, B.N. Finck, Rhabdomyolysis-associated mutations in human LPIN1 Lead to loss of phosphatidic acid Phosphohydrolase activity, JIMD Rep 23 (2015) 113–122.
[43] A. Zeharia, A. Shaag, R.H. Houtkooper, T. Hindi, P. de Lonlay, G. Erez, L. Hubert, A. Saada, Y. de Keyzer, G. Eshel, F.M. Vaz, O. Pines, O. Elpeleg, Mutations in LPIN1 cause recurrent acute myoglobinuria in childhood, Am. J. Hum. Genet. 83 (4) (2008) 489–494.
[44] P. Zhang, M.A. Verity, K. Reue, Lipin-1 regulates autophagy clearance and intersects with statin drug effects in skeletal muscle, Cell Metab. 20 (2) (2014) 267–279.
[45] A. Buerger, O. Rozhitskaya, M.C. Sherwood, A.L. Dorfman, E. Bisping, E.D. Abel, W.T. Pu, S. Izumo, P.Y. Jay, Dilated cardiomyopathy resulting from high-level myocardial expression of Cre-recombinase, J. Card. Fail. 12 (5) (2006) 392–398.
[46] T. Rashid, I. Nemazanyy, C. Paolini, T. Tatsuta, P. Crespin, D. de Villeneuve, S. Brodesser, P. Benit, P. Rustin, M.A. Baraibar, O. Agbulut, A. Olivier, F. Protasi, T. Langer, R. Chrast, P. de Lonlay, H. de Foucauld, B. Blaauw, M. Pende, Lipin1 deficiency causes sarcoplasmic reticulum stress and chaperone-responsive myopathy, EMBO J. 38 (1) (2019).
[47] T.R. Peterson, S.S. Sengupta, T.E. Harris, A.E. Carmack, S.A. Kang, E. Balderas, D. A. Guertin, K.L. Madden, A.E. Carpenter, B.N. Finck, D.M. Sabatini, mTOR complex 1 regulates lipin 1 localization to control the SREBP pathway, Cell 146 (3) (2011) 408–420.
[48] J.J. Ruprecht, E.R.S. Kunji, The SLC25 mitochondrial carrier family: structure and mechanism, Trends Biochem. Sci. 45 (3) (2020) 244–258.
[49] C. Thangaratnarajah, J.J. Ruprecht, E.R. Kunji, Calcium-induced conformational changes of the regulatory domain of human mitochondrial aspartate/glutamate carriers, Nat. Commun. 5 (2014) 5491.
[50] H. Yoon, Y. Zhang, J. Pain, E.R. Lyver, E. Lesuisse, D. Pain, A. Dancis, Rim2, a pyrimidine nucleotide exchanger, is needed for iron utilization in mitochondria, Biochem. J. 440 (1) (2011) 137–146.
[51] H. Beinert, R.H. Holm, E. Munck, Iron-sulfur clusters: nature's modular, multipurpose structures, Science 277 (5326) (1997) 653–659.
[52] S.E. Wiley, A.N. Murphy, S.A. Ross, P. van der Geer, J.E. Dixon, MitoNEET is an iron-containing outer mitochondrial membrane protein that regulates oxidative capacity, Proc. Natl. Acad. Sci. U. S. A. 104 (13) (2007) 5318–5323.
[53] M. Krüger, M. Moser, S. Ussar, I. Thievessen, C.A. Luber, F. Forner, S. Schmidt, S. Zanivan, R. Fässler, M. Mann, SILAC mouse for quantitative proteomics uncovers kindlin-3 as an essential factor for red blood cell function, Cell 134 (2) (2008) 353–364.
[54] A. Shevchenko, H. Tomas, J. Havlis, J.V. Olsen, M. Mann, In-gel digestion for mass spectrometric characterization of proteins and proteomes, Nat. Protoc. 1 (6) (2006) 2856–2860.
[55] J. Rappsilber, M. Mann, Y. Ishihama, Protocol for micro-purification, enrichment, pre-fractionation and storage of peptides for proteomics using StageTips, Nat. Protoc. 2 (8) (2007) 1896–1906.
[56] J.R. Wisniewski, A. Zougman, N. Nagaraj, M. Mann, Universal sample preparation method for proteome analysis, Nat. Methods 6 (5) (2009) 359–362.
[57] J. Cox, M. Mann, MaxQuant enables high peptide identification rates, individualized p.p.b.-range mass accuracies and proteome-wide protein quantification, Nat. Biotechnol. 26 (12) (2008) 1367–1372.
[58] J. Cox, N. Neuhauser, A. Michalski, R.A. Scheltema, J.V. Olsen, M. Mann, Andromeda: a peptide search engine integrated into the MaxQuant environment, J. Proteome Res. 10 (4) (2011) 1794–1805.
[59] V.G. Tusher, R. Tibshirani, G. Chu, Significance analysis of microarrays applied to the ionizing radiation response, Proc. Natl. Acad. Sci. U. S. A. 98 (9) (2001) 5116–5121.
[60] H. Nolte, T.D. MacVicar, F. Tellkamp, M. Kruger, Instant clue: a software suite for interactive data visualization and analysis, Sci. Rep. 8 (1) (2018) 12648.
[61] Y. Nemoto, P. De Camilli, Recruitment of an alternatively spliced form of synaptojanin 2 to mitochondria by the interaction with the PDZ domain of a mitochondrial outer membrane protein, EMBO J. 18 (11) (1999) 2991–3006.
[62] J.L. Pohjoismäki, S. Goffart, H. Tyynismaa, S. Willcox, T. Ide, D. Kang, A. Suomalainen, P.J. Karhunen, J.D. Griffith, I.J. Holt, Human heart mitochondrial DNA is organized in complex catenated networks containing abundant four-way junctions and replication forks, J. Biol. Chem. 284 (32) (2009) 21446–21457.
[63] Y. Fujiki, A.L. Hubbard, S. Fowler, P.B. Lazarow, Isolation of intracellular membranes by means of sodium carbonate treatment: application to endoplasmic reticulum, J. Cell Biol. 93 (1) (1982) 97–102.
[64] V. Kozjak-Pavlovic, F. Prell, B. Thiede, M. Götz, D. Wosiek, C. Ott, T. Rudel, C1orf163/RESA1 is a novel mitochondrial intermembrane space protein connected to respiratory chain assembly, J. Mol. Biol. 426 (4) (2014) 908–920.
[65] H. Lörchner, J. Pöling, P. Gajawada, Y. Hou, V. Polyakova, S. Kostin, J.M. Adrian-Segarra, T. Boettger, A. Wietelmann, H. Warnecke, Myocardial healing requires Reg3 [beta]-dependent accumulation of macrophages in the ischemic heart, Nat. Med. 21 (4) (2015) 353–362.
[66] C.A. Schneider, W.S. Rasband, K.W. Eliceiri, NIH image to ImageJ: 25 years of image analysis, Nat. Methods 9 (7) (2012) 671–675.
[67] C. Becker, A. Kukat, K. Szczepanowska, S. Hermans, K. Senft, C.P. Brandscheid, P. Maiti, A. Trifunovic, CLPP deficiency protects against metabolic syndrome but hinders adaptive thermogenesis, EMBO Rep. 19 (5) (2018), e45126.
[68] I. Wittig, H.P. Braun, H. Schagger, Blue native PAGE, Nat. Protoc. 1 (1) (2006) 418–428.
[69] V. Kumar, J.E. Bouameur, J. Bar, R.H. Rice, H.T. Hornig-Do, D.R. Roop, N. Schwarz, S. Brodesser, S. Thiering, R.E. Leube, R.J. Wiesner, P. Vijayaraj, C. B. Brazel, S. Heller, H. Binder, H. Loffler-Wirth, P. Seibel, T.M. Magin, A keratin scaffold regulates epidermal barrier formation, mitochondrial lipid composition, and activity, J. Cell Biol. 211 (5) (2015) 1057–1075.
[70] M. Schwaiger, E. Rampler, G. Hermann, W. Miklos, W. Berger, G. Koellensperger, Anion-exchange chromatography coupled to high-resolution mass spectrometry: a powerful tool for merging targeted and non-targeted metabolomics, Anal. Chem. 89 (14) (2017) 7667–7674.
[71] J.M. Wong, P.A. Malec, O.S. Mabrouk, J. Ro, M. Dus, R.T. Kennedy, Benzoyl chloride derivatization with liquid chromatography-mass spectrometry for targeted metabolomics of neurochemicals in biological samples, J. Chromatogr. A 1446 (2016) 78–90.
[72] P. Giesbertz, J. Ecker, A. Haag, B. Spanier, H. Daniel, An LC-MS/MS method to quantify acylcarnitine species including isomeric and odd-numbered forms in plasma and tissues, J. Lipid Res. 56 (10) (2015) 2029–2039.

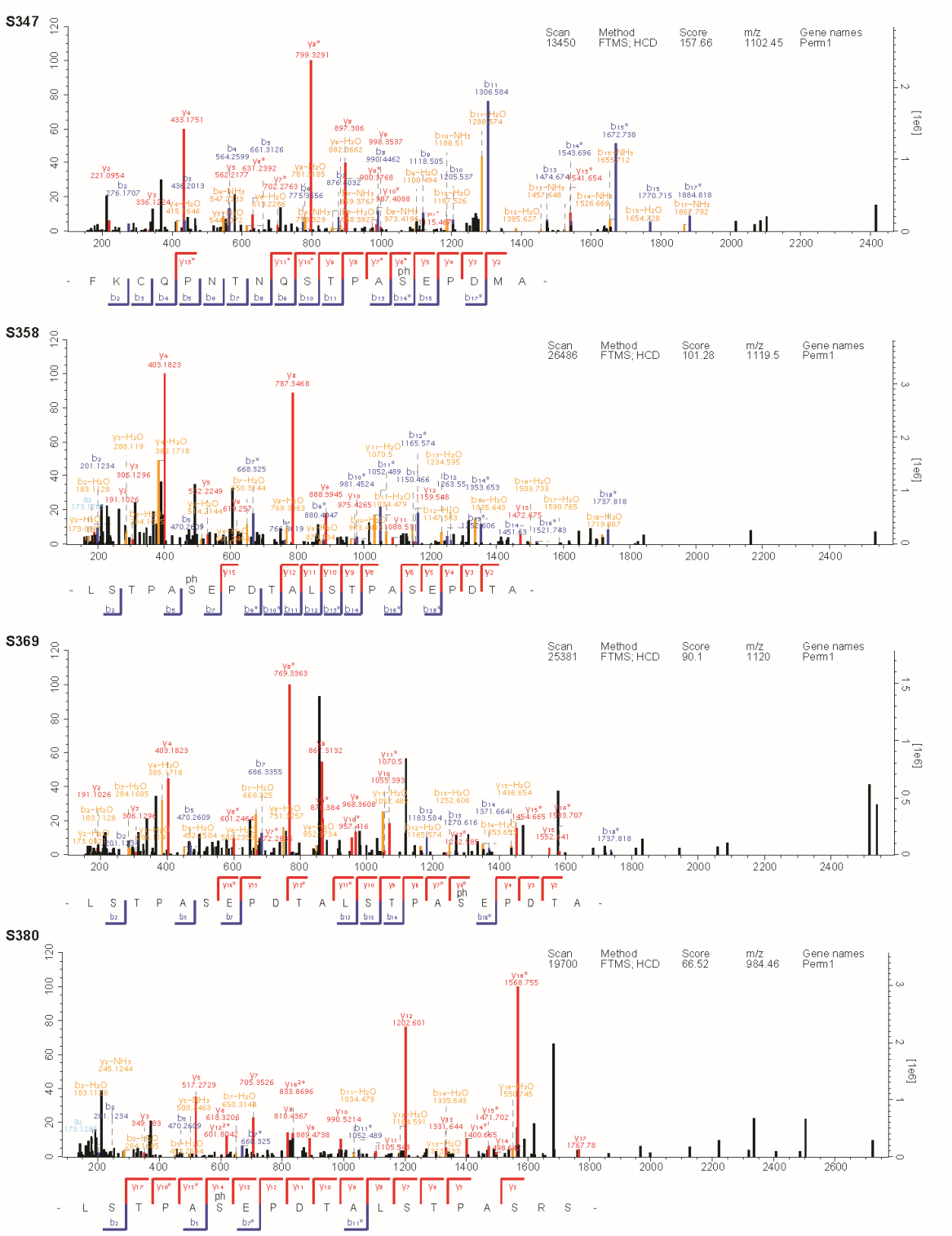


Supplementary Fig. S1. Further parameters of phosphopeptide and proteome analysis during post-natal heart development. (A) Detailed overview of experimental strategy to determine phosphorylation and protein regulation in post-natal hearts. Neonatal hearts from non-labelled mice isolated 2 (P2), 10 (P10), and 20 (P20) days after birth were mixed 1:1 with age-matched hearts from Lys6(13C6-Lysine)-labelled SILAC mice as a spike-in standard. For proteomic analysis, samples were in-gel digested with LysC. For phosphoproteomic analysis, samples were processed by the Filter-aided sample preparation (FASP) method, fractionated by Strong Cation Exchange Chromatography (SCX), and phosphopeptides were enriched using TiO2 beads. (B) Bar diagrams visualizing (left) the relative amount of mono- (1×), di- (2×), and poly- (≥ 3×) phosphorylated sites and (right) the number identified and quantified phosphosites containing serine (S), threonine (T), and tyrosine (Y). (C) Density plots of Andromeda score distribution for phosphorylated and unmodified peptides. (D + E) Pearson correlation of the biological duplicates for the phosphopeptide (D) and proteomic (E) analysis.

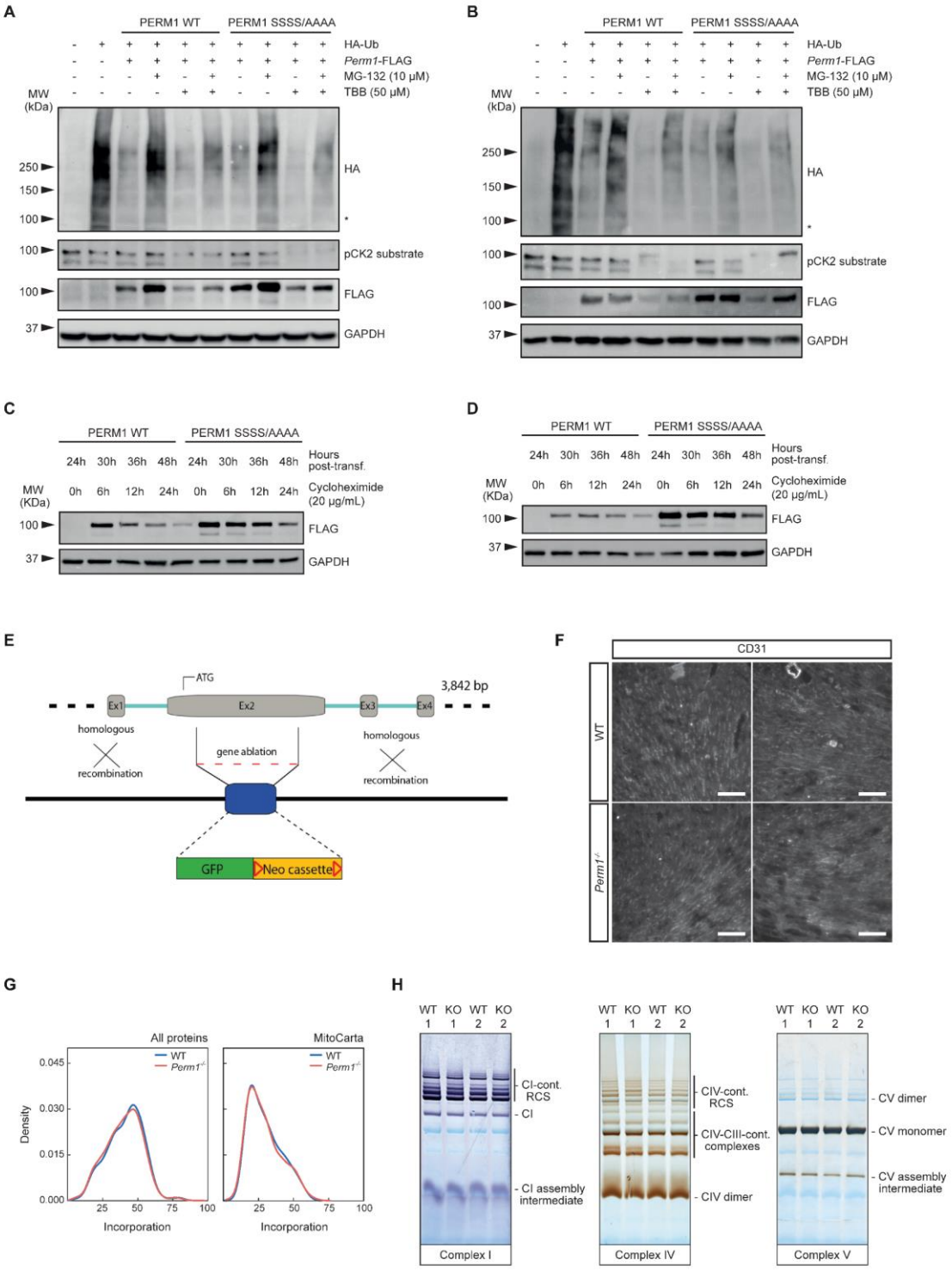


Supplementary Fig. S2. Regulation of Titin phosphorylation and organ-wide expression of PERM1. (A) Sequence landscape of Titin, including *Z*-disk, N2BUS, N2A, PEVK, and M-band regions, depicting differential phosphosite regulation during post-natal development. Sites in bold letters are significantly regulated (cut-off set to FDR 0.05 and a fold-change >1.5). (B) qPCR analysis confirming the presence of *Perm1* in contractile tissues and upregulation of *Perm1* during embryonic development. (C) Comparison of the protein half-lives of all proteins, mitochondrial proteins, OMM, and IMM proteins based on their Lys6-incorporation rates in the heart tissue of wild-type mice fed a SILAC diet for 7, 14, and 28 days. Values are mean ± 0.95 CI (*n* = 3).

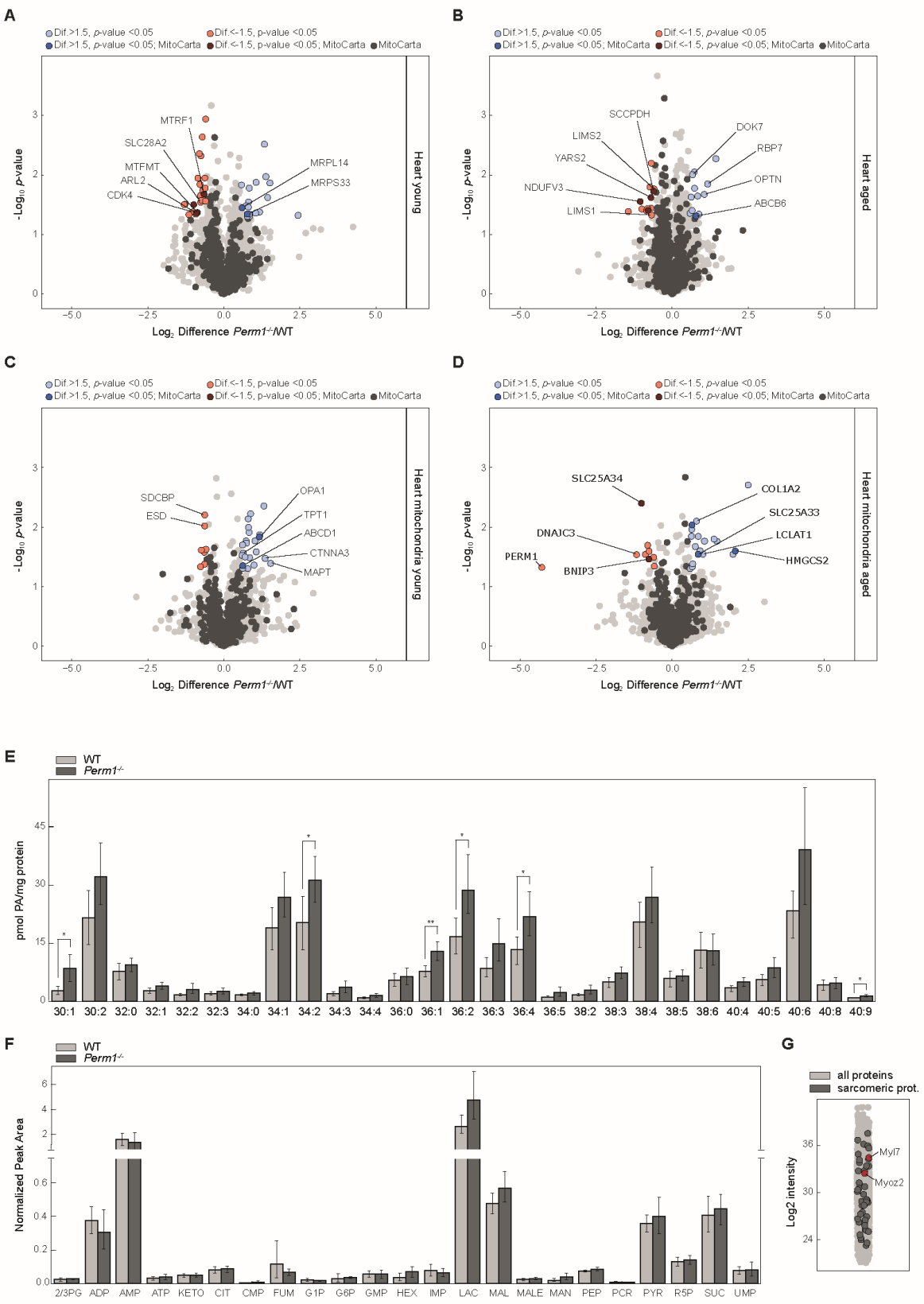
OMM (outer mitochondrial membrane); IMM (inner mitochondrial membrane).



Supplementary Fig. S3. Phosphorylation within the PEST motif of PERM1. MS/MS spectra of CK2- dependent phosphosites within the 56-amino acid PEST motif of PERM1 obtained by digestion with the unspecific protease elastase.



Supplementary Fig. S4. Generation and characterization of PERM1 PEST regulation and *Perm1*$^{-/-}$ mice. (A + B) Western blot replicates used for quantification of ubiquitination assay shown in Fig. 4E (n = 3). (C + D) Western blot replicates used for quantification of cycloheximide treatment shown in Fig. 4F (n = 3). (E) Scheme used to generate *Perm1* knock-out mice by homologous recombination. The coding region of *Perm1* in exon 2 was replaced by a GFP cassette. (F) Immunohistochemical staining for CD31/PECAM of mouse heart cross sections showed no differences between *Perm1*$^{-/-}$ mice and wild-type mice. Scale, 100 µm. (G) Density plot of Lys6-incorporation rates of MitoCarta 2.0 proteins and the complete dataset of brain tissue from *Perm1*$^{-/-}$ and wild-type mice after feeding mice a SILAC diet for 14 days. Equal labelling of proteins was observed in *Perm1*$^{-/-}$ and wild-type mice (n = 3 mice per group). (H) In-gel activity assay of crude heart mitochondria separated on a BN-PAGE indicated no difference in activity of respiratory chain complexes I, IV, and V between *Perm1*$^{-/-}$ mice and wild-type mice (RCS; respiratory chain super complexes).


A
B
C
D
E
F
G
Dif.>1.5, p-value <0.05
Dif.<-1.5, p-value <0.05
Dif.>1.5, p-value <0.05; MitoCarta
Dif.<-1.5, p-value <0.05; MitoCarta
MitoCarta
-Log10 p-value
Log2 Difference Perm1-/-/WT
Heart young
Heart aged
Heart mitochondria young
Heart mitochondria aged
MTRF1
SLC28A2
MTFMT
ARL2
CDK4
MRPL14
MRPS33
SCCPDH
LIMS2
YARS2
NDUFV3
LIMS1
DOK7
RBP7
OPTN
ABCB6
SDCBP
ESD
OPA1
TPT1
ABCD1
CTNNA3
MAPT
SLC25A34
DNAJC3
PERM1
BNIP3
COL1A2
SLC25A33
LCLAT1
HMGCS2
WT
Perm1-/-
pmol PA/mg protein
30:1 30:2 32:0 32:1 32:2 32:3 34:0 34:1 34:2 34:3 34:4 36:0 36:1 36:2 36:3 36:4 36:5 38:2 38:3 38:4 38:5 38:6 40:4 40:5 40:6 40:8 40:9
Normalized Peak Area
2/3PG ADP AMP ATP KETO CIT CMP FUM G1P G6P GMP HEX IMP LAC MAL MALE MAN PEP PCR PYR R5P SUC UMP
all proteins
sarcomeric prot.
Log2 intensity
Myl7
Myoz2

Supplementary Fig. S5. Proteomic analyses, metabolomics and sarcomeric proteins in *Perm1*-deficient hearts. (A-D) Volcano plot depicting significantly regulated proteins in *Perm1*$^{-/-}$ (A + B) heart tissue and heart mitochondria isolated (C + D) from 3-month-old (A + C) and 24-month-old (B + D) mice compared to wild-type mice (heart young *n* = 4 mice per group; heart aged *n* = 2 mice per group; mitochondria young *n* = 5 mice per group; mitochondria aged *n* = 3 mice per group). Cut-off was set to $p < 0.05$ and a fold change >1.5. Darker colours indicate the MitoCarta 2.0 annotations. (E) Phospholipidomic analysis PA species of *Perm1*$^{-/-}$ and wild-type hearts, showing overall enhanced amount of all PA species. Values are normalized to the protein content of *Perm1*$^{-/-}$ and control hearts (*n* = 8 mice per group). (F) Peak areas of anionic metabolites measured in mitochondria isolated from *Perm1*$^{-/-}$ and wild-type hearts. Peak areas were normalized to internal standards (*n* = 6 mice per group). Abbreviations are defined in SI Table S6. (G) Gitter plot depicting overall $\log_2$ intensities of all proteins and sarcomeric proteins in the heart tissues of *Perm1*−/− and wild-type mice at 11 pm; only unique peptides were considered in the analysis.

Data are mean ± 0.95 CI. * and ** $p < 0.05$ and 0.01, respectively, Welch's t-test.

Publication II: PERM1 interacts with the MICOS-MIB complex to connect the mitochondria and sarcolemma via ankyrin B.

nature COMMUNICATIONS

ARTICLE

https://doi.org/10.1038/s41467-021-25185-3 OPEN

PERM1 interacts with the MICOS-MIB complex to connect the mitochondria and sarcolemma via ankyrin B

Theresa Bock[1,8], Clara Türk[2,8], Sriram Aravamudhan[3], Lena Keufgens[1], Wilhelm Bloch[4], Dieu Hien Rozsivalova[1], Vanina Romanello[5], Leonardo Nogara[5], Bert Blaauw[5], Aleksandra Trifunovic[1,6], Thomas Braun[7] & Marcus Krüger[1,6]✉

Skeletal muscle subsarcolemmal mitochondria (SSM) and intermyofibrillar mitochondria subpopulations have distinct metabolic activity and sensitivity, though the mechanisms that localize SSM to peripheral areas of muscle fibers are poorly understood. A protein interaction study and complexome profiling identifies PERM1 interacts with the MICOS-MIB complex. Ablation of *Perm1* in mice reduces muscle force, decreases mitochondrial membrane potential and complex I activity, and reduces the numbers of SSM in skeletal muscle. We demonstrate PERM1 interacts with the intracellular adaptor protein ankyrin B (ANKB) that connects the cytoskeleton to the plasma membrane. Moreover, we identify a C-terminal transmembrane helix that anchors PERM1 into the outer mitochondrial membrane. We conclude PERM1 functions in the MICOS-MIB complex and acts as an adapter to connect the mitochondria with the sarcolemma via ANKB.

[1] Institute for Genetics, Cologne Excellence Cluster on Cellular Stress Responses in Aging-Associated Diseases (CECAD), Cologne, Germany. [2] BASF SE, Metabolomics and Proteomics, Ludwigshafen am Rhein, Germany. [3] Cell Signaling Technology, Leiden, Netherlands. [4] Department of Molecular and Cellular Sport Medicine, Institute of Sport Medicine and Cardiovascular Research, German Sport University Cologne, Cologne, Germany. [5] Venetian Institute of Molecular Medicine (VIMM), Department of Biomedical Sciences Padova, University of Padova, Padova, Italy. [6] Center for Molecular Medicine (CMMC), University of Cologne, Cologne, Germany. [7] Max Planck Institute for Heart and Lung Research, Bad Nauheim, Germany. [8] These authors contributed equally: Theresa Bock, Clara Türk. ✉email: marcus.krueger@uni-koeln.de

Skeletal muscle possesses remarkable plasticity and can rapidly adapt to environmental factors such as workload, nutrient supply and neuronal stimulation[1]. For example, physical activity increases the number of mitochondria and their oxidative capacity. Moreover, muscle activity improves the regeneration of damaged muscles and promotes vascularization of the skeletal muscles[2]. Previous studies revealed two mitochondrial subpopulations: subsarcolemmal mitochondria (SSM), located below the sarcolemmal membrane, and interfibrillar mitochondria (IFM), situated between myofibrils[3]. IFM are smaller and have a more compact shape, while SSM are larger and own a lamellar structure. High-resolution electron microscopy revealed the existence of additional mitochondrial subpopulations[4], which may also differ in their protein composition, respiration, and sensitivity to metabolic changes[5]. Studies of cardiac mitochondria demonstrated that SSM are more susceptible to cellular stress, such as ischemic injury and calcium overload, than IFM[6]. However, the mechanisms that determine the position and regulate the activity of different mitochondrial subpopulations remain largely unknown.

Activation of mitochondrial gene expression depends on the key transcriptional coactivators peroxisome proliferator-activated receptor γ coactivator 1α (PGC-1α) and the estrogen-related receptor α (ERRα)[7]. Enhanced muscle workload upregulates PGC-1α activity and promotes mitochondrial biogenesis[8]. Conversely, loss of function of PGC-1α results in defects in cardiac and skeletal muscle energetics and causes cardiomyopathy[9]. Similarly, muscle workload increases the intracellular calcium ion concentration and activates the Ca^{2+}/calmodulin-dependent protein kinase II (CaMKII) and protein kinase p38. Activation of this cascade increases PGC-1α protein expression and mitochondrial biogenesis[10]. Additionally, PGC-1α-dependent transcription factors, such as CREB and MEF2, are activated via a feed-forward loop[11]. PGC-1- and ERR-induced regulator in muscle 1 (PERM1) was recently identified to regulate the expression of PGC-1α and ERRα targets to enhance mitochondrial biogenesis and adaptive oxidative metabolism in skeletal muscle[12]. PERM1 protein expression is mainly restricted to heart and skeletal muscle, indicating PERM1 functions as a tissue-specific regulator of mitochondrial biogenesis in response to exercise. *Perm1* loss- and gain-of-function experiments in cell culture[12] and adenoviral-mediated overexpression in mouse muscles revealed that PERM1 regulates muscle-related pathways modulating muscle contraction, vascularization and metabolic activity[13].

PERM1 has been detected in the nucleus and the cytosol[12] but also in the outer mitochondrial membrane (OMM)[14]. Casein kinase (CK2)-mediated phosphorylation of the PEST motif leads to degradation of PERM1[14]. However, little is known about the mechanisms by which PERM1 increases oxidative capacity and mitochondrial biogenesis. A previous study showed that PERM1 interacts with CaMKII and induced phosphorylation of p38[15]. In addition, PERM1 regulates *Gadd45g* and *Nr4A3*, possibly also through CaMKII, which are involved in the control of exercise-responsive gene expression and oxidative capacity.

The mitochondrial contact site and cristae organizing system (MICOS) complex is involved in the regulation of mitochondrial metabolic activity[16] and plays an important role for the organization of the inner mitochondrial membrane (IMM) and cristae formation. It is composed of MIC10 (MINOS1), MIC13 (QIL1), MIC19 (CHCHD3), MIC25 (CHCHD6), MIC26 (APOO), MIC27 (APOOL) and MIC60 (Mitofilin; IMMT)[17–20]. The MICOS core complex localizes to the inner mitochondrial membrane and closely interacts with the proteins that form the mitochondrial intermembrane space bridging (MIB) complex, which connects the inner and outer mitochondrial membrane. The MIB complex partially localizes in the OMM, thereby constituting the sorting and assembly machinery (SAM), which associates with other OMM proteins, such as channel proteins, components of the protein translocases, and mitochondrial fusion machines. Notably, MIC60, a central subunit of the MICOS complex, interacts with all known MICOS and MIB members. Depletion of MIC60 leads to a severe loss of cristae structures and reduced oxidative capacity[21]. Moreover, the stability of the MICOS–MIB complex is directly connected to biogenesis and assembly of respiratory chain complexes. For example, SAM50 is a critical stabilizing protein of the MIB complex responsible for protein transport, assembly of respiratory chain complexes and regulation of cristae integrity[22].

In this study, we demonstrate that genetic ablation of *Perm1* in mice reduces the number of mitochondria in peripheral areas of muscle fibers, which compromises running capacity and skeletal muscle force production. Comprehensive mass spectrometry-based mapping of protein-protein interactions revealed that PERM1 interacts with several members of the MICOS–MIB complex and cytoskeletal adaptor proteins such as vimentin and ankyrin B. Native gel electrophoresis in combination with mass spectrometry demonstrated PERM1 co-migrated with the mature MICOS–MIB complex at 2.2 MDa. Moreover, deletion of a predicted transmembrane helix in the C-terminus of PERM1 led to specific loss of the interaction with MICOS-MIB proteins.

Results

Deletion of *Perm1* reduces muscle force without morphometric changes in skeletal muscle architecture. To gain further insight into the physiological role of PERM1, we ablated *Perm1* in the mouse by replacing the coding region of exon 2 with a GFP cassette as described in[14]. Successful deletion of *Perm1* was confirmed by immunoblotting (Fig. 1a). $Perm1^{-/-}$ mice are viable and fertile without obvious changes in body and muscle weight. Hematoxylin and eosin staining showed no obvious changes in $Perm1^{-/-}$ muscle fibers (SI Fig. 1a). Immunostaining using antibodies directed against PERM1 and the heavy myosin chains (*Myh7, Myh2*) demonstrated that PERM1 is enriched within the subsarcolemmal regions in type IIa fibers, which contain higher numbers of mitochondria compared to slow type I and fast type IIb fibers. (SI Fig. 1b). Notably, the abundance of PERM1 correlated with the abundance of PCG-1α, which is highest in type IIa muscle fibers[23]. Detailed morphometric analysis of various fiber types in tibialis anterior (TA), extensor digitorum longus (EDL), and soleus muscle revealed no obvious fiber-type switches or changes in fiber diameter (SI Fig. 1c). Immunohistochemical staining using a CD31/PECAM1 antibody did not reveal any obvious alterations in the vascularization of $Perm1^{-/-}$ skeletal muscles (SI Fig. 1d).

Next, we subjected $Perm1^{-/-}$ and wild-type control littermates to forced running experiments and tested muscle strength. Treadmill exercise with increasing speed revealed no differences between mutants and wild-type controls up to moderate velocity of 12 m/min (Fig. 1b). However, $Perm1^{-/-}$ mutants did not withstand 16 m/min for two minutes, while 70% of control mice endured this stress for two minutes. The respiratory exchange ratio (RER) was not altered between $Perm1^{-/-}$ and control animals, indicating no significant changes in fuel sources (Fig. 1c). Assessment of limb muscle performance using an inverted screen test revealed a significantly shorter hold time for $Perm1^{-/-}$ mutants compared to wild-type controls (Fig. 1d). In another muscle strength test, mice were lifted by the tail and given a fine-meshed net supplemented with a range of weights. $Perm1^{-/-}$ mice had significantly reduced ability to carry weights from 59 g

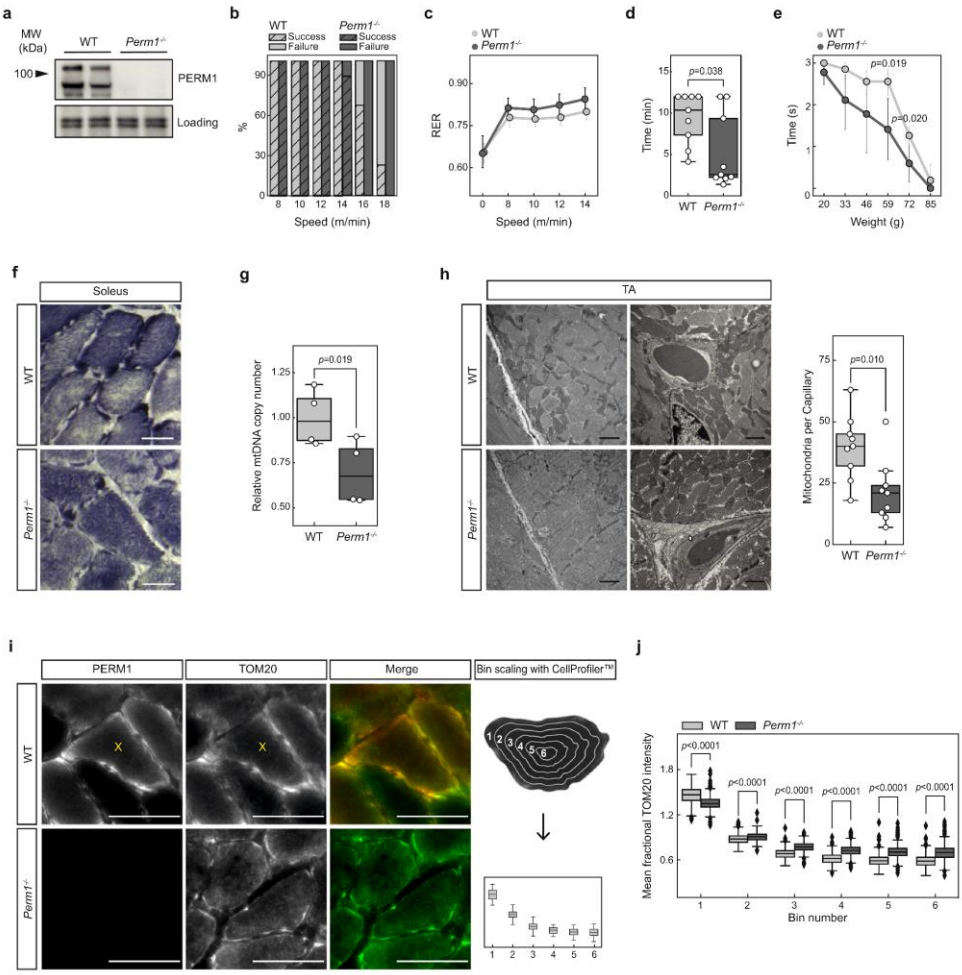


Fig. 1 Deletion of *Perm1* reduces muscle force and alters the localization of subsarcolemmal mitochondria. a Western blot depicting successful depletion of *Perm1* in *Perm1*$^{-/-}$ TA muscle. Correct genotype was confirmed by western blotting for each mouse used in the whole study ($n > 20$ mice per group). **b**, **c** Forced running experiments with metabolic respiratory exchange ratio (RER) measurements. **b** Percentage of wild-type and *Perm1*$^{-/-}$ mice that succeeded or failed to run at the indicated speed for two minutes each ($n = 9$ mice per group). **c** RER (VCO_2/VO_2) of wild-type and *Perm1*$^{-/-}$ mice running at the indicated speed ($n = 9$ mice per group). **d** Inverted screen test; the time *Perm1*$^{-/-}$ and wild-type mice held their body weight on an inverted grid is shown ($n = 9$ mice per group). **e** Weight test; the time *Perm1*$^{-/-}$ and wild-type mice grasped increasing weights is shown ($n = 9$ mice per group). **f** Succinate dehydrogenase (SDH) of soleus muscle from *Perm1*$^{-/-}$ mice indicated an altered overall distribution of mitochondria compared to wild-type control. Scale 25 µm. **g** qPCR analysis showed decreased in mtDNA copy number in *Perm1*$^{-/-}$ soleus muscle compared to wild-type controls ($n = 3$ mice per group). **h** Left: Electron microscopic inspection of TA muscle showed decreased mitochondrial density at capillaries in *Perm1*$^{-/-}$ mice compared to wild-type mice. Scale 1 µm. Right: Number of mitochondria per capillary in *Perm1*$^{-/-}$ and wild-type mice ($n = 2$ mice per group, 10 quantified capillaries). **i** Immunohistochemical staining of soleus muscle indicated co-localization of PERM1 (red) with TOM20 (green). Scale 50 µm. Schematic visualization of bin scaling of a single muscle fiber for TOM20 intensity quantification. **j** Mean fractional intensity of TOM20 signals in bins 1–6 from *Perm1*$^{-/-}$ and wild-type soleus muscle fibers. Intensity is reduced at subsarcolemmal sites and increased within interfibrillar mitochondria in *Perm1*$^{-/-}$ muscles compared to wild-type control ($n = 2$ mice per group, 507 quantified fibers). Data (**c**, **e**) are presented as mean values ±0.95 CI. Box plots (**d**, **g**, **h**, **j**) represent the median, 25th, and 75th percentiles, maximum and minimum are connected through whiskers, and individual data points are added on top (**d**, **g**, **h**). Outliers are defined as $Q_1 - 1.8$ interquartile range (IQR) and $Q_3 + 1.8$ IQR. (**c**–**e**, **g**, **h**) unpaired two-sided Student's *t* test, (**j**) unpaired two-sided Mann–Whitney *U*-test. Source data are provided as Source Data file.

upwards compared to controls (Fig. 1e). Next, we measured the force generated by the gastrocnemius muscle in living animals after electrical stimulation. *Perm1*$^{-/-}$ exhibited reduced strength compared to controls at all stimulation frequencies, although the differences did not reach statistical significance (*p*-value 0.09; SI Fig. S1e). Overall, the running performance, muscle strength and in vivo muscle stimulation experiments demonstrated that loss of PERM1 leads to reduced muscle strength and endurance. Thus, it will be interesting to investigate effects of *Perm1* deletion on force development in individual muscle groups with different fiber types and explore how PERM1 affects mitochondrial activity under normal and exercise conditions.

Loss of *Perm1* reduces formation of SSM. Next, we visualized the enzymatic activity of the mitochondrial succinate dehydrogenase (SDH) in soleus muscle cross-sections. SDH signals were mainly detected in subsarcolemmal areas, reflecting the higher density of mitochondria at the periphery where the diffusion distances for oxygen and metabolites are shorter[24]. Importantly, we observed decreased SDH signal intensities at subsarcolemmal areas in *Perm1*$^{-/-}$ fibers and a shift towards increased intensity in central areas (Fig. 1f). mtDNA copy number was lower in *Perm1*$^{-/-}$ compared to wild-type control soleus muscle, suggesting a reduced mitochondrial content (Fig. 1g). Electron microscopy (EM) analysis of mitochondrial morphology revealed no changes in mitochondrial size and cristae formation (Fig. 1h, SI Fig. S2a). Consistent with the SDH staining, we observed the reduced formation of SSM in *Perm1*$^{-/-}$ mutants, particularly close to capillaries (Fig. 1h).

To quantify mitochondrial distribution more precisely, we stained for TOM20, which co-localized with PERM1 at the periphery of muscle fibers, and determined the staining intensity from the periphery to the center of the muscle fibers. (Fig. 1i). We divided the cross-sectional area of single muscle fibers into six scaled bins and quantified the mean fractional TOM20 intensity for more than 500 fibers ($n = 2$). Since we observed a significant reduction in TOM20 in the first bin, next to the sarcolemma, in *Perm1*$^{-/-}$ mutants compared to wild-type control sections (Fig. 1j), we hypothesize that inactivation of *Perm1* specifically reduces SSM, without affecting the IFM population.

Loss of *Perm1* reduces the abundance of the MICOS/MIB complex in SSM. Since *Perm1* ablation affected the localization of SSM, we investigated whether PERM1 protein expression is more abundant in SSM than IFM in wild-type TA muscles. Consistent with the immunohistochemistry, we observed a higher PERM1 protein expression in SSM than IFM, while the majority of mitochondrial proteins, including OMM and MICOS–MIB members, were evenly distributed (Supplementary Data 1; Fig. 2a, b). We next compared SSM and IFM populations from *Perm1*$^{-/-}$ and wild-type control mice. While we observed almost no protein changes in the IFM population (Fig. 2c), analysis of SSM mitochondria identified 62 regulated proteins, including several OMM and MICOS–MIB complex members (Fig. 2d–f). It should be noted that more sarcomeric proteins were detected in the *Perm1*$^{-/-}$ SSM population compared to wild-type SSM, indicating altered associations of *Perm1*-deficient SSM with cytoskeletal and sarcomeric structures (Fig. 2f, blue circles).

Overall, the quantitative proteomics demonstrated that SSM are significantly more affected by *Perm1* ablation than IFM and that loss of PERM1 affects the protein expression of members of the MICOS–MIB complex.

Inactivation of *Perm1* affects mitochondrial proteins related to transportation and breakdown of reactive oxygen species in skeletal muscle tissue. In a previous quantitative proteomic analysis of *Perm1*$^{-/-}$ heart tissue, we showed that PERM1 has a stronger effect on protein expression during nocturnal activities than under daytime resting conditions[14]. To quantify circadian PERM1 protein expression, we isolated skeletal muscle tissues from wild-type mice every six hours and performed immunoblot analysis. Densitometric analysis revealed upregulation of PERM1 during the night when the physical activity of mice is at its peak (Fig. 3a).

To identify proteins that directly depend on PERM1, we measured the proteome of muscles during active nighttime and during daytime when PERM1 levels decrease. In total, we quantified 4686 proteins and observed 129 significantly regulated proteins (Fig. 3b–e, SI Fig. 2b–f; Supplementary Data 2); 18% of the quantified proteins in the nighttime proteomic dataset represent mitochondrial proteins. Interestingly, the overall fold-changes in mitochondrial proteins were significantly lower in *Perm1*$^{-/-}$ mice compared to wild-type controls (Fig. 3b), while the fold-changes for all proteins were similar between the genotypes. This result was substantiated by immunoblotting with the mitochondrial marker protein TOM20 (Fig. 3c). Collectively, this finding suggests an overall reduction in the mitochondrial content of *Perm1*$^{-/-}$ skeletal muscle, which is in line with the reduction of mtDNA. Downregulated mitochondrial proteins included proteins associated with OXPHOS function and OXPHOS assembly, namely SCO2 and NDUFAF3, surfeit locus protein 1 (SURF1), and cytochrome *c* oxidase subunit 3 (COX3; Fig. 3d).

Next, we isolated mitochondria from *Perm1*$^{-/-}$ and wild-type TA muscles and mass spectrometric analysis identified 2884 proteins, including 453 mitochondrial proteins (Fig. 3e, Supplementary Data 2). We observed 58 significantly regulated proteins, of which 28 were increased and 30 decreased. Knockdown of *Perm1* in C2C12 cells downregulated mRNA expression of the OMM carnitine palmitoyltransferase CPT1B after PGC-1α induction[12]. Similarly, we observed reduced CPT1B protein expression in *Perm1*$^{-/-}$ mitochondria during the night, suggesting attenuated transport of acylcarnitine.

Another essential transport protein, sorting and assembly factor SAM50 is a member of the MIB complex involved in sorting beta-barrel proteins at the OMM after import by the TOM complex. We observed a 1.5-fold reduction (*p*-value 0.03) in SAM50 in *Perm1*$^{-/-}$ mitochondria compared to controls. In addition, FAM120A, another protein downregulated in *Perm1*$^{-/-}$ mitochondria, is related to oxidative stress signaling and has been linked to the family of constitutive coactivators of the PPARγ family due to its sequence similarity. A recent study that named FAM120 oxidative stress-associated Src activator (OSSA) reported the protein functions as an activator of PI3K-AKT signaling and antiapoptotic pathways[25]. PERM1 is required for activation of selective PGC-1α target genes. Depletion of *Perm1* in PGC-1α-stimulated cells reduced the expression of several genes related to mitochondrial energy metabolism, including the DNA-directed RNA polymerase POLRMT and mitochondrial dimethyladenosine transferase 1 and 2 (TFB1M, TFB2M)[13]. Accordingly, we observed significant downregulation of POLRMT in *Perm1*$^{-/-}$ skeletal muscle tissue during the night. In contrast, the mitochondrial replication factor TFAM and POLRMT interactors TFB1M and TFB2M were not altered in *Perm1*$^{-/-}$ mutants. Enhanced degradation of mitochondria could also reduce the amount of mtDNA and mitochondrial proteins. However, markers of mitochondrial fusion/fission and mitophagy, such as mitofusin-1/2, OPA1, sequestosome (p62), and several autophagy-related proteins (ATG5, ATG7, ATGl1) were not altered in *Perm1*$^{-/-}$ mutants (Supplementary Data 2). Additionally, the apoptosis-inducing protein BNIP3 was severely reduced in both *Perm1*$^{-/-}$ whole muscle tissues and isolated mitochondria[26]. We substantiated the downregulation of BNIP3 by immunoblotting (Fig. 3f).

Besides diurnal changes of PERM1, we were also interested in PERM1 regulation during aging. We could not observe obvious changes in PERM1 protein expression levels between 3-month-old (young) and 24-month-old (aged) in TA and soleus muscles of wild-type mice (SI Fig. S2f). However, comparison of TA and soleus muscles of 2-year-old *Perm1*$^{-/-}$ mutants and aged-matched wild-type control animals ($n = 3$; SI Fig. S2b, c) revealed significant differences in expression of 60 out of 3522 proteins,

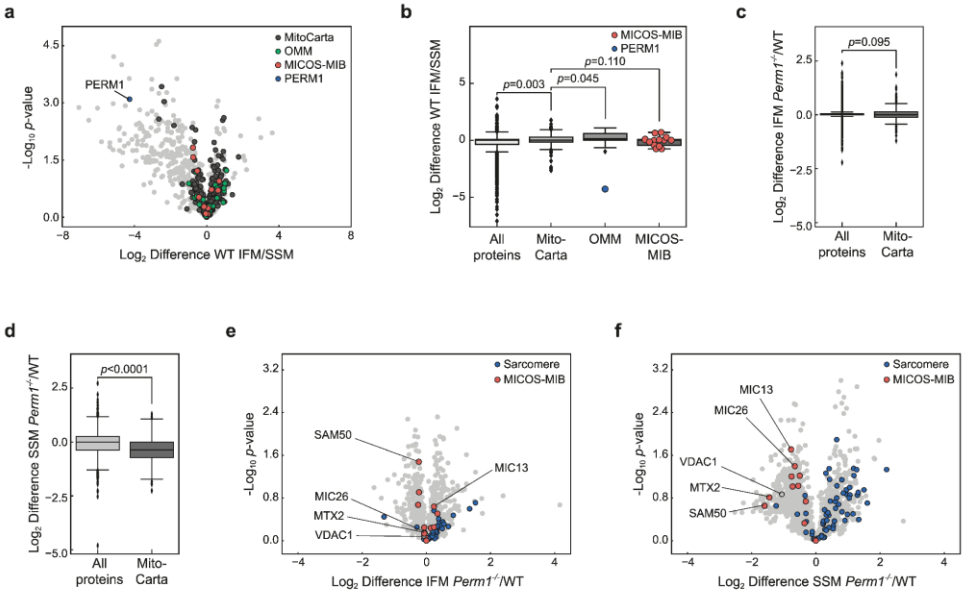


Fig. 2 PERM1 is specifically enriched in SSM, and SSM are altered in *Perm1*$^{-/-}$ muscles. a, **b** Volcano plot (**a**) and boxplot (**b**) depicting the regulation of PERM1, MitoCarta-annotated, OMM, and MICOS-MIB proteins in isolated IFM and SSM from wild-type TA muscle. Mitochondrial and OMM proteins are enriched in IFM. Inversely, PERM1 is clearly more abundant in the SSM fraction ($n = 3$ mice per group). **c**, **d** Comparison of $\log_2$ differences in MitoCarta 2.0 proteins compared to the complete dataset revealed no changes in the overall regulation of mitochondrial proteins in (**c**) isolated IFM of *Perm1*$^{-/-}$ TA muscle compared to wild-type control, though MitoCarta-annotated proteins were significantly reduced in (**d**) isolated SSM from *Perm1*$^{-/-}$ TA muscle compared to wild-type control ($n = 3$ mice per group). **e**, **f**) Volcano plots highlighting the regulation of sarcomeric proteins and proteins of the MICOS–MIB complex in (**e**) isolated IFM from *Perm1*$^{-/-}$ TA compared to wild-type control and in (**f**) isolated SSM from *Perm1*$^{-/-}$ TA compared to wild-type control ($n = 3$ mice per group). Box plots (**b**, **c**, **d**, **e**) represent the median, 25th, and 75th percentiles, maximum and minimum are connected through whiskers. Outliers are defined as Q_1-1.8 IQR and Q_3+1.8 IQR. **b**–**d** unpaired two-sided Mann-Whitney *U*-test. Source data are provided in Supplementary Data 1.

including 17 mitochondrial proteins (Supplementary Data 2), including prohibitin (PHB) and SIRT3, which were decreased in aged *Perm1*$^{-/-}$ muscles.

In summary, ablation of *Perm1* leads to dysregulation of several proteins related to membrane transport and inactivation of reactive oxygen species (ROS). Since mitochondria are the main source of oxidative stress, this dysregulation could lead to cellular damage and reduced mitochondrial function. However, it remains unclear whether ablation of *Perm1* directly regulates the expression of these proteins or reflects a secondary adaptation.

***Perm1*-deficient muscles exhibit reduced OXPHOS activity and higher turnover of mitochondrial proteins**. Since muscle strength data and proteomic analyses indicated reduced mitochondrial function, we examined the activity of the electron transport chain in mitochondria isolated from a mixture of several mouse leg muscles by high-resolution respirometry (Oroboros, O2k). Notably, oxygen flux was lower at all stages in *Perm1*$^{-/-}$ samples compared to the wild-type controls ($n = 3$; Fig. 4a).

In addition to impairing oxidative phosphorylation, imbalanced mitochondrial metabolism may induce rapid depolarization of the inner mitochondrial membrane potential. Therefore, we isolated single muscle fibers from *Perm1*$^{-/-}$ flexor digitorum brevis (FDB) and quantified mitochondrial membrane potential. Mitochondria from *Perm1*$^{-/-}$ fibers showed higher depolarization when ATP synthase was inhibited by oligomycin, indicating that *Perm1*$^{-/-}$ fibers are partially dependent on the reverse activity of ATP synthase to maintain membrane potential due to proton leakage-consuming proton-motive force (Fig. 4b).

To explore whether the turnover of mitochondria is affected, we used pulsed-SILAC labeling of living animals to monitor newly synthesized proteins via incorporation of the isotope-labeled amino acid $^{13}C_6$-lysine (Lys6) by LC-MS/MS. A diet containing Lys6 was administrated to *Perm1*$^{-/-}$ and wild-type control littermates for 14 days ($n = 3$). Skeletal muscle tissue was isolated and subjected to LC-MS/MS analysis to measure incorporation of stable isotopes (Supplementary Data 3). Brain tissue, which does not express *Perm1*, from the same animals was used as a control. In accordance with previous labeling studies[27], we observed a Lys6-labeling rate of 29 ± 14% for mitochondria, substantially lower than the total proteome rate of 45 ± 18% (Fig. 4c). Interestingly, MICOS–MIB complex members had even lower Lys6-labeling rates of 20 ± 6% and thus are among the mitochondrial proteins with the lowest turnover. Conversely, PERM1 had a high Lys6-labeling rate of 58% (Fig. 4c, blue circle), followed by DNAJC11 (39%; Fig. 4c, green circle). We observed similar patterns by calculating the half-lives of these proteins in a dataset of soleus muscles of mice fed with a Lys6 diet for 1–4 weeks (S1 Fig. S3a; Supplementary Data 5). This finding might indicate that PERM1 and DNAJC11 have distinct stability and function compared to other OMM proteins or MICOS–MIB complex members. Similarly, OXPHOS complex assembly factors showed comparably high Lys6-labeling rates of 48 ± 12%.

Next, we compared the Lys6-incorporation rates of *Perm1*$^{-/-}$ and wild-type controls. No differences in Lys6-incorporation rates were observed in brain tissue (SI Fig. S3b). In contrast, analysis of

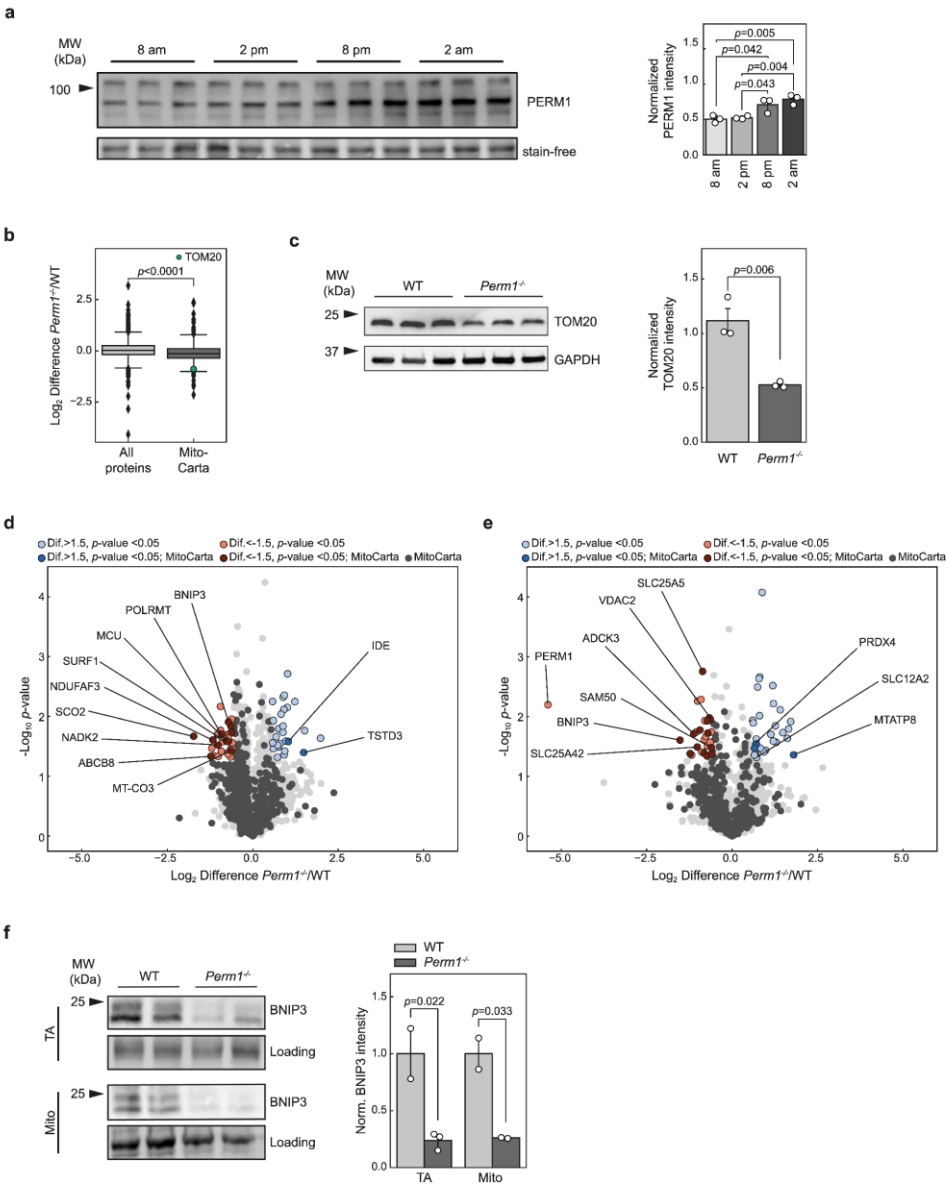


Fig. 3 Inactivation of *Perm1* affects mitochondrial proteins related to transportation and breakdown of ROS. a Protein levels of PERM1 at different timepoints in TA muscle determined by western blotting. Normalized protein levels are expressed relative to the mean levels of each protein in the stain-free control ($n = 3$ mice per time point). **b** Comparison of the $\log_2$ differences in MitoCarta 2.0 proteins compared to the complete dataset revealed overall downregulation of mitochondrial proteins in TA muscle isolated from *Perm1*$^{-/-}$ mice compared to wild-type controls ($n = 2$ mice per group). **c** Western blot and quantification of TOM20 in *Perm1*$^{-/-}$ TA muscle and wild-type controls, substantiating the reduced mitochondrial content ($n = 3$ mice per group). **d**, **e** Volcano plots depicting significantly regulated proteins in *Perm1*$^{-/-}$ TA muscle (**d**) and isolated TA muscle mitochondria (**e**) at 11 pm compared to wild-type controls ($n = 2$ mice per group). Cut-off was defined as $p < 0.05$ with a fold change >1.5. Darker colors indicate the MitoCarta 2.0 annotations. **f** Western blot and quantification, depicting downregulation of BNIP3 in TA muscle and isolated TA muscle mitochondria from *Perm1*$^{-/-}$ mice. BNIP3 levels are expressed relative to the mean levels in wild-type control samples ($n = 2$ mice per group). Box plot (**b**) represents the median, 25th, and 75th percentiles, maximum and minimum are connected through whiskers. Outliers are defined as Q_1-1.8 IQR and Q_3+1.8 IQR. **a**, **d**, **e** Unpaired two-sided Student's *t* test, S_0=0.1, (**c**) unpaired two-sided Student's *t* test, (**b**) unpaired two-sided Mann–Whitney *U*-test. Source data are provided as Source Data file and in Supplementary Data 2.

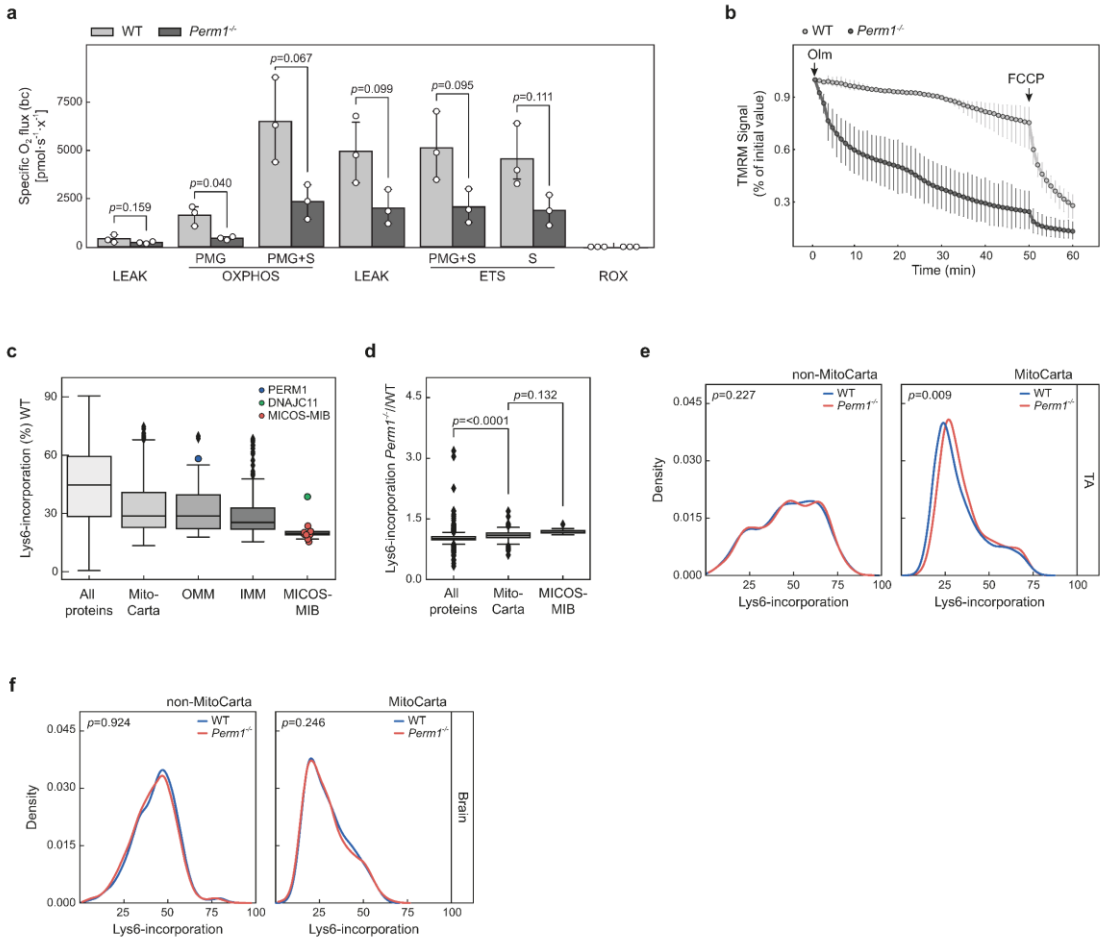
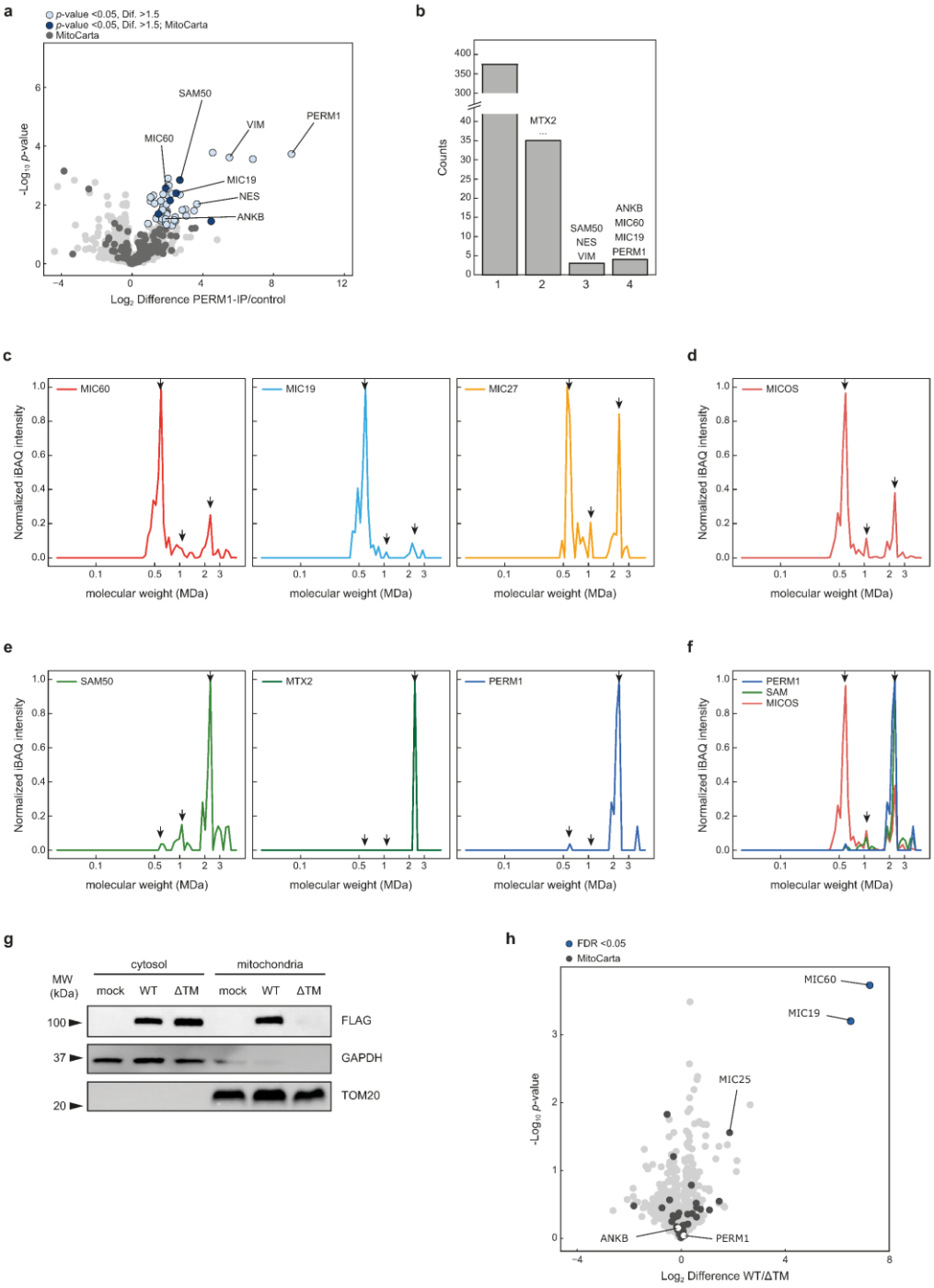


Fig. 4 *Perm1*-deficient muscles show reduced oxygen flux and faster turnover of mitochondrial proteins. a High-resolution respirometry of isolated muscle mitochondria showing decreased specific oxygen flux in isolated *Perm1*$^{-/-}$ mitochondria compared to wild-type controls ($n = 3$ mice per group). **b** FDB muscle fibers were loaded with 2.5 nM TMRM. Arrows indicate the addition of 5 µM oligomycin and 4 µM FCCP ($n = 10$ fibers in wild-type, $n = 20$ fibers in *Perm1*$^{-/-}$). **c** Comparison of the Lys6-incorporation rates of all proteins, mitochondrial proteins, OMM proteins, IMM proteins, and proteins of the MICOS-MIB complex in wild-type mice fed a SILAC diet for 14 days ($n = 3$ mice per group). DNAJC11 and PERM1 had higher incorporation rates than other MICOS-MIB proteins. **d** Ratios of *Perm1*$^{-/-}$ to wild-type control Lys6-incorporation rates for MitoCarta 2.0 proteins and MICOS-MIB proteins in comparison to the complete TA muscle dataset after feeding with a SILAC diet for 14 days. Enhanced labeling of mitochondrial proteins and MICOS-MIB proteins was observed in *Perm1*$^{-/-}$ mice ($n = 3$ mice per group). **e**, **f** Density plots of the ratios of *Perm1*$^{-/-}$ to wild-type control Lys6-incorporation for non-MitoCarta 2.0 and MitoCarta 2.0-annotated proteins, showing enhanced labeling of mitochondrial proteins in *Perm1*$^{-/-}$ (**e**) TA but not in (**f**) *Perm1*$^{-/-}$ brain. Data (**a**) are presented as mean values ± 0.95 CI. Box plots (**c**, **d**) represent the median, 25th, and 75th percentiles, maximum and minimum are connected through whiskers. Outliers are defined as Q_1-1.8 IQR and Q_3+1.8 IQR. (**a**) paired two-sided Student's *t* test, (**d**, **e**, **f**) unpaired two-sided Mann-Whitney *U*-test. Source data are provided as Source Data file and in Supplementary Data 3. PMG (pyruvate, malate, glutamate), S (succinate), ETS (electron transfer system), ROX (residual oxygen consumption), Olm (oligomycin).

skeletal muscle tissue revealed enhanced Lys6-incorporation rates for *Perm1*$^{-/-}$ mitochondrial proteins compared to controls. This effect was even more pronounced for MICOS–MIB complex members (Fig. 4d). Selected MS spectra of MIC60 and SAM50 are shown in SI Fig. S3c, d. The density and scatter plots illustrate the shift to higher Lys6-incorporation rates in the TA muscle, but not brain, of *Perm1*$^{-/-}$ mutants compared to wild-type controls (Fig. 4e, f, SI Fig. S3e, h). This effect was most pronounced for MIC13, with a ~1.4-fold higher Lys6-labeling in *Perm1*$^{-/-}$ mutants than wild-type (SI Fig. 3e, f). We concluded that *Perm1*$^{-/-}$ mitochondria, particularly MICOS–MIB members, have a higher turnover compared to mitochondria from wild-type control muscles. Overall, loss of PERM1 significantly impaired oxidative phosphorylation and enhanced membrane depolarization, which may increase protein synthesis, especially of MIB complex members.

PERM1 interacts with components of the mitochondrial intermembrane bridging complex. To clarify which proteins interact with PERM1, we performed affinity enrichment mass spectrometry in TREx-293 cells stably overexpressing *Perm1*-FLAG and C2C12 cells transiently overexpressing *Perm1*-FLAG.



A PERM1 antibody was employed to identify endogenous PERM1 interactors in skeletal muscle and heart (Supplementary Data 4, Fig. 5a, SI Fig. S4a–c). A volcano plot was used to visualize PERM1 interactors (Fig. 5a) and the frequency with which these candidates were found is shown in Fig. 5b. Interestingly, we found that PERM1 interacts with several MICOS–MIB complex members, including MIC60, MIC19, SAM50 and MTX2. The interaction of PERM1 with SLC25A5 might explain the reduced protein abundance of this transporter in *Perm1*$^{-/-}$ mitochondria (SI Fig. S4a, b). Detection of ankyrin B (ANKB or ANK2) and the intermediate filament proteins vimentin and nestin suggest that PERM1 connects the OMM to cytoskeletal structures. Reverse

Fig. 5 PERM1 interacts with components of the mitochondrial intermembrane bridging complex. a Volcano plot depicting significantly enriched proteins after immunoprecipitation of endogenous PERM1 in TA muscle ($n = 3$ mice per group). Cut-off was set to $p < 0.05$ with a fold change >1.5. Dark circles indicate MitoCarta 2.0 annotation. **b** Bar diagram showing the number of significantly enriched proteins (same cut-off as in volcano plot) identified in one, two, three, or all four immunoprecipitation approaches highlighting the most frequently found proteins. **c**–**f** Complexome profiling of muscle mitochondria; iBAQ-values were maximum normalized. Arrows indicate the three main complex assemblies. **c** Single profiles of the MICOS complex proteins MIC60, MIC19, and MIC27. **d** Summary plot of all MICOS complex members detected (MIC10, MIC19, MIC26, MIC27, and MIC60). **e** Single profiles of the SAM complex proteins SAM50 and MTX2, as well PERM1. **f** Summary plot of all detected MICOS complex members (red line), SAM components (green line; SAM50, MTX2), and PERM1 (blue line). **g** Deletion of the transmembrane helix in PERM1 resulted in loss of PERM1 in the mitochondrial fraction, as visualized by immunoblotting of cytosolic and mitochondrial fractions obtained from HEK-293T cells transfected with FLAG-tagged wild-type *Perm1* and FLAG-tagged ΔTM mutant. **h** Volcano plot depicting significantly enriched proteins after immunoprecipitation of PERM1 in HEK-293T cells transfected with FLAG-tagged wild-type *Perm1* and FLAG-tagged ΔTM mutant ($n = 3$ samples per group). The cut-off was an FDR < 0.05; dark circles indicate MitoCarta 2.0 annotations. MICOS proteins MIC60 and MIC19 were only found in wild-type immunoprecipitates, while ANKB and PERM1 were similarly enriched in wild-type and ΔTM immunoprecipitates. **a** unpaired two-sided Student's *t* test, $S_0 = 0.1$, **h** unpaired two-sided Student's *t* test, S_0=0.1, permutation-based FDR=0.05, 500 randomizations. Source data are provided as Source Data file and in Supplementary Data 4.

immunoprecipitations confirmed that MIC60 and MIC19 interact with PERM1 (SI Fig. S4d). Immunoblotting revealed similar levels of PERM1, MIC60 and MTX2 expression between different muscle groups, suggesting a similar structure of the MICOS–MIB complex (SI Fig. S4e).

To further investigate the interaction between PERM1 and the MICOS–MIB complex, we performed complexome profiling of mitochondria isolated from skeletal muscle by blue-native gel electrophoresis (BN-PAGE) and mass spectrometry. Each BN-PAGE lane was sliced into 70 sections and subjected to MS analysis. Intensity-Based Absolute Quantification (iBAQ) was used to quantify the proteins. All protein intensities were normalized and the profiles of selected MICOS (Fig. 5c, d, SI Fig. S4f) and MIB (Fig. 5e, f) complex members were plotted[28]. To assign protein intensities according to their size in Dalton (Da), respiratory chain complex standards of known sizes were used for normalization. The MICOS–MIB complex appears in different forms, depending on its maturation stage: (i) the 500–700 kDa IMM/intermembrane space (IMS) complex, which contains all MICOS subunits; (ii) the 800 and 1400 kDa SAM complex (SAM50, MTX1 + 2) that associates with the OMM; and (iii) the mature MICOS–MIB complex with a molecular weight between 2.2 and 2.8 MDa.

The 85 kDa protein PERM1 was mainly detected at a molecular weight of ~2.2 MDa in isolated mitochondria from muscle tissue (Fig. 5e). The core MICOS complex protein MIC60 was identified in all three maturing forms of the complex, whereas the MIB complex proteins SAM50 and MTX2 had similar migration profiles to PERM1 with a signal at ~2.2 MDa. Thus, we conclude PERM1 is a member of the mature MICOS–MIB complex in skeletal muscle tissue.

PERM1 anchors to the OMM via a conserved transmembrane helix. Next, we examined the PERM1 amino acid sequence to identify domains that potentially interact with proteins of the MICOS–MIB complex. Although most of the PERM1 protein is intrinsically disordered, a secondary structure and topology prediction of all-helix integral membrane proteins using MEMSAT3[29] predicted a hydrophobic transmembrane helix from amino acids 740–755 at the carboxyl-terminus of PERM1, which is followed by a 52 amino acids long tail. Furthermore, the C-terminal segment (732–803) shows high sequence conservation between human, mouse and bovine PERM1, while the overall amino acid sequence identity is lower than 50%. This may indicate that PERM1 anchors into the outer mitochondrial membrane via its C-terminal domain.

To test this hypothesis, we deleted amino acids 736–759 in the PERM1-FLAG construct. Strikingly, separation of the cytosolic and mitochondrial fractions of HEK-293T cells transfected with the mutant PERM1 (hereafter referred to as ΔTM mutant) resulted in the loss of PERM1 in the mitochondrial fractions, while overexpressed wild-type PERM1 was present in both mitochondrial and cytosolic fractions (Fig. 5g). Furthermore, deletion of the hydrophobic transmembrane helix prevented interactions between PERM1 and MIC60, MIC19, and MIC25 in immunoprecipitation experiments (Fig. 5h, Supplementary Data 4). In contrast, no differences were observed in the interaction of ΔTM PERM1 with ANKB compared to wild-type PERM1. We concluded that the C-terminal helical structure is responsible for mitochondrial localization of PERM1 and its interaction with the MICOS–MIB complex.

Altered localization of the adaptor protein ankyrin B in *Perm1*$^{-/-}$ muscles. We found that PERM1 does not only interact with members of the MICOS–MIB complex, but also with several proteins associated with membrane and cytoskeletal structures including ANKB, an adaptor protein that interacts with the cytoskeleton and connects transmembrane proteins with the sarcolemma[30] (Fig. 5a). The PERM1-ANKB interaction was verified by co-immunoprecipitating FLAG-tagged *Perm1* and HA-tagged *AnkB* in TREx-293 cells (Fig. 6a). Immunostaining confirmed co-localization of PERM1 and ANKB in the periphery of soleus muscle fibers (Fig. 6b). Interestingly, we also observed a reduction in the ANKB signals at the periphery of *Perm1*$^{-/-}$ mutant muscles. This finding was similar to the results of immunostaining with the TOM20 antibody (Fig. 1j). To quantify the reduction in ANKB, we separated each fiber into six bins (as shown in Fig. 1i) and measured the intensity of ANKB in *Perm1*$^{-/-}$ and wild-type muscle sections ($n = 4$). ANKB signal intensity was significantly lower at subsarcolemmal sites and higher within interfibrillar regions in *Perm1*$^{-/-}$ mutants (Fig. 6c, 2299 quantified fibers). These results validate the interaction of PERM1 with ANKB and suggest this interaction could be responsible for the localization of mitochondria at the sarcolemma.

Discussion

We here demonstrate that PERM1 interacts with the MICOS–MIB complex in mitochondria and with the intracellular adaptor protein ankyrin B to tether a subpopulation of skeletal muscle mitochondria to the sarcolemma. We show that PERM1 is required for mitochondria, providing the energy to achieve full muscle strength. So far, detailed knowledge about the physiological role of PERM1 was missing. PERM1, which rapidly upregulated when human skeletal muscle tissue becomes physically active, was recently described as a tissue-specific regulator of oxidative capacity in cultured muscle cells[12, 31, 32]. In addition, a previous study suggested that PERM1 is required for expression of PGC-1α/ERR target genes in C2C12 myotubes, for PGC-1α-

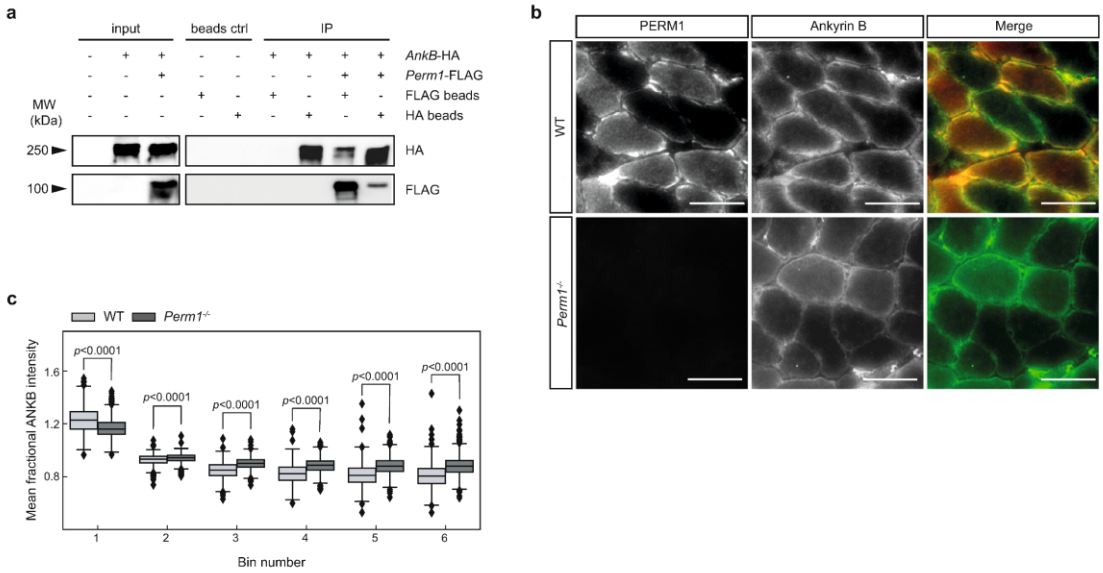


Fig. 6 PERM1 associates with ankyrin B and the interaction with the MICOS–MIB complex is dependent on the transmembrane helix. a PERM1 interacts with ANKB, as indicated by immunoprecipitation of FLAG-tagged *Perm1* and HA-tagged ankyrin-B in TREx-293 cells stably expressing *Perm1*-FLAG. Protein lysates were immunoprecipitated with anti-FLAG beads and anti-HA beads and immunoblotted with anti-FLAG and anti-HA antibodies. **b** Immunohistochemical staining of soleus muscle revealed co-localization of PERM1 (red) with ANKB (green). Scale, 50 µm. **c** Mean fractional intensity of ANKB signals in bins 1–6 from *Perm1*$^{-/-}$ and wild-type soleus muscle fibers. ANKB staining intensity was reduced at subsarcolemmal sites and increased within interfibrillar mitochondria in *Perm1*$^{-/-}$ muscles compared to wild-type controls ($n = 4$ mice per group, 2299 quantified fibers). Box plot (c) represents the median, 25th, and 75th percentiles, maximum and minimum are connected through whiskers. Outliers are defined as Q_1–1.8 IQR and Q_3+1.8 IQR. (c) unpaired two-sided Mann-Whitney *U*-test. Source data are provided as Source Data file.

induced mitochondrial biogenesis, and maximal oxidative capacity during physical activity[13]. Although PERM1 was reported to localize to the cytosol and the nucleus, we recently showed that PERM1 associates with the OMM[14], suggesting that PERM1 might shuttle between mitochondria and the nucleus. Quantitative interactome screenings demonstrated that PERM1 physically interacts with MICOS–MIB subunits, which was confirmed by BN-PAGE analysis indicating that PERM1 co-migrates with the mature MICOS–MIB complex (Fig. 5). We hypothesize that the C-terminal transmembrane helix anchors PERM1 in the OMM, while the most C-terminal, 52 amino acid sequence, may extend into the IMS to allow interaction with MIC60 and MIC19. Further experiments are required to investigate the mechanisms that integrate PERM1 into the membrane and to answer the question whether PERM1 is involved in mitochondrial transport processes.

Previous studies demonstrated that SSM and IFM have distinct biochemical properties, capacities for respiration, and sensitivities to metabolic stress. Since PERM1 is enriched in SSM and loss of PERM1 results in a strong reduction in SSM, we hypothesize that PERM1 is critical for the specific functions of SSM and IFM. Several mitochondrial inner and outer membrane transporters were downregulated in *Perm1* mutant skeletal muscles. We assume that PERM1 stabilizes the MICOS–MIB complex and prevents degradation of its subunits, since in vivo labeling with the stable isotope Lys6 demonstrated increased synthesis of several MICOS–MIB members including SAM50, MTX2 and MIC13 in *Perm1*$^{-/-}$ mutants (Fig. 4f).

Circadian rhythm regulates numerous transcriptional and translational processes that influence cellular metabolism and mitochondrial activity. We recently showed that CK2-dependent phosphorylation promotes rapid breakdown of PERM1 by ubiquitination. Interestingly, CK2 is involved in the control of the mammalian circadian clock, since inhibition of CK2 activity decreases the amplitude and increases the period of circadian gene expression oscillations[33]. Moreover, the activity of CK2 regulation of the carbohydrate metabolism is modulated by insulin[34], indicating a central role for CK2 in regulating insulin-sensitivity, energy homeostasis and tissue remodeling. In contrast to CK2, which is upregulated in skeletal muscle of patients with diabetes mellitus type 2, PERM1 is decreased, further supporting a close association with insulin-dependent metabolism and mitochondrial activity[35]. The lower CK2 levels during the night, when mice are more active, coincide with reduced phosphorylation and degradation of PERM1, which increases mitochondrial activity. Hence, it is tempting to speculate that CK2-dependent PERM1 phosphorylation determines the circadian rhythm of PERM1 and thereby contributes to the circadian regulation of mitochondrial activity. We recently described more than 30 phosphorylation sites on PERM1 in cardiomyocytes. Thus, it seems likely that in addition to CK2 other kinases, including PKC, CDC2 and p38, phosphorylate and regulate PERM1. Phosphoproteomics profiling of *Perm1*$^{-/-}$ and wild-type muscles under sedentary and activated conditions might help to decipher the mechanisms by which kinases regulate PERM1 and mitochondrial activity. In particular, analysis of mouse models of insulin resistance, such as the *db/db* mouse or administration of high caloric diets, may shed further light on this interplay.

Our data suggest that PERM1 is not a central structural component of the MICOS–MIB complex, but rather functions as a modulator of its activity or a sensor for energy requirements. The formation of cristae junctions and contact sites is a dynamic process that, depending on energy demands, involves continuous remodeling. The changes in PERM1 protein expression, its short half-life of ~4 days (SI Fig. S3a), and rapid degradation by CK2-

dependent phosphorylation of the PEST domain[14] might potentially contribute to remodeling processes in mitochondria and thereby control mitochondrial energy production.

Interestingly, we observed a reduction in oxygen flow in all measured stages and mitochondrial dysfunction in *Perm1*-deficient muscles as indicated by enhanced mitochondrial membrane depolarization while no signs of apoptosis and mitophagy were apparent. In fact, we detected a strong downregulation of the proapoptotic factor BNIP3 and a reduction of the voltage-dependent anion channel VDAC2, which is part of the mitochondrial permeability transition pore facilitating cytochrome *c* release and induction of apoptosis. These observations make it not only unlikely that removal of SSM in *Perm1*$^{-/-}$ muscles is mediated by mitophagy, but also suggest that absence of *Perm1*, together with the loss of BNIP3, leads to accumulation of damaged mitochondria. Genetic inactivation of *Bnip3* results in changes in the mitochondrial membrane potential and reduced oxygen consumption in the liver[36], which was also seen in *Perm1*$^{-/-}$ mutants.

In *Drosophila*, the MICOS component MIC60 controls mitochondrial motility by regulating protein levels of the OMM protein and Rho GTPase Miro, which anchors mitochondria to microtubule motors[37]. Mammalian skeletal muscle mitochondria display a similar subcellular distribution as the microtubular network and there is a close connection between the structural organization of mitochondria and energy flux[38]. Mitochondria accumulate at the periphery of muscles, and in particular, close to capillaries[39], which reduces the distance for the diffusion of oxygen and metabolites from the capillaries to mitochondria. Moreover, SSM are thought to be primarily involved in the generation of the mitochondrial proton-motive force near capillaries, whereas IFM, which need to be close to myofibrils for efficient supply of ATP or other high-energy phosphates, use the generated proton-motive force to produce ATP[4]. Disruption of the finely balanced mitochondrial network by removal of components linking mitochondria to the microtubular and intermediate filament networks or breakdown of the intermediate filament network, will disrupt division of labor within mitochondrial subpopulations and reduce muscle strength[38].

Our protein-protein interaction screening also identified the intermediate filament proteins vimentin and nestin, as well as ankyrin B (ANKB) as potential interactors of PERM1 (Fig. 3a). Vimentin co-localizes with mitochondria, regulates mitochondrial distribution, and influences the rate of ATP synthesis and mitochondrial membrane potential[40]. Heteropolymeric intermediate filaments consisting of nestin and vimentin are responsible for the connection of myofibrillary Z-lines via interactions with α-actinin to ANKB-containing costameres at sarcolemma[41, 42]. ANKB is one of three members of the ankyrin family of plasma membrane adaptor proteins involved in the organization and anchoring of integral membrane complexes to the spectrin- and actin-based cytoskeleton. Moreover, ANKB functions as an adaptor protein for dystrophin and dynactin and ankyrin-dependent organization of those proteins are required to maintain sarcolemmal integrity during physical exercise[43]. Loss of ANKB leads to the intracellular distribution of dystrophin and destabilization of costamere-associated microtubules and muscle fragility[42]. As ANKB also exhibits an intracellular localization[44] and regulates the axonal transport of several organelles, including mitochondria, ANKB is assumed to serve as a core protein involved in intracellular organelle transport[45]. We demonstrated that ANKB co-localizes with PERM1 and mitochondria at the sarcolemma of skeletal muscles. Interestingly, *Perm1* ablation led to a reduction in ANKB at sarcolemma (Fig. 6). We reason that PERM1 and ANKB mediate the anchorage of the mitochondria-associated cytoskeleton to the sarcolemma, albeit it seems also possible that impaired mitochondrial transport along microtubules is responsible for the loss of SSM in *Perm1*$^{-/-}$ mutants.

The characterized PERM1-ANKB interaction may reflect a novel mechanism of how mitochondria are recruited and connected to the sarcolemma in skeletal muscle tissue. Numerous structural and functional interactions have been associated with the integration of the mitochondria and the cytoskeleton, which influences the localization and modulates the activity and turnover of mitochondria. The dual interaction of PERM1 with the MICOS–MIB complex and intermediate filaments represents an unknown mechanism of how mitochondria are connected to the cytoskeleton and indicates that PERM1 is instrumental for the formation of the spatially organized, functional mitochondrial network that makes skeletal muscles strong.

Methods

Antibodies. The antibodies used for immunoblotting, immunoprecipitation and immunohistochemistry were: PERM1 (Sigma, #HPA031711), diluted 1:1,000 for immunoblotting, 1:100 for immunohistochemistry; BNIP3 (Cell Signaling, #3769), diluted 1:1,000; TOM20 (Abcam, #ab56783), diluted 1:100 for immunohistochemistry; TOM20 (Sigma, #HPA011562), diluted 1:5,000 for immunoblotting, 1:100 for immunohistochemistry; GAPDH (Invitrogen, #AM4300), diluted 1:10,000 for immunoblotting; Ankyrin B (Invitrogen, #33-3700), diluted 1:1000 for immunoblotting, 1:100 for immunohistochemistry; MYH7 (Developmental Studies Hybridoma Bank [DSHB], BA-F8), MYH2 (DSHB, SC-71), MYH4 (DSHB, BF-F3), CD31/PECAM (BD Pharmingen, #553370), all diluted 1:100 for immunohistochemistry; anti-FLAG M2-HRP (Sigma, #A8592), anti-HA-HRP (Miltenyi, #130-091-972), Alexa Fluor 350 anti-mouse IgG2b (Life Technologies, #A-21140), Alexa Fluor 488 anti-mouse IgG1 (Life Technologies, #A-21121), Alexa Fluor 546 anti-mouse IgM (Life Technologies, #A-21045), Alexa Fluor 546 anti-rabbit (H+L) (Life Technologies, #A-11010), Alexa Fluor 488 anti-rat (Life Technologies, #A-11006), anti-mouse HRP (Sigma, #A9044) and anti-rabbit HRP (Sigma, #A0545), all diluted 1:4,000 for immunoblotting and 1:200 for immunohistochemistry.

Generation of Perm1$^{-/-}$ mice. *Perm1*$^{-/-}$ mice were generated in the mouse facility of the Max-Planck-Institute in Bad Nauheim and transferred to the CECAD mouse facility via embryo transfer, as previously described[14]. All animal experiments were performed in accordance with national and institutional guidelines and procedures were approved by the responsible local authorities in Germany (Landesamt für Natur, Umwelt und Verbraucherschutz Nordrhein-Westfalen, Germany). Mice were housed at 22 ± 2 °C, with a humidity of 55 ± 10%, and an air exchange rate of 15 times per hour on a 12 h light-dark cycle with free access to food and water.

Plasmids. The mouse PERM1 coding sequence was cloned into the pcDNA5/TO vector containing a C-terminal FLAG tag, as previously described[14]. AnkyrinB-2XHA was a gift from Vann Bennett (Addgene plasmid #31057; http://n2t.net/addgene:31057; RRID: Addgene_31057)[42].

To generate the transmembrane mutant, amino acids 736-759 were deleted from the *Perm1*-FLAG plasmid using the In-Fusion cloning technique (TaKaRa Bio Inc.) following the manufacturer's instructions. In brief, 10 ng *Perm1*-FLAG plasmid was amplified using PrimeSTAR GXL DNA polymerase (TaKaRa Bio Inc.). The PCR product was isolated by gel extraction and incubated with DpnI (Thermo Fisher) at 37 °C for 1 h. The In-Fusion cloning reaction was performed as recommended, and the reaction mixture was transformed into competent DH5α cells. Primers are listed in Supplementary Table 1.

Treadmill and weight experiments. Treadmill and weights experiments were performed in collaboration with the group of Prof. Dr. Bloch at German Sport University, Cologne. After the experiments, the mice were placed back in their cage and returned to the mouse room with free access to water and food.

Treadmill running. Mice ($n = 9$) were placed individually on a treadmill (Columbus Instruments). The speed was started at 8 m/min and increased by 2 m/min every two minutes up to 18 m/min. Mice were gently placed back at the correct position if they stopped running. The session was terminated when the mouse met either of the exhaustion criteria: if the mouse was replaced on the treadmill for the third time or stopped running for more than 10 s.

Inverted screen. The strength of the *Perm1*$^{-/-}$ and wild-type mice was measured as previously described[46]. The inverted screen test was performed following the Kondziella protocol[47]. The screen is a 43 cm square of wire mesh consisting of 12 mm squares of 1 mm diameter with a 4 cm-deep wooden surround. Mice ($n = 9$) were placed individually in the center of the wire mesh and the screen was rotated to an inverted position and held steadily 40–50 cm above a padded surface. The

time until the mouse could not hold on to the screen anymore was recorded; the test was terminated after 12 min.

Weight test. Weight tests were conducted using a series of six weights ranging from 20 and 85 g; the lightest weight was offered first. The weights were attached to wires that can be grabbed by the claws of the mouse. The mice ($n = 9$) were held by the middle of the tail and lowered so they could grasp the weight on the laboratory bench. A maximal holding time of 3 s was allowed; if the mouse dropped the weight in less than 3 s, the time was recorded. If the weight was dropped, the mouse was rested for about 10 s and offered the same weight again; failing three times was the termination criteria.

Skeletal muscle force measurements. Skeletal muscle force in vivo was determined as described previously[48]. Briefly, mice were anesthetized by intraperitoneal injection of xylazine (Xilor; 20 mg/kg) and Zoletil (10 mg/kg). Z small incision was made from the knee to the hip, to expose the sciatic nerve. Before the branch of the sciatic nerve, Teflon-coated 7 multi-stranded steel wires (AS 632; Cooner Sales, Chatsworth, CA, USA) were implanted with sutures on either side of the sciatic nerve. To avoid recruitment of the ankle dorsal flexors, the common peroneal nerve was cut. Torque production of the plantar flexors after nerve stimulation was measured using a muscle lever system (Model 305 C; Aurora Scientific, Aurora, ON, Canada). Normalized muscle force was determined by dividing absolute force by muscle mass.

Cell culture. All cell lines were cultivated as an adherent fibroblastoid monolayers in 10 cm dishes in DMEM (Gibco) supplemented with 10% FBS and 1× Penicillin-Streptavidin-Glutamine mix at 37 °C and 5% CO_2. Cells were washed once with ice-cold PBS, harvested in 500 µL RIPA buffer supplemented with protease and phosphatase inhibitors, incubated for 30 min at 4 °C with rotating, and DNA was sheared by sonification. Lysates were centrifuged at 18,000 *g* for 10 min and 4 °C to pellet cell debris.

Immunohistochemistry. Cross-sections of soleus and TA (10 µm) were prepared by snap-freezing whole muscles in liquid nitrogen-cooled isopentane. Sections were fixed in −20 °C cold acetone for 8 min, blocked in 0.1% Triton, 5% goat serum and 2% BSA in TBS for 1 h at RT, incubated with the primary antibody in 1:10 blocking solution in a humidified chamber at 4 °C overnight, mounted with Aqua Poly mount (Polysciences) and imaged using a DMi8A inverse microscope (Leica).

Quantitative image analysis was done using the cell image analysis software CellProfiler™ (version 3.1.9)[49] to quantify the intensity of the TOM20 and ANKB signals across the muscle fibers. Two pipelines were generated: The first pipeline was created to identify single muscle fibers in an entire muscle cross-section to generate a binary image mask for further analysis. To identify the fiber outlines, the cross-sections were additionally stained with antibodies against type I (BA-F8) and type IIa (SC-71) fibers. Here, a combination of the images of the type I and type IIa fiber staining and an enhanced image of the TOM20/ANKB staining was used for mask generation. In the second pipeline, the generated binary image mask was used to measure the object intensity distribution of the TOM20/ANKB staining in six scaled bins per muscle fiber. Fibers that were not correctly recognized with the image mask were manually excluded from the analysis. The mean fractional intensity for each bin calculated as the fraction of total intensity normalized by the fraction of pixels for each bin was used for statistical analysis (unpaired two-sided Mann-Whitney *U*-test).

Pulsed SILAC labeling of Perm1$^{-/-}$ mice. Time-dependent Lys6-incorporation assays were conducted to monitor protein synthesis in vivo. In the first study, three mice of each genotype (*Perm1*$^{-/-}$ and wild-type control) were voluntarily fed a Lys6-containing SILAC diet for two weeks (3.0 g of ^{13}C6-lysine containing diet; Silantes GmbH, Lys(6)-SILAC-Mouse Diet, purity > 97%). In the second study, wild-type mice were labeled for 7–28 days ($n = 3$ mice per time point) with the Lys6-containing SILAC diet. Several organs and tissues were prepared for LC/MS-MS analysis. Briefly, the tissues were lyophilized overnight, homogenized with a Precellys™ tissue homogenizer, and a small amount of powder was lysed with modified RIPA buffer (100 mM Tris/HCl pH 7.5, 300 mM NaCl, 2% Nonidet P40, 2 mM EDTA, 0.2% sodium deoxycholate), and protein samples were subsequently in-gel digested with the protease LysC overnight to generate peptides that contain at least one lysine.

Tissue lysis. Mouse tissues were snap frozen in liquid nitrogen, ground to a fine powder using a mortar and pestle, and resuspended in modified RIPA buffer (100 mM Tris/HCl pH 7.5, 300 mM NaCl, 2% Nonidet P40, 2 mM EDTA, 0.2% sodium deoxycholate) supplemented with protease and phosphatase inhibitors at a buffer to tissue ratio of 15:1 Lysates was then incubated with rotation for 30 min at 4 °C, sonicated for 10 min at 30 s intervals at 4 °C using a Bioruptor® Pico (Diagenode). Cell debris was pelleted by centrifugation at 18,000 *g* for 10 min at 4 °C.

Protein concentration determination. Protein concentrations were determined using the Pierce Protein Assay (Thermo Fisher). BSA standard solutions (0.05 mg/mL to 1.0 mg/mL) were generated by diluting 2 mg/mL BSA solution (Thermo Fisher). Protein samples were diluted 1:10 in modified RIPA buffer (100 mM Tris/HCl pH 7.5, 300 mM NaCl, 2% Nonidet P40, 2 mM EDTA, 0.2% sodium deoxycholate). Absorption was measured at 660 nm using an EnSpire® Multimode Plate Reader (Perkin Elmer). To enable measurement of protein samples diluted in SDS-containing buffer, Pierce 660 nm Protein Assay Reagent was supplemented with Ionic Detergent Compatibility Reagent (Thermo Fisher) according to manufacturer's instructions.

Immunoprecipitations. To immunoprecipitate PERM1 in TREx-293 cells, cells stably expressing *Perm1*-FLAG or the control To5-STOP-FLAG vector were cultivated to 70-80% confluency as described above, treated with 10 µg/mL doxycycline for approximately 15 h, and lysed as described above. After removing cell debris, the supernatants were transferred into new precooled tubes and 40 µL anti-FLAG (Miltenyi) beads were added. The mixtures were incubated for 60 min at 4 °C with rotation and. separated using the magnetic µMACS system (Miltenyi) at 4 °C. The µColumns were equilibrated with lysis buffer, loaded with the lysate-bead-suspension, washed thrice with 200 µL lysis buffer, and washed thrice with 50 mM ammonium bicarbonate (ABC). Elution was performed at RT by applying 20 µL urea buffer (6 M Urea, 2 M Thiourea) for 10 min and collecting the eluate with 50 µL urea buffer. Finally, samples were prepared for MS analysis by in-solution/on-bead digestion.

To immunoprecipitate PERM1 in C2C12 cells, 6×10^5 cells were seeded on day 1. On day 2, the cells were transfected with *Perm1*-FLAG or the control vector TO5-FLAG-STOP using GeneJuice® Transfection Reagent (Novagen). Cells were harvested 24 h after transfection, as described above and immunoprecipitated as described for TREx-293 cells. To mimic the natural environment of PERM1 in the body, 100 µL of whole muscle and heart lysates prepared from wild-type mice were added with the anti-FLAG beads.

To immunoprecipitate endogenous PERM1 from tissue, 40 mg samples TA muscles and hearts from wild-type mice were lysed as described above. Protein concentrations were determined using Pierce Protein Assay. Two aliquots of 800 µg protein per sample were diluted to 500 µL with modified RIPA buffer (100 mM Tris/HCl pH 7.5, 300 mM NaCl, 2% Nonidet P40, 2 mM EDTA, 0.2% sodium deoxycholate): 40 µL Protein A beads and 0.9 µg PERM1 antibody was added to one aliquot; only 40 µL Protein A beads were added to the control sample. Immunoprecipitation steps were performed as described above.

To immunoprecipitate AnkB, cells stably expressing *Perm1*-FLAG were cultivated to 60-70% confluency prior to transfection with AnkyrinB-2XHA or control empty HA vector using the calcium phosphate method. In brief, 8 µg of DNA was incubated with 37 µg of 2 M $CaCl_2$ and 300 µg 2× HBS (50 mM HEPES, 280 mM NaCl, 1.5 mM NaH_2PO_4, pH 7.0) for 30 min. Next, the mixture was added to the cultured cells and incubated for 24 h. After 9-10 h, the media was exchanged by fresh media containing 10 µg/mL doxycycline. Cells were harvested and lysed as described above. Immunoprecipitation was performed using the magnetic µMACS system (Miltenyi) as described above using anti-HA beads (Miltenyi).

Immunoprecipitation of the ΔTM mutant of PERM1 in HEK-293T cells was performed using the calcium phosphate transfection method, as described above.

Isolation of mitochondria from tissue. Freshly collected heart or muscle samples were washed once in cold PBS, incubated on ice in 4 mL Mito buffer A (220 mM mannitol, 70 mM sucrose, 20 mM HEPES/KOH, 0.5 mM PMSF, 2 mg/mL BSA, 1 mM EDTA/Tris pH 7.4) supplemented with protease and phosphatase inhibitors, homogenized in a motor-driven potter (20 strokes, 1000 rpm) and cell debris was pelleted at 800 *g* for 5 min at 4 °C. The supernatants were collected, the pellet was homogenized again (20 strokes, 1000 rpm), centrifuged at 800 *g* for 5 min at 4 °C, the supernatant was combined with the supernatant from the first homogenization, and centrifuged at 8000 *g* for 5 min at 4 °C. The supernatant was discarded and the pellet was resuspended in 1 mL Mito buffer B (220 mM mannitol, 70 mM sucrose, 20 mM HEPES/KOH, 0.5 mM PMSF, 1 mM EDTA/Tris pH 7.4), centrifuged twice at 8000 *g* for 5 min at 4 °C and the mitochondrial pellet was resuspended in 1 mL buffer B. Finally, the samples were centrifuged at 10,000 *g* for 5 min at 4 °C and the mitochondria were resuspended in 300–500 µL Mito buffer B.

To investigate the localization of the ΔTM mutant, the cytosolic and mitochondrial fractions of cultured cells were separated, as described above. After homogenization at 8000 *g* and centrifugation, the resulting supernatant was designated as the cytosolic fraction and cleared twice by centrifugation at 8000 *g* for 5 min at 4 °C.

Isolation of SSM and IFM. Dissected muscles from the mouse hind limb were washed in 2 mL of Isolation buffer (180 mM KCl, 10 mM EDTA, pH 7.4) on ice. After drying the tissue, it was weighed and cut into smaller pieces with sharp scissors. Depending on the muscle weight, the samples were supplied with four volumes of KEA buffer (180 mM KCl, 10 mM EDTA, 0.5% BSA pH 7.4) compared to the muscle weight (1 mg tissue/4 µl KEA) and homogenized in a motor-driven potter (10 strokes, 2000 rpm). Subsequently, after carefully transferring the homogenate to a tube, it was centrifuged at 100 *g* for 10 min. The supernatant containing the SSM was placed on ice in a new tube while the pellet was weighed and resuspended with two volumes of KEA buffer compared to the pellet weight.

For the collection of the IFM, Nagase (Protease XXIV, Sigma P-8038, 0.1 mg/mL) was added in a 5 µl Nagase/1 mL resuspended pellet ratio for 35 sec with immediate centrifugation at 5900 *g* for 5 min. The supernatant was discarded, and the pellet was resuspended with one volume of KEA buffer and centrifuged at 100 *g* for 10 min. Afterwards, the supernatant containing the IFM and the SSM containing tube were centrifuged at 5900 *g* for 10 min. The pellets were washed three times with one volume of KME buffer (100 mM KCL, 0.5 mM EGTA, pH 7.4) and centrifuged at 5900 *g* for 10 min. After the final washing step, the SSM and IFM were resuspended in 0.5 volumes of KME buffer.

In-gel digestion and sample purification. Proteomic samples of TA muscle tissue and isolated TA muscle mitochondria were prepared using a modified version of the in-gel digestion protocol by[50]. Briefly, lysates were precipitated overnight in four volumes (*v:v*) of ice-cold acetone. Protein pellets were extracted by centrifugation at 13,000 *g* for 10 min and dissolved in Bolt LDS sample buffer (Invitrogen). Dithiothreitol (DTT) was added to a final concentration of 10 mM. The mixtures were heated at 70 °C for 10 min, cooled to room temperature, iodoacetamide (IAA) was added to a final concentration of 55 mM and incubated in the dark for 20 min. Proteins were separated using Bolt 4–12% Bis–Tris Plus gels (Invitrogen), Coomassie-stained, and each lane was cut into six to ten slices. Each slice was chopped into 1 mm cubes, destained with 50% ACN and dehydrated with 100% ACN, digested with 3 ng/µL trypsin/LysC solution (90% trypsin/10% LysC) for 30 min at 4 °C, 50 mM ABC was added to the swollen gel pieces, incubated overnight at 37 °C and digestion was stopped by acidifying the samples with trifluoroacetic acid (TFA). Tryptic peptides were extracted with increasing concentrations of ACN and organic compounds were evaporated using a SpeedVac concentrator Plus (Eppendorf). Acidified samples were desalted using Stop and Go extraction tips[51].

In-solution/on-bead digestion. Eluates from immunoprecipitation experiments were prepared for MS analysis by in-solution/on-bead digestion. Urea-containing samples were reduced by applying DTT at a final concentration of 5 mM for 1 h at RT, alkylated with a final concentration of 40 mM IAA for 30 min in the dark at RT, digested with 1 µL LysC for 2-3 h at RT, diluted with 50 mM ABC to a urea concentration of 2 M, incubated with 1 µL 0.5 mg/mL trypsin overnight at RT, acidified to 1% FA and purified using StageTips.

MS-based proteome analysis. Proteome samples were analyzed using a liquid chromatography tandem mass spectrometry set up in a Q-Exactive™ Plus Hybrid Quadrupole-Orbitrap™ (Thermo Fisher). Chromatographic peptide separation was achieved on PoroShell 120 packed 50 cm analytical columns coupled to an EASY-nLC 1000 HPLC system and a binary buffer system consisting of buffer A (0.1% FA) and buffer B (80% ACN, 0.1% FA). In-gel digested samples were analyzed over a 150 min gradient, raising the content of buffer B from 9 to 29% over 119 min, from 29 to 68% over 5 min, and from 68% to 95% over 16 min. The column was washed with 95% buffer B, buffer B was reduced to 5% over 5 min and the column was re-equilibrated with 5% buffer B for 5 min. Full MS spectra (300–1,750 *m/z*) were recorded at a resolution (R) of 70,000, maximum injection time (max. IT) of 20 ms and AGC target of 3e6. The ten most abundant ion peptides in each full MS scan were selected for HCD fragmentation at nominal collisional energy (NCE) of 25. MS2 spectra were recorded at R = 17,500, maximum IT of 60 ms, and AGC target of 5e5 (Xcalibur version 3.1).

Samples derived from immunoprecipitations and subsequent in-solution/on-bead digestion were measured over a 100-min gradient. The content of buffer B was increased from 13 to 48% within 75 min, increased to 75% over 5 min, washed with 95% buffer B for 10 min, reduced to 5% within 5 min and re-equilibrated with 5% buffer B for 5 min.

MS data processing and analysis. Raw MS data were analyzed using MaxQuant analysis software and the implemented Andromeda software (1.5.3.8)[52, 53]. Peptides and proteins were identified using the mouse UniProt database with common contaminants (FASTA file downloaded on 16/6/2017, size: 16,890 entries). All MaxQuant parameters were set to default values. Trypsin was selected as the digestion enzyme; a maximum of two missed cleavages was allowed. For SILAC, peptide pairs were quantified by setting Lys6 as the heavy label. Enzyme specificity was set to LysC with an additional allowance of cleavage N-terminal to proline.

Methionine oxidation and N-terminal acetylation were set as variable modifications; carbamidomethylation of cysteines was chosen as a fixed modification. Except for the SILAC-labeled samples, the label-free quantification (LFQ) algorithm was used to quantify the measured peptides and the match between runs option was enabled to quantify peptides with a missing MS2 spectrum. A minimum ratio count of 2 was used for SILAC quantification.

Statistical analysis was performed using Perseus (1.5.5.3-1.6.5.0) software. Potential contaminants and reverse peptides were excluded, and values were $\log_2$ transformed. Two-sided *t*-tests were used to identify differentially expressed proteins between genotypes (*Perm1*$^{-/-}$ or wild type) or conditions (immunoprecipitation or control). Identified peptides were annotated with the following Gene Ontology terms: Biological Process, Molecular Function, Cellular Compartment, and Kyoto Encyclopedia of Genes and Genomes terms. Graphical visualizations were achieved using Instant Clue software[54].

Western blot analysis. Protein lysates (10–20 µg) were incubated with 4x Laemmli buffer and 50 mM DTT for 10 min at 70 °C and SDS-PAGE was performed according to standard procedures using stain-free casting solutions from Bio-Rad. Proteins were electroblotted onto polyvinylidene fluoride (PVDF) membranes using a Trans-Blot Turbo Transfer System (Bio-Rad). Unblotted gels were developed using the ChemiDoc™ Touch Imaging System (Bio-Rad) with the stain-free option. Blotted membranes were developed using Clarity Western ECL Substrate (Bio-Rad). The intensities of the bands were quantified and normalized to the stain-free image using ImageJ software (version 1.8.0)[55].

Complexome profiling of mitochondria. Complexome profiling of mitochondria isolated from heart and muscle tissue was performed as previously described[56]. Freshly isolated mitochondria were lysed under non-denaturing conditions with 1% digitonin, 100 µg protein samples were loaded onto native gradient gels to separate the intact proteins complexes using a buffer containing Coomassie, as previously described[57]. Each gel lane was cut into 70 pieces and prepared for mass spectrometry analysis by in-gel digestion. Raw data were analyzed using iBAQ and individual profiles were analyzed with the NOVA tool (version 0.5.7)[28].

Oxygen consumption measurements. Oxygraphic measurements were performed on 40 µg of isolated muscle mitochondria as previously described[14]. The Oxygraph-2k (Oroboros Instruments) was used to measure oxygen consumption rate. The mitochondria were added after air equilibration of the mitochondrial respiration buffer. First, the OXPHOS state for complex I was determined by adding 5 mM pyruvate, 2 mM malate, 10 mM glutamate, and 2 mM ADP. Convergent electron flow through complexes I and II was measured by adding 10 mM succinate. Next, LEAK respiration was assessed by inhibition of the ATP synthase with oligomycin (1.5 µg/mL). Carbonyl cyanide-p- trifluoromethoxy-phenylhydrazone (FCCP, 0.5 µM) was titrated to determine maximal electron transfer system (ETS) capacity. Subsequently, complex I was inhibited by the addition of 0.5 µM rotenone to determine the maximal ETS capacity with electron flow through complex II only. Finally, residual oxygen consumption (ROX) was measured by inhibiting complex III using 2.5 µM antimycin A. Analysis was performed using the DatLab software (version 7.4.0.4; Oroboros Instruments.

Determination of relative mtDNA copy number. DNA was extracted from tissue lysates and qPCR was performed as previously described[14] to determine the relative mtDNA content of the soleus muscle tissues of *Perm1*$^{-/-}$ mice. DNA was extracted from tissue lysates by incubation at 55 °C overnight in 350 µl DNA extraction buffer (0.5% SDS, 0.1 M NaCl, 50 mM Tris/HCl pH 8.0, 20 mM EDTA) supplemented with proteinase K. 350 µL phenol-chloroform-isoamylalcohol was added to the samples, mixed gently, and centrifuged for 5 min at 500 *g* and 4 °C. The upper phase was transferred to a new tube and 350 µL phenol-chloroform-isoamylalcohol was added, mixed gently, and centrifuged as before. The upper phase was transferred to a new tube, mixed with 650 µL of 100% ethanol and 65 µL of 7.5 mM ammonium acetate, incubated at −20 °C for 1 h. centrifuged at 15,000 *g* for 30 min at 4 °C, and the pellet was washed with 70% ethanol and resuspended in 10 mM Tris/HCl pH 8.5.

The extracted DNA (25 ng) was subsequently used for qPCR with two technical replicates. The expression of the cytochrome B gene (primers: GCTTTCCACTTCATCTTACCATTT and TGTTGGGTTGTTTGATCCTG) was normalized to the nuclear beta-actin gene (primers: GGAAAAGAGCCTCAGGGCAT and GAAGAGCTATGAGCTGCCTGA). The qPCR reactions were performed using KiCqStart® SYBR® Green qPCR ReadyMix™ (Sigma) on a CFX connect real-time PCR detection system (Bio-Rad) at 95 °C for 7 min, followed by 35 cycles of 95 °C for 10 s and 60 °C for 30 s. Data were collected using the CFX Manager™ Software for Bio-Rad CFX Real-Time PCR systems (version 3.0). Primers are listed in Supplementary Table 1.

Determination of mitochondrial membrane potential in FDB fibers. Mitochondrial membrane potential was measured in isolated fibers FDB muscles as previously described[58]. FDB myofibers were placed in 1 mL Tyrode's buffer and loaded with 2.5 nM TMRM supplemented with 1 µM cyclosporine H (a P-glycoprotein inhibitor) for 30 min at 37 °C. Sequential images of TMRM fluorescence were acquired every 60 s using a 20× magnification 0.5 numerical aperture UPLANSL objective (Olympus). Oligomycin (Olm, 5 µM) was added after 3 min and the protonophore carbonyl cyanide *p*-trifluoromethoxy-phenylhydrazone (FCCP, 4 µM) was added after 50 min. Images of TMRM fluorescence were acquired, stored, and analyzed over mitochondrial regions of interest using ImageJ software (1.8.0).

Electron microscopy. Electron microscopy studies were performed with the assistance of the CECAD imaging facility. Tissues were dissected, fixed overnight in 2.5% glutaraldehyde, dehydrated in an ascending acetone series, embedded in

epoxy resin, sectioned using an ultramicrotome, mounted on a grid and examined using a JEOL JEM2100PLUS electron microscope.

Statistics and reproducibility. Statistical tests used for the individual experiments are provided in the figure legends of the respective figure. If not stated differently, immunoblottings, immunoprecipitations, immunohistochemical staining experiments, and in-vitro studies were conducted at least two times independently. All attempts of replication were successful.

Reporting summary. Further information on research design is available in the Nature Research Reporting Summary linked to this article.

Data availability

The mass spectrometry proteomics data have been deposited to the ProteomeXchange Consortium via the PRIDE partner repository[59] with the dataset identifier PXD025745. All unique materials generated are readily available from the authors. Source data are provided with this paper.

Received: 20 May 2020; Accepted: 20 July 2021;
Published online: 12 August 2021

References

1. Schiaffino, S. & Reggiani, C. Fiber types in mammalian skeletal muscles. *Physiol. Rev.* **91**, 1447–1531 (2011).
2. Hawley, J. A., Hargreaves, M., Joyner, M. J. & Zierath, J. R. Integrative biology of exercise. *Cell* **159**, 738–749 (2014).
3. Riva, A., Tandler, B., Loffredo, F., Vazquez, E. & Hoppel, C. Structural differences in two biochemically defined populations of cardiac mitochondria. *Am. J. Physiol. Heart Circ. Physiol.* **289**, H868–H872 (2005).
4. Glancy, B. et al. Mitochondrial reticulum for cellular energy distribution in muscle. *Nature* **523**, 617–620 (2015).
5. Koves, T. R. et al. Subsarcolemmal and intermyofibrillar mitochondria play distinct roles in regulating skeletal muscle fatty acid metabolism. *Am. J. Physiol. Cell Physiol.* **288**, C1074–C1082 (2005).
6. Palmer, J. W., Tandler, B. & Hoppel, C. L. Heterogeneous response of subsarcolemmal heart mitochondria to calcium. *Am. J. Physiol.* **250**, H741–H748 (1986).
7. Lin, J., Handschin, C. & Spiegelman, B. M. Metabolic control through the PGC-1 family of transcription coactivators. *Cell Metab.* **1**, 361–370 (2005).
8. Lin, J. et al. Transcriptional co-activator PGC-1 alpha drives the formation of slow-twitch muscle fibres. *Nature* **418**, 797–801 (2002).
9. Rowe et al. coactivators in cardiac development and disease. *Circ. Res.* **107**, 825–838 (2010).
10. Ojuka, E. O., Jones, T. E., Han, D. H., Chen, M. & Holloszy, J. O. Raising Ca2 + in L6 myotubes mimics effects of exercise on mitochondrial biogenesis in muscle. *FASEB J.* **17**, 675–681 (2003).
11. Handschin, C., Rhee, J., Lin, J., Tarr, P. T. & Spiegelman, B. M. An autoregulatory loop controls peroxisome proliferator-activated receptor gamma coactivator 1alpha expression in muscle. *Proc. Natl Acad. Sci. USA* **100**, 7111–7116 (2003).
12. Cho, Y., Hazen, B. C., Russell, A. P. & Kralli, A. Peroxisome proliferator-activated receptor gamma coactivator 1 (PGC-1)- and estrogen-related receptor (ERR)-induced regulator in muscle 1 (Perm1) is a tissue-specific regulator of oxidative capacity in skeletal muscle cells. *J. Biol. Chem.* **288**, 25207–25218 (2013).
13. Cho, Y. et al. Perm1 enhances mitochondrial biogenesis, oxidative capacity, and fatigue resistance in adult skeletal muscle. *FASEB J.* **30**, 674–687 (2016).
14. Aravamudhan, S. et al. Phosphoproteomics of the developing heart identifies PERM1 - An outer mitochondrial membrane protein. *J. Mol. Cell. Cardiol.* **154**, 41–59 (2021).
15. Cho, Y. et al. Perm1 regulates CaMKII activation and shapes skeletal muscle responses to endurance exercise training. *Mol. Metab.* **23**, 88–97 (2019).
16. Zerbes, R. M. et al. Mitofilin complexes: conserved organizers of mitochondrial membrane architecture. *Biol. Chem.* **393**, 1247–1261 (2012).
17. Pfanner, N. et al. Uniform nomenclature for the mitochondrial contact site and cristae organizing system. *J. Cell Biol.* **204**, 1083–1086 (2014).
18. Huynen, M. A., Muhlmeister, M., Gotthardt, K., Guerrero-Castillo, S. & Brandt, U. Evolution and structural organization of the mitochondrial contact site (MICOS) complex and the mitochondrial intermembrane space bridging (MIB) complex. *Biochim. Biophys. Acta* **1863**, 91–101 (2016).
19. Guarani, V. et al. QIL1 is a novel mitochondrial protein required for MICOS complex stability and cristae morphology. *Elife* **4**, e06265 (2015).
20. Rampelt, H. et al. Assembly of the mitochondrial cristae organizer Mic10 is regulated by Mic26-Mic27 antagonism and cardiolipin. *J. Mol. Biol.* **430**, 1883–1890 (2018).
21. John, G. B. et al. The mitochondrial inner membrane protein mitofilin controls cristae morphology. *Mol. Biol. Cell* **16**, 1543–1554 (2005).
22. Ott, C. et al. Sam50 functions in mitochondrial intermembrane space bridging and biogenesis of respiratory complexes. *Mol. Cell Biol.* **32**, 1173–1188 (2012).
23. Gouspillou, G. et al. The relationship between muscle fiber type-specific PGC-1α content and mitochondrial content varies between rodent models and humans. *PloS ONE* **9**, e103044–e103044 (2014).
24. Kayar, S. R., Claassen, H., Hoppeler, H. & Weibel, E. R. Mitochondrial distribution in relation to changes in muscle metabolism in rat soleus. *Respir. Physiol.* **64**, 1–11 (1986).
25. Tanaka, M. et al. A novel RNA-binding protein, Ossa/C9orf10, regulates activity of Src kinases to protect cells from oxidative stress-induced apoptosis. *Mol. Cell Biol.* **29**, 402–413 (2009).
26. Gustafsson, A. B. Bnip3 as a dual regulator of mitochondrial turnover and cell death in the myocardium. *Pediatr. Cardiol.* **32**, 267–274 (2011).
27. Kallabis, S. et al. High-throughput proteomics fiber typing (ProFiT) for comprehensive characterization of single skeletal muscle fibers. *Skelet. Muscle* **10**, 7 (2020).
28. Giese, H. et al. NOVA: a software to analyze complexome profiling data. *Bioinformatics* **31**, 440–441 (2015).
29. Jones, D. T. Improving the accuracy of transmembrane protein topology prediction using evolutionary information. *Bioinformatics* **23**, 538–544 (2007).
30. Bennett, V. & Healy, J. Organizing the fluid membrane bilayer: diseases linked to spectrin and ankyrin. *Trends Mol. Med* **14**, 28–36 (2008).
31. Schild, M. et al. Basal and exercise induced label-free quantitative protein profiling of m. vastus lateralis in trained and untrained individuals. *J. Proteom.* **122**, 119–132 (2015).
32. Brinkmann, C. et al. Endurance training alters YKL40, PERM1, and HSP70 skeletal muscle protein contents in men with type 2 diabetes mellitus. *Endocr. Res.* **44**, 1–8 (2019).
33. Tsuchiya, Y. et al. Involvement of the protein kinase CK2 in the regulation of mammalian circadian rhythms. *Sci. Signal* **2**, ra26 (2009).
34. Al Quobaili, F. & Montenarh, M. CK2 and the regulation of the carbohydrate metabolism. *Metabolism* **61**, 1512–1517 (2012).
35. Wu, C., Xu, G., Tsai, S. A., Freed, W. J. & Lee, C. T. Transcriptional profiles of type 2 diabetes in human skeletal muscle reveal insulin resistance, metabolic defects, apoptosis, and molecular signatures of immune activation in response to infections. *Biochem. Biophys. Res. Commun.* **482**, 282–288 (2017).
36. Glick, D. et al. BNip3 regulates mitochondrial function and lipid metabolism in the liver. *Mol. Cell Biol.* **32**, 2570–2584 (2012).
37. Tsai, P. I., Papakyrikos, A. M., Hsieh, C. H. & Wang, X. Drosophila MIC60/mitofilin conducts dual roles in mitochondrial motility and crista structure. *Mol. Biol. Cell* **28**, 3471–3479 (2017).
38. Mado, K. et al. On the role of tubulin, plectin, desmin, and vimentin in the regulation of mitochondrial energy fluxes in muscle cells. *Am. J. Physiol. Cell Physiol.* **316**, C657–C667 (2019).
39. Kayar, S. R., Conley, K. E., Claassen, H. & Hoppeler, H. Capillarity and mitochondrial distribution in rat myocardium following exercise training. *J. Exp. Biol.* **120**, 189–199 (1986).
40. Nekrasova, O. E. et al. Vimentin intermediate filaments modulate the motility of mitochondria. *Mol. Biol. Cell* **22**, 2282–2289 (2011).
41. Bellin, R. M., Huiatt, T. W., Critchley, D. R. & Robson, R. M. Synemin may function to directly link muscle cell intermediate filaments to both myofibrillar Z-lines and costameres. *J. Biol. Chem.* **276**, 32330–32337 (2001).
42. Ayalon, G., Davis, J. Q., Scotland, P. B. & Bennett, V. An ankyrin-based mechanism for functional organization of dystrophin and dystroglycan. *Cell* **135**, 1189–1200 (2008).
43. Bennett, V. & Baines, A. J. Spectrin and ankyrin-based pathways: metazoan inventions for integrating cells into tissues. *Physiol. Rev.* **81**, 1353–1392 (2001).
44. He, M., Tseng, W. C. & Bennett, V. A single divergent exon inhibits ankyrin-B association with the plasma membrane. *J. Biol. Chem.* **288**, 14769–14779 (2013).
45. Lorenzo, D. N. et al. A PIK3C3-ankyrin-B-dynactin pathway promotes axonal growth and multiorganelle transport. *J. Cell Biol.* **207**, 735–752 (2014).
46. Deacon, R. M. Measuring the strength of mice. *J. Vis. Exp.* (2013).
47. Kondziella, W. A new method for the measurement of muscle relaxation in white mice. *Arch. Int. Pharmacodyn. Ther.* **152**, 277–284 (1964).
48. Baraldo, M. et al. Skeletal muscle mTORC1 regulates neuromuscular junction stability. *J. Cachexia Sarcopenia Muscle* **11**, 208–225 (2020).
49. Lamprecht, M. R., Sabatini, D. M. & Carpenter, A. E. CellProfiler: free, versatile software for automated biological image analysis. *Biotechniques* **42**, 71–75 (2007).

50. Shevchenko, A., Tomas, H., Havlis, J., Olsen, J. V. & Mann, M. In-gel digestion for mass spectrometric characterization of proteins and proteomes. *Nat. Protoc.* **1**, 2856–2860 (2006).
51. Rappsilber, J., Mann, M. & Ishihama, Y. Protocol for micro-purification, enrichment, pre-fractionation and storage of peptides for proteomics using StageTips. *Nat. Protoc.* **2**, 1896–1906 (2007).
52. Cox, J. & Mann, M. MaxQuant enables high peptide identification rates, individualized p.p.b.-range mass accuracies and proteome-wide protein quantification. *Nat. Biotechnol.* **26**, 1367–1372 (2008).
53. Cox, J. et al. Andromeda: a peptide search engine integrated into the MaxQuant environment. *J. Proteome Res.* **10**, 1794–1805 (2011).
54. Nolte, H., MacVicar, T. D., Tellkamp, F. & Kruger, M. Instant clue: a software suite for interactive data visualization and analysis. *Sci. Rep.* **8**, 12648 (2018).
55. Schneider, C. A., Rasband, W. S. & Eliceiri, K. W. NIH Image to ImageJ: 25 years of image analysis. *Nat. Methods* **9**, 671–675 (2012).
56. Heide, H. et al. Complexome profiling identifies TMEM126B as a component of the mitochondrial complex I assembly complex. *Cell Metab.* **16**, 538–549 (2012).
57. Wittig, I. & Schagger, H. Structural organization of mitochondrial ATP synthase. *Biochim. Biophys. Acta* **1777**, 592–598 (2008).
58. Mammucari, C. et al. FoxO3 controls autophagy in skeletal muscle in vivo. *Cell Metab.* **6**, 458–471 (2007).
59. Perez-Riverol, Y. et al. The PRIDE database and related tools and resources in 2019: improving support for quantification data. *Nucleic Acids Res.* **47**, D442–D450 (2019).

Acknowledgements

The authors acknowledge Lena Abraham for technical assistance and Kerstin Selbach for helpful comments on this manuscript. We thank the CECAD Proteomics and Imaging Facility (and Janine Klask) for their support in mass spectrometry and electron microscopy. This work was supported by the Cologne Cluster of Excellence on Cellular Stress Responses in Aging-associated Diseases (CECAD) EXC 299/2, the Deutsche Forschungsgemeinschaft (DFG, German Research Fundation) SFB 1218 under project number 269925409 and the Center for Molecular Medicine Cologne.

Author contributions

T.B., C.T., S.A., M.K. designed the experiments and analyzed results. L.K. performed Lys6 incorporation analysis and calculated absolute half-lives. W.B. performed running experiments and weight tests. V.R., L.N., and B.B. performed skeletal muscle force and mitochondrial membrane potential measurements. D.H.R. performed oxygraphic measurements. Th.Br. and A.T. provided guidance throughout the study. M.K. wrote the manuscript and all authors read and approved the final version of the manuscript.

Funding

Open Access funding enabled and organized by Projekt DEAL.

Competing interests

The authors declare no competing interests.

Additional information

Supplementary information The online version contains supplementary material available at https://doi.org/10.1038/s41467-021-25185-3.

Correspondence and requests for materials should be addressed to M.Küg.

Peer review information *Nature Communications* thanks the anonymous reviewers for their contributions to the peer review of this work.

Reprints and permission information is available at http://www.nature.com/reprints

Publisher's note Springer Nature remains neutral with regard to jurisdictional claims in published maps and institutional affiliations.

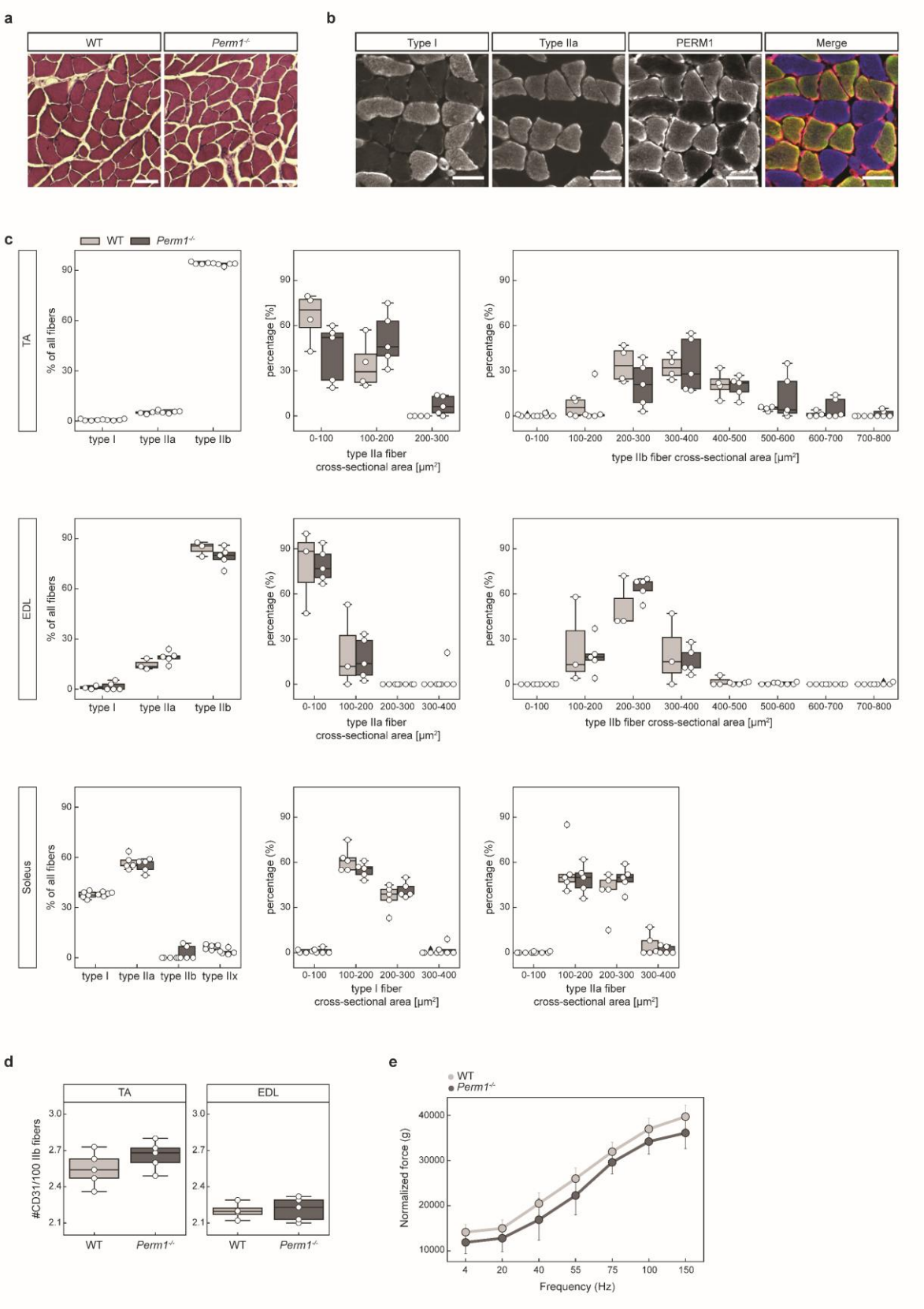
Open Access This article is licensed under a Creative Commons Attribution 4.0 International License, which permits use, sharing, adaptation, distribution and reproduction in any medium or format, as long as you give appropriate credit to the original author(s) and the source, provide a link to the Creative Commons license, and indicate if changes were made. The images or other third party material in this article are included in the article's Creative Commons license, unless indicated otherwise in a credit line to the material. If material is not included in the article's Creative Commons license and your intended use is not permitted by statutory regulation or exceeds the permitted use, you will need to obtain permission directly from the copyright holder. To view a copy of this license, visit http://creativecommons.org/licenses/by/4.0/.

© The Author(s) 2021

Name	Purpose	Target vector	Forward primer	Reverse primer
Perm1_FLAGtag	plasmid generation for expression of Perm1 in cell culture	pcDNA5/TO_MCS_FLAGtag	AAAGGGAAAGGTACCATGGACAACTTCCAGTACAG	TTTCCCTTTCTCGAGGCAGCTGGGGTTTGA
Perm1_dTM	deletion of transmembrane domain	pcDNA5/TO_Perm1_FLAGtag	GCCCCCTCTCAGATCTACAAGCCCCAGATGC	GATCTGAGAGGGGGCTCCGTAGTTCC
mtDNA_b_actin	mtDNA copy number qPCR	/	GGAAAAGAGCCTCAGGGCAT	GAAGAGCTATGAGCTGCCTGA
mtDNA_cytb	mtDNA copy number qPCR	/	GCTTTCCACTTCATCTTACCATTT	TGTTGGGTTGTTTGATCCTG

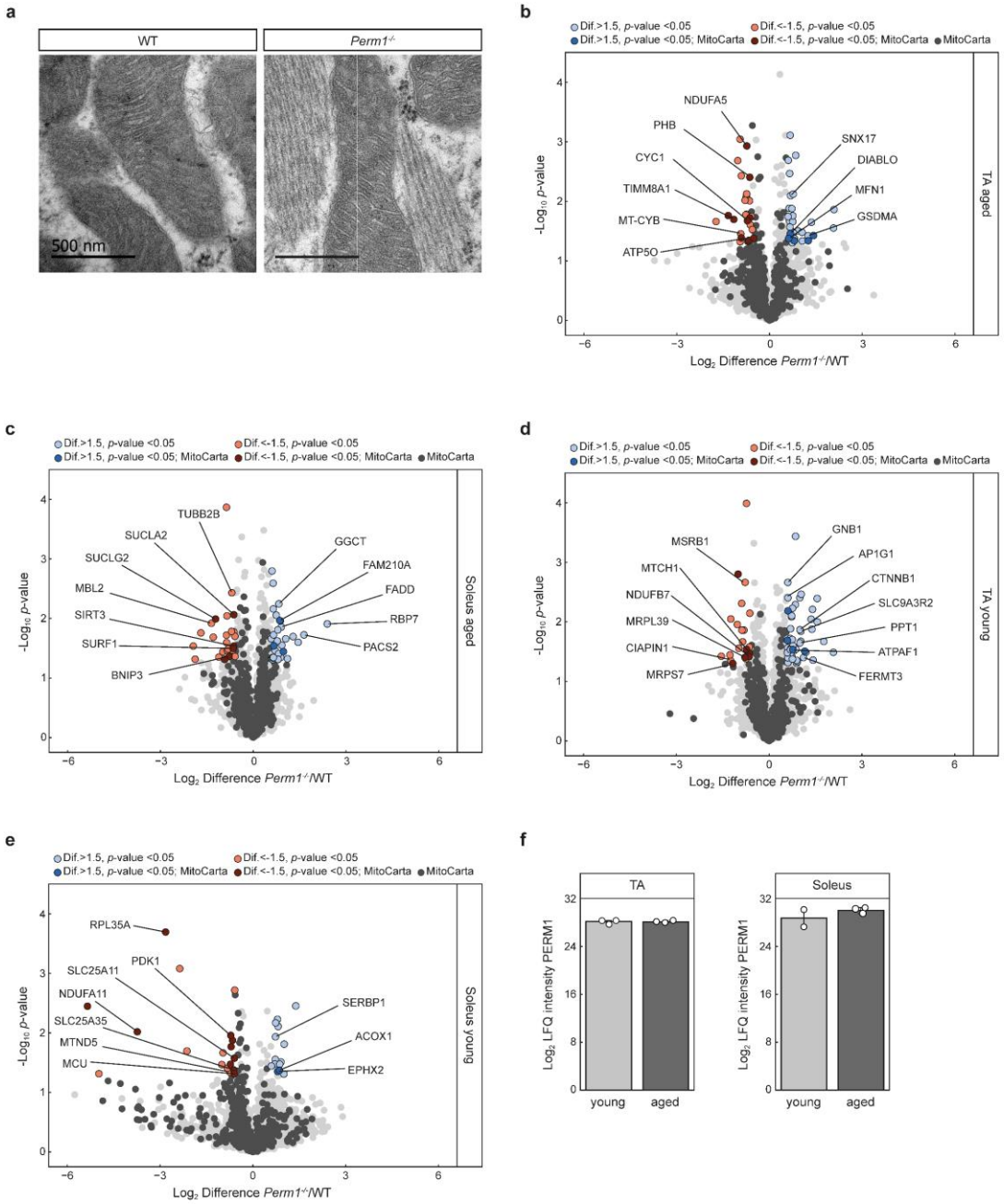
Supplementary Table 1. List of primers.

Detailed list of all primers used in this study.


a
WT
Perm1-/-
b
Type I
Type IIa
PERM1
Merge
c
WT
Perm1-/-
TA
EDL
Soleus
% of all fibers
type I
type IIa
type IIb
type IIx
percentage [%]
percentage (%)
type IIa fiber cross-sectional area [µm²]
type IIb fiber cross-sectional area [µm²]
type I fiber cross-sectional area [µm²]
d
TA
EDL
#CD31/100 IIb fibers
e
Normalized force (g)
Frequency (Hz)

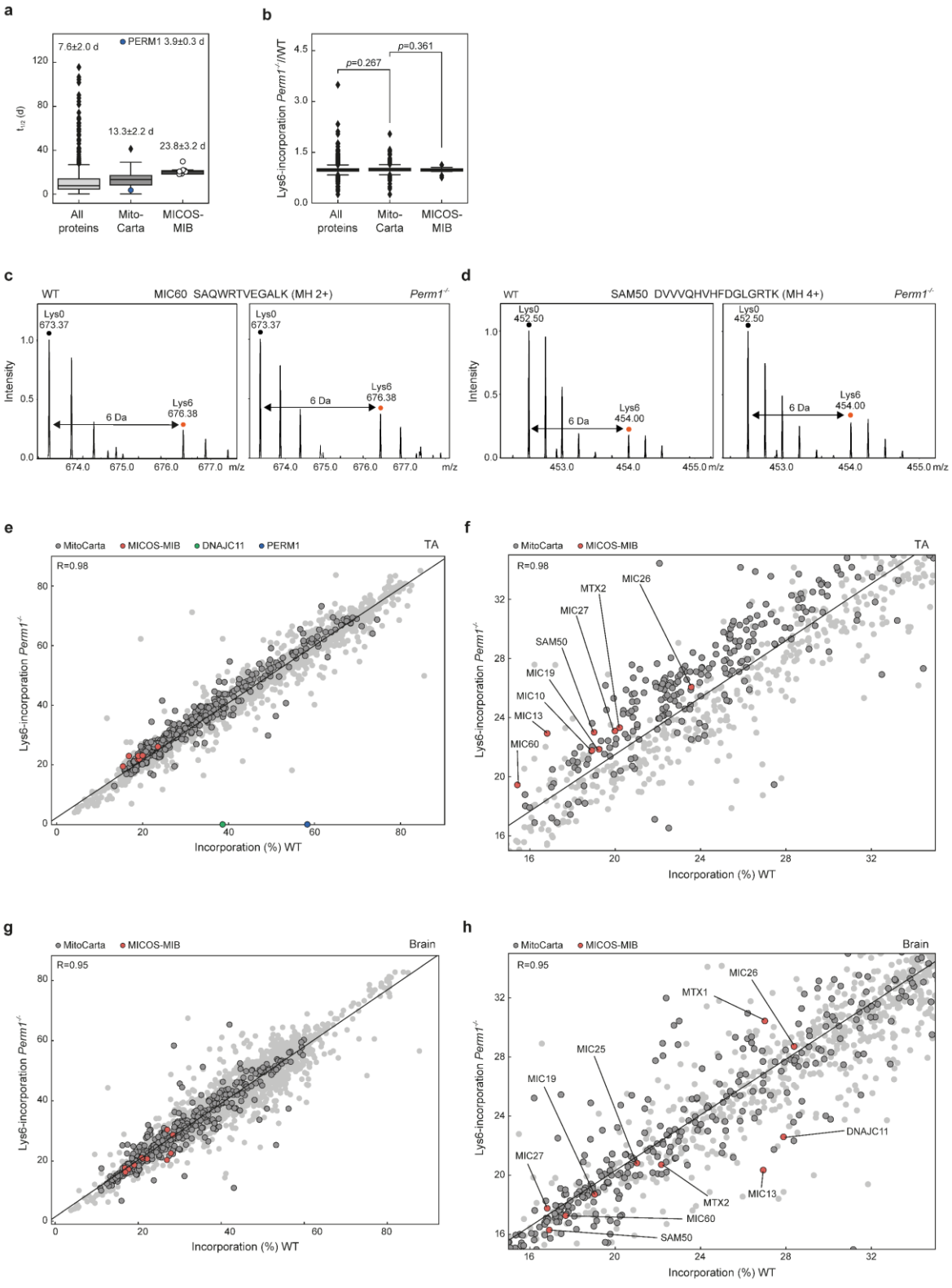
Supplementary figure 1. Deletion of *Perm1* causes no changes in fiber-type composition and cross-sectional area. (a) Hematoxylin and eosin (H&E) staining of mouse soleus cross sections demonstrated no changes between *Perm1*$^{-/-}$ mice and wild-type controls. Scale, 50 µm. (b) Immunohistochemical staining of soleus muscles of wild-type mice using myosin heavy chain-specific antibodies MyHC-I (type I fibers, blue) and MyHC-IIa (type IIa fibers, green) and anti-PERM1 (red) revealed localization of PERM1 predominantly in type IIa fibers. Scale, 50 µm. (c) Quantification of (left) fiber-type composition (right) and fiber cross-sectional area [µm^2] in the TA (top), EDL (middle) and soleus (bottom) muscles of *Perm1*$^{-/-}$ and wild-type mice based on staining with myosin heavy chain specific antibodies (*n*=3-5 mice per group). (d) Quantification of the number of capillaries per 100 type IIb fibers in the TA (left) and EDL (right) muscles of *Perm1*$^{-/-}$ and wild-type mice based on staining with a CD31/PECAM antibody (*n*=5 mice per group). (e) Force generated by the gastrocnemius muscle of *Perm1*$^{-/-}$ and wild-type control mice after electrical stimulation normalized for muscle mass at indicated frequencies (*n*=8 mutant mice; *n*=12 wild-type mice). *p*-value (Genotype) = 0.09, *p*-value (Frequency) = 1.6E-13, *p*-value (Frequency x Genotype) = 6.0E-04; two-way ANOVA.

Box plots (c+d) represent the median, 25th, and 75th percentiles, maximum and minimum are connected through whiskers, and individual data points are added on top. Outliers are defined as Q_1–1.8 IQR and Q_3+1.8 IQR. Data (e) are presented as mean values ± 0.95 CI. Source data are provided as Source Data file.


a
WT
Perm1-/-
500 nm
b
Dif.>1.5, p-value <0.05
Dif.<-1.5, p-value <0.05
Dif.>1.5, p-value <0.05; MitoCarta
Dif.<-1.5, p-value <0.05; MitoCarta
MitoCarta
NDUFA5
PHB
CYC1
TIMM8A1
MT-CYB
ATP5O
SNX17
DIABLO
MFN1
GSDMA
TA aged
-Log10 p-value
Log2 Difference Perm1-/-/WT
c
TUBB2B
SUCLA2
SUCLG2
MBL2
SIRT3
SURF1
BNIP3
GGCT
FAM210A
FADD
RBP7
PACS2
Soleus aged
d
MSRB1
MTCH1
NDUFB7
MRPL39
CIAPIN1
MRPS7
GNB1
AP1G1
CTNNB1
SLC9A3R2
PPT1
ATPAF1
FERMT3
TA young
e
RPL35A
PDK1
SLC25A11
NDUFA11
SLC25A35
MTND5
MCU
SERBP1
ACOX1
EPHX2
Soleus young
f
TA
Soleus
Log2 LFQ intensity PERM1
young
aged

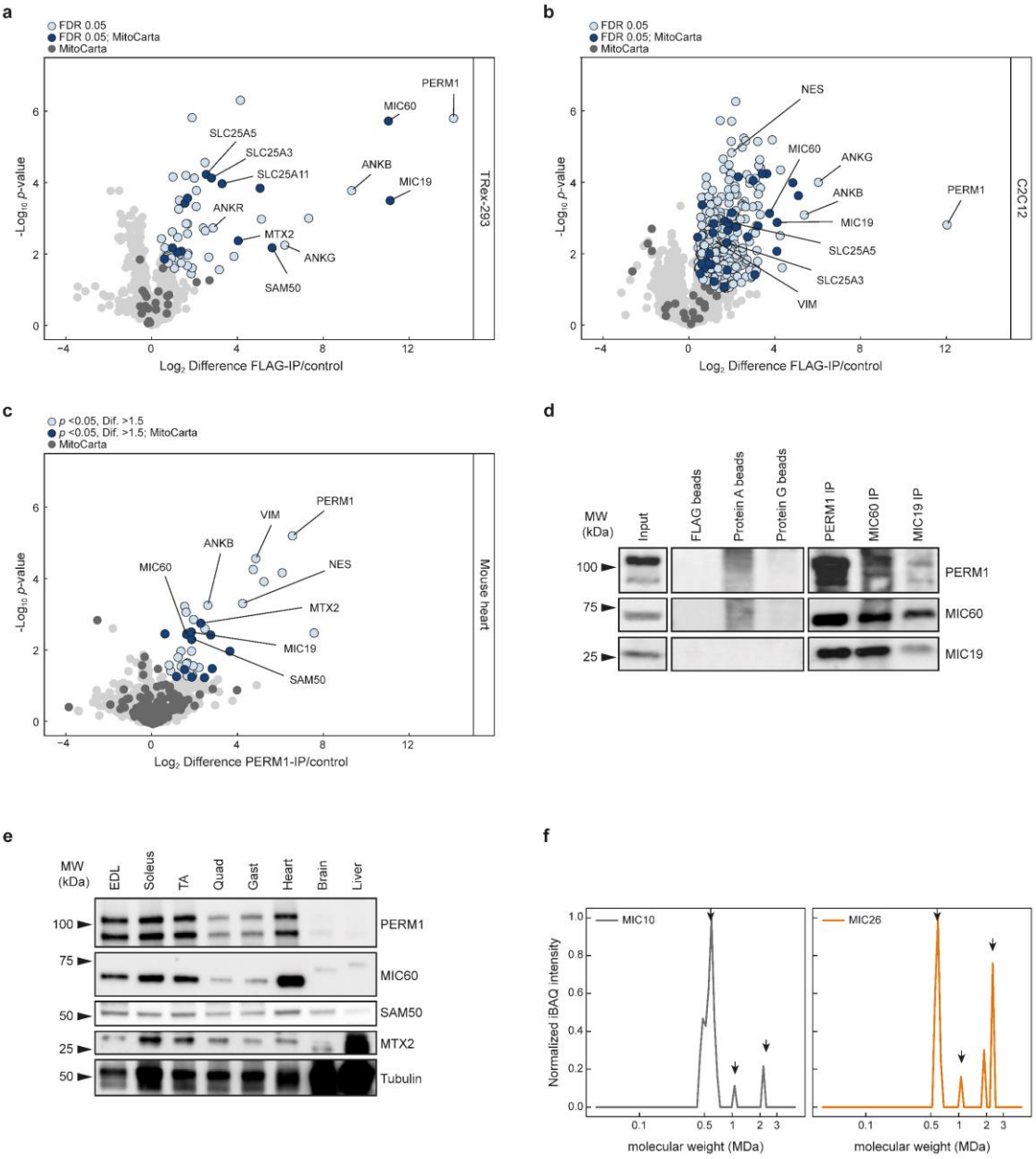
Supplementary Figure 2. Cristae structure and proteomic analysis of young and aged whole TA and soleus muscle tissues from *Perm1*-deficient mice. (a) Electron microscopic analysis of TA muscle showing intact mitochondrial cristae structures in *Perm1*$^{-/-}$ mice and wild-type mice. Scale, 500 nm. (b-e) Volcano plots depicting significantly regulated proteins in *Perm1*$^{-/-}$ (b+c) TA and soleus muscle tissues (d+e) of (b+d) 3-month-old and (c+e) 24-month-old mice compared to wild-type mice (TA young n=3 mice per group; TA aged n=3 mice per group; soleus young n=2 mice per group; soleus aged n=3 mice per group). Cut-off was defined as $p < 0.05$ with a fold change >1.5. Darker colors indicate the MitoCarta 2.0 annotations. (f) Comparison of the $\log_2$ LFQ intensities of PERM1 obtained in young and aged TA and soleus muscles from *Perm1*$^{-/-}$ and wild-type mice. PERM1 LFQ intensity was based on 27 unique peptides (TA young n=3 mice per group; TA aged n=3 mice per group; soleus young n=2 mice per group; soleus aged n=3 mice per group).

(b-e) unpaired two-sided Student's t-test, S_0=0.1. Data (f) are presented as mean values ± 0.95 CI. Source data are provided as Source Data file and in Supplementary Data S2.


a
PERM1 3.9±0.3 d
7.6±2.0 d
13.3±2.2 d
23.8±3.2 d
t1/2 (d)
All proteins
Mito-Carta
MICOS-MIB
b
p=0.267
p=0.361
Lys6-incorporation Perm1-/-/WT
c
WT
MIC60 SAQWRTVEGALK (MH 2+)
Perm1-/-
Lys0 673.37
Lys6 676.38
6 Da
Intensity
m/z
d
SAM50 DVVVQHVHFDGLGRTK (MH 4+)
Lys0 452.50
Lys6 454.00
e
MitoCarta
MICOS-MIB
DNAJC11
PERM1
TA
R=0.98
Lys6-incorporation Perm1-/-
Incorporation (%) WT
f
MIC26
MTX2
MIC27
SAM50
MIC19
MIC10
MIC13
MIC60
g
Brain
R=0.95
h
MIC25
DNAJC11

Supplementary Figure 3. pSILAC-labelling of TA and brain tissues. (a) Calculated half-lives of mitochondrial and MICOS-MIB proteins in soleus muscles of mice fed with a Lys diet for 1-4 weeks (*n*=3 mice per timepoint). (b) Lys6-incorporation rates of MitoCarta-annotated proteins and MICOS-MIB complex-associated proteins were comparable in *Perm1*$^{-/-}$ mice and wild-type controls fed a SILAC diet for 14 days (*n*=3 mice per group). (c+d) MS- spectra of MIC60 (c) and SAM50 (d) in wild-type and *Perm1*$^{-/-}$ TA muscle depicting light (Lys0) and heavy (Lys6) labeled peptides from mice fed a SILAC diet for 14 days. (e-h) Scatter plots of the ratios of *Perm1*$^{-/-}$ to wild-type control Lys6-incorporation in (e+f) TA muscle and (g+h) brain tissue; proteins of the MICOS-MIB complex are highlighted. The Lys6-incorporation rates for PERM1 and DNAJC11 were retroactively added to the *x*-axis in (e), since these proteins were exclusively detected in wild-type muscles.

Box plots (a+b) represent the median, 25th, and 75th percentiles, maximum and minimum are connected through whiskers. Outliers are defined as Q_1–1.8 IQR and Q_3+1.8 IQR. (b) unpaired two-sided Mann-Whitney *U*-test. Source data are provided in Supplementary Data S3+S5.


a
FDR 0.05
FDR 0.05; MitoCarta
MitoCarta
PERM1
MIC60
SLC25A5
SLC25A3
SLC25A11
ANKB
MIC19
ANKR
MTX2
ANKG
SAM50
TRex-293
-Log10 p-value
Log2 Difference FLAG-IP/control
b
FDR 0.05
FDR 0.05; MitoCarta
MitoCarta
NES
MIC60
ANKG
ANKB
PERM1
MIC19
SLC25A5
SLC25A3
VIM
C2C12
-Log10 p-value
Log2 Difference FLAG-IP/control
c
p <0.05, Dif. >1.5
p <0.05, Dif. >1.5; MitoCarta
MitoCarta
PERM1
VIM
ANKB
MIC60
NES
MTX2
MIC19
SAM50
Mouse heart
-Log10 p-value
Log2 Difference PERM1-IP/control
d
MW (kDa)
Input
FLAG beads
Protein A beads
Protein G beads
PERM1 IP
MIC60 IP
MIC19 IP
100
75
25
PERM1
MIC60
MIC19
e
MW (kDa)
EDL
Soleus
TA
Quad
Gast
Heart
Brain
Liver
100
75
50
25
50
PERM1
MIC60
SAM50
MTX2
Tubulin
f
MIC10
MIC26
Normalized iBAQ intensity
molecular weight (MDa)
molecular weight (MDa)

Supplementary Figure 4. Various PERM1 immunoprecipitation approaches and complexome profiling of heart mitochondria. (a-c) Volcano plots depicting significantly enriched proteins after immunoprecipitation of PERM1 in (a) TREx-293 cells stably expressing *Perm1*-FLAG, (b) undifferentiated C2C12 cells transfected with *Perm1*-FLAG, and (c) heart from wild-type mice. (n=3 samples per group and experiment). (d) Co-immunoprecipitation of *Perm1*-FLAG, MIC60, and MIC19 in TREx-293 cells stably overexpressing *Perm1*-FLAG and subsequent Western blotting using antibodies against PERM1, MIC60, and MIC19. (e) Protein levels of PERM1, MIC60, SAM50, and MTX2 in various mouse muscles and organs. (f) Complexome profiling of muscle mitochondria. Profiles of MIC10 and MIC26; iBAQ-values were maximum normalized. Arrows indicate the three main complex assemblies.

(a,b) unpaired two-sided Student's *t*-test, S_0=0.1, permutation-based FDR=0.05, 500 randomizations. (c) unpaired two-sided Student's *t*-test, S_0=0.1. Source data are provided as Source Data file and in Supplementary Data S4.